

# Electro-optic Control of Quantum Measurements

Benjamin Caird Buchler

A thesis submitted for the degree of  
Doctor of Philosophy of the  
The Australian National University

September, 2001



---

# Declaration

---

This thesis is an account of research undertaken between January 1998 and September 2001 at The Department of Physics, Faculty of Science, The Australian National University, Canberra, Australia.

Except where acknowledged in the customary manner, the material presented in this thesis is, to the best of my knowledge, original and has not been submitted in whole or part for a degree in any university.

---

Benjamin C. Buchler  
September, 2001



---

# Acknowledgements

---

Firstly, I would like to thank my supervisors Hans Bachor and David McClelland. Together they have cultivated an excellent research environment and filled the labs with many talented people. In particular, the strong international collaborations that have been active during my PhD have contributed to a stimulating work environment, as well as opening many doors overseas.

Without a doubt, the most direct influence on my work has come from Ping Koy Lam, Malcolm Gray and Timothy Ralph. I deeply admire the careful and thorough approach Ping Koy has to experimental work. My experiments were laid on the very solid foundations which he built. Mal was not only a constant source of inspiration and new ideas, he was also largely responsible for designing the electronics required for our experiments. Without reliable electronics, many of the experiments in this thesis would have been impractical. My third supervisor, Tim, was whisked away to Queensland mid-PhD. I found his capacity to transform complex ideas into experimentally achievable goals to be quite remarkable, as was his patience when explaining these new schemes to me.

I have had the good fortune to work with many talented people, both inside and outside my own small research group. Daniel Shaddock, Bram Slagmolen, Warwick Bowen, Elanor Huntington, Jessica Lye, Cameron Fletcher and John Close have provided a constant supply of fresh ideas and fresh humour. This is always important for lab work which has the potential to be dull at times. I would specifically like to thank Dan Shaddock and Warwick Bowen for their help with the modulation-free SHG experiment and Elanor Huntington for assistance with the phase feedforward experiment. Most importantly, I am grateful for the timely arrival of Ulrik Andersen. Without him, the QND experiments would not have been so successful.

I would also like to extend my thanks to Friedrich König, Christine Silberhorn and Gerd Leuchs at the Universität Erlangen. The time I spent in Erlangen added greatly to my appreciation of experimental quantum optics.

The support of the workshop staff has been tremendous. Often these are the people I turned to when, through my own lack of foresight, something had to be done yesterday. To Brett Brown, Paul MacNamara, Russell Koehne and Chris Woodland - thank you for all the last minute machining and repairing.

The administrative staff have also been invaluable. Whenever packages went missing or forms needed filling Zeta Hall, Jenny Willcoxson and Susan Maloney were always willing to lend a hand, or tell me what to do.

Outside work hours, there have been numerous friends, housemates and parents who have helped when the work was not going according to plan. Much of the time, they would not have been aware of the help they were giving, since it mostly consisted of putting up with some cranky moods which I could not adequately explain. For all those times - thanks and sorry.

Finally to Michelle: your companionship and love through it all has been important beyond measure.



---

# Abstract

---

The performance of optical measurement systems is ultimately limited by the quantum nature of light. In this thesis, two techniques for circumventing the standard quantum measurement limits are modelled and tested experimentally. These techniques are electro-optic control and the use of squeezed light.

An optical parametric amplifier is used to generate squeezing at 1064nm. The parametric amplifier is pumped by the output of a second harmonic generation cavity, which in turn is pumped by a Nd:YAG laser. By using various frequency locking techniques, the quadrature phase of the squeezing is stabilised, therefore making our squeezed source suitable for long term measurements. The best recorded squeezing is 5.5dB (or 70%) below the standard quantum limit. The stability of our experiment makes it possible to perform a time domain measurement of photocurrent correlations due to squeezing. This technique allows direct visualisation of the quantum correlations caused by squeezed light.

On the road to developing our squeezed source, methods of frequency locking optical cavities are investigated. In particular, the tilt locking method is tested on the second harmonic generation cavity used in the squeezing experiment. The standard method for locking this cavity involves the use of modulation sidebands, therefore leading to a noisy second harmonic wave. The modulation free tilt-locking method, which is based on spatial mode interference, is shown to be a reliable alternative.

In some cases, electro-optic control may be used to suppress quantum measurement noise. Electro-optic feedback is investigated as a method for suppressing radiation pressure noise in an optical cavity. Modelling shows that the ‘squashed’ light inside a feedback loop can reduce radiation pressure noise by a factor of two below the standard quantum limit. This result is then applied to a thermal noise detection system. The reduction in radiation pressure noise is shown to give improved thermal noise sensitivity, therefore proving that the modified noise properties of light inside a feedback loop can be used to reduce quantum measurement noise.

Another method of electro-optic control is electro-optic feedforward. This is also investigated as a technique for manipulating quantum measurements. It is used to achieve noiseless amplification of a phase quadrature signal. The results clearly show that a feedforward loop is a phase sensitive amplifier that breaks the quantum limit for phase insensitive amplification. This experiment is the first demonstration of noiseless phase quadrature amplification.

Finally, feedforward is explored as a tool for improving the performance of quantum nondemolition measurements. Modelling shows that feedforward is an effective method of increasing signal transfer efficiency. Feedforward is also shown to work well in conjunction with meter squeezing. Together, meter squeezing and feedforward provide a comprehensive quantum nondemolition enhancement package. Using the squeezed light from our optical parametric amplifier, an experimental demonstration of the enhancement scheme is shown to achieve record signal transfer efficiency of  $T_s + T_m = 1.81$ .





---

# Contents

---

Declaration	iii
Acknowledgements	v
Abstract	vii
Summary of symbols and acronyms	xix
<b>1 Introduction</b>	<b>1</b>
<b>2 The basics: theoretical quantum optics and experimental techniques</b>	<b>5</b>
2.1 Quantum light . . . . .	5
2.1.1 States of light . . . . .	6
2.2 Sidebands and modulation of light . . . . .	8
2.2.1 Classical modulation of light . . . . .	8
2.2.2 Quantum sidebands . . . . .	10
2.3 Linearisation of the operators . . . . .	11
2.4 Multimode quantum optics: the noise spectra . . . . .	12
2.4.1 Power spectra and frequency domain uncertainty relations . . . . .	13
2.5 Experimental devices . . . . .	15
2.5.1 Beamsplitters . . . . .	15
2.5.2 Optical attenuation and measuring with a photodetector . . . . .	15
2.5.3 Balanced homodyne detection . . . . .	17
2.6 Open quantum systems and the quantum Langevin equation . . . . .	21
2.7 Optical cavities . . . . .	23
2.8 Cavity locking . . . . .	26
2.8.1 Modulation locking . . . . .	27
2.8.2 Spatial mode locking . . . . .	29
2.9 Locking homodyne detection . . . . .	30
2.10 Summary . . . . .	31
<b>3 Phase signal amplification</b>	<b>33</b>
3.1 Introduction . . . . .	33
3.2 Feedforward amplification . . . . .	36
3.3 Phase quadrature feedforward . . . . .	38
3.4 The experiment . . . . .	42
3.5 Conclusion . . . . .	45
<b>4 Improving quantum nondemolition measurement</b>	<b>47</b>
4.1 Introduction . . . . .	47
4.2 QND Criteria: an overview . . . . .	48
4.2.1 Signal transfer coefficients . . . . .	50

---

4.2.2	Conditional variance . . . . .	51
4.3	QND enhancement . . . . .	52
4.3.1	Pre-enhancement . . . . .	52
4.3.2	Post-enhancement with feedforward . . . . .	52
4.4	The sensitivity . . . . .	57
4.5	Conclusion . . . . .	61
<b>5</b>	<b>Suppressing radiation pressure noise with feedback</b>	<b>63</b>
5.1	Introduction . . . . .	63
5.2	Quantum feedback theory . . . . .	65
5.2.1	In-loop field properties . . . . .	67
5.2.2	Out-of-loop field properties . . . . .	67
5.3	Measurement of cavity detuning . . . . .	68
5.3.1	Fields exiting the cavity . . . . .	68
5.3.2	Cavity configurations . . . . .	69
5.3.3	Power scaling of the detuning signals . . . . .	71
5.4	Including feedback in the measurement model . . . . .	72
5.4.1	Feedback reduces photon number noise in a cavity . . . . .	74
5.4.2	What limits does this system beat? . . . . .	75
5.5	Detuning measurement via the cavity locking signal . . . . .	77
5.6	Thermal noise spectra . . . . .	80
5.7	Thermal noise detection models . . . . .	82
5.7.1	Impedance matched cavities with and without squashing. . . . .	84
5.7.2	Reflective single ended cavities . . . . .	84
5.8	Conclusions . . . . .	86
<b>6</b>	<b>Second harmonic generation</b>	<b>87</b>
6.1	Introduction . . . . .	87
6.2	Requirements of a frequency doubler . . . . .	87
6.2.1	Nonlinear susceptibility . . . . .	87
6.2.2	Phase matching . . . . .	88
6.3	Equations of cavity SHG . . . . .	91
6.4	Locking cavity SHG . . . . .	93
6.5	Experimental comparison of tilt and modulation locking . . . . .	96
6.5.1	Results . . . . .	97
6.5.2	Mechanical stability and optimisation . . . . .	101
6.6	Conclusion . . . . .	102
<b>7</b>	<b>Squeezing from an optical parametric amplifier</b>	<b>103</b>
7.1	Introduction . . . . .	103
7.2	OPA theory . . . . .	104
7.2.1	Classical parametric amplification . . . . .	104
7.2.2	Quantum behaviour of an OPA . . . . .	105
7.3	Experimental design . . . . .	107
7.3.1	The mode cleaner cavity . . . . .	107
7.3.2	The OPA cavity . . . . .	110
7.3.3	Locking the squeezing quadrature . . . . .	111
7.3.4	Homodyne detection locking . . . . .	112

---

7.4	Experimental results . . . . .	112
7.4.1	Regenerative gain . . . . .	112
7.4.2	Vacuum squeezing . . . . .	113
7.4.3	Locked squeezing results . . . . .	115
7.5	Correlation measurements . . . . .	116
7.5.1	A more detailed theory of correlation measurement . . . . .	118
7.6	Conclusions . . . . .	120
<b>8</b>	<b>Quantum nondemolition experiments: realisation of enhancement</b>	<b>121</b>
8.1	Introduction . . . . .	121
8.2	Experimental design . . . . .	122
8.3	QND results with the 50% beamsplitter . . . . .	122
8.3.1	The definition and measurement of the transfer coefficients. . . . .	123
8.3.2	Measurement of the conditional variance . . . . .	125
8.3.3	The addition of feedforward to the 50% beamsplitter . . . . .	126
8.3.4	Summary of the 50% beamsplitter results . . . . .	129
8.4	How ND is the QND? . . . . .	130
8.5	QND with a 92/8 beamsplitter . . . . .	130
8.5.1	Measurement of the transfer coefficients. . . . .	131
8.5.2	Conditional variance measurements . . . . .	133
8.5.3	Summary of the 92% beamsplitter results . . . . .	133
8.6	Comparison to other QND experiments . . . . .	135
8.7	Conclusion . . . . .	135
<b>9</b>	<b>Conclusions and future possibilities</b>	<b>137</b>
<b>A</b>	<b>Electronic noise</b>	<b>141</b>
<b>B</b>	<b>Circuit designs</b>	<b>143</b>
	<b>Bibliography</b>	<b>151</b>



---

# List of Figures

---

1.1	Thesis structure . . . . .	2
2.1	The ‘ball on stick’ picture of quantum states . . . . .	8
2.2	Phase and amplitude modulation sidebands . . . . .	9
2.3	The sideband picture of quantum states . . . . .	11
2.4	A beamsplitter . . . . .	15
2.5	A model of an inefficient photodiode . . . . .	16
2.6	Self-homodyne detection . . . . .	17
2.7	Homodyne detection of the phase quadrature . . . . .	19
2.8	An empty optical cavity with various input and output fields. . . . .	23
2.9	Classical response of a cavity . . . . .	25
2.10	Noise filtering properties of an optical cavity . . . . .	26
2.11	General principle of cavity locking . . . . .	27
2.12	Pound-Drever-Hall locking . . . . .	28
2.13	Dither locking . . . . .	29
2.14	Spatial mode separation by a cavity . . . . .	29
2.15	Tilt locking signal arising from the interference of spatial modes . . . . .	30
3.1	Loss of signal-to-noise ratio due to attenuation . . . . .	33
3.2	Phase insensitive amplifier . . . . .	34
3.3	A general feedforward loop . . . . .	36
3.4	A phase quadrature feedforward loop . . . . .	38
3.5	Design of the phase feedforward experiment . . . . .	42
3.6	Input to the phase feedforward amplifier . . . . .	43
3.7	Output of the phase feedforward amplifier . . . . .	44
4.1	A general QND system . . . . .	49
4.2	Feedforward applied to a general QND system . . . . .	53
4.3	Effect of the gain phase in feedforward . . . . .	55
4.4	Feedforward applied to a squeezed light beamsplitter . . . . .	56
4.5	Feedforward applied to an OPA QND system . . . . .	57
4.6	A general QND scheme with feedforward and sensitivity correction . . . . .	58
4.7	Sensitivity as a function of squeezing . . . . .	59
4.8	QND performance with sensitivity correction . . . . .	61
5.1	An electro-optic feedback loop . . . . .	65
5.2	Cavity inside a feedback loop . . . . .	72
5.3	Effect of feedback on the intra-cavity noise as a function of the cavity mirror reflectivities . . . . .	72
5.4	Effect of laser power on thermal noise measurement . . . . .	82
5.5	Optimum laser power for different thermal noise measurement configurations . . . . .	83
5.6	Thermal noise measurement with impedance matched cavities . . . . .	84

---

5.7	Thermal noise measurement using a single ended cavity and ideal laser . . .	85
5.8	Thermal noise measurement using a single ended cavity and laser with classical intensity noise	85
6.1	Frequency doubling. . . . .	88
6.2	Three-wave mixing processes. . . . .	89
6.3	Harmonic conversion efficiency as a function of temperature and wavelength	90
6.4	The inputs and outputs of a quantum model for SHG and parametric amplification	91
6.5	Harmonic generation efficiency as a function of the input coupler reflectivity	93
6.6	Effect of modulation in a second harmonic generator . . . . .	94
6.7	Measurement of intensity modulation in the second harmonic due to cavity modulation	95
6.8	Schematic of the second harmonic generation experiment . . . . .	96
6.9	Error signals for the second harmonic generation cavity . . . . .	97
6.10	Comparison of the second harmonic intensity noise spectra with tilt-locking and modulation locking	98
6.11	Fluctuations in second harmonic power compared to the modulation and tilt error signals	100
7.1	Regenerative gain of an optical parametric amplifier. . . . .	105
7.2	Detailed diagram of the OPA squeezing experiment. . . . .	108
7.3	Mode cleaning cavity . . . . .	109
7.4	The OPA crystal . . . . .	110
7.5	Measured regenerative gain of the OPA as a function of pump power. . . .	113
7.6	Scanned squeezed vacuum measurement . . . . .	114
7.7	Frequency spectrum of the squeezing . . . . .	115
7.8	Time stability of the squeezing . . . . .	116
7.9	Setup for measuring quantum correlations . . . . .	117
7.10	Correlation measurement results . . . . .	118
7.11	Intensity correlations between two entangled beams . . . . .	120
7.12	Phase correlations between two entangled beams . . . . .	120
8.1	Diagram of the QND experiment with a beamsplitter . . . . .	122
8.2	Signal transfer coefficient data for the 50% beamsplitter . . . . .	123
8.3	Meter transfer coefficient data for the 50% beamsplitter . . . . .	124
8.4	Squeezing used for the QND experiments . . . . .	126
8.5	Simplified diagram of the QND experiment with feedforward. . . . .	126
8.6	Response of the New Focus 4104 amplitude modulator . . . . .	127
8.7	Transfer coefficient data for the 50% beamsplitter with feedforward . . . .	128
8.8	Conditional variance data for the 50% beamsplitter with feedforward . . . .	128
8.9	Comparison of theory with experimental results for the 50% beamsplitter .	129
8.10	Meter transfer coefficient data with the 92% beamsplitter . . . . .	131
8.11	Signal transfer coefficient data with the 92% beamsplitter . . . . .	131
8.12	Conditional variance measurement with the 92% beamsplitter and no feedforward	132
8.13	Conditional variance measurement with feedforward used to maximise $T_s$ and 92% beamsplitter	132
8.14	Conditional variance measurement with the 92% beamsplitter and feedforward used to correct signal gain	
8.15	Comparison of theory to experimental results for the 92% beamsplitter . . .	134
8.16	Summary of QND results compared with other published experiments . . .	135
A.1	Raw data for vacuum squeezing . . . . .	141
A.2	Vacuum squeezing data without electronic noise . . . . .	142
B.1	Low noise detector circuits . . . . .	143

---

B.2	Tilt detector circuit . . . . .	144
B.3	Piezo-electric servo circuit . . . . .	145
B.4	Laser servo circuit . . . . .	146
B.5	Temperature controller circuit: front panel . . . . .	147
B.6	Temperature controller circuit: PID . . . . .	148
B.7	Temperature controller circuit: Power supply . . . . .	148
B.8	Signal box circuit . . . . .	149





---

# List of Tables

---

2.1	Comparison of some states of light you might meet in a quantum optics laboratory.	9
5.1	Summary of thermal noise detection models. . . . .	86
6.1	Stability parameters of the second harmonic generator locked using both modulation and T	
8.1	QND results with a 50/50 beamsplitter. . . . .	129
8.2	QND results with a 92/8 beamsplitter. . . . .	134



---

# Summary of symbols and acronyms

---

Term	Definition
1: $\Delta$	Standard deviation (square-root of variance, $\Delta^2$ )
2: $\Delta$	In chapter 5, cavity detuning.
$\alpha$	Classical cavity mode amplitude
$\varepsilon$	Beamsplitter transmission
$\eta_z$	Detector efficiency
$\kappa$	Total decay rate of a cavity
$\kappa_{\text{in}}$	Coupling rate of cavity input mirror
$\kappa_{\text{out}}$	Coupling rate of cavity output mirror
$\kappa_l$	Coupling rate of cavity loss
$\omega$	Frequency of sidebands relative to carrier
$\Omega$	Frequency of carrier wave
$A_z$ ( $A_z^\dagger$ )	Annihilation (creation) operator of a travelling wave
$\bar{A}_z$	Classical amplitude of a travelling wave
$a$ ( $a^\dagger$ )	Annihilation (creation) operator of a cavity mode
$C_{s,m}$	Correlation between $s$ and $m$
cw	Continuous wave
DC	Direct current (Sometimes used more generally to mean low frequency)
$I_z$	Photocurrent due to $A_z$
OPA	Optical parametric amplifier
$n$	photon number operator
QND	Quantum nondemolition
QNL	Quantum noise limit
RBW	Resolution bandwidth
RF	Radio frequency
SHG	Second harmonic generator
SNR	Signal-to-noise ratio
$T_s$	Signal transfer coefficient
$T_m$	Meter transfer coefficient
VBW	Video bandwidth
$V_z^+$	Amplitude noise spectrum of the field $A_z$
$V_z^-$	Phase noise spectrum of the field $A_z$
$V_{s m}$	Conditional variance between $s$ and $m$
$X_z$	General quadrature of $A_z$
$X_z^+$	Amplitude quadrature of $A_z$
$X_z^-$	Phase quadrature of $A_z$
$X_z^\theta$	$\theta$ quadrature of $A_z$

---

# Introduction

---

Lasers provide the ability to measure the physical world with extraordinary accuracy. In applications ranging from the detection of distant stars, such as gravitational wave astronomy [102], to probing the smallest details, as in atomic force microscopy [95], lasers are being used to push back the frontiers of measurement technology.

In general, optical sensors perform well due to the high sensitivity and low noise of laser emitters and photodetectors. This is so much the case, that optical sensors can be limited by quantum mechanical uncertainty rather than the classical noise sources which normally plague mechanical devices. For example, a mechanical gyroscope will be limited by internal friction and mechanical stability well before reaching any limits due to quantum mechanics. These mechanical noise sources could be attacked with extreme mechanical engineering, with an extreme cost to match. Laser gyroscopes, on the other hand, are already performing close to the quantum limit [128]. Their sensitivity is so great that very large laser gyroscopes may soon be used to probe minute refractive index changes due to charge-parity violation [114].

This thesis has everything to do with gravitational wave detection, atomic force microscopy and laser gyroscopes, although they may not be mentioned a great deal outside this introduction. The models and experiments presented here demonstrate methods to overcome the quantum limits to laser measurement technology that are now becoming apparent.

A second motivation for probing the quantum properties of light is ‘quantum information’. Quantum effects, such as superposition and the uncertainty principle, may be used to manipulate the transmission and storage of information in ways that are not possible in classical systems. Since the realisation that a ‘quantum computer’ based on quantum data manipulation may out-perform a classical computer [6], there has been an intensive search for a suitable quantum resource. One possibility is optical computation based on non-classical states of light [69]. An optical quantum computer would require methods for generating the required quantum states of light and quantum limited detection systems to measure the output of the computer. Even if a quantum computer were not all-optical, methods for detecting the computed output may rely on optical measurement technology. Either way, the quantum properties of light are likely to play a key role in quantum information.

In this thesis, two major methods of manipulating the quantum nature of light are explored:

- Quantum electro-optic control: quantum control may be divided into two parts. The first is feedforward. This technique has been shown in our laboratories as a method for noiseless amplification of quantum limited signals. Feedforward may therefore

be applied to reduce problems associated with optical loss. It may also be applied as a method for preparing quantum states when combined with squeezed light. The second quantum control technique is feedback. Feedback is useful for suppressing noise on a laser beam. Modelling shows that the noise of a laser beam inside a feedback loop may fall below the quantum limit that exists outside the loop. The modified in-loop noise can be harnessed to improve the signal-to-noise performance of some types of measurement.

- Squeezing: the noise inherent to a laser beam is a result of the Heisenberg uncertainty principle, and cannot be removed. It can, however, be manipulated so that one variable of the laser light is forced to be quiet while the majority of the noise due to the uncertainty principle is pushed onto the conjugate variable. So long as the measurement system which is to be enhanced by the squeezing only depends on the noise of the quiet variable then the measurement will be more precise due to the squeezing. In particular we apply squeezing to make a ‘quantum nondemolition’ measurement of a laser beam.

The flow of the information contained in this thesis is shown in figure 1.1.

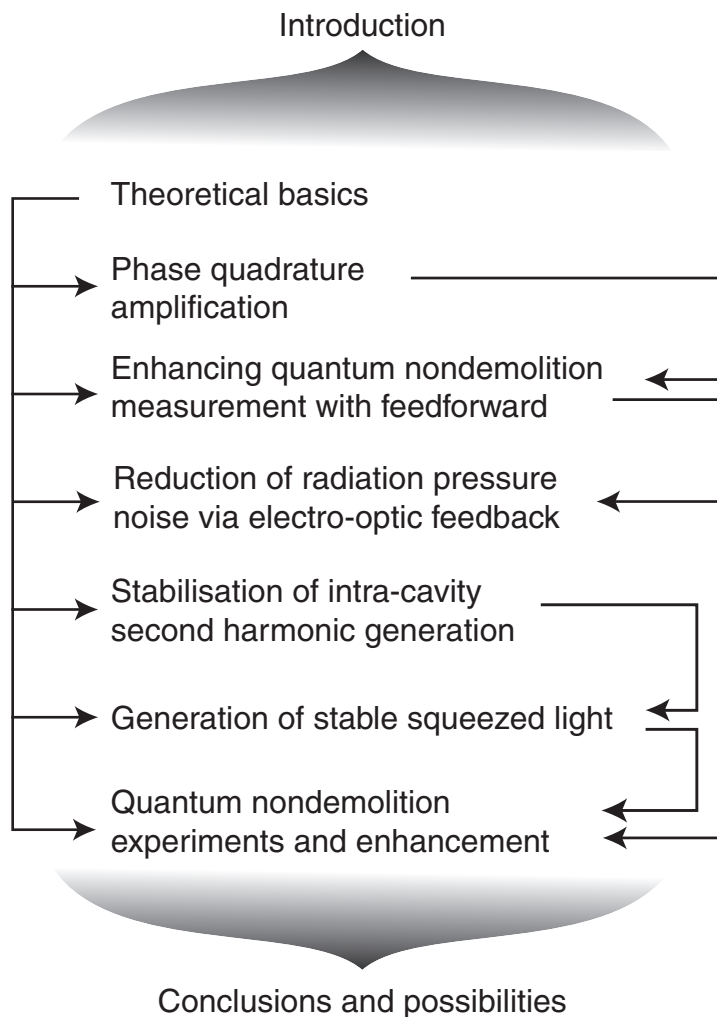


**Figure 1.1:** Thesis structure

Following this introduction, chapter 2 covers the theoretical necessities for the rest of the thesis. In particular we show how problems may be solved in quantum optics using linearised operators. This allows analytic modelling of complex experiments, without ignoring the quantum behaviour.

Chapter 3 contains an introduction to signal amplification in laser beams, and shows how feedforward can provide noiseless amplification. We then demonstrate noiseless amplification of the phase quadrature of a laser beam.

Chapter 4 presents theoretical modelling of feedforward applied to quantum nondemolition measurement. The theory shows how the noiseless amplification of a feedforward loop may be used to improve the performance of a general quantum nondemolition measurement system. This model is applied to two example systems. This chapter forms the basis for the experiment of chapter 8, where the QND enhancement scheme is implemented.

Chapter 5 contains a discussion of electro-optic feedback applied to a thermal noise measurement system. The modelling shows that feedback may be used to reduce the amount of radiation pressure noise without affecting the thermal noise behaviour of the experiment. The ability of feedback to help in this case is due to the quantum nondemolition nature of the nonlinear coupling between the noise of the photons inside a cavity and the motion of the cavity mirrors. The model is applied to a simple pendulum system and shows a potential increase in the sensitivity of thermal noise detection.

Chapter 6 is an introduction to  $\chi^{(2)}$  nonlinear processes. We show how a second harmonic generator may be locked to a pump laser without modulation so that the second harmonic spectrum is also free of modulation. Our second harmonic generator is used as the pump source for the squeezing experiments.

Chapter 7 describes the layout and results obtained from our squeezing optical parametric amplifier. In particular we discuss the techniques used to lock the squeezing phase so that the squeezing may be used to make long-term measurements. We also speculate on the factors which limit the amount of squeezing obtained in our amplifier.

Chapter 8 contains an implementation of the quantum nondemolition experiment described in chapter 4. Using the squeezed state generated from the parametric amplifier and an electro-optic feedforward loop, we produce results which show the significant advantages which may be gained by using feedforward enhancement.

Finally, chapter 9 contains some concluding remarks about the future of the technologies that have been explored.

---

## Publications

A large proportion of the work presented in the following chapters has been published in peer reviewed journals. Below is a summary of these publications:

- B.C. Buchler, U.L. Andersen, P.K. Lam, H.-A. Bachor and T.C. Ralph, *Squeezing more from a quantum nondemolition measurement*, To be published in Physical Review A, Rapid Communications, January 2002.
- D.A. Shaddock, B.C. Buchler, W.P. Bowen, M.B. Gray and P.K. Lam *Modulation-free control of a continuous-wave second-harmonic generator*, Journal of Optics A: Pure & Applied Optics. **2**, 400 (2000)
- B.C. Buchler , P.K. Lam and T.C. Ralph *Enhancement of quantum nondemolition measurements with an electro-optic feedforward amplifier* Physical Review A. **60**, 4943 (1999)
- B.C. Buchler , E.H. Huntington and T.C. Ralph *Noiseless phase quadrature amplification via an electro-optic feedforward technique*, Physical Review A. **60**, 529 (1999)
- B.C. Buchler , M.B. Gray, D.A. Shaddock, T.C. Ralph and D.E. McClelland, *Suppression of classic and quantum radiation pressure noise by electro-optic feedback*, Optics Letters. **24**, 259 (1999).
- T.C. Ralph, P.K. Lam, E.H. Huntington, B.C. Buchler, D.E. McClelland and H.-A. Bachor, *Quantum electro-optic control*, Optics and Photonics News, **9**, 44 (1998)

Publications of work not covered in this thesis are:

- T.C. Ralph, E.H. Huntington, C.C. Harb, B.C. Buchler, P.K. Lam, D.E. McClelland and H.-A. Bachor, *Understanding and controlling laser intensity noise*. Optical and Quantum Electronics. **31**, 583 (1999).
- P.K. Lam and T.C. Ralph and B.C. Buchler and D.E. McClelland and H.-A. Bachor and J. Gao, *Optimization and transfer of vacuum squeezing from an optical parametric oscillator*, Journal of Optics B: Quantum & Semiclassical Optics. **1**, 469 (1999).
- B.C. Buchler, E.H. Huntington, C.C. Harb and T.C. Ralph, *Feedback control of laser intensity noise*. Physical Review A. **57**, 1286 (1998).
- E.H. Huntington, B.C. Buchler, C.C. Harb, T.C. Ralph, D.E. McClelland and H.-A. Bachor, *Feedback control of the intensity-noise of injection locked lasers*. Optics Communications. **145** 359 (1998).

Work Submitted for publication:

- V. Delaubert, D.A. Shaddock, P.K. Lam, B.C. Buchler, H.-A. Bachor and D.E. McClelland , *Generation of a phase flipped Gaussian mode for optical measurements*, Submitted to Journal of Optics A (July 2001)

---

# The basics: theoretical quantum optics and experimental techniques

---

Throughout this thesis, some basic theoretical tools will be used to explain experiments. In particular, the fluctuations of the quantum fields will be linearised about their steady states. This allows analytic modelling of complex experimental setups, both existing and potential. An analytic method has the advantage of giving clear insight into the physical processes within an experiment. The contents of this chapter include:

- The basics of quantum light.
- A linearised model of quantum light.
- Application of this model to attenuation, detection, squeezing and optical cavities.
- Some key experimental techniques such as homodyne detection of the phase quadrature and laser frequency locking.

## 2.1 Quantum light

The Heisenberg uncertainty principle [58] is one of the most profound results of 20th century physics. It was this idea of never knowing everything about an object that led to the demise of the “Newtonian universe”, where sufficient information about the present would allow prediction of the future. For the usual example of position ( $p$ ) and momentum ( $q$ ) the uncertainty relation is given by

$$\Delta(p) \Delta(q) \geq \frac{\hbar}{2} \quad (2.1)$$

where  $\Delta(X)$  is the standard deviation of an operator  $X$ . The deviation is related to the variance and the expectation values by

$$\Delta^2(X) = [\Delta(X)]^2 = \langle X^2 \rangle - \langle X \rangle^2 \quad (2.2)$$

where  $\Delta^2(X)$  is the variance of  $X$ , and  $\langle X \rangle$  is the expectation value of  $X$ . The uncertainty principle is strongly connected to the idea of commutation relations [85]. For any two



observables  $A$  and  $B$  with the commutation relation

$$[A, B] = C \quad (2.3)$$

there exists an uncertainty principle given by

$$\Delta(A) \Delta(B) \geq \frac{|(C)|}{2}. \quad (2.4)$$

The uncertainty principle as it applies to the detection of an optical field may be setup as follows. Starting with the creation ( $a^\dagger$ ) and annihilation ( $a$ ) operators for the electromagnetic field, a Hermitian operator may be defined as

$$X^\theta = ae^{-i\theta} + a^\dagger e^{i\theta}. \quad (2.5)$$

This operator may be evaluated at  $\theta = 0$  and  $\theta = \pi/2$  to give the operator pair,

$$X^+ = a + a^\dagger \quad \text{and} \quad (2.6)$$

$$X^- = -i(a - a^\dagger), \quad (2.7)$$

which may also be used to define the arbitrary quadrature operator via

$$X^\theta = X^+ \cos \theta + X^- \sin \theta. \quad (2.8)$$

The operators  $X^+$  and  $X^-$  are Hermitian and therefore represent measurable quantities. In the following chapters,  $X^+$  is referred to as the amplitude quadrature and  $X^-$  as the phase quadrature. It is the properties of these quadrature operators that are typically measured in quantum optics experiments.

The commutation relation between the creation and annihilation operators,  $[a, a^\dagger] = 1$ , results in the commutation relation

$$[X^+, X^-] = 2i \quad (2.9)$$

between the phase and amplitude quadratures of the field. The result is that there is an uncertainty relation between the phase and amplitude quadratures of the electromagnetic field given by

$$\Delta(X^+) \Delta(X^-) \geq 1. \quad (2.10)$$

In the event that a state of light satisfies  $\Delta(X^+) \Delta(X^-) = 1$  the state is said to be “minimum uncertainty”. The majority of the work in this thesis is aimed at manipulating this uncertainty relation to improve a quantum limited measurement.

### 2.1.1 States of light

There are numerous states of light which may be generated in a quantum optics laboratory. The summary here is somewhat brief, a full and clear discussion may be found in quantum optics texts such as those written by Scully [106] or Walls and Milburn [117].

#### The vacuum state

The vacuum state  $|0\rangle$  of the electromagnetic field is one which has no photons, i.e.  $\langle 0|n|0\rangle = 0$ . This does not, however, mean it is free from fluctuations. The variance of the phase

and amplitude quadratures are

$$\Delta^2(X^+) = \Delta^2(X^-) = 1. \quad (2.11)$$

The variances are minimum and equal. It is this non-zero variance of the vacuum which is often invoked to preserve the uncertainty principle in a wide range of measurement scenarios. A simple example is the beamsplitter with an empty port. A quantum vacuum is incident on the empty port and beats with the two output fields of the beamsplitter. The two outputs are therefore less than perfect copies of one another (see section 2.5.3). The vacuum noise is also referred to as “quantum noise” and “shot noise”. A variance which is measured to be less than noise of a vacuum state is referred to as sub-shot noise or below the quantum noise limit (QNL).

### The coherent state

The coherent state of light  $|\alpha\rangle$  is a minimum uncertainty state, with equal uncertainty in the amplitude and phase quadratures. The quadrature variances are therefore identical to those of the vacuum state. The coherent state does contain photons, however, and may be written in terms of the number states  $|n\rangle$  as

$$|\alpha\rangle = e^{-|\alpha|^2/2} \sum_n \frac{\alpha^n}{\sqrt{n!}} |n\rangle. \quad (2.12)$$

This is a Poissonian distribution of photon number states with the peak at  $\alpha^2$ . Furthermore, the expectation value of the photon number in the field is  $\alpha^2$ . A coherent state may be generated from a vacuum state by using the displacement operator  $D$

$$\begin{aligned} D(\alpha) &= e^{(\alpha a^\dagger - \alpha^* a)} \quad \text{so that} \\ D(\alpha)|0\rangle &= |\alpha\rangle \end{aligned} \quad (2.13)$$

### The squeezed state

The squeezed state of light is one for which the variance of the quadratures is no longer equal, and one of the variances falls below 1. For example, the amplitude squeezed state would have the properties

$$\Delta^2(X^+) < 1 \quad \text{and} \quad (2.14)$$

$$\Delta^2(X^-) > 1. \quad (2.15)$$

A minimum uncertainty squeezed state also requires that  $\Delta(X^+)\Delta(X^-) = 1$ . Real experiments tend not to produce minimum uncertainty squeezed states due to optical loss, which couples in some amount of quantum vacuum noise. (Exactly this effect will be seen in chapter 7.) The properties of the squeezed state may be deduced through the use of the “squeeze operator” defined in terms of the squeeze parameter,  $r$ , as

$$\begin{aligned} S(\rho) &= e^{\frac{1}{2}(\rho^* a^2 - \rho a^{\dagger 2})} \quad \text{where} \\ \rho &= r e^{i\phi} \end{aligned} \quad (2.16)$$

The angle  $\phi$  is the quadrature angle of the squeezing, measured with respect to some local oscillator. The squeeze parameter is assumed to be positive ( $r \geq 0$ ). In conjunction with

the displacement operator, the squeezed state,  $|\alpha, \rho\rangle$ , is constructed from the vacuum state as:

$$|\alpha, \rho\rangle = D(\alpha)S(\rho)|0\rangle. \quad (2.17)$$

Assuming, for simplicity, that the angle of the squeezing in phase space ( $\phi$ ) is zero, the properties of the squeezed state are found to be

$$\begin{aligned} \text{photon number } \langle n \rangle &= \sinh^2 r + \alpha^2 \\ \text{amplitude quadrature standard deviation } \Delta(X^+) &= e^{-r} \\ \text{phase quadrature standard deviation } \Delta(X^-) &= e^r \end{aligned} \quad (2.18)$$

In this case, if squeeze parameter  $r$  is greater than 0, then we will have an amplitude quadrature squeezed state.

The vacuum, coherent, and amplitude squeezed states may be represented in phase space as via the “ball on stick” picture, as shown in figure 2.1. Note that the squeezed

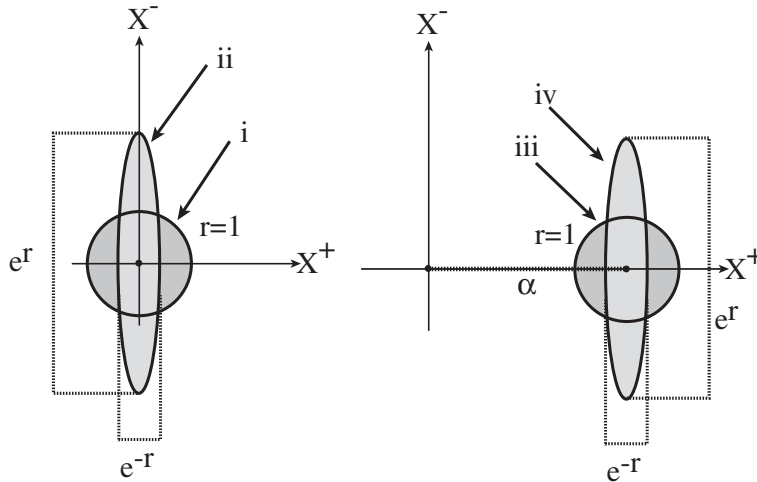


**Figure 2.1:** The “ball on stick” picture. i) A vacuum state, standard deviation of 1 in each quadrature and no coherent amplitude; ii) A vacuum squeezed state, asymmetric uncertainty, no coherent amplitude; iii) A coherent state with amplitude  $\alpha$  and uncertainty of 1 in each quadrature and iv) An amplitude squeezed coherent state.

state need not have a coherent amplitude  $\alpha$ . In this case we are dealing with a “squeezed vacuum state”. Squeezed vacua do actually contain some photons, since  $\langle n \rangle = \sinh^2 r$ . The greater degree of squeezing, the more photons in the beam. The essential properties of the vacuum, coherent and squeezed states are summarised in table 2.1.

## 2.2 Sidebands and modulation of light

### 2.2.1 Classical modulation of light

An alternative to the ball and stick model of quantum light (shown in figure 2.1) is the “sideband model”. Light is frequently used to carry signals. This is typically achieved by modulating the phase or amplitude of the light at some frequency  $\omega$  which is much less than the optical frequency of the light. Such modulation may be visualised by the addition of modulation sidebands to the optical carrier at frequencies  $\pm\omega$  relative to the

State	Photon number, $\langle n \rangle$	Amplitude quadrature uncertainty, $\Delta(X^+)$	Phase quadrature uncertainty, $\Delta(X^-)$
Vacuum, $ 0\rangle$	0	1	1
Coherent, $ \alpha\rangle$	$\alpha^2$	1	1
Squeezed vacuum, $ 0, \rho\rangle$	$\sinh^2 r$	$e^{-r}$	$e^r$
Squeezed coherent, $ \alpha, \rho\rangle$	$\alpha^2 + \sinh^2 r$	$e^{-r}$	$e^r$

**Table 2.1:** Comparison of some states of light you might meet in a quantum optics laboratory.

carrier frequency. It is the phase of the carrier with respect to the sidebands that distinguishes amplitude modulation (AM) from phase modulation (PM). Different possible configurations of sidebands that give amplitude and phase modulation are shown in figure 2.2. To obtain modulation in the lab, we typically use an electro-optic modulator (EOM). An oscillating electric field at frequency  $\omega$  applied to an EOM removes photons from the carrier field and places them in sidebands at  $\pm\omega$ . EOMs may be configured to give phase or amplitude sidebands [133].

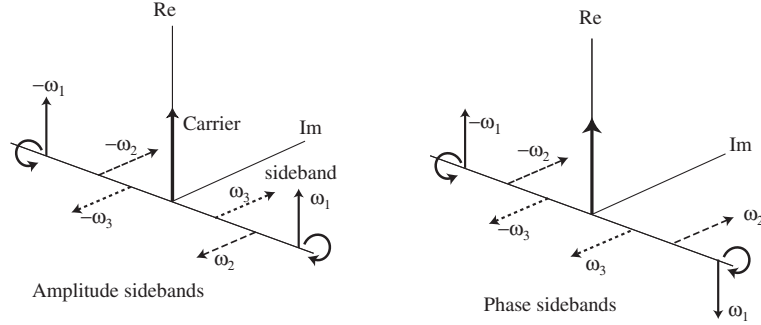


**Figure 2.2:** Phase and amplitude modulation of an optical carrier. The left-hand figure shows amplitude modulation at frequencies  $\omega_1, \omega_2$  and  $\omega_3$ . The right-hand figure shows phase modulation at  $\omega_1, \omega_2$  and  $\omega_3$ .

Formally, a phase modulated beam,  $E$ , may be written as

$$E = E_0 e^{i(\Omega t + d \cos \omega t)} \quad (2.19)$$

where  $E_0$  is the classical amplitude,  $\Omega$  is the optical frequency,  $\omega$  is the modulation frequency and  $d$  is the modulation depth. Assuming the modulation depth is small ( $d \ll 1$ )  $E$  may be expressed as

$$E = E_0 e^{i\Omega t} (1 + id \cos \omega t) = E_0 e^{i\Omega t} \left( \underbrace{1}_{*} + \underbrace{\frac{id}{2}(e^{-i\omega t} + e^{i\omega t})}_{**} \right) \quad (2.20)$$

where the term ‘\*’ is the carrier and the terms ‘\*\*’ are the phase sidebands.

Similarly, amplitude modulation may be written as

$$E = E_0 e^{i\Omega t} (1 + d \cos \omega t) = E_0 e^{i\Omega t} \left( \underbrace{1}_* + \underbrace{\frac{d}{2}(e^{i\omega t} + e^{-i\omega t})}_{**} \right) \quad (2.21)$$

where the terms ‘\*\*’ are now the amplitude sidebands.

Another class of modulation is “frequency modulation”. This is very closely related to phase modulation, but there is a subtle distinction. Considering the case of phase modulation as in equation 2.19, we can write the phase of the field,  $\Phi$ , as everything which multiplies the  $i$ , i.e.

$$\Phi = \Omega t + d \cos \omega t. \quad (2.22)$$

Moving into a frame rotating at the carrier frequency ( $\Omega$ ) we see that the phase modulation,  $\Delta\Phi_{\text{PM}}$ , is given by

$$\Delta\Phi_{\text{PM}} = d \cos \omega t \quad (2.23)$$

as expected. A frequency modulated field requires frequency fluctuations,  $\Delta\Omega$ , in a frame rotating at the carrier frequency. For example we might have

$$\Delta\Omega = -d \sin \omega t. \quad (2.24)$$

Remembering that frequency is the time derivative of the phase, we find that the phase fluctuations for a frequency modulated beam with  $\Delta\Omega = -d \sin \omega t$  are given by

$$\Delta\Phi_{\text{FM}} = \frac{d \cos \omega t}{\omega}. \quad (2.25)$$

A field with frequency modulation given by equation 2.24 is therefore given by

$$E = E_0 e^{i(\Omega t + \frac{d \cos \omega t}{\omega})}. \quad (2.26)$$

This behaves in an identical manner to phase modulation, provided we are only dealing with a single frequency sinusoidal modulation. In the case that the modulation term becomes a combination of frequency terms, the  $1/\omega$  dependence in the frequency modulation changes the relative size of the modulation sidebands at the different frequencies.

### 2.2.2 Quantum sidebands

The utility of the sideband model for quantum optics is this: quantum noise can be thought of as sidebands due to the vacuum field beating with the carrier mode as shown in the left of figure 2.3. These sidebands are a consequence of the ground state energy of the harmonic oscillator,  $\hbar\omega/2$ . The result is broadband (white) amplitude and phase noise. The sidebands are all of the same size and exist along the positive and negative frequency axis (where the zero of frequency is at the carrier wave frequency). For a coherent state, the phase of each sideband is random. This means that there is no preference for the carrier to be amplitude or phase modulated by the quantum noise. The quantum noise is therefore distributed equally between the amplitude and phase quadratures.

Squeezing is the reduction of the amplitude *or* phase noise below the standard quantum limit, i.e. below the limit set by minimum and equal noise in the phase and amplitude sidebands. We can imagine that this is due to the creation of a correlation between

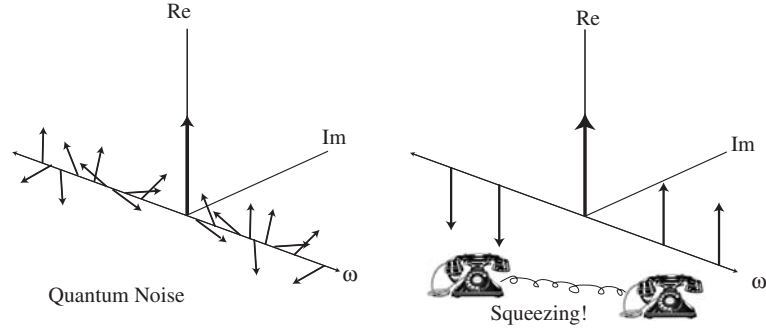


**Figure 2.3:** Left: quantum noise has random sidebands of equal size at all frequencies giving white phase and amplitude noise. Right: squeezing is a correlation of the positive and negative sidebands giving reduced noise in one quadrature and increased noise in the other.

the upper ( $+\omega$ ) and lower ( $-\omega$ ) sidebands. At the frequencies where squeezing occurs, the sidebands become synchronised with one another rather than being fully random, as illustrated in the right of figure 2.3. Amplitude squeezing at sideband frequency  $\omega$  occurs when the random quantum sidebands at  $\omega$  are converted to phase sidebands. In this case the phase noise will increase, while the lack of quantum amplitude modulation at that frequency means the intensity noise will be squeezed.

## 2.3 Linearisation of the operators

To explain and predict the results of our experiments an analytic form of quantum optics is preferable. Analytic expressions give a clearer picture of the physical processes in an experimental setup. The most common method of generating analytic results in quantum optics is to expand the operators about their steady state values and then linearise the resulting expressions to first order in the fluctuation terms. The first application of linearisation to quantum optics dates back to Yurke [137] who used it to model squeezing in a cavity. It has since been applied to many quantum optical systems with much success.

To linearise our equations the following substitution for the (Heisenberg picture) annihilation and creation operators are used:

$$a = \alpha + \delta a, \quad a^\dagger = \alpha^* + \delta a^\dagger \quad (2.27)$$

where  $\alpha$  is the (complex) expectation value  $\langle a \rangle$ , and  $\delta a$  is the operator for the fluctuations of  $a$ , so that  $\langle \delta a \rangle = 0$ . Similarly,  $\langle a^\dagger \rangle = \alpha^*$  and  $\langle \delta a^\dagger \rangle = 0$ . These substitutions may be used to simplify the calculation of the quadrature variances. Substituting equations 2.27 into 2.2 we find:

$$\begin{aligned} \Delta^2(X^+) &= \langle (\delta a + \delta a^\dagger)^2 \rangle = \langle \delta X^{+2} \rangle \\ \Delta^2(X^-) &= \langle (-i(\delta a - \delta a^\dagger))^2 \rangle = \langle \delta X^{-2} \rangle \end{aligned} \quad (2.28)$$

The variance may therefore be found by evaluating a single expectation value.

A useful example of linearisation is the calculation of the photon number variance. It is the photon number that is measured by an ideal photodetector, so many theoretical descriptions of measurements are based on photon number calculations, and the variance

of the photon number. The linearised version of  $n$  may be calculated as follows:

$$\begin{aligned} n &= a^\dagger a = (\alpha^* + \delta a^\dagger)(\alpha + \delta a) \\ &= \alpha^2 + \alpha(\delta a + \delta a^\dagger) + \delta a^\dagger \delta a \\ &\approx \alpha^2 + \alpha \delta X_a^+ \end{aligned} \quad (2.29)$$

where  $\alpha$  is assumed to be real (that is to say, we have chosen the amplitude quadrature  $X^+$  to correspond to the intensity of the field by setting  $\alpha$  real). In the final step, terms of order  $\delta^2$  have been ignored (this is the linearisation). This is valid provided the fluctuations of the optical field are much less than the average power of the field. Using equation 2.28, the linearised variance of the photon number may now be calculated:

$$\Delta^2(n) = \alpha^2 \langle \delta X_a^{+2} \rangle = \alpha^2 \Delta^2(X_a^+). \quad (2.30)$$

Considering the example of an amplitude squeezed state, equations 2.30 and 2.18 show that the linearised variance of the photon number is given by

$$\Delta^2(n) = \alpha^2 e^{-2r}, \quad (2.31)$$

therefore showing that the intensity noise of a detected bright squeezed beam is below the quantum noise limit (QNL) for  $r > 0$ . If the variance of the photon number were to be calculated in full it can be shown that [117]

$$\Delta^2 n = \alpha^2 e^{-2r} + 2 \cosh^2 r \sinh^2 r \quad (\text{assuming } \alpha \text{ real}). \quad (2.32)$$

Comparing equations 2.31 and 2.32, we see that for the linearised formalism to hold requires that  $\alpha^2 e^{-2r} \gg 2 \cosh^2 r \sinh^2 r$ . Rearranging this inequality shows that the requirement can be given in terms of the amplitude quadrature variance:

$$\begin{aligned} \alpha^2 e^{-2r} &\gg 2 \cosh^2 r \sinh^2 r \\ \Rightarrow \alpha^2 &\gg \frac{1}{8}(e^{6r} + e^{-2r} + 2e^{-2r}) \\ \Rightarrow \alpha^2 &\gg \frac{1}{8}e^{6r} \quad (\text{for } r > 1) \\ \Rightarrow \alpha^2 &\gg \frac{1}{8(\Delta^2 X^+)^3}. \end{aligned} \quad (2.33)$$

To put this in perspective, the squeezed states we generate in the lab are typically detected with 1mW of optical power at a wavelength of  $1\mu\text{m}$  giving  $\alpha^2 = 10^{17}$ . This means we require the variance of the amplitude quadrature ( $\Delta^2 X^+$ ) to be much greater than  $10^{-6}$  for linearisation to be valid. A variance of  $10^{-6}$  corresponds to 60dB of quantum noise suppression. Given that the most amplitude quadrature squeezing ever observed stands at around 7dB [75, 104], we are in little danger of breaking the requirements of linearisation on an everyday basis.

## 2.4 Multimode quantum optics: the noise spectra

Up to this point we have been dealing with idealised single optical modes. For cases where frequency dependent effects are important, a formalism to deal with a continuum of optical modes is required. These situations include such important processes as detection of a

frequency spectrum via a spectrum analyser and propagation of a beam through an optical cavity. We start by defining the frequency domain operator for a mode in the continuum,  $\tilde{A}(\omega)$ , where the frequency  $\omega$  is defined relative to some optical carrier frequency  $\Omega$ . For vacuum or coherent states, the commutator of modes at two different frequencies is given by [117]:

$$[\tilde{A}(\omega_1), \tilde{A}^\dagger(\omega_2)] = \delta(\omega_1 - \omega_2). \quad (2.34)$$

The time domain operator may be found as the Fourier transform of the frequency domain operator

$$A(t) = \int_{-\infty}^{\infty} \tilde{A}(\omega) e^{-i\omega t} d\omega. \quad (2.35)$$

The time domain operator then obeys the two-time commutation relation

$$[A(t_1), A^\dagger(t_2)] = \delta(t_1 - t_2) \quad (2.36)$$

where  $A^\dagger(t)$  is defined as

$$A^\dagger(t) = [A(t)]^\dagger = \int_{-\infty}^{\infty} \tilde{A}^\dagger(\omega) e^{i\omega t} d\omega. \quad (2.37)$$

The quadrature operators obey the two-frequency commutator relation:

$$[\tilde{X}^+(\omega_1), \tilde{X}^-(\omega_2)] = 2i\delta(\omega_1 - \omega_2), \quad [X^+(t_1), X^-(t_2)] = 2i\delta(t_1 - t_2). \quad (2.38)$$

### 2.4.1 Power spectra and frequency domain uncertainty relations

Experimentally, the most commonly used tool to evaluate the noise of a beam of light incident on a photodetector is a spectrum analyser, which measures the power spectrum  $S(\omega)$  of the fluctuations of the field in some bandwidth about the optical carrier frequency. For a stochastic variable  $\delta x(t)$  with an average value of zero, the spectral power density is defined as the fourier transform of the autocorrelation function  $G(\tau)$  [117]:

$$S(\omega) = \frac{1}{2\pi} \int_T G(\tau) e^{-i\omega\tau} d\tau. \quad (2.39)$$

Here  $T$  is the detection time, and it is assumed that  $1/T$  is much greater than any frequency component of interest. We may therefore extend this integration to cover all time. The autocorrelation function is defined as:

$$G(\tau) = \langle \delta x(t) \delta x(t + \tau) \rangle. \quad (2.40)$$

What we need now is an expression for the power spectrum of the field fluctuations. Evaluating  $(\langle \delta \tilde{X}(\omega_1) [\delta \tilde{X}(\omega_2)]^\dagger \rangle)$  gives:

$$\begin{aligned} \langle \delta \tilde{X}(\omega_1) [\delta \tilde{X}(\omega_2)]^\dagger \rangle &= \left\langle \int_{-\infty}^{\infty} \int_{-\infty}^{\infty} \delta X(t_1) e^{-i\omega_1 t_1} \delta X(t_2) e^{i\omega_2 t_2} dt_1 dt_2 \right\rangle \\ &= \left\langle \int_{-\infty}^{\infty} \int_{-\infty}^{\infty} \delta X(t_2 + \tau) \delta X(t_2) e^{-i(\omega_1 - \omega_2)t_2} e^{-i\omega_1 \tau} dt_2 d\tau \right\rangle \\ &\quad \text{where } t_1 = t_2 + \tau \\ &= \frac{1}{2\pi} \delta(\omega_1 - \omega_2) \int_{-\infty}^{\infty} \langle \delta X(t_2 + \tau) \delta X(t_2) \rangle e^{i\omega_2 \tau} d\tau \\ &= \delta(\omega_1 - \omega_2) S(\omega_1). \end{aligned} \quad (2.41)$$



The two-frequency correlation function is therefore related to the spectral power density. In an experiment, the value of the power spectrum at some frequency  $\omega_2$  is measured over some bandwidth  $B$  about the frequency  $\omega_2$ . This bandwidth is the resolution bandwidth (RBW) of the spectrum analyser. To accurately measure the spectrum,  $B$  is chosen so that the value of the spectral density is approximately constant over the range of  $B$ . This ensures that the details of the spectrum are not blurred in the measurement. The bandwidth limited spectrum  $S_B(\omega_2)$  is therefore defined as:

$$\begin{aligned}
S_B(\omega_2) &= \int_{\omega-B/2}^{\omega+B/2} \int_{-\infty}^{\infty} \langle \delta\tilde{X}(\omega_1) [\delta\tilde{X}(\omega_2)]^\dagger \rangle d\omega_1 d\omega_2 \\
&= \int_{\omega-B/2}^{\omega+B/2} \int_{-\infty}^{\infty} \delta(\omega_1 - \omega_2) S(\omega_1) d\omega_1 d\omega_2 \\
&= S(\omega_2) \int_{\omega-B/2}^{\omega+B/2} d\omega_2 \quad (\text{Since } S(\omega_2) \text{ is constant over } B) \\
&= S(\omega_2) \times B = \left\langle |\delta\tilde{X}(\omega_2)|^2 \right\rangle \times B.
\end{aligned} \tag{2.42}$$

The normalised power spectrum is therefore given by (dropping the subscript 2)

$$V(\omega) = \frac{S_B(\omega)}{B} = \left\langle |\delta\tilde{X}(\omega)|^2 \right\rangle \tag{2.43}$$

where we have normalised out the measurement bandwidth. The spectrum,  $V$ , is the frequency domain equivalent to the variance,  $\Delta^2$ , introduced in the time domain. In particular, for vacuum noise,  $\left\langle |\delta\tilde{X}(\omega)|^2 \right\rangle = 1$ , giving

$$V(\omega) = 1. \tag{2.44}$$

As a simple example, we may find the power spectrum of a directly detected laser beam. The linearised frequency domain fluctuation operator for the photon number is given by  $\bar{A}\delta\tilde{X}^+(\omega)$ , where  $\bar{A}$  is the average field amplitude. The photon number spectrum is therefore given by

$$\begin{aligned}
V_n(\omega) &= \bar{A}^2 \langle |\delta\tilde{X}^+(\omega)|^2 \rangle \\
&= \bar{A}^2 V^+(\omega).
\end{aligned} \tag{2.45}$$

In other words, frequency domain detection of the photon number gives the spectrum of the amplitude quadrature of the beam scaled by the optical power in the beam. This is directly analogous to the time domain result in equation 2.30. In the case of detecting a coherent beam  $V^+(\omega) = 1$ , giving  $V_n(\omega) = \bar{A}^2$ . This is the quantum noise limit. If we ever measure a spectrum with  $V_n(\omega) < \bar{A}^2$ , then we have an intensity squeezed state.

In analogy with the time domain case, the commutation relations for the frequency domain quadrature operators give the frequency domain uncertainty principle [110, 132]:

$$V^+(\omega)V^-(\omega) \geq 1. \tag{2.46}$$

This implies that at each frequency, the phase and amplitude power spectra obey a Heisenberg uncertainty relation. Measurement of the phase and amplitude spectra therefore provides direct access to the uncertainty principle. The method used to measure these

spectra is will be described shortly.

Typically when doing calculations of frequency spectra, we will find expressions for the output field quadrature in terms of input vacuum terms. For example, suppose we find that for a given system we have vacuum inputs  $\delta\tilde{X}_1(\omega)$  and  $\delta\tilde{X}_2(\omega)$  and a calculation gives

$$\tilde{X}^+(\omega) = f(\omega)\delta\tilde{X}_1(\omega) + g(\omega)\delta\tilde{X}_2(\omega). \quad (2.47)$$

The two vacua are uncorrelated, so that terms like  $\langle\delta\tilde{X}_1(\omega)\delta\tilde{X}_2(\omega)\rangle$  are equal to zero. The spectrum of this hypothetical output would then be given by

$$V^+ = \left\langle\left|\delta\tilde{X}^+(\omega)\right|^2\right\rangle = |f(\omega)|^2V_1^+(\omega) + |g(\omega)|^2V_2^+(\omega) = |f(\omega)|^2 + |g(\omega)|^2. \quad (2.48)$$

In general, the frequency or time arguments for the operators and spectra will not be written explicitly. In other words,  $A(t) = A$ ,  $\tilde{A}(\omega) = \tilde{A}$  and  $V(\omega) = V$ .

## 2.5 Experimental devices

### 2.5.1 Beamsplitters

A ubiquitous device in optics is the beamsplitter, as shown in figure 2.4. The relationship

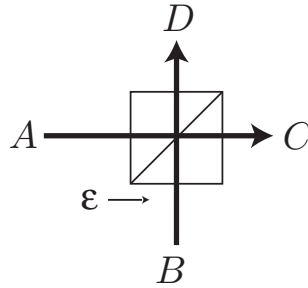


**Figure 2.4:** A beamsplitter with transmission  $\varepsilon$ .

between the fields  $A$ ,  $B$ ,  $C$ , and  $D$  is given by conservation of energy. One solution is

$$\begin{aligned} C &= \sqrt{\varepsilon}A - \sqrt{1-\varepsilon}B \\ D &= \sqrt{1-\varepsilon}A + \sqrt{\varepsilon}B \end{aligned} \quad (2.49)$$

where the transmissivity of the beamsplitter is given by  $\varepsilon$ . Other solutions involve imaginary phase which tend to make calculations more complex than necessary. These equations will be used in the following sections to explain experimental measuring techniques. The beamsplitter equations are identical for the time and frequency domain operators. The frequency domain version of equations 2.49 are simply obtained by adding a tilde ( $\sim$ ) above the field operators.

### 2.5.2 Optical attenuation and measuring with a photodetector

To measure the intensity noise spectrum,  $V^+$ , of a laser beam, the light is aligned onto a photodiode. The power spectrum of the photocurrent ( $I$ ) is then measured on a spectrum analyser. Ideally, there is a one-to-one correspondence between the incident photons and the electrons in the diode photocurrent. The electronic current is therefore expected to

be a faithful reproduction of the photon number, so that

$$\begin{aligned} I &= A^\dagger A \quad \text{and} \\ V_I &= \bar{A}^2 V^+ = \bar{A}^2 \langle |\delta\tilde{X}^+|^2 \rangle. \end{aligned} \quad (2.50)$$

Of concern for experiments in quantum optics is the efficiency of the photodiode. If some of the photons are lost, via reflection for example, then they are not converted into photocurrent and the electrical statistics will not be an ideal representation of the photon statistics. To see how this affects detection we model a real detector as shown in figure 2.5.

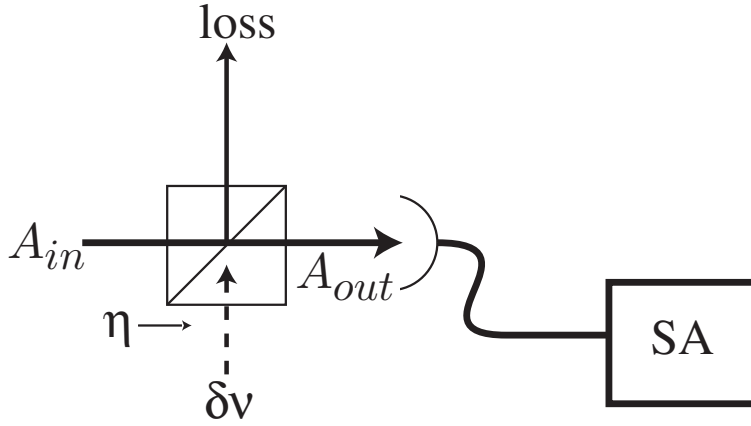


**Figure 2.5:** Direct detection with photodetector with efficiency  $\eta$ .

An inefficient detector is represented by a beamsplitter with transmission  $\eta$ , followed by an ideal detector. The efficiency of the whole detection system is therefore  $\eta$ . The remaining portion of light ( $1 - \eta$ ) is never converted into current. The effect of the beamsplitter is to introduce a quantum vacuum,  $\delta\nu$ , into the light observed by the ideal detector. The detected photocurrent spectrum is therefore given by  $V_I = V_{N_{\text{out}}}$  where  $N_{\text{out}} = A_{\text{out}}^\dagger A_{\text{out}}$ . Equations 2.49 gives

$$\tilde{A}_{\text{out}} = \sqrt{\eta}\tilde{A}_{\text{in}} + \sqrt{1-\eta}\delta\tilde{\nu}. \quad (2.51)$$

The photocurrent due to this field is now given by  $\tilde{A}_{\text{out}}^\dagger \tilde{A}_{\text{out}}$ . Referring to equation 2.29, the photocurrent is found to be

$$I = \eta\bar{A}^2 + \sqrt{\eta}\bar{A}(\sqrt{\eta}\delta\tilde{X}_{A_{\text{in}}}^+ + \sqrt{1-\eta}\delta\tilde{X}_{\nu}^+) \quad (2.52)$$

where the first term is the DC photocurrent and the second term contains the fluctuations. Now using equation 2.43 (and remembering that the spectrum of the quantum noise  $\langle |\delta\tilde{X}_{\nu}^+|^2 \rangle$  is just 1) we obtain

$$V_I = \eta\bar{A}^2[(\eta V_{A_{\text{in}}}^+ + (1-\eta))]. \quad (2.53)$$

To obtain a result that is normalised to the QNL, we must divide by the photon number,  $\bar{A}^2$ , to give

$$V_I^{\text{norm}} = \eta V_{A_{\text{in}}}^+ + (1-\eta). \quad (2.54)$$

This is a result which has applications beyond detector modelling. Remembering that  $V_I = V_{A_{\text{out}}}$ , we find that this equation describes any situation where a beam is attenuated

by a lossy optical element. In the ideal case where  $\eta = 1$ , the normalised spectrum is exactly equal to  $V_{A_{in}}^+$ . This means that the normalised spectrum is, ideally, a measure of the amplitude quadrature spectrum.

One important situation which clearly demonstrates the effect of loss, is the measurement of a squeezed beam. Considering the case of a perfectly amplitude squeezed beam, so that  $V_{A_{in}}^+ \rightarrow 0$ , the detected intensity noise spectrum is given by

$$V_I^{\text{norm}} \rightarrow (1 - \eta). \quad (2.55)$$

This says that the most squeezing that can actually be observed with a 90% efficient detector is  $V = 0.1$ , even if you have made a perfect squeezing machine. This argument holds true for all forms of optical loss, be it poor detection or poor quality optics. The bottom line is that attenuation is bad for squeezing. The importance of low loss photodetectors and optical components in squeezing experiments is therefore paramount. As a final note, it is worth exploring exactly what effect the loss has on the detected variance. As  $\eta \rightarrow 0$  we see that the spectrum approaches 1. This says that poor detection makes the beam look more like a coherent state. This is because the vacuum state and coherent state share identical noise statistics. As less light is detected, the effect of the vacuum mode becomes more pronounced and the variance approaches that of the coherent state.

### 2.5.3 Balanced homodyne detection

#### Self-homodyne detection

When doing quantum optics experiments, the quantity of interest is the spectrum of the field relative to the QNL. In the above example of detection, it was shown that normalising to the QNL means dividing by the optical power. The QNL is not a constant, rather it depends on the power present in the beam being detected. How can this normalisation be done experimentally? The preferred method is via balanced homodyne detection, as shown in figure 2.6. This situation is also known as self-homodyne detection.

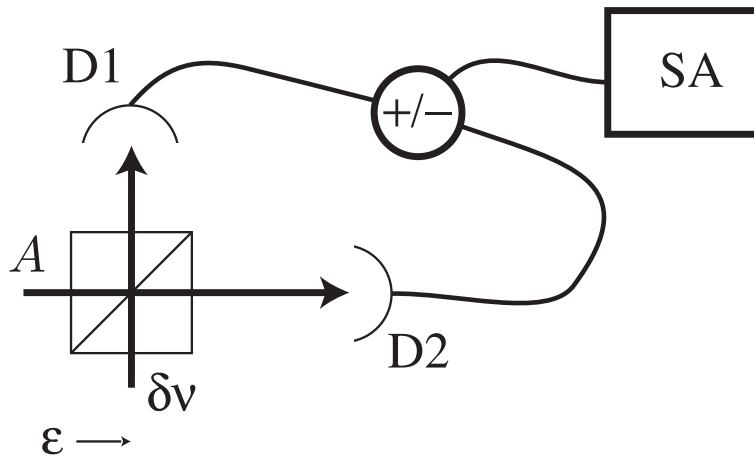


**Figure 2.6:** A self-homodyne detection system, the beamsplitter ratio is  $\epsilon = \frac{1}{2}$ .

It is assumed that the beam  $\delta\nu$  is a vacuum, the beamsplitter ratio is  $\epsilon = \frac{1}{2}$  and that we have detectors of efficiency  $\eta$ . Referring to equation 2.52, the photocurrent fluctuation

operators are found to be:

$$\delta\tilde{I}_1 = \frac{\sqrt{\eta}\bar{A}}{2} \left( \sqrt{\eta}(\delta\tilde{X}_A^+ + \delta\tilde{X}_\nu^+) + \sqrt{1-\eta}\delta\tilde{X}_{d1} \right). \quad (2.56)$$

$$\delta\tilde{I}_2 = \frac{\sqrt{\eta}\bar{A}}{2} \left( \sqrt{\eta}(\delta\tilde{X}_A^+ - \delta\tilde{X}_\nu^+) + \sqrt{1-\eta}\delta\tilde{X}_{d2} \right) \quad (2.57)$$

where  $\tilde{X}_{d1}$  and  $\tilde{X}_{d2}$  arise from the detector loss. Considering the sum and difference of the photocurrents gives

$$\delta\tilde{I}_1 + \delta\tilde{I}_2 = \sqrt{\eta}\bar{A} \left[ \sqrt{\eta}\delta\tilde{X}_A^+ + \frac{\sqrt{1-\eta}}{\sqrt{2}}(\delta\tilde{X}_{d1} + \delta\tilde{X}_{d2}) \right] \quad (2.58)$$

$$\delta\tilde{I}_1 - \delta\tilde{I}_2 = \sqrt{\eta}\bar{A} \left[ \sqrt{\eta}\delta\tilde{X}_\nu^+ + \frac{\sqrt{1-\eta}}{\sqrt{2}}(\delta\tilde{X}_{d1} - \delta\tilde{X}_{d2}) \right]. \quad (2.59)$$

This leads to the sum and difference spectra

$$V_{I1+I2} = \eta\bar{A}^2(\eta V_A^+ + 1 - \eta) \quad (2.60)$$

$$V_{I1-I2} = \eta\bar{A}^2(\eta V_\nu^+ + 1 - \eta) = \eta\bar{A}^2 \quad (\text{using } V_\nu^+ = 1). \quad (2.61)$$

The spectrum of the difference photocurrent is therefore the QNL of the bright beam. The sum output is a measurement of the spectrum of the input field, tempered by the detector efficiency. The normalised amplitude quadrature spectrum is therefore measured experimentally by evaluating

$$\frac{V_{I1+I2}}{V_{I1-I2}} = \eta V_A^+ + 1 - \eta \quad (2.62)$$

which, in the limit of ideal detection ( $\eta = 1$ ), gives the amplitude quadrature spectrum exactly.

## Measuring the phase quadrature spectrum

Balanced homodyne detection may also be used to find the spectrum of the phase quadrature [136]. Referring to figure 2.7 we now consider the case of  $B e^{-i\theta}$  being a bright beam with amplitude  $\bar{B}$  such that  $\bar{B} \ll \bar{A}$ .

The beam  $A$  is referred to as the local oscillator, and it will be used to measure the  $\theta$  quadrature of  $B e^{-i\theta}$ . The phase term  $e^{-i\theta}$  therefore plays a role in this derivation. Previously, the phase has been arbitrary and  $\theta$  was therefore set to 0. Another complication is the mode-matching of  $A$  and  $B e^{-i\theta}$ . In the case of self-homodyne detection, the vacuum is always perfectly mode-matched with the bright beam because the vacuum has modes covering all space-time. This is not the case when one has to align two bright beams on a beamsplitter. Inevitably, the beamsplitter will not be perfectly flat, or the polarisation of the two beams not perfectly matched. The effect of these mechanisms is to reduce the fringe visibility of the interference. This will reduce the detection efficiency. To model less than ideal mode-matching, we will assume that co-propagating with  $A$  is the mode  $H$ , which contains some power. The mode  $H$  is orthogonal to both  $A$  and  $B e^{-i\theta}$  and will therefore not interfere with either. The power in  $H$  will instead beat with the appropriate vacuum mode  $\nu_h$  which enters with  $B e^{-i\theta}$ . It is also assumed that the classical amplitudes of the fields  $A$  and  $B e^{-i\theta}$  are  $\bar{A}$  and  $\bar{B} e^{-i\theta}$  respectively. Considering the interaction of  $A$

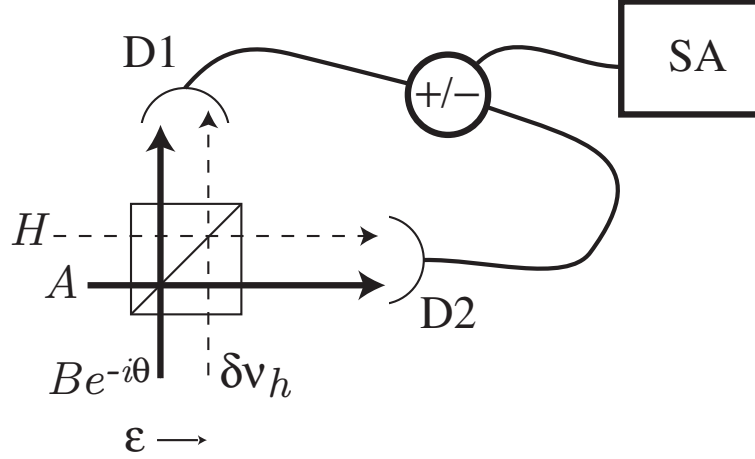


**Figure 2.7:** A homodyne detection system with 2 bright beams. The beamsplitter ratio is  $\epsilon = \frac{1}{2}$ . The interfering modes are indicated on the diagram.

and  $B e^{-i\theta}$  gives:

$$\begin{aligned} \delta\tilde{I}1 + \delta\tilde{I}2 &= \sqrt{\eta}(\bar{A}\sqrt{\eta}\delta\tilde{X}_A^+ + \bar{B}\sqrt{\eta}\delta\tilde{X}_B^+) \\ &+ \sqrt{\frac{\eta(1-\eta)}{2}} \left[ (\bar{A} + \bar{B}e^{-i\theta})\delta\nu_{d1} + (\bar{A} + \bar{B}e^{i\theta})\delta\nu_{d1}^\dagger \right. \\ &\left. + (\bar{A} - \bar{B}e^{-i\theta})\delta\nu_{d2} + (\bar{A} - \bar{B}e^{i\theta})\delta\nu_{d2}^\dagger \right] \end{aligned} \quad (2.63)$$

$$\begin{aligned} \delta\tilde{I}1 - \delta\tilde{I}2 &= \sqrt{\eta}\bar{A}[\sqrt{\eta}(\delta\tilde{B}e^{-i\theta} + \delta\tilde{B}^\dagger e^{i\theta})] \\ &+ \sqrt{\eta}\bar{B}[\sqrt{\eta}(\delta\tilde{A}e^{i\theta} + \delta\tilde{A}^\dagger e^{-i\theta})] \\ &+ \sqrt{\frac{\eta(1-\eta)}{2}} \left[ (\bar{A} + \bar{B}e^{-i\theta})\delta\nu_{d1} + (\bar{A} + \bar{B}e^{i\theta})\delta\nu_{d1}^\dagger \right. \\ &\left. - (\bar{A} - \bar{B}e^{-i\theta})\delta\nu_{d2} - (\bar{A} - \bar{B}e^{i\theta})\delta\nu_{d2}^\dagger \right]. \end{aligned} \quad (2.64)$$

Ignoring terms proportional to  $\bar{B}$  (using  $\bar{B} \ll \bar{A}$ ) these reduce to

$$\delta\tilde{I}1 + \delta\tilde{I}2 = \sqrt{\eta}\bar{A} \left[ \sqrt{\eta}\delta\tilde{X}_A^+ + \sqrt{\frac{1-\eta}{2}} (\delta\tilde{X}_{d1}^+ + \delta\tilde{X}_{d2}^+) \right] \quad (2.65)$$

$$\delta\tilde{I}1 - \delta\tilde{I}2 = \sqrt{\eta}\bar{A} \left[ \sqrt{\eta}\delta\tilde{X}_B^\theta + \sqrt{\frac{1-\eta}{2}} (\delta\tilde{X}_{d1}^+ - \delta\tilde{X}_{d2}^+) \right], \quad (2.66)$$

therefore giving

$$V_{I1+I2} = \eta\bar{A}^2(\eta V_A^+ + (1-\eta)) \quad (2.67)$$

$$V_{I1-I2} = \eta\bar{A}^2(\eta V_B^\theta + (1-\eta)). \quad (2.68)$$

The difference photocurrent is found to be a measure of the  $\theta$  quadrature of the field  $B e^{-i\theta}$ . In this way the phase quadrature may be measured by the homodyne system. Note that to normalise, we block the input  $B$  so that it is replaced by the quantum vacuum. This

will give the quantum noise as in equation 2.61

$$V_B^\theta = \frac{V_{I1-I2}}{[V_{I1-I2}]_{B \text{ blocked}}}. \quad (2.69)$$

The sum term,  $V_{I1+I2}$ , simply gives the noise of the local oscillator, and is independent of  $B e^{-i\theta}$ .

We now turn to the case of imperfect mode-matching, i.e. we consider the interference of the mode  $H$  with the vacuum  $\delta\nu_h$ . Fortunately, this is just the case shown in figure 2.6. The contribution to the sum and difference photocurrents due to the field  $H$  comes directly from equations 2.59, giving

$$\delta\tilde{I}_{1H} + \delta\tilde{I}_{2H} = \sqrt{\eta}\bar{H}[\sqrt{\eta}\delta\tilde{X}_H^+ + \frac{\sqrt{1-\eta}}{\sqrt{2}}(\delta\tilde{X}_{H,d1}^+ + \delta\tilde{X}_{H,d2}^+)] \quad (2.70)$$

$$\delta\tilde{I}_{1H} - \delta\tilde{I}_{2H} = \sqrt{\eta}\bar{H}[\sqrt{\eta}\delta\tilde{X}_h^+ + \frac{\sqrt{1-\eta}}{\sqrt{2}}(\delta\tilde{X}_{H,d1}^+ - \delta\tilde{X}_{H,d2}^+)] \quad (2.71)$$

where  $\bar{H}$  is the classical amplitude of  $H$  and the detector noise terms are  $\delta\tilde{X}_{H,d1}^+$  and  $\delta\tilde{X}_{H,d2}^+$ . The power in  $H$  is a part of the total local oscillator power. If the total local oscillator amplitude is  $\bar{A}$ , then we make the substitutions  $\bar{A} \rightarrow \sqrt{\eta_h}\bar{A}$  and  $\bar{H} \rightarrow \sqrt{1-\eta_h}\bar{A}$ . Adding equations 2.71 and 2.66 with these replacements gives:

$$\delta\tilde{I}_1 - \delta\tilde{I}_2 = \sqrt{\eta}\bar{A} \left[ \sqrt{\eta_h}\delta\tilde{X}_B^\theta + \sqrt{1-\eta_h}\sqrt{\eta}\delta\tilde{X}_h^+ + \frac{\sqrt{1-\eta}}{\sqrt{2}}(\delta\tilde{X}_{d1,T}^+ + \delta\tilde{X}_{d2,T}^+) \right] \quad (2.72)$$

where we have defined the total vacuum noise sources due to the detectors as  $\delta\tilde{X}_{d1,T}^+ = \sqrt{\eta_h}\delta\tilde{X}_{d1}^+ + \sqrt{1-\eta_h}\delta\tilde{X}_{H,d1}^+$  and  $\delta\tilde{X}_{d2,T}^+ = \sqrt{\eta_h}\delta\tilde{X}_{d2}^+ + \sqrt{1-\eta_h}\delta\tilde{X}_{H,d2}^+$ . Evaluating the noise spectrum gives

$$V_{I1-I2}^{\text{tot}} = \eta\bar{A}^2[\eta\eta_h V_B^\theta + 1 - \eta\eta_h]. \quad (2.73)$$

Comparing with the result of beam attenuation considered in section 2.5.2, we see that  $\eta_h$  looks like an extra attenuation term. This says that if the proportion  $\eta_h$  of the light is lost into a mode which does not interfere with  $B e^{-i\theta}$ , then the effect is that of an optical loss  $\eta_h$  in the homodyne system. The normalised spectrum may still be measured by blocking the beam  $B$  and using equation 2.69.

To measure the mode-matching efficiency in the lab, we can find the fringe visibility  $\mathcal{V}$ , which is defined as

$$\mathcal{V} = \frac{P_{\text{max}} - P_{\text{min}}}{P_{\text{max}} + P_{\text{min}}} \quad (2.74)$$

where  $P_{\text{max}}$  is the maximum power in the fringe (constructive interference) and  $P_{\text{min}}$  is the minimum (destructive interference). This assumes that the power in the two beams are equal. Therefore taking  $|\bar{A}|^2 = |\bar{B}|^2$ , we find that

$$\mathcal{V} = \frac{2\sqrt{\eta_h}|\bar{A}\bar{B}|}{\eta_h|\bar{A}|^2 + |\bar{B}|^2 + (1-\eta_h)|\bar{A}|^2} = \sqrt{\eta_h}. \quad (2.75)$$

Finally, the homodyne efficiency  $\eta_h$  is given by

$$\eta_h = \mathcal{V}^2. \quad (2.76)$$

## 2.6 Open quantum systems and the quantum Langevin equation

The term ‘open quantum system’ is used to describe a quantum system that interacts irreversibly with the greater universe. In reality all systems (other than the universe itself) are open, which means that any realistic model of a quantum system must include some irreversible interaction with the universe. One easy example of an open quantum system is the partial absorption of a beam by a broadband attenuator. This may be modelled as a beamsplitter, so that the loss in transmitted power adds some vacuum noise to the beam. The difference is that the power reflected from the beamsplitter is effectively thrown away so that the addition of the vacuum noise by absorption is irreversible<sup>1</sup>. The case of broadband absorption is easy, it is frequency independent and the beamsplitter model is all that is required. If the open system in question is more complex, then we must resort to a more complex theoretical treatment. One such method is the quantum Langevin equation. This is an example of a stochastic differential equation similar in form to that used by Langevin in 1908 to describe Brownian motion [41]. It was first proposed as a method for dealing with open quantum systems by Haken [51]. The formalism used here was developed by Gardiner and Collett [40].

In order to describe the significance of the quantum Langevin equation we will consider the example of a harmonic oscillator. This is particularly relevant because an optical cavity may be modelled as a harmonic oscillator.

A classical model of a perfect, lossless harmonic oscillator has the equation

$$\dot{x} = i\Omega x \quad (2.77)$$

so that on integration the variable  $x$  will oscillate indefinitely with angular frequency  $\Omega$ . This is a closed system which exchanges no energy with the rest of the universe. External interaction, such as that due to a frictional force, can be introduced through a damping term. We can assume that the reservoir into which this energy is dissipated is at absolute zero so that the reservoir does not add any fluctuations to the system. The equation for this *open* system is

$$\dot{x} = (i\Omega - \gamma)x \quad (2.78)$$

where  $\gamma$  is the damping rate. Such damping leads to exponential decay of the parameter  $x$ . This type of equation is commonly used to model damped classical systems.

How can an equivalent damping term due to the interaction with the universe be included in a quantum system? For a closed quantum system with Hamiltonian  $H_{\text{rev}}$ , the motion of an operator  $a$  is given by

$$\dot{a} = \frac{1}{i\hbar}[a, H_{\text{rev}}] \quad (2.79)$$

Because this system is closed the Hamiltonian is reversible, hence the name  $H_{\text{rev}}$ . If the system were a lossless harmonic oscillator, then the Hamiltonian would be

$$H_{\text{rev}} = -\Omega\hbar a^\dagger a \quad (2.80)$$

---

<sup>1</sup>If both the outputs of a beamsplitter are available, the vacuum noise may be removed by recombining the transmitted and reflected fields at a second beamsplitter



where  $a^\dagger$  and  $a$  are the boson creation and annihilation operators respectively. Using the commutation relation  $[a, a^\dagger] = 1$  gives an equation of motion for the undamped quantum harmonic oscillator of

$$\dot{a} = i\Omega a \quad (2.81)$$

which is exactly analogous to the equation of motion for the undamped classical oscillator.

To model an *open* quantum system extra terms must be included to describe the exchange of energy with the rest of the universe. To find what form these terms take we model the universe as a reservoir with an infinite number of modes and a Hamiltonian  $H_B$ :

$$H_B = i\hbar \int_{-\infty}^{\infty} \Omega \tilde{B}^\dagger(\Omega) \tilde{B}(\Omega) d\Omega \quad (2.82)$$

where  $\tilde{B}^\dagger(\Omega)$  and  $\tilde{B}(\Omega)$  are the (frequency domain) boson creation and annihilation operators respectively. This reservoir is allowed to interact irreversibly with an arbitrary system operator,  $\tilde{c}$ , so that the Hamiltonian for the interaction,  $H_{\text{irrev}}$  is given by

$$H_{\text{irrev}} = i\hbar \int_{-\infty}^{\infty} \sqrt{2\gamma} (\tilde{B}^\dagger(\Omega) \tilde{c} - \tilde{c}^\dagger \tilde{B}(\Omega)) d\Omega \quad (2.83)$$

where  $2\gamma$  is a coupling constant which is assumed to be independent of frequency (This is known as the first Markov approximation). It was shown by Gardiner and Collett [40] that we can use these Hamiltonians to rewrite the Heisenberg equation of motion for the system operator  $\tilde{c}$  as

$$\dot{\tilde{c}} = \underbrace{\frac{1}{i\hbar} [\tilde{c}, H_{\text{rev}}]}_* - \underbrace{\left\{ [a, \tilde{c}^\dagger] \left( \gamma \tilde{c} + \sqrt{2\gamma} \delta B(t) \right) - \left( \gamma \tilde{c}^\dagger + \sqrt{2\gamma} \delta B^\dagger(t) \right) [a, \tilde{c}] \right\}}_{**} \quad (2.84)$$

where  $\delta B(t)$  is defined with respect to some arbitrary time  $t_0$  as

$$\delta B(t) = \int_{-\infty}^{\infty} e^{-i\Omega(t-t_0)} \tilde{B}_0(\Omega) d\Omega \quad (2.85)$$

Equation 2.84 is known as the quantum Langevin equation. The first part (\*) is the equation of motion of the closed, reversible system (equation 2.79). The second part (\*\*) is due to the irreversible interaction of the system with the reservoir. To see what effect this interaction has on the equation of motion of the harmonic oscillator, we can substitute the harmonic oscillator system Hamiltonian (equation 2.80) in the quantum Langevin equation and find the equation of motion of the operator  $a$ :

$$\dot{a} = (i\Omega - \gamma)a - \sqrt{2\gamma} \delta B. \quad (2.86)$$

Moving into a frame of reference rotating with the oscillation by making the substitution  $a = ae^{-i\Omega t}$  and  $B = Be^{-i\Omega t}$  we find:

$$\dot{a} = -\gamma a - \sqrt{2\gamma} \delta B. \quad (2.87)$$

The motion of the operator  $a$  is seen to be damped at a rate  $\gamma$  which is half the coupling constant defined in the irreversible Hamiltonian. The motion of  $a$  is also governed by  $\delta B$ . This is a fluctuation operator with an expectation value of zero. It can be interpreted as a noise input to the system, a field which randomly kicks the motion of the operator  $a$ . Noise introduced by loss is common in many physical processes. Loss into a thermal

reservoir with some temperature leads to the fluctuation dissipation theorem [76]. However in this model, the noise is a consequence of the commutation relation between creation and annihilation operators rather than some classical temperature of the reservoir. The noise input to this quantum system is required to maintain the bosonic commutation relations in the presence of loss.

## 2.7 Optical cavities

The treatment of the simple harmonic oscillator above may be extended to model an optical cavity with multiple loss terms. These loss terms can then be related to measurable quantities such as scattering loss and mirror reflectivities. A general empty cavity is shown in figure 2.8. This diagram shows a ring cavity which has spatially separated inputs and outputs making the diagram easier to follow. The theoretical results apply equally to linear cavities.

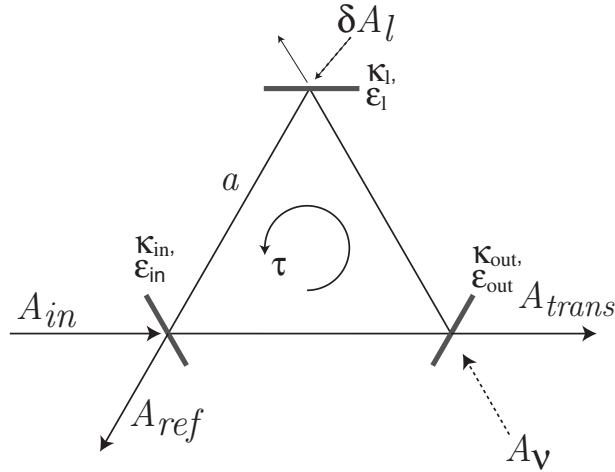


**Figure 2.8:** An empty optical cavity with various input and output fields.

The various optical fields are:

- $a$ , the cavity mode;
- $A_{in}$ , the input field to the cavity;
- $A_{trans}$ , the output field from the cavity;
- $\delta A_\nu$ , the vacuum mode at the output mirror; and
- $\delta A_l$ , vacuum mode coupled in by intra-cavity loss.

There are also coupling rates for the modes at each of the cavity mirrors. These are:

- $\kappa_{in}$ , the coupling rate through the input mirror;
- $\kappa_{out}$ , the coupling rate through the output mirror; and
- $\kappa_l$ , the output coupling rate of the cavity mode due to intra-cavity loss.

Each of these coupling rates has a corresponding transmissivity  $\varepsilon_{(\text{in,out,l})}$ . The final variable shown on figure 2.8 is  $\tau$ , the round-trip time. The units of the capitalised fields are  $s^{-1/2}$  to give the photon number of these fields ( $A^\dagger A$ ) units of  $s^{-1}$ . These are travelling waves and are therefore measured in photons per second. This is distinct to the lower case mode  $a$  which is dimensionless because it is a mode in a cavity and the operator,  $a^\dagger a$ , just counts the number of photons in the cavity.

Starting from the quantum Langevin equation defined in the previous section, it can be shown that the equation of motion for an empty cavity is given by

$$\dot{a} = (i\Omega_c - \kappa)a + \sqrt{2\kappa_{\text{in}}}A_{\text{in}}e^{i\Omega_f t} + \sqrt{2\kappa_l}\delta A_l + \sqrt{2\kappa_{\text{out}}}\delta A_\nu \quad (2.88)$$

where we now have a pump field with frequency  $\Omega_f$  which may be different to the cavity frequency  $\Omega_c$ . Also,  $\kappa$  is the total cavity damping rate, given by  $\kappa_l + \kappa_{\text{in}} + \kappa_{\text{out}}$ . Moving into a frame rotating with the pump field by making the substitution  $z_i = z_i e^{-i\Omega_f t}$  for all operators  $z_i$ , simplifies equation 2.88 to

$$\dot{a} = -(\kappa + i\Delta)a + \sqrt{2\kappa_{\text{in}}}A_{\text{in}} + \sqrt{2\kappa_l}\delta A_l + \sqrt{2\kappa_{\text{out}}}\delta A_\nu \quad (2.89)$$

where  $\Delta = \Omega_f - \Omega_c$  is the detuning between the cavity and the pump field. Provided we are dealing only with high finesse cavities, which means that  $\varepsilon_{(\text{in,out,l})} \ll 1$ , the damping rates may be expressed in terms of the transmissivity of the mirrors and loss elements in cavity as:

$$\begin{aligned} \kappa_{\text{in}} &= \frac{\varepsilon_{\text{in}}}{2\tau} \\ \kappa_{\text{out}} &= \frac{\varepsilon_{\text{out}}}{2\tau} \\ \kappa_l &= \frac{\varepsilon_l}{2\tau}. \end{aligned} \quad (2.90)$$

Assuming perfect resonance between the cavity and pump field so that  $\Delta = 0$ , taking the Fourier transform of equation 2.89 gives

$$\begin{aligned} i\omega\tilde{a} &= -\kappa\tilde{a} + \sqrt{2\kappa_{\text{in}}}\tilde{A}_{\text{in}} + \sqrt{2\kappa_l}\delta\tilde{A}_l + \sqrt{2\kappa_{\text{out}}}\delta\tilde{A}_\nu \\ \Rightarrow \tilde{a} &= \frac{\sqrt{2\kappa_{\text{in}}}\tilde{A}_{\text{in}} + \sqrt{2\kappa_{\text{out}}}\delta\tilde{A}_\nu + \sqrt{2\kappa_l}\delta\tilde{A}_l}{i\omega + \kappa} \end{aligned} \quad (2.91)$$

where  $\omega$  is a small frequency shift about the optical carrier frequency. To calculate the reflected ( $\tilde{A}_{\text{ref}}$ ) and transmitted ( $\tilde{A}_{\text{trans}}$ ) fields, we can use the relations [40]

$$\tilde{A}_{\text{ref}} = \sqrt{2\kappa_{\text{in}}}\tilde{a} - \tilde{A}_{\text{in}} \quad \text{and} \quad \tilde{A}_{\text{trans}} = \sqrt{2\kappa_{\text{out}}}\tilde{a} - \delta\tilde{A}_\nu. \quad (2.92)$$

This gives:

$$\tilde{A}_{\text{ref}} = \frac{(2\kappa_{\text{in}} - \kappa - i\omega)\tilde{A}_{\text{in}} + 2\sqrt{\kappa_{\text{in}}\kappa_{\text{out}}}\delta\tilde{A}_\nu + 2\sqrt{\kappa_{\text{in}}\kappa_l}\delta\tilde{A}_l}{i\omega + \kappa} \quad (2.93)$$

$$\tilde{A}_{\text{trans}} = \frac{2\sqrt{\kappa_{\text{out}}\kappa_{\text{in}}}\tilde{A}_{\text{in}} + (2\kappa_{\text{out}} - \kappa - i\omega)\delta\tilde{A}_\nu + 2\sqrt{\kappa_{\text{out}}\kappa_l}\delta\tilde{A}_l}{i\omega + \kappa}. \quad (2.94)$$

Ignoring the quantum behaviour of the cavities for the time being, we can plot the transmission and reflection of the cavity as a function of the frequency  $\omega$ . This is done by ignoring the  $\delta$  terms in the above equations. Figure 2.9 shows the calculated response of a

high finesse overcoupled cavity (i.e.  $\kappa_{\text{in}} > \kappa_{\text{out}} + \kappa_l$ ). This shows the phase and amplitude of the fields to be strongly dependant on the frequency of the field relative to the resonant frequency of the cavity.

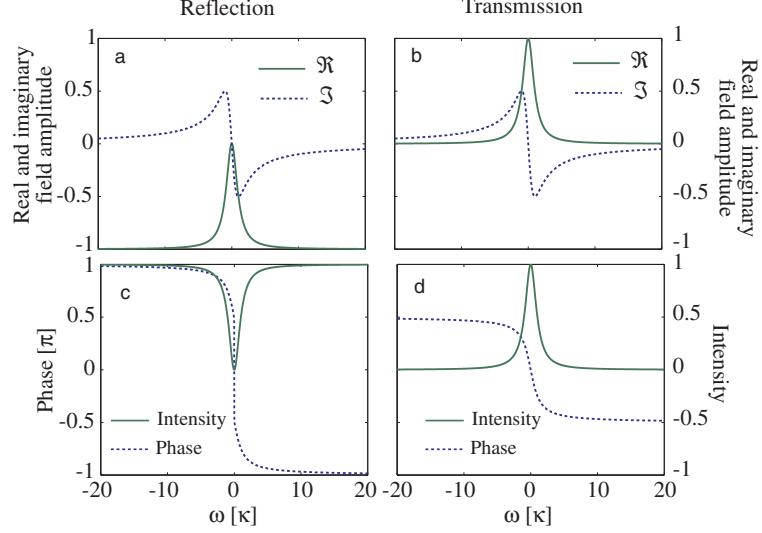


**Figure 2.9:** Response of a high finesse overcoupled cavity in terms of the real, imaginary parts of the field (a, b) and the phase and intensity (c, d). Parameters are  $\kappa_{\text{in}} = 0.6$ ,  $\kappa_{\text{out}} = 0.4$  and  $\kappa_l = 0$ .

The quantum behaviour of the cavity made be probed by using the complete form of equations 2.94 to find the field spectra  $V^\pm$ . The calculation is done by:

- finding the quadrature operators  $\delta\tilde{X}^\pm$  using equations 2.94; and then
- evaluating the spectra  $V^\pm$  by applying equation 2.43 to the quadrature operators.

The frequency domain quadrature operator is given by

$$\tilde{X}^\pm = \mathcal{F}(X^\pm) = \mathcal{F}(A) + \mathcal{F}(A^\dagger) \quad (2.95)$$

To find  $\mathcal{F}(A^\dagger)$  requires the result from Fourier theory that

$$\mathcal{F}(g^*(t)) = \tilde{g}^*(-\omega). \quad (2.96)$$

This means that the  $\mathcal{F}(A^\dagger)$  will be given by

$$\mathcal{F}(A^\dagger) = \tilde{A}^\dagger(-\omega). \quad (2.97)$$

From equations 2.94 we therefore find the quadrature fluctuations (taking the fluctuating part of  $\tilde{X}_{\text{in}}^\pm$  to be  $\delta\tilde{X}_{\text{in}}^\pm$ ):

$$\delta\tilde{X}_{\text{ref}}^\pm = \frac{(2\kappa_{\text{in}} - \kappa - i\omega)\delta\tilde{X}_{\text{in}}^\pm + 2\sqrt{\kappa_{\text{in}}\kappa_{\text{out}}}\delta\tilde{X}_\nu^\pm + 2\sqrt{\kappa_{\text{in}}\kappa_l}\delta\tilde{X}_l^\pm}{i\omega + \kappa} \quad (2.98)$$

$$\delta\tilde{X}_{\text{trans}}^\pm = \frac{2\sqrt{\kappa_{\text{out}}\kappa_{\text{in}}}\delta\tilde{X}_{\text{in}}^\pm + (2\kappa_{\text{out}} - \kappa - i\omega)\delta\tilde{X}_\nu^\pm + 2\sqrt{\kappa_{\text{out}}\kappa_l}\delta\tilde{X}_l^\pm}{i\omega + \kappa}, \quad (2.99)$$

and the spectra are therefore given by

$$V_{A_{\text{ref}}}^{\pm} = 1 + \frac{((2\kappa_{\text{in}} - \kappa)^2 + \omega^2)(V_{A_{\text{in}}}^{\pm} - 1)}{\omega^2 + \kappa^2} \quad (2.100)$$

$$V_{A_{\text{trans}}}^{\pm} = 1 + \frac{4\kappa_{\text{out}}\kappa_{\text{in}}(V_{A_{\text{in}}}^{\pm} - 1)}{\omega^2 + \kappa^2}. \quad (2.101)$$

Assuming some classical laser noise (in this case,  $V_{\text{in}}^{\pm} = 10$ ) we obtain the plots shown in figure 2.10. This shows clearly the frequency filtering effect of an optical cavity. In the transmitted field, the spectrum of the laser is at the QNL for  $|\omega| \gg \kappa$ . Conversely, for the reflected field, the laser noise is at the QNL near  $\omega = 0$  and is equal to the input laser noise for  $|\omega| \gg \kappa$ . This ability to frequency filter the laser is important for “mode cleaning” cavities. Excess laser noise is an experimental reality which hinders the progress of an otherwise feasible experiment. By using a low linewidth cavity ( $\kappa$  small) some of this noise may be stripped from the transmitted beam to form a quieter, more ideal laser source. A mode cleaning cavity is used in the experiments of chapter 7.

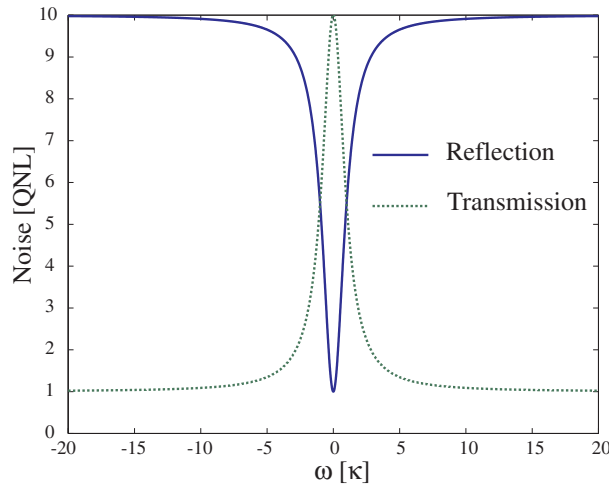


**Figure 2.10:** Reflected and transmitted noise for an impedance matched cavity. Parameters are  $V_{\text{in}}^{\pm} = 10$ ,  $\kappa_{\text{in}} = 0.6$ ,  $\kappa_{\text{out}} = 0.4$  and  $\kappa_l = 0$

## 2.8 Cavity locking

The final theoretical model which I will consider in this chapter is that of a frequency locking system. Most of the experiments in later chapters require the optical frequency of a laser to be held on resonance with an optical cavity. To do this requires the generation of a signal that measures the difference between the laser frequency and the cavity frequency. We require that this signal changes sign as the laser passes through the cavity resonance, so that by looking at the signal one can tell which way the system needs to be adjusted to go back to resonance. This signal can then be used in a feedback system to lock the cavity and laser frequencies. There are many auxiliary considerations when actually locking an optical cavity. Most of these are to do with non-ideal electronics. For the time being we will just consider the generation of an error signal from a cavity, and worry about what to do with the signal in the later experimental chapters. The problem, in essence, is drawn in figure 2.11. The idea is to find a signal in the reflected beam of the cavity which can

be used to feedback to the laser frequency or the length of the cavity.

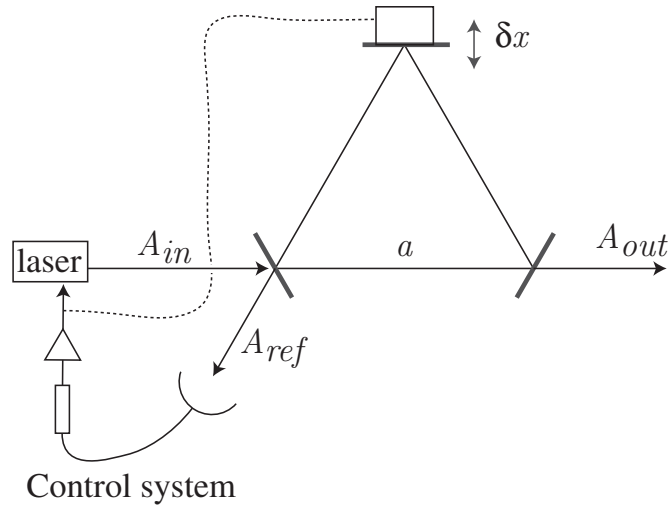


**Figure 2.11:** A cavity locking system. The control may be applied to the laser frequency (solid line) or the cavity length (dashed line).

### 2.8.1 Modulation locking

This is one of the most common methods for frequency locking. It comes in two flavours which are very closely related. One of these is the “Pound-Drever-Hall” (PDH) locking method [30]. In this technique, phase modulation sidebands are placed on the laser input to the cavity. When the cavity is detuned from resonance, the phase shift of the carrier converts the phase modulation into amplitude modulation, which may then be used to derive an error signal. The other method is “dither locking”, where the length of the cavity is modulated. This generates frequency modulation of the reflected and transmitted fields. Just like the PDH method, cavity detuning converts the frequency modulation into amplitude modulation which may be used to gather an error signal.

Considering first the PDH method, a modulator may be used to place phase sidebands at a frequency  $\gamma$  on the laser, outside the cavity bandwidth. Taking the example of an overcoupled cavity<sup>2</sup>, the sidebands are reflected with a  $\pi$  phase shift (see figure 2.9 (c)). We can now consider two cases of the carrier frequency. The first is that of the carrier exactly on resonance. Any carrier light reflected from the cavity (the amount will depend on the impedance matching) will be reflected with no phase shift. The interaction of the reflected sidebands and the carrier will give a phase modulated beam. Measuring the intensity of this light will therefore show no modulation at the sideband frequency.

The second situation is the carrier being slightly away from perfect resonance ( $\pm\omega$  in figure 2.12). The reflected carrier power will now increase. More importantly, the carrier is phase shifted relative to the sidebands. The carrier and sidebands in the reflected field will no longer beat to form pure PM, forming instead a field with some degree of AM. The photocurrent generated by detecting the reflected field will therefore have amplitude modulation,  $M$ , given by

$$M = S \sin \gamma t \sin \theta \tag{2.102}$$

<sup>2</sup>The method works with any kind of cavity, the overcoupled case is given as one possible example

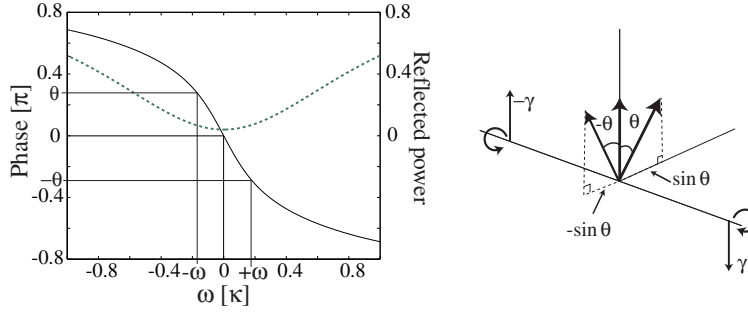


**Figure 2.12:** PDH locking of a cavity. Left: a shift of the carrier away from resonance causes a phase shift of the reflected beam. The sign of the phase shift depends on whether the carrier is above or below resonance. This diagram is a magnified version of figure 2.9 (c). Right: the angle of the carrier relative to the phase modulation sidebands (at  $\pm\gamma$ ) changes when the carrier is off-resonance. This gives amplitude modulation proportional to  $\sin \theta$ .

where  $S$  is the power in the sidebands and  $\sin \theta$  is the amount of AM due the phase shift  $\theta$  (see figure 2.12). What we need to measure is the phase shift  $\theta$ . This is achieved by multiplying the photocurrent due to the reflected field by a copy of the modulation ( $\sin \gamma t$ ) using a mixer. The mixer output  $X$  will be given by

$$X \propto S \sin^2 \gamma t \sin \theta = \frac{1}{2} S \sin \theta (1 - \cos 2\gamma t). \quad (2.103)$$

Ignoring the  $2\gamma t$  term (experimentally this means using a low pass filter) and assuming we are close to resonance so that we are dealing only with small phase changes ( $\sin \theta \approx \theta$ ), we find

$$X_{DC} \propto \frac{1}{2} S \theta. \quad (2.104)$$

This is the error signal required to hold the cavity on resonance. PDH locking also works when the phase sidebands are inside the cavity linewidth. In this case, the amplitude of one sideband will be attenuated compared to the other as the cavity moves away from resonance. This is due to the intensity response of the cavity shown by the dashed line of figure 2.9 (c). The differential change in sideband intensity leads to amplitude modulation of the reflected signal, with the sign of the modulation depending on the direction of the detuning. If we consider the case of the positive sideband being attenuated by a factor  $(1 - \delta)$  and the negative sideband a factor  $(1 + \delta)$ , then from equation 2.20 we can write [107]

$$\begin{aligned} E_{\text{ref}} &= E_0 e^{i\Omega t} \left[ 1 + \frac{d}{2} \left( (1 + \delta) e^{-i\gamma t} - (1 - \delta) e^{i\gamma t} \right) \right] \\ &= E_0 e^{i\Omega t} \left[ 1 + \frac{d}{2} \left( e^{-i\gamma t} - e^{i\gamma t} + \underbrace{\frac{d\delta}{2} (e^{-i\gamma t} + e^{i\gamma t})}_{*} \right) \right]. \end{aligned} \quad (2.105)$$

The ‘\*’ term may be identified as amplitude modulation (see equation 2.21). When mixed down, much like the previous case, a locking signal will be found. If the sidebands are within the cavity linewidth, then a locking signal may also be obtained on the transmitted field of the cavity, through the same attenuation argument.

The other form of modulation locking, dither locking, works by modulating the resonant frequency of the cavity as shown in figure 2.13.

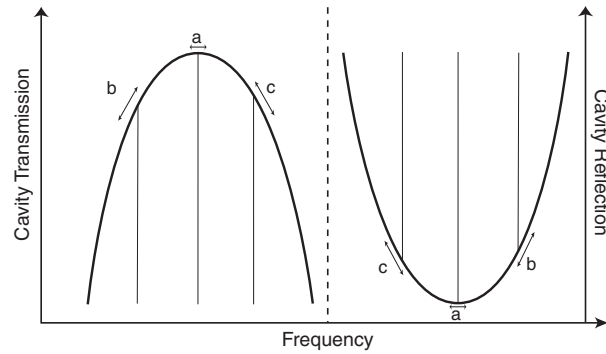


**Figure 2.13:** Dither locking. If the laser frequency is at position  $a$  gives no AM to reflected/transmitted field, positions  $b$  and  $c$  give opposite sign AM.

When the laser is exactly on resonance, modulation of the cavity length gives no AM due to the local flatness of the transmission or reflection response (position  $a$ ). If the cavity drifts off resonance, to position  $b$  for example, then the fields exiting the cavity will be amplitude modulated. In position  $c$  amplitude modulation will be also generated but of opposite sign to position  $b$ . Modulation of cavity length is equivalent to laser frequency modulation which, for sinusoidal modulation, is identical to phase modulation (see section 2.2). The dither locking signal is therefore derived in an identical manner to the case of PDH locking where the sidebands are within the cavity linewidth.

### 2.8.2 Spatial mode locking

A somewhat different method for frequency locking is the spatial mode locking technique or “tilt-locking” [108]. In this method, the cavity is misaligned as shown in figure 2.14. If we imagine that the  $TEM_{00}$  mode is resonant with the cavity, then the other spatial modes will, in general, not be resonant due to the differing Gouy phase shift of the different spatial modes [111].

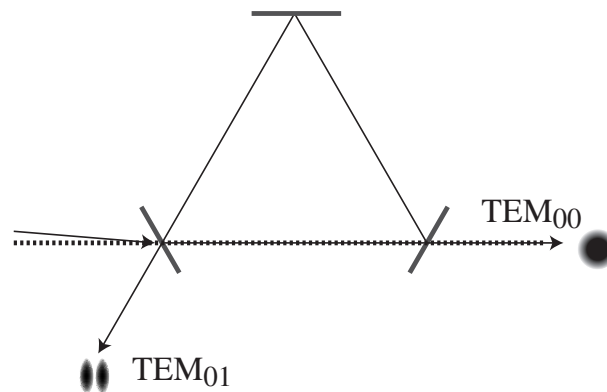


**Figure 2.14:** A cavity with a tilted input mode. For the  $TEM_{00}$  mode the optical frequency is resonant with the cavity. The Gouy phase shift means that the  $TEM_{01}$  mode is reflected from the cavity.

In the case of a small tilt to the cavity input beam (shown by the offset to the dotted line) the input  $TEM_{00}$  mode will be decomposed into the transmitted 00 mode and reflected 00 and 01 modes. When the 00 mode is tuned onto resonance, the optical phase



of the reflected 01 beam is advanced by  $\pi/2$  on one side of the 01 pattern, and  $-\pi/2$  on the other, relative to the reflected 00 mode. As the carrier frequency drifts away from resonance, the phase of the 00 mode will shift relative to the two halves of the 01 mode. The 01 mode is unchanged because it is far from resonance. The error signal is therefore obtained by detecting the interference between the 01 and 00 mode on a split photodiode as shown in part 1 of figure 2.15.

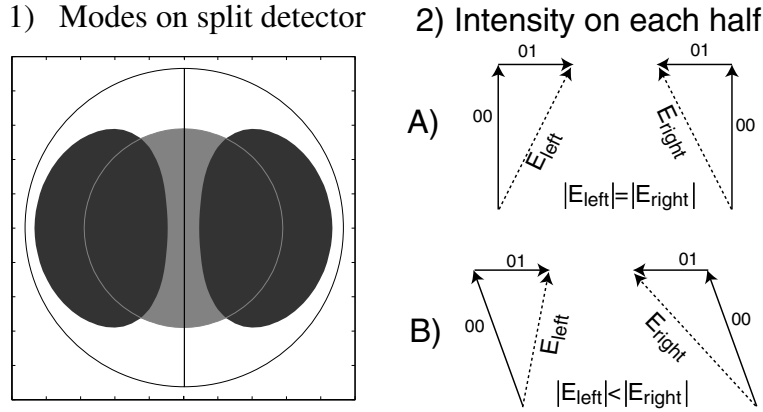


**Figure 2.15:** 1: the pattern of the 00 mode (light grey) and 01 mode (dark grey) on the split detector. 2: the interference of the fields for the case of A: 00 on resonance and B: 00 slightly away from resonance.

The cases in part 2 of figure 2.15 show how the intensities of the field on the left and right hand half of the detector vary as the carrier moves away from resonance. The error signal is found by subtracting the DC photocurrents of the two detector halves of the split detector.

$$I_{\text{Error}} = I_{\text{left}} - I_{\text{right}}. \quad (2.106)$$

The tilt-locking method has the advantage of being cheaper than modulation locking as only DC electronics are required. An extensive comparison of tilt locking and modulation locking is carried out for a second harmonic generator in chapter 6.

## 2.9 Locking homodyne detection

Two beam interferometers, such as a homodyne detectors, also require locking. In the case of homodyning, there are two cases to consider: 1) locking to phase quadrature detection, and 2) locking to amplitude quadrature detection.

To lock to the phase quadrature, we consider the classical interference of the two bright beams  $A$  and  $B e^{-i\theta}$  of figure 2.7. The subtraction of the DC photocurrents from the two detectors is given by

$$\bar{I}_1 - \bar{I}_2 = \eta \bar{A} \bar{B} \cos \theta. \quad (2.107)$$

The subtraction of the DC photocurrents therefore provides a zero-crossing at  $\theta = \pi/2$ , which will serve as an error signal for locking to phase quadrature detection.

Locking to the amplitude quadrature means fixing the subtraction of equation 2.107 to a maximum or minimum, since we require  $\theta = 0$  or  $\theta = \pi$ . Locking to a turning point of the homodyne system is therefore analogous to locking to a cavity resonance. It may be achieved using an identical technique, namely by phase modulating of one of the beams. When the detection is locked to the amplitude quadrature, the phase modulation will not

be seen in the subtracted signal, giving a zero in the demodulation signal. If the detection phase drifts, the demodulation of the subtracted photocurrents gives a positive or negative voltage depending on the direction of the drift, therefore providing a zero-crossing error signal.

## 2.10 Summary

The tools presented in this chapter are central to the material in this thesis. In particular:

- quantum noise and uncertainty
- attenuation
- detection
- sidebands and modulation
- optical cavities and
- cavity locking

will be concepts common to all that follows.



---

# Phase signal amplification

---

In this chapter the concept of electro-optic control as a method of noiseless signal amplification is introduced. The basic theory of phase insensitive amplifiers is presented and used to show how they must introduce excess noise. Theoretical modelling of feedforward is then used to demonstrate the phase sensitive behaviour of this technique. Electro-optic feedforward is then applied to a phase modulation signal to break the phase insensitive amplifier limit. This experiment is the first demonstration of noiseless phase quadrature amplification.

This work has been published as “Noiseless phase quadrature amplification via an electro-optic feedforward technique”, B.C. Buchler, E.H. Huntington, and T.C. Ralph, *Physical Review A* **60** 529 (1999).

## 3.1 Introduction

A signal that is close to the quantum noise limit (QNL) is a fragile thing. Attenuation of the beam containing the signal adds vacuum noise, thereby bringing the signal even closer to the noise-floor, as shown in part A of figure 3.1. Eventually, given enough attenuation, the signal may be lost altogether. A simple method to rectify this problem would be to amplify the signal. The signal, and the surrounding noise-floor, will then be moved to a level well above the quantum noise. Addition of vacuum noise to a signal that is a long way above the QNL will not affect the signal-to-noise ratio, as shown in part B of figure 3.1. Such amplification therefore makes the signal robust to attenuation.

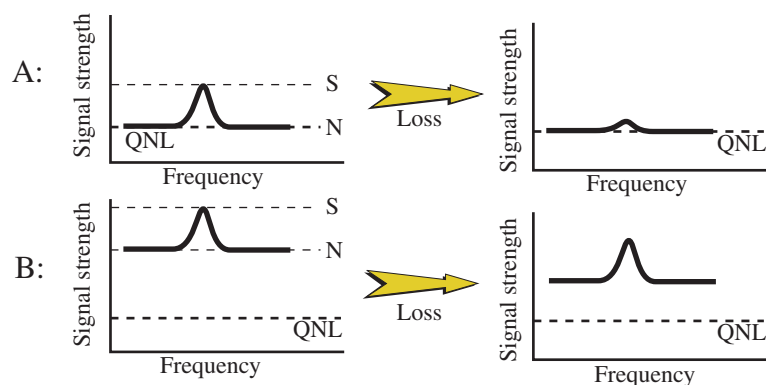


**Figure 3.1:** A: attenuation of a signal (S) with noise-floor (N) at the QNL leads to a reduction in the signal-to-noise ratio. B: attenuation of a signal that is amplified above the QNL has no such problem.

What sort of amplifiers are suitable for the job? It was first shown by Haus [55] and Caves [27] that regular laser amplifiers must introduce extra noise as a result of quantum mechanics. The reason is that these amplifiers are phase insensitive. A phase insensitive amplifier does not distinguish between the phase and amplitude quadratures of the laser light and therefore amplifies the phase and amplitude quadratures equally. To model this device, we assume the amplification acts directly on the annihilation operator, as shown in figure 3.2.



**Figure 3.2:** Phase insensitive amplifier

The input field is amplified by the factor  $\sqrt{G}$ . If we consider the amplification process without the additional noise source (shown in shaded box) then we obtain a commutator for the output field of  $G[\delta A, \delta A^\dagger] = G$ . If  $G$  is anything other than unity, the output field will violate the bosonic commutation relation. The amplifier cannot work in this manner.

If, on the other hand, a source of vacuum noise is added to the output ( $\delta\nu^\dagger$  in shaded box of figure 3.2) we obtain a commutator

$$G[\delta A, \delta A^\dagger] + H[\delta\nu^\dagger, \delta\nu] = G - H. \quad (3.1)$$

We may now force  $G - H$  to be equal to 1 by requiring  $H = G - 1$ . The phase insensitive amplifier, therefore, only works when this source of vacuum noise is included in the model. In this analysis, no attention has been paid to the actual mechanism that introduces the extra noise, it has simply arisen as a consequence of the bosonic commutation relation. In detailed modelling of a laser amplifiers, the noise is found to be associated with spontaneous emission [25].

The existence of extra noise in phase insensitive amplification can be justified via the uncertainty principle. Consider the case of noiseless phase insensitive amplification with high signal gain. In this case, both the phase and amplitude quadratures of an input beam will be amplified well above the QNL. Such a beam may be split into two parts via a beamsplitter. The beamsplitter will introduce an amount of vacuum noise into the output beams, but this will not affect the signal-to-noise ratio of the two beams because the signals are so far above the QNL. The phase quadrature of one beam may now be measured, while the amplitude quadrature of the other beam is measured. The result would be an accurate determination of both quadratures, which is a violation of the uncertainty relation of equation 2.10. The amount of noise added during phase insensitive amplification is just the right amount to preserve this uncertainty relation [27].

The noise performance of a signal processing device may be considered in terms of the ‘signal transfer coefficient’, which compares the input signal-to-noise ratio with the output signal-to-noise ratio. This signal transfer coefficient will now be derived for a phase insensitive amplifier. Consider an input beam with an amplitude quadrature spectrum of  $V_{\text{in}}^+$ . Contained within this spectrum is a signal with measured spectral power of  $S$  surrounded by a noise-floor with spectral power  $N$  (see figure 3.1). The signal-to-noise

ratio of the input beam may be calculated as

$$\text{SNR}_{\text{in}} = \frac{S - N}{N} = \frac{S}{N} - 1. \quad (3.2)$$

In this calculation it is important to include the contribution to  $S$  due to the noise-floor  $N$ . The power of the pure signal (in the numerator of the above equation) is therefore given by  $S - N$ . If the noise is at the QNL (as in figure 3.1 A), we have  $N = 1$ , so that

$$\text{SNR}_{\text{in}} = S - 1. \quad (3.3)$$

Application of a phase insensitive amplifier to the input spectrum,  $V_{\text{in}}^+$ , gives an output spectrum of

$$V_{\text{out}}^+ = GV_{\text{in}}^+ + G - 1. \quad (3.4)$$

The output signal power is found by substituting  $S$  for  $V_{\text{in}}^+$ , giving  $GS + G - 1$ . The output noise is found by substituting  $V_{\text{in}}^+ = 1$ , giving  $2G - 1$ . The signal-to-noise ratio is therefore given by

$$\text{SNR}_{\text{out}} = \frac{GS + G - 1}{2G - 1} - 1 = \frac{G}{2G - 1}(S - 1). \quad (3.5)$$

In the limit of large gain, the signal-to-noise ratio of the output (equation 3.5) becomes half that of the input (equation 3.3). This is sometimes known as the ‘‘3dB amplifier penalty’’. The implication is that the phase insensitive amplifier is a source of noise that can degrade the signal-to-noise ratio.

The signal transfer coefficient,  $T_s$ , may be defined as:

$$T_s = \frac{\text{SNR}_{\text{in}}}{\text{SNR}_{\text{out}}}. \quad (3.6)$$

The signal transfer of a quantum limited phase insensitive amplifier is therefore given by

$$T_s = \frac{G}{2G - 1}, \quad (3.7)$$

which approaches 1/2 in the limit of large gain.

To surpass this signal transfer limit requires a ‘phase sensitive amplifier’ [27]. A phase sensitive amplifier acts differentially on the phase and amplitude quadratures. This avoids the violation of the uncertainty principle that would result from noiseless amplification of both quadratures. An example of a phase sensitive amplifier is the optical parametric amplifier, where one quadrature is amplified while the conjugate is de-amplified. Levenson *et al.* [77] showed 9dB of amplification with  $T_s = 0.66$  using this method. Another technique that surpasses the phase insensitive limit is to detect the beam completely, then use the resulting photocurrent to drive a light emitting diode. This technique has shown  $T_s = 0.79$  with gain of 8dB [44] and  $T_s = 0.9$  with gain of over 20dB [98]. The obvious flaw in this detection and re-emission method is that all of the input beam is lost, meaning the optical phase of the beam is lost, and the output beam lacks spatial and temporal coherence with the input beam.

Electro-optic control may also be used as a noise-free amplifying tool. Feedback systems have been shown to work theoretically [115]<sup>1</sup> as noiseless amplifiers. Noiseless amplification using a feedback loop is derived explicitly during the discussion of feedback in

<sup>1</sup>Noiseless amplification is not the main point of this reference, but it is actually all there in the theory.

chapter 5.

The remainder of this chapter will be devoted to a discussion of noiseless amplification via electro-optic feedforward. Quantum limited feedforward was first demonstrated by Mertz *et al.* as a method of generating squeezed light from the correlated output beams of an optical parametric oscillator [84]. Feedforward amplification was first demonstrated by Lam *et al.* [72]. The value of feedforward extends well beyond noiseless amplification and squeezing generation. Transportation and modulation of information at the quantum limit is central to many quantum information systems including quantum teleportation [39, 97], quantum nondemolition measurements [21] and quantum computation [69]. In the following section, a model of feedforward will be presented using amplitude signals. In section 3.3 this theory is expanded to include phase quadrature signals. The model is then compared to experimental results in section 3.4.

## 3.2 Feedforward amplification

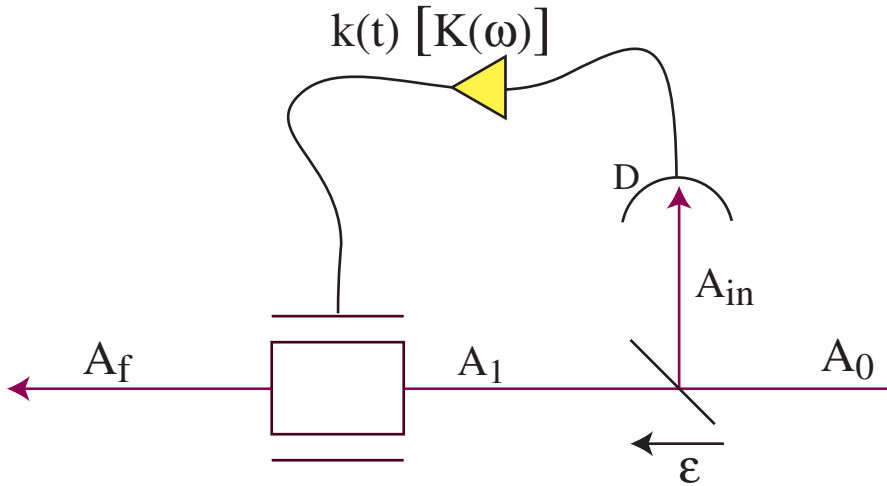


**Figure 3.3:** A feedforward loop with beamsplitter transmissivity  $\epsilon$ .

A feedforward loop is shown in figure 3.3. A part of the input beam is tapped off using a beamsplitter and detected. The signal is then added back to a modulator further downstream. How can this behave as a phase sensitive amplifier? The output of the system is the field  $A_f$ . This field will have some dependence on the modulation imposed upon it. Labelling this modulation as  $\frac{1}{2}\delta X_r$ , the output field may be written as

$$A_f = A_1 + \frac{1}{2}\delta X_r^+ = \sqrt{\epsilon}A_0 - \sqrt{1-\epsilon}\delta\nu + \frac{1}{2}\delta X_r^+. \quad (3.8)$$

The factor of  $1/2$  is arbitrary, and chosen for later convenience only. The sign of the feedforward is also arbitrary, and chosen to be positive. The next step is to describe  $X_r$  in terms of the photocurrent of detector  $D$ . From equation 2.52 the linearised photocurrent due to the detector is found to be

$$I = \eta\bar{A}_{in}^2 + \sqrt{\eta}\bar{A}_{in}(\sqrt{\eta}\delta X_{in}^+ + \sqrt{1-\eta}\delta X_D^+). \quad (3.9)$$

The feedforward fluctuations,  $\delta X_r$ , will now be given by the convolution of the fluctuations

in  $I$  and the impulse response of the filtering and amplifying electronics in the feedforward loop,  $k(t)$ :

$$\delta X_r^+ = \sqrt{\eta} \bar{A}_{\text{in}} \int_0^T k(\tau) \left( \sqrt{\eta} \delta X_{\text{in}}^+(t - \tau) + \sqrt{1 - \eta} \delta X_D^+(t - \tau) \right) d\tau. \quad (3.10)$$

Using this equation for  $\delta X_r$  in equation 3.8 gives

$$\begin{aligned} \delta A_f &= \sqrt{\varepsilon} \delta A_0 - \sqrt{1 - \varepsilon} \delta \nu \\ &+ \frac{1}{2} \sqrt{\eta} \bar{A}_{\text{in}} \int_0^T k(\tau) \left( \sqrt{\eta} (\sqrt{1 - \varepsilon} \delta X_0^+(t - \tau) + \sqrt{\varepsilon} \delta X_\nu^+(t - \tau)) + \sqrt{1 - \eta} \delta X_D^+(t - \tau) \right) d\tau. \end{aligned} \quad (3.11)$$

Taking the Fourier transform of  $\delta A_f$  gives the frequency domain expression

$$\delta \tilde{A}_f = \sqrt{\varepsilon} \delta \tilde{A}_0 - \sqrt{1 - \varepsilon} \delta \tilde{\nu} + \frac{1}{2} \sqrt{\eta} \bar{A}_{\text{in}} K(\omega) \left( \sqrt{\eta} (\sqrt{1 - \varepsilon} \delta \tilde{X}_0^+ + \sqrt{\varepsilon} \delta \tilde{X}_\nu^+) + \sqrt{1 - \eta} \delta \tilde{X}_D^+ \right). \quad (3.12)$$

The amplitude quadrature of the output field therefore becomes

$$\delta \tilde{X}_f^+ = (\sqrt{\varepsilon} + G(\omega) \sqrt{1 - \varepsilon}) \delta \tilde{X}_0^+ + (G(\omega) \sqrt{\varepsilon} - \sqrt{1 - \varepsilon}) \delta \tilde{X}_\nu^+ + G(\omega) \frac{\sqrt{1 - \eta}}{\sqrt{\eta}} \delta \tilde{X}_D^+ \quad (3.13)$$

where we have defined  $G(\omega) = \eta \bar{A}_{\text{in}} K(\omega)$ . Calculating the noise spectrum,  $V_f^+$ , of the output from the feedforward loop gives

$$V_f^+ = \underbrace{|\sqrt{\varepsilon} + G(\omega) \sqrt{1 - \varepsilon}|^2 V_0^+}_{*} + \underbrace{|G(\omega) \sqrt{\varepsilon} - \sqrt{1 - \varepsilon}|^2}_{**} + \underbrace{|G(\omega) \frac{\sqrt{1 - \eta}}{\sqrt{\eta}}|^2}_{***}. \quad (3.14)$$

From this equation it is clear that we may choose gain,  $G$ , such that the contribution from the vacuum noise (\*\*\*) entering at the beamsplitter may be fully eliminated. In particular, in the case of ideal photodetection ( $\eta = 1$ ) we find that  $G(\omega) = \sqrt{1 - \varepsilon} / \sqrt{\varepsilon}$  gives

$$V_f^+ = \frac{1}{\varepsilon} V_0^+. \quad (3.15)$$

In this case, amplification by the factor  $1/\varepsilon$  has been obtained with no additional noise input. The value of  $T_s$ , in this ideal case, is a perfect 1. An additional feature of the system is tunable gain. The amplification factor is  $1/\varepsilon$ . Therefore, as the beamsplitter becomes more reflective so that a higher proportion of the input light is detected by  $D$ , the more amplification is possible.

Feedforward amplification may explained by the division of the beamsplitter vacuum fluctuations  $\delta \nu$ . The component of  $\delta \nu$  imposed on the signal beam (i.e. the beam which goes through the modulator) is anti-correlated with the component of  $\delta \nu$  imposed on the light passed to the detector  $D$ . The result is that that for a unique value of *positive* feedforward gain, the modulator will be driven such that the signal it imposes exactly cancels the beamsplitter vacuum fluctuations originally introduced onto the signal beam. Feedforward is a phase sensitive amplifier because the modulator (in this case an amplitude modulator) has no effect on the conjugate quadrature of the light. The first demonstration of this technique was performed using amplitude signals by Lam *et al.*. In this work a signal transfer coefficient of  $T_s = 0.88$  was found with a gain of 22 times.

The type of amplification obtained with feedforward is referred to as signal ampli-



cation. The size of the signal sidebands has been increased by the modulation, although the carrier amplitude is actually reduced by the transmission through the beamsplitter. This is different to the idea of broadband amplification where the coherent amplitude of the beam is amplified together with the signal sidebands. To overcome the carrier attenuation, the output of the feedforward amplifier may be used to injection lock a slave laser. The output of the slave laser now has increased carrier amplitude while the signal sidebands are unaffected. Injection locking therefore reverses the carrier attenuation of the feedforward loop. Injection locking and feedforward used together provide a method to tailor the signal and carrier power individually. This technique has been demonstrated by Huntington *et al.* [62]. An alternative method of reversing the carrier attenuation due to feedforward is to inject a bright beam into the empty port of the feedforward beamsplitter. Correct choice of power in this field will, just like injection locking, restore the lost carrier amplitude.

### 3.3 Phase quadrature feedforward

The model of the previous section will now be generalised to include feedforward of phase quadrature information. The system to be modelled is shown in figure 3.4. At the input to the system is a beam containing a phase signal. Part of this beam is sent to the homodyne detector,  $H1$ , by a beamsplitter of transmissivity  $\epsilon$ . The remaining light is passed through an electro-optic phase modulator,  $EOM$ , which is controlled by the signal detected at  $H1$ .

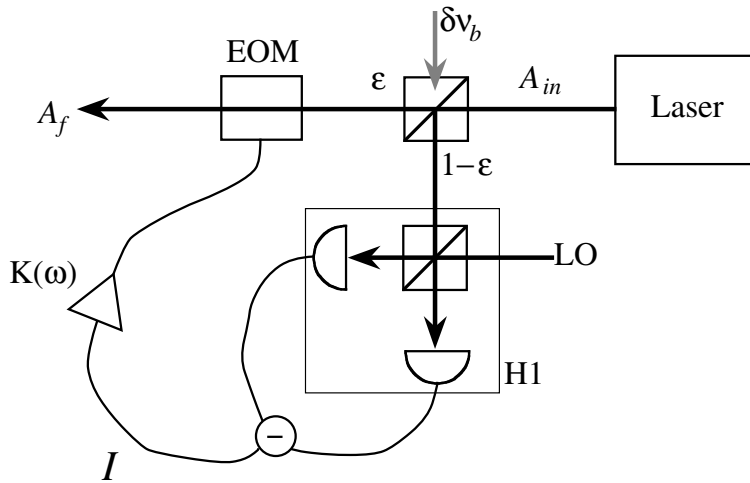


**Figure 3.4:** A schematic diagram showing the components required for noiseless phase quadrature amplification using phase feedforward.

A theoretical model of the behaviour of this system will be generated using the usual linearised operator approach. The time domain annihilation operator for the input beam to our system,  $A_{in}$ , may be written as

$$A_{in} = \bar{A}_{in} + \delta A_{in} \quad (3.16)$$

where  $\bar{A}$  is the mean value of the field amplitude and  $\delta A$  is the time dependent component of the field with an expectation value of zero. Embedded in this time dependant component is the signal information and quantum noise carried by the beam. After traversing the

beam path through the beamsplitter and *EOM*, the field operator  $A_f$  for the output can be written as

$$A_f = \sqrt{\varepsilon}\bar{A}_{\text{in}} + \sqrt{\varepsilon}\delta A_{\text{in}} - \sqrt{1-\varepsilon}\delta\nu_b + i\frac{1}{2}\delta X_r \quad (3.17)$$

where  $\delta\nu_b$  is the vacuum input due to the beamsplitter and  $i\frac{1}{2}\delta X_r$  is a modulation imposed on the beam by the *EOM*. The imaginary phase of this term indicates pure phase modulation, while the factor of a half is arbitrary, as in the previous development of feedforward. The operator  $\delta X_r$  will be a function of fluctuations detected in the homodyne detection system, *H1*.

Homodyne detection was modelled in section 2.5.3. It measures a particular quadrature of a low power beam by mixing it with a much more intense local oscillator beam on a 50/50 beamsplitter [136]. The phase difference between the local oscillator and the signal beam,  $\theta$ , determines which quadrature of the signal beam is measured. The output of the system is the difference of the photocurrents from the two photodiodes. The form of this current may be calculated by finding the difference of the photon number operators (i.e.  $A^\dagger A$ ) for the fields incident on each of the detectors. To simplify matters we will linearise the equations by neglecting all terms greater than first order in the fluctuation operators. The form of the subtracted photocurrent fluctuations is given by equation 2.72 to be

$$\begin{aligned} \delta I = & \sqrt{\eta_d}\bar{A}_{\text{in}}\sqrt{\eta_h\eta_d(1-\varepsilon)}\delta X_{\text{in}}^\theta \\ & + \sqrt{\eta_d}\bar{A}_{\text{in}}\sqrt{\eta_d}\left(\sqrt{\eta_h\varepsilon}\delta X_b^\theta + \sqrt{1-\eta_h}\delta X_h^+\right) \\ & + \sqrt{\eta_d}\bar{A}_{\text{in}}\frac{\sqrt{1-\eta_d}}{\sqrt{2}}(\delta X_{d1}^+ + \delta X_{d2}^+), \end{aligned} \quad (3.18)$$

where we have defined the general quadrature of an operator  $z$  to be

$$\delta X_z^\theta = e^{-i\theta}z + e^{i\theta}z^\dagger. \quad (3.19)$$

The quantum noise terms,  $\delta X_{d1}^+$  and  $\delta X_{d2}^+$ , result from the efficiency,  $\eta_d$ , of the two photodetectors in the homodyne system. The mode-matching efficiency of the homodyne system,  $\eta_h$ , also gives rise to a source of quantum noise, namely  $\delta X_h^+$ . The mode-matching efficiency,  $\eta_h$ , is given by the square of the fringe visibility in the homodyne system as in section 2.5.3.

The form of the modulation  $\delta X_r$  imposed by the *EOM* will be given by a convolution of  $\delta I$ , the time dependent part of the current, and the impulse response of the feedforward electronics,  $k(t)$ . We may therefore write

$$\delta X_r = \int_0^T k(u)\delta I(t-u)du. \quad (3.20)$$

Combining equations 3.17, 3.18 and 3.20, as well as choosing the phase of the homodyne detection system to be  $\pi/2$  so that the phase quadrature is being fed-forward, the final form of the fluctuations in the output beam of the *EOM* will be given by

$$\begin{aligned}
\delta A_f &= \sqrt{\varepsilon} \delta A_{\text{in}} - \sqrt{1-\varepsilon} \delta \nu_b \\
&+ i\sqrt{\eta_d} \bar{A}_{\text{in}} \frac{1}{2} \int_0^T k(u) \left[ \sqrt{\eta_h \eta_d (1-\varepsilon)} \delta X_{\text{in}}^-(t-u) \right. \\
&+ \sqrt{\eta_d} \left( \sqrt{\eta_h \varepsilon} \delta X_b^-(t-u) + \sqrt{1-\eta_h} \delta X_h^+(t-u) \right) \\
&\left. + \frac{\sqrt{1-\eta_d}}{\sqrt{2}} \left( \delta X_{d1}^+(t-u) + \delta X_{d2}^+(t-u) \right) \right] du. \tag{3.21}
\end{aligned}$$

Taking the Fourier transform of this equation gives the frequency domain operator for the output field annihilation operator as

$$\begin{aligned}
\delta \tilde{A}_f &= \sqrt{\varepsilon} \delta \tilde{A}_{\text{in}} - \sqrt{1-\varepsilon} \delta \tilde{\nu}_b \\
&+ i\sqrt{\eta_d} \bar{A}_{\text{in}} \frac{1}{2} K(\omega) \left[ \sqrt{\eta_h \eta_d (1-\varepsilon)} \delta \tilde{X}_{\text{in}}^- \right. \\
&+ \sqrt{\eta_d} \left( \sqrt{\eta_h \varepsilon} \delta \tilde{X}_b^- + \sqrt{1-\eta_h} \delta \tilde{X}_h^+ \right) \\
&\left. + \frac{\sqrt{1-\eta_d}}{\sqrt{2}} \left( \delta \tilde{X}_{d1}^+ + \delta \tilde{X}_{d2}^+ \right) \right]. \tag{3.22}
\end{aligned}$$

where  $\tilde{X}_z$  is the Fourier transform of  $X_z$ . This equation may be used to find the  $\phi$  quadrature of the output:

$$\begin{aligned}
\delta \tilde{X}_f^\phi &= \left( G(\omega) \sin \phi \sqrt{(1-\varepsilon)} \delta \tilde{X}_{\text{in}}^- + \sqrt{\varepsilon} \delta \tilde{X}_{\text{in}}^\phi \right) \\
&+ \left( G(\omega) \sin \phi \sqrt{\varepsilon} \delta \tilde{X}_b^- - \sqrt{1-\varepsilon} \delta \tilde{X}_b^\phi \right) \\
&+ G(\omega) \sin \phi \left[ \sqrt{\frac{1-\eta_h}{\eta_h}} \delta \tilde{X}_h^+ \right. \\
&\left. + \frac{\sqrt{1-\eta_d}}{\sqrt{2\eta_h \eta_d}} \left( \delta \tilde{X}_{d1}^+ + \delta \tilde{X}_{d2}^+ \right) \right], \tag{3.23}
\end{aligned}$$

where  $G(\omega) = \eta_d \sqrt{\eta_h} \bar{A}_{\text{in}} K(\omega)$ . Using  $X^\phi = X^+ \cos \phi + X^- \sin \phi$  (equation 2.8) this simplifies to

$$\begin{aligned}
\delta \tilde{X}_f^\phi &= \sin \phi \left( G(\omega) \sqrt{(1-\varepsilon)} + \sqrt{\varepsilon} \right) \delta \tilde{X}_{\text{in}}^- + \cos \phi \sqrt{\varepsilon} \delta \tilde{X}_{\text{in}}^+ \\
&+ \sin \phi \left( G(\omega) \sqrt{\varepsilon} - \sqrt{1-\varepsilon} \right) \delta \tilde{X}_b^- + \cos \phi \sqrt{1-\varepsilon} \delta \tilde{X}_b^+ \\
&+ G(\omega) \sin \phi \left[ \sqrt{\frac{1-\eta_h}{\eta_h}} \delta \tilde{X}_h^+ \right. \\
&\left. + \frac{\sqrt{1-\eta_d}}{\sqrt{2\eta_h \eta_d}} \left( \delta \tilde{X}_{d1}^+ + \delta \tilde{X}_{d2}^+ \right) \right], \tag{3.24}
\end{aligned}$$

The spectrum of  $A_f$ , normalised to the QNL, can now be obtained for arbitrary quadrature phase angle by evaluating  $V_f^\phi = \langle |\delta \tilde{X}_f^\phi|^2 \rangle$ . Using the result that the spectra of the quantum noise sources are all equal to one, we obtain

$$\begin{aligned}
 V_f^\phi &= \sin^2 \phi \left| G(\omega) \sqrt{(1-\varepsilon)} + \sqrt{\varepsilon} \right|^2 V_{\text{in}}^- + \varepsilon \cos^2 \phi V_{\text{in}}^+ \\
 &+ \sin^2 \phi \left| G(\omega) \sqrt{\varepsilon} - \sqrt{1-\varepsilon} \right|^2 + \cos^2 \phi (1-\varepsilon) \\
 &+ |G(\omega)|^2 \frac{(1-\eta_d \eta_h) \sin^2 \phi}{\eta_h \eta_d},
 \end{aligned} \tag{3.25}$$

To investigate the action of the feedforward system on the phase quadrature, we take  $\phi = \pi/2$  so that

$$\begin{aligned}
 V_f^- &= \left| \sqrt{\varepsilon} + G(\omega) \sqrt{(1-\varepsilon)} \right|^2 V_{\text{in}}^- \\
 &+ \left| G(\omega) \sqrt{\varepsilon} - \sqrt{1-\varepsilon} \right|^2 \\
 &+ |G(\omega)|^2 \frac{(1-\eta_d \eta_h)}{\eta_h \eta_d}.
 \end{aligned} \tag{3.26}$$

This is, not surprisingly, identical to the result obtained with amplitude signals, except for the additional noise source due to the homodyne efficiency. As before, a value of the electronic gain may be chosen such that the second term in equation 3.26 becomes zero. If we assume ideal homodyne and detector efficiency, the value of the gain required for cancellation is

$$G(\omega) = \sqrt{\frac{1-\varepsilon}{\varepsilon}}. \tag{3.27}$$

With this gain, the phase noise of the beam at the output of the feedforward modulator is given by

$$V_f^- = \frac{V_{\text{in}}^-}{\varepsilon}. \tag{3.28}$$

Once again, assuming perfect in-loop detection, the system can now be seen to behave as a noiseless amplifier for phase quadrature signals with signal amplification of  $\varepsilon^{-1}$ .

When detection losses are considered (detection inefficiency was not considered during the introductory treatment of feedforward), matters become a little more complex. The optimum gain is no longer that which gives total cancellation of the beamsplitter vacuum noise. This is because the extra noise due to detection scales with feedforward gain. The result is that the optimum gain level is less than that found for ideal detection. To evaluate the performance of this system with imperfect detection we use the signal transfer  $T_s$ , defined by equation 3.6. Using equation 3.26, the optimum value of the gain  $G$  may be calculated. We find that

$$G(\omega) = \eta_h \eta_d \sqrt{\frac{(1-\varepsilon)}{\varepsilon}}, \tag{3.29}$$

giving a maximum possible signal transfer of

$$T_s = \varepsilon(1 - \eta_h \eta_d) + \eta_h \eta_d. \tag{3.30}$$

Now that the theory has explicit quadrature phase dependence, the phase sensitive nature of feedforward amplification is clearly evident. To see this, equation 3.25 may be considered once again, this time with  $\phi = 0$ , to test the amplitude noise of the output field. The result is that 3.25 reduces to

$$V_f^+ = \varepsilon V_{\text{in}}^+ + 1 - \varepsilon, \tag{3.31}$$

which shows that the amplitude quadrature has not been amplified, on the contrary, it has been de-amplified by a factor of  $\varepsilon$ . A source of vacuum noise ( $1 - \varepsilon$ ) has also been added. This vacuum noise can, in principle, be replaced by a squeezed state. Additional vacuum noise is therefore not a compulsory feature of the feedforward. What is required, is the deamplification by a factor of  $\varepsilon$ . If this condition were relaxed, then a noiseless phase insensitive amplifier could be constructed from consecutive phase and amplitude feedforward loops. The de-amplification is therefore necessary to preserve the uncertainty relation between the phase and amplitude quadratures.

### 3.4 The experiment

An experiment to verify the phase feedforward model was set up, as shown in figure 3.5. The light source was a single mode Nd:YAG laser pumped by a diode laser array. The output power of the laser was 300mW at 1064nm. Most of the light was dumped at the 96% beamsplitter. Of the remaining light, 99.75%, was tapped off for the local oscillator beams  $LO1$  and  $LO2$ . The remaining light formed the signal beam for the phase feedforward. The electronics used for the feedforward consisted of a bandpass filter and two high gain amplifiers to ensure sufficient gain at the signal frequency. A variable electronic attenuator was used to adjust the overall gain of the loop.

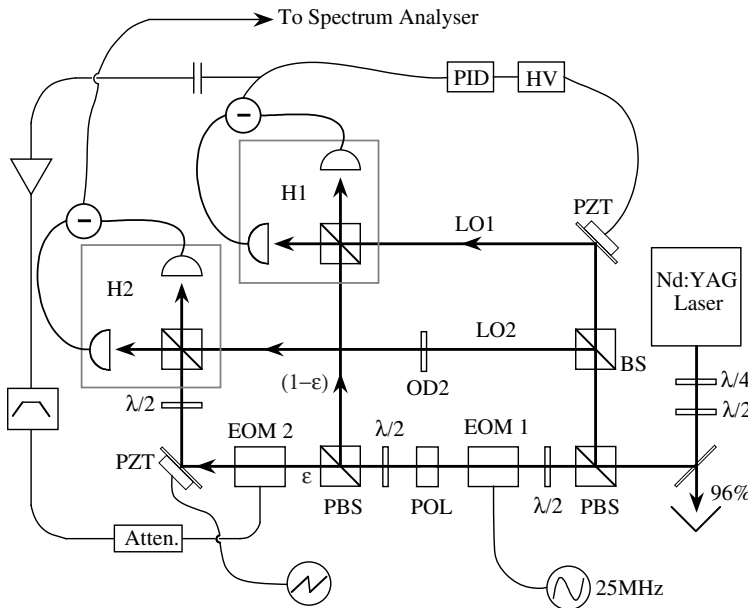


**Figure 3.5:** The layout of our phase feedforward experiment. Atten.= variable electronic attenuator (Hatfield), BS= beamsplitter, HV= high voltage amplifier, EOM=electro-optic modulator,  $\lambda/2$ =half-wave plate,  $\lambda/4$ =quarter-wave plate, OD2= 1% transmission neutral density filter, PBS=polarising beamsplitter, PID= mirror control servo, POL= vertically oriented PBS, PZT=piezoelectric actuator

A 25MHz phase signal was imposed on the beam using the phase modulator  $EOM 1$ . The laser was quantum noise limited at this modulation frequency. The signal was measured using the homodyne detection systems  $H1$  and  $H2$ . The homodyne system  $H1$  consisted of two identical low noise detectors with a quantum efficiency of  $\eta_d = 0.91 \pm 0.02$  [47]. The homodyne efficiency was measured to be  $\eta_h = 0.94 \pm 0.02$ , therefore giving  $H1$  a

total detection efficiency ( $\eta_d\eta_h$ ) of 86%. Homodyne system *H2* contained similar detectors also with a quantum efficiency of  $\eta_d = 0.91 \pm 0.02$ . The homodyne efficiency of *H2* was  $0.88 \pm 0.02$ , therefore giving a total detection efficiency of 80%.

The homodyne system *H1* was locked to the phase quadrature by using the DC voltage from the subtraction of the photocurrents of the homodyne system as an error signal. This is possible because the homodyne system measures the phase quadrature when the power in the two detectors is balanced. A subtraction of the DC voltage from the detectors gives a zero-crossing error signal (see section 2.9).

The phase modulation imposed by *EOM 1* is shown in figure 3.6, as measured using a spectrum analyser (*Hewlett-Packard 3589 A*). The upper trace shows the signal level with 100% of the signal beam directed into the locked homodyne system *H1*. The signal is observed to be  $8.0 \pm 0.4\text{dB}$  above the quantum noise floor, which is shown at 0dB.

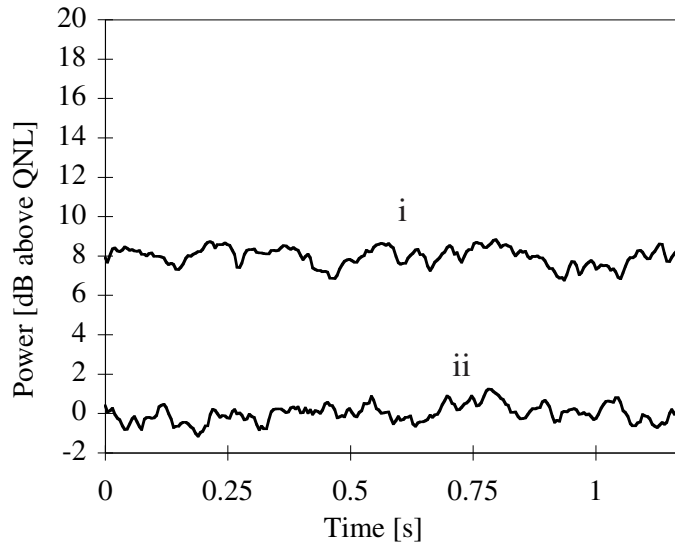


**Figure 3.6:** Trace *i* shows a plot of the input phase signal at  $25\text{MHz}$ . This measurement was made with 100% of the signal beam directed into the homodyne detector *H1* and is therefore a measurement of  $V_{\text{in}}$ . Trace *ii* shows the background noise-floor, which is at the QNL. The spectrum analyser was set on a resolution bandwidth of  $100\text{Hz}$  and video bandwidth  $3\text{Hz}$ .

We then altered our system so that 80% of the light was directed to *H1* while the remaining 20% was passed through *EOM 2* to the homodyne detector *H2*. This corresponds to  $\varepsilon = 0.2$  in the above theory. The signal measured by *H1* was used to drive *EOM 2* through the feedforward loop. The result is shown in figure 3.7. The homodyne system *H2* was swept. Measurements are therefore plotted as a function of the phase of *LO2*. Having a swept homodyne system allows us to demonstrate the phase sensitive nature of the feedforward system.

Trace *i* shows the signal power at  $25\text{MHz}$  on the phase quadrature to be  $17.6 \pm 0.2\text{dB}$  above the QNL. Comparing this to the input signal (trace *i* of figure 3.6), the signal gain of the system is found to be  $9.6 \pm 0.4\text{dB}$ .

Trace *ii* of figure 3.7 shows the phase quadrature noise-floor (measured at frequencies around the signal) to be  $9.5 \pm 0.4\text{dB}$  above the QNL. The difference between traces *i* and *ii*, when the phase of *LO2* is  $\pi/2$ , shows the feed-forward signal to be  $8.1 \pm 0.4\text{dB}$  above the noise-floor.

A theoretical fit of this data may be obtained using equation 3.25. This is also shown

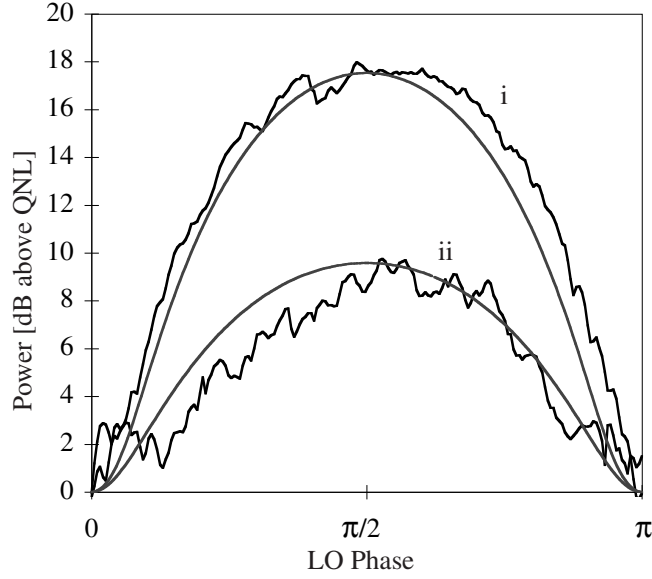


**Figure 3.7:** The output of the feedforward system. Trace *i* shows the signal output of the amplifier as measured by *H2*. Trace *ii* shows the noise floor of the amplifier output. RBW=100Hz, VBW=3Hz.

in figure 3.7. The only free parameter in this fit is the gain  $K(\omega)$  which we take to be a constant  $K$  at a fixed frequency of 25MHz. The value of  $K$  used to give this fit is 3.2, which is 70% (or 2.4dB) larger than the calculated optimum. However with high signal gain the system is insensitive to detuning from optimum  $K$  [72]. For example, in the limit of large  $K$ , the  $T_s$  of our system is predicted to approach 0.68, which is still better than the phase insensitive amplifier limit. This insensitivity means good signal transfer is achievable even if the system is not perfectly optimised.

Importantly, figure 3.7 demonstrates that the system is truly phase sensitive. The amplitude quadrature of the signal beam (as measured at phase angles of 0 and  $\pi$ ) is shown to be quantum noise limited, as predicted by the theory.

From a noiseless amplification point of view, the system appears very successful. We measure an input signal of  $8.0 \pm 0.4$ dB above the noise and retrieve an output signal  $8.1 \pm 0.4$ dB above the noise. To rigorously determine how our system rates as a noiseless amplifier, we must employ the signal transfer ratio defined in equation 3.6. In this equation,  $\text{SNR}_{\text{in}}$  is the optical (*not* detected) signal-to-noise ratio of the input beam and  $\text{SNR}_{\text{out}}$  is the optical signal-to-noise of the output beam. The optical signal-to-noise ratios may be inferred from the known detection efficiencies of the homodyne detectors, *H1* and *H2*, by using equation 2.54. This equation relates the photocurrent spectrum to the photon number spectrum. In this case, one must work backwards from the measured photocurrent to find the optical signal and noise powers.

Considering the total efficiency of *H1* (86%), we can infer an optical signal-to-noise ratio of  $\text{SNR}_{\text{in}} = 6.2 \pm 0.7$  (on a linear scale). From the total efficiency of the homodyne system *H2* (80%), we find the optical  $\text{SNR}_{\text{out}}$  to be  $5.6 \pm 0.6$  (again on a linear scale). These signal-to-noise ratios give  $T_s = 0.90 \pm 0.14$ . The uncertainty in this result is largely due to the swept operation of *H2*.

Using equation 3.30 we find that the detector and homodyne efficiencies of *H1* limit the maximum achievable  $T_s$  to 0.88, which is in agreement with our experimental results.

---

The maximum transfer coefficient achievable using a phase insensitive amplifier with  $10dB$  signal gain is 0.53, which our system easily exceeds.

### 3.5 Conclusion

We have developed a theoretical model of a phase feedforward network and shown that it can behave as a noiseless phase quadrature amplifier in the limit of ideal homodyne detection. Experimental results with a Nd:YAG laser source demonstrate the practicality of the system. A signal transfer ratio of  $T_s = 0.9 \pm 0.14$  with a signal gain of  $10dB$  was measured. This result constitutes the first demonstration of noiseless phase quadrature amplification.

The relative simplicity of feedforward and the demonstrated insensitivity to non-optimum gain makes this system an ideal add-on to any experiment where near QNL phase signals need to be made robust to optical loss.





---

# Improving quantum nondemolition measurement

---

In this chapter, the effect of feedforward on quantum nondemolition measurements is investigated. The modelling shows that the information manipulation abilities of feedforward constitute a ‘post-enhancement’ technique that is able to improve the performance of a range of quantum nondemolition measurement systems. The ideas of this chapter are put to practice in chapter 8.

The theory presented in this chapter has been published as: “B.C. Buchler , P.K. Lam and T.C. Ralph *Enhancement of quantum nondemolition measurements with an electro-optic feedforward amplifier* Physical Review A. **60**, 4943 (1999)”

## 4.1 Introduction

If the position of a free particle is determined with sufficient accuracy, Heisenberg’s uncertainty principle necessarily implies an unpredictable momentum. The uncertainty in the momentum means that the future position of the particle is also uncertain. A second measurement of the position will therefore be affected by the initial measurement. Consider instead, a measurement of the momentum of the particle. Although the momentum measurement will cause increased uncertainty in the position, this does not impinge upon future measurements of the momentum. For the free particle Hamiltonian, momentum is therefore a “quantum nondemolition” variable. Multiple measurements may be made of the momentum with no error on the  $n^{\text{th}}$  measurement due to the  $(n - 1)^{\text{th}}$ . A general condition for a variable to be QND is that it commutes with the system Hamiltonian. It was Braginsky who first wrote on the possibility of such a measurement [12, 13, 14]. Braginsky, and later Thorne [116] considered the possibility of using a QND read-out system in a gravitational wave detection scheme. Largely due to the relative ease of optical experimentation over mechanical systems, most implementations of QND have involved making measurements of quadratures of the electromagnetic field [45], which are QND variables [117]. Optical QND has been suggested as the tool for many physical applications including the generation of squeezed light [21, 46, 131], improving laser gyroscope performance [114], entanglement purification [31] state preparation [28] and quantum computation [61].

The efficiency of a given QND system depends on the internal dynamics of the machine and the environment in which it is placed. Often, it may be more practical to manipulate the environment to improve the performance of a QND device, since the internal dynamics are not always accessible. Enhancement of QND by modifying the environment is the focus of this chapter.

One technique for improving QND is the use of a squeezed meter input. This method was suggested theoretically in 1980 by Shapiro [109] and has since been demonstrated experimentally by Bruckmeier *et al.* [19]. The introduction of the meter squeezing occurs at the input to the QND machine and we will refer to this as “pre-enhancement”. The new idea presented here is the use of electro-optic feedforward as a tool for QND enhancement. Electro-optic enhancement of QND has been considered previously in a feedback configuration by Wiseman [121]. Feedforward has previously shown its usefulness as a noiseless amplifier [62, 72, 96]. By placing a QND machine inside a feedforward loop the signal-to-noise ratio of the signal output may be improved. This occurs at the output of a QND machine and we will therefore describe it as “post-enhancement”.

The use of a noiseless amplifier to improve the signal output highlights a challenge to the validity of the standard QND criteria. Strong noiseless amplification shifts the QND output to a level well above the quantum noise. The signal satisfies all the regular QND criteria, yet the signal is obviously different to the original since it is now very robust to optical attenuation. This problem has been discussed previously by Levenson *et al.* [77]. We use a parameter called “sensitivity” [96] to quantify the effect. We show that the sensitivity of an amplified signal can be recovered by mixing the signal output with a bright squeezed beam.

The layout of the chapter is as follows: in section 4.2 the standard QND criteria are introduced. Section 4.3 is a discussion of enhancement techniques. Theoretical descriptions of meter squeezing and feedforward enhancement are developed. This theory is used to model two QND machines; the squeezed light beamsplitter and an optical parametric amplifier. In both cases the models show significant gains can be made using post-enhancement, especially when used in conjunction with pre-enhancement. Lastly, in section 4.4, the sensitivity problem is discussed and a solution using an additional source of squeezing is modelled.

## 4.2 QND Criteria: an overview

We begin by examining the working of QND via the linearised formalism of chapter 2. For the optical systems considered here, signals will be encoded on a quadrature of the quantised EM field. If we have a field described by the time domain boson operator  $S$ , we can consider making a non-destructive measurement of the general quadrature  $X_s^{\text{in}}$  given by

$$X_s^{\text{in}} = e^{-i\theta} S + e^{i\theta} S^\dagger. \quad (4.1)$$

To access the information in this quadrature, we follow the recipe outlined in chapter 2. Firstly, assuming the signals are small compared to the power in the beam, only fluctuations about the steady state expectation value of  $X_s^{\text{in}}$  will be important. For this reason we will express our QND theory in terms of the fluctuation operators denoted by a ‘ $\delta$ ’, for example the fluctuations of  $X_s^{\text{in}}$  about the steady state are given by  $\delta X_s^{\text{in}}$ . Secondly, we switch to the frequency domain version of this fluctuation operator,  $\delta \tilde{X}_s^{\text{in}}(\omega)$ , where the ‘ $\sim$ ’ indicates the Fourier domain fluctuation operator. This operator is used to derive expressions for the spectral variances of the field which are the commonly measured quantity in optical QND. The spectral variance  $V_s^{\text{in}}(\omega)$  is given by (see equation 2.43)

$$V_s^{\text{in}}(\omega) = \langle |\delta \tilde{X}_s^{\text{in}}(\omega)|^2 \rangle. \quad (4.2)$$

We will generally refer to  $\delta\tilde{X}_s^{\text{in}}(\omega)$  and  $V_s^{\text{in}}(\omega)$  as the more compact  $\delta\tilde{X}_s^{\text{in}}$  and  $V_s^{\text{in}}$  respectively.

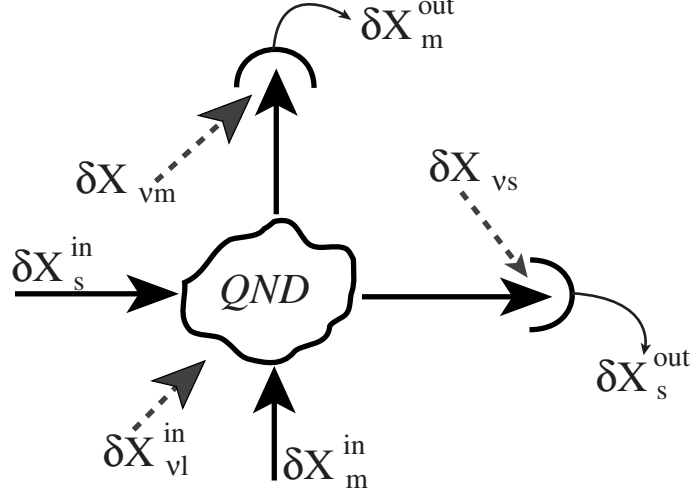


**Figure 4.1:** The inputs and outputs of a general QND system.  $\delta X_s^{\text{in}}$  is the signal input,  $\delta X_m^{\text{in}}$  is the meter input,  $\delta X_{vl}^{\text{in}}$  is quantum noise due to internal loss,  $\delta X_{vm}$  and  $\delta X_{vs}$  are quantum noise due to detector inefficiency,  $\delta X_m^{\text{out}}$  and  $\delta X_s^{\text{out}}$  are the meter and signal output photocurrents respectively.

A general QND scheme is shown in figure 4.1. We begin with a signal  $\delta\tilde{X}_s^{\text{in}}$  that we wish to measure non-destructively using a meter input  $\delta\tilde{X}_m^{\text{in}}$ . An internal loss term,  $\delta\tilde{X}_{vl}$ , is also included. The signal and meter outputs of the system are detected with efficiencies  $\eta_s$  and  $\eta_m$  respectively. These efficiencies are associated with the additional vacuum fluctuations  $\delta\tilde{X}_{vs}$  and  $\delta\tilde{X}_{vm}$ . In order to evaluate the success of the QND system, we compare the signal and meter photocurrents which have statistics given by the operators  $\delta\tilde{X}_s^{\text{out}}$  and  $\delta\tilde{X}_m^{\text{out}}$ . These operators may be expressed using the matrix equation

$$\begin{pmatrix} \delta\tilde{X}_s^{\text{out}} \\ \delta\tilde{X}_m^{\text{out}} \end{pmatrix} = \begin{pmatrix} \sqrt{\eta_s} & 0 \\ 0 & \sqrt{\eta_m} \end{pmatrix} \begin{pmatrix} a & b & c \\ d & e & f \end{pmatrix} \begin{pmatrix} \delta\tilde{X}_s^{\text{in}} \\ \delta\tilde{X}_m^{\text{in}} \\ \delta\tilde{X}_{vl} \end{pmatrix} + \begin{pmatrix} \sqrt{1-\eta_s} & 0 \\ 0 & \sqrt{1-\eta_m} \end{pmatrix} \begin{pmatrix} \delta\tilde{X}_{vs} \\ \delta\tilde{X}_{vm} \end{pmatrix}. \quad (4.3)$$

The matrix of coefficients  $a \dots f$  in equation 4.3 are parameters determined by the internal dynamics of a given QND device. In particular, the coefficients  $a, b, d$  and  $e$  define the internal strength of coupling between the meter/signal inputs and meter/signal outputs. A machine which introduces extra quantum noise due to internal loss will have  $c$  and  $f$  non-zero.

The aim of QND measurement is to simultaneously observe and preserve the input signal. For ideal nondemolition, we require  $\delta\tilde{X}_s^{\text{out}} = \delta\tilde{X}_s^{\text{in}}$ . On the other hand, an ideal measurement will be made when  $\delta\tilde{X}_m^{\text{out}} = G\delta\tilde{X}_s^{\text{in}}$  where  $G$  is a known constant<sup>1</sup>. These two conditions are always satisfied when  $d = G$ ,  $a, \eta_s, \eta_m = 1$  and  $b, c, e, f = 0$ . A

<sup>1</sup>Note that the presence of  $G$  allows for possible amplification of the meter output. This is acceptable

system which could produce such a result is a perfect QND machine. For any meter and signal input, the meter output contains an exact copy of the signal input (with a known amplification  $G$ ), and the signal output is undisturbed. Since it makes a perfect non-destructive measurement of a quadrature, it necessarily implies an infinite variance in the complementary quadrature. Unsurprisingly, such a system has not been developed. Instead we must content ourselves with non-ideal QND systems, where  $a, \eta_m$  and  $\eta_s$  are not unity, and  $b, c, e, f$  are non-zero. Under these conditions some signal is lost, the meter is not a perfect copy of the input signal and extra noise may be added due to internal loss.

#### 4.2.1 Signal transfer coefficients

In order to evaluate the non-ideal performance of a QND device, two parameters [59, 63, 93] are commonly used. The first is the signal transfer. For an ideal measurement, the signal-to-noise ratio (SNR) on the meter output is identical to the signal-to-noise of the signal input. We define the meter transfer coefficient  $T_m$  as

$$T_m = \frac{SNR_m^{\text{out}}}{SNR_s^{\text{in}}}, \quad (4.4)$$

so that in the case of an ideal measurement,  $T_m = 1$ . Signal transfer coefficients were also used earlier in the context of noiseless amplification (see section 3.1).

It is also required that the SNR of the signal output is not degraded by the measurement process. The signal transfer coefficient,  $T_s$ , is therefore defined as

$$T_s = \frac{SNR_s^{\text{out}}}{SNR_s^{\text{in}}}, \quad (4.5)$$

so that for ideal preservation of the signal,  $T_s = 1$ . The first parameter used to evaluate QND measurement is the total signal transfer coefficient,  $T_{s+m}$ , defined as

$$T_{s+m} = T_s + T_m. \quad (4.6)$$

If the SNR of the meter and signal outputs is identical to that of the signal input, then the QND system is behaving in an ideal fashion and we have  $T_{s+m} = 2$ . A classical measurement system has  $T_{s+m} \leq 1$ , so for the system to have some QND properties we require

$$T_{s+m} > 1. \quad (4.7)$$

Equation 4.3 may be used with equation 4.2 to derive the spectra of the output fields. These spectra can be used to find the transfer coefficients,  $T_s$  and  $T_m$ , by applying the method of section 3.1. After some algebra, the result is:

$$T_s = \frac{\eta_s |a|^2}{\eta_s [|a|^2 + |b|^2 V_m^{\text{in}} + |c|^2] + 1 - \eta_s} \quad (4.8)$$

$$T_m = \frac{\eta_m |d|^2}{\eta_m [|d|^2 + |e|^2 V_m^{\text{in}} + |f|^2] + 1 - \eta_m}. \quad (4.9)$$

---

since we do not require the meter output to be identical in size to the signal input, just that it contains a faithful copy of the information of the signal input.

### 4.2.2 Conditional variance

The second measure of a QND system is the conditional variance  $V_{s|m}$ . This measures the correlation of the meter and signal output and is defined as

$$V_{s|m} = V_s^{\text{out}} (1 - C_{s,m}^2) \quad (4.10)$$

where  $C_{s,m}$  is the correlation between the signal and meter beams. Writing this correlation explicitly in terms of the quadratures gives

$$V_{s|m} = V_s^{\text{out}} \left( 1 - \frac{|\langle \delta \tilde{X}_s^{\text{out}} \delta \tilde{X}_m^{\text{out}} \rangle|^2}{V_s^{\text{out}} V_m^{\text{out}}} \right) = V_s^{\text{out}} - \frac{|\langle \delta \tilde{X}_s^{\text{out}} \delta \tilde{X}_m^{\text{out}} \rangle|^2}{V_m^{\text{out}}} \quad (4.11)$$

The conditional variance is the accuracy with which one may measure the signal beam, assuming that one has all the information carried by the meter beam. If the conditional variance is less than the QNL, then it is possible to determine the signal with precision below the QNL. Naturally enough, a QND device requires  $V_{s|m} < 1$ , and in the limit of a perfect QND device,  $V_{s|m} = 0$ .

A conditional variance measurement is dependant on the information contained in the meter beam. There is, however, no obligation to use the information in the meter beam and in fact, it is sometimes not required. For example, imagine a meter that is in no way correlated with the signal beam, while the noise on the signal beam is squeezed below the QNL. In this case the conditional variance is less than one and equal to the amount of squeezing on the signal beam, since the amount of squeezing sets the precision with which the signal beam may be measured. This is independent of any information on the meter beam, which plays no part in the measurement. Of course, if the meter beam were to be correlated with the signal beam in this example, then one may use the meter information to improve the measurement of the signal beam. The new noise-floor will then be even less than the squeezed noise of the signal beam. Another way of describing the conditional variance is, therefore, as the level to which the noise-floor of the signal output beam may be suppressed by using the information of the meter beam.

An expression for the conditional variance may be found by using equation 4.3 in equation 4.11, the result being

$$V_{s|m} = \eta_s \left[ |a|^2 V_s^{\text{in}} + |b|^2 V_m^{\text{in}} + |c|^2 \right] + 1 - \eta_s - \frac{\eta_s \eta_m |adV_s^{\text{in}} + beV_m^{\text{in}} + cf|^2}{\eta_m [|d|^2 V_s^{\text{in}} + |e|^2 V_m^{\text{in}} + |f|^2] + 1 - \eta_m}. \quad (4.12)$$

Having derived expressions for the conditional variance and signal transfer, we may now consider the QND properties of a very simple measurement device, namely, a beamsplitter. For a 50/50 beamsplitter with coherent signal and meter inputs and ideal detectors, we have  $a = -b = d = e = 1/\sqrt{2}$ ,  $c = f = 0$ ,  $V_m^{\text{in}} = V_s^{\text{in}} = 1$  and  $\eta_s = \eta_m = 1$ . The signal transfer ratio and conditional variance may be evaluated using equations 4.8, 4.9 and 4.12. We find that  $T_{s+m} = 1$  and  $V_{s|m} = 1$ . This device is clearly an imperfect QND device in fact, it has no QND properties at all according to the above definitions. We will now examine some methods which can be applied to any non-ideal QND device to enhance its functionality.

## 4.3 QND enhancement

### 4.3.1 Pre-enhancement

When a QND system is letting you down and no further advantage can be gained by improving the internal workings of the device, other ways of improving the system need to be considered. (This is particularly true for a beamsplitter where there are no adjustable parts at all!)

If the parameters  $b$  and  $e$  of equation 4.3 cannot be reduced, then their effect can be minimised by suppressing the fluctuations on the meter beam. This is done by squeezing  $\delta\tilde{X}_m^{\text{in}}$ . By preparing the meter beam in this way, any imperfect QND device can be enhanced. This idea has been discussed previously by various authors. Shapiro [109] and Holland [59] discuss using a beamsplitter with a squeezed meter as a QND device. This idea has since been realised experimentally by Bruckmeier [19]. With a 3.7dB squeezed meter beam, a signal transfer  $T_{s+m} = 1.29$  and conditional variance  $V_{s|m} = 0.73$  were measured. Assuming ideal detection (i.e.  $\eta_m = \eta_s = 1$ ) and no internal loss (i.e.  $c = f = 0$ ), the enhancement achievable in this experiment is limited only by the amount of squeezing since  $V_m^{\text{in}} \rightarrow 0$  implies  $T_{s+m} \rightarrow 2$  and  $V_{s|m} \rightarrow 0$ . The best vacuum squeezing reported to date is 7dB [75] which would produce  $T_{s+m} = 1.53$  and  $V_{s|m} = 0.38$  with a 50/50 beamsplitter and an achievable 95% efficient detection.

A squeezed meter has also been used to improve the performance of an already functional QND device. Bruckmeier *et al.* [20] used a 3.4dB squeezed meter to improve the performance of a QND system which used an optical parametric amplifier (OPA). In this system, the meter and signal beams were injected into the OPA and the nonlinear interaction between the two formed a QND coupling. The OPA was run using a vacuum meter input and  $T_{s+m} = 1.05$  and  $V_{s|m} = 0.56$  were measured. The meter was then replaced with a squeezed vacuum input with the result that  $T_{s+m}$  was increased to 1.12, and  $V_{s|m}$  reduced to 0.53.

These examples demonstrate the utility of this form of QND enhancement. A second complementary strategy for QND improvement will now be considered.

### 4.3.2 Post-enhancement with feedforward

As demonstrated in section 3.1, a phase insensitive amplifier has a 3dB noise penalty associated with high-gain amplification [55]. It was also shown in chapter 3, that electro-optic feedforward can act as a phase sensitive amplifier [62, 72] with no such noise penalty. A feedforward loop works by detecting a portion of the input light. The photocurrent may then be used to control a modulator in the signal beam down-stream from the tap-off point. Quantitatively, the noise penalty associated with amplification may be expressed in terms of the signal transfer coefficient. A standard linear amplifier has  $T_s = 1/2$  (for high gain) whereas a feedforward amplifier can attain  $T_s = 1$  in the limit of ideal in-loop photodetection. Equation 4.6 makes it apparent that bringing  $T_s$  closer to 1 will allow superior values of  $T_{s+m}$  to be achieved.

The use of feedforward in QND enhancement is shown in figure 4.2. The meter output is used to modulate the signal output. In this way some of the signal degradation due to the measurement process can be compensated by careful use of the information on the meter beam. No extra manipulation of the meter beam is required to implement feedforward, so the meter transfer coefficient is not affected. The effect of feedforward is modelled by modifying equation 4.3 to include coupling between the meter output and the

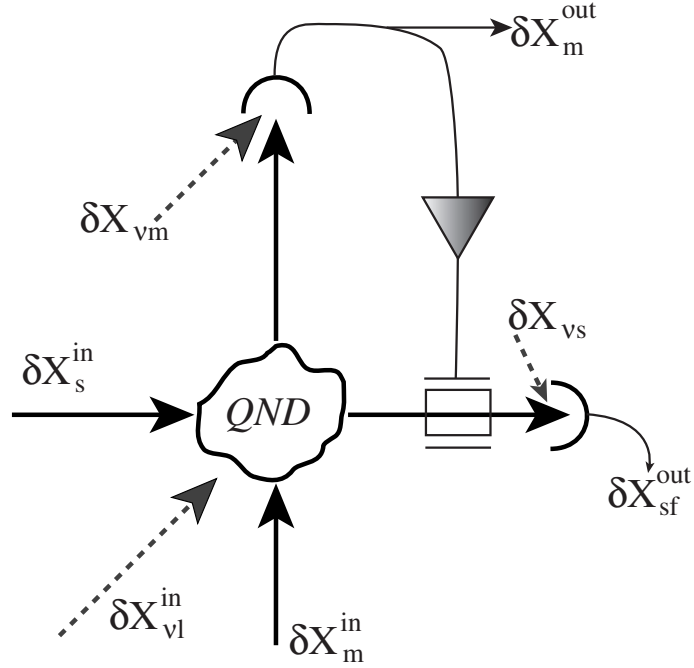


**Figure 4.2:** The inputs and outputs of a general QND system with feedforward. Parameters are the same as those shown in figure 4.1 with the exception that  $\delta\tilde{X}_{\nu s}$  is now the quantum noise for the combined effect of modulator loss and signal detector inefficiency.

signal output. The derivation may be done using the same method as used for feedforward in chapter 3. The new equation for the QND device is:

$$\begin{pmatrix} \delta\tilde{X}_{sf}^{\text{out}} \\ \delta\tilde{X}_m^{\text{out}} \end{pmatrix} = \begin{pmatrix} \sqrt{\eta_s} & G\sqrt{\eta_m\eta_s} \\ 0 & \sqrt{\eta_m} \end{pmatrix} \begin{pmatrix} a & b & c \\ d & e & f \end{pmatrix} \begin{pmatrix} \delta\tilde{X}_s^{\text{in}} \\ \delta\tilde{X}_m^{\text{in}} \\ \delta\tilde{X}_{\nu l} \end{pmatrix} + \begin{pmatrix} \sqrt{1-\eta_s} & G\sqrt{\eta_s(1-\eta_m)} \\ 0 & \sqrt{1-\eta_m} \end{pmatrix} \begin{pmatrix} \delta\tilde{X}_{\nu s} \\ \delta\tilde{X}_{\nu m} \end{pmatrix}. \quad (4.13)$$

The quantity  $G$  is the gain of the feedforward loop. In general it is complex and a function of frequency. Having terms dependent on  $G$  in the off-diagonal elements of equation 4.13 has the effect of coupling the signal output to the meter output as required. We note that the addition of a modulator causes some attenuation of the signal beam prior to detection. This is accounted for theoretically by modifying the value of the signal detection efficiency  $\eta_s$  to include loss due to the modulator.

Equation 4.13 clarifies the mechanism by which feedforward aids QND. It can be used to cancel the effect of the noise terms in the signal output. For example, by satisfying  $b\sqrt{\eta_s} + G\sqrt{\eta_s\eta_m}e = 0$  we can make the signal output  $\delta\tilde{X}_s^{\text{out}}$  independent of the meter noise  $\delta\tilde{X}_m^{\text{in}}$ . The system requires efficient detection of the meter beam, otherwise the additional noise due to that detection efficiency may ruin any benefit derived from the elimination of the meter noise. In fact, this effect has important implications for the optimisation of a feedforward loop. In the presence of poor meter detection, the optimum gain is below that which gives perfect cancellation of the noise term. There is a trade off between the



reduced noise from the cancellation and the increased noise from the detection loss. The optimum  $T_s$  and feedforward gain were calculated in section 3.3 in the case of non-ideal meter detection.

Feedforward has no effect on  $T_m$  since the feedforward all occurs downstream of the meter detection. Equation 4.9 is therefore still used to calculate  $T_m$ . The effect of feedforward on the conditional variance is small.  $V_{s|m}$  is actually independent of the gain  $G$ . The only impact on  $V_{s|m}$  comes from vacuum noise added by the extra attenuation due to the modulator in the signal beam. Under typical experimental conditions, the loss in an amplitude modulator may be as low as 5%. With feedforward applied, equation 4.12 may still be used to evaluate  $V_{s|m}$  although  $\eta_s$  now includes this extra attenuation due to the modulator. Feedforward greatly modifies  $T_s$ . Starting from equation 4.13 we obtain

$$T_s = \frac{\eta_s |a + G\sqrt{\eta_m}d|^2}{\eta_s [ |a + G\sqrt{\eta_m}d|^2 + |b + G\sqrt{\eta_m}e|^2 V_m^{\text{in}} + |c + G\sqrt{\eta_m}f|^2 + |G|^2(1 - \eta_m) ] + 1 - \eta_s}. \quad (4.14)$$

Using this result, we can model the effect of feedforward on QND for some specific systems.

### Example 1: the beamsplitter

If we consider a beamsplitter QND device with transmission  $\varepsilon$ , The matrix  $a \dots f$  in equation 4.13 becomes

$$\begin{pmatrix} \sqrt{\varepsilon} & -\sqrt{1-\varepsilon} & 0 \\ \sqrt{1-\varepsilon} & \sqrt{\varepsilon} & 0 \end{pmatrix}. \quad (4.15)$$

Before showing the effect of feedforward on QND, we will consider the effect of feedforward gain,  $G$ , on the value of  $T_s$ . Figure 4.3 shows contours of  $T_s$  mapped as a function of the magnitude and the phase of  $G$  for a vacuum meter input ( $V_m^{\text{in}} = 1$ ). The best performance of the system is for a phase of  $0^\circ$ . The magnitude of  $G$  has been normalised by the optimum value so that  $G = 0\text{dB}$  corresponds to the optimum gain magnitude which, as discussed above, depends on the meter detection loss. The plot shows the design requirements of a feedforward loop under typical operating conditions with a 50/50 beamsplitter. The gain must be controlled to within  $20^\circ$  of the optimum phase and within 2dB of the optimum magnitude to maintain  $T_s > 0.9$ . This diagram also demonstrates the operation of a feedforward loop as a noise-eater. When the phase is at  $180^\circ$  the feedforward loop can cancel all of the signal on the signal output beam and  $T_s$  drops to 0.

Equations 4.9, 4.12 and 4.14 may be used to evaluate the QND performance of the system as a function of the input vacuum squeezing  $V_m$ . In figure 4.4 we consider values of meter squeezing between 0 and 7dB with no feedforward and optimised feedforward.

For a 50/50 beamsplitter, (lines  $i$  and  $i_f$ ) we see the expected increase in  $T_{s+m}$  with feedforward. Also demonstrated is the minor degradation of  $V_{s|m}$  by the modulator loss. However it is apparent that we can do better. Feedforward improves  $T_s$ , leaving  $T_m$  unchanged. Figure 4.3 shows that with a 50/50 beamsplitter ratio  $T_s$  may be improved to over 0.9. Unfortunately  $T_m$  will remain stuck at  $\sim 0.5$  limiting the maximum  $T_{s+m}$ . The way around this is to reduce the beamsplitter ratio  $\varepsilon$ . For example, with  $\varepsilon = 0.1$  ninety percent of the light is detected by the feedforward detector so that  $T_m$  is now increased to  $\approx 0.9$ . These conditions are shown by lines  $ii$  and  $ii_f$  of figure 4.4. Without feedforward,  $T_{s+m}$  is reduced compared to the case of the 50/50 beamsplitter (line  $i$  compared to line  $ii$ ). This is because the gains in the value of  $T_m$  are more than cancelled out by the degradation

of  $T_s$ . With feedforward,  $T_s$  is recovered while simultaneously taking advantage of the improved  $T_m$ . The end result is that with  $\varepsilon = 0.1$  and  $V_m = -7\text{dB}$  feedforward can improve the  $T_{s+m}$  of the beamsplitter from 1.18 to 1.87. Another advantage of this setup is an improvement in  $V_{s|m}$  which is 0.29 for  $\varepsilon = 0.5$  (with  $V_m = -7\text{dB}$ ) compared to 0.2 for  $\varepsilon = 0.1$ .

An interesting limit to this system becomes apparent when  $\varepsilon$  goes to 0. This means that the signal input is completely detected. This is equivalent to removing the beamsplitter altogether and eliminating any optical interaction between the meter and signal beams. For the feedforward to be meaningful we would require some power in the squeezed meter beam to ensure a signal output beam with coherent amplitude. The complete detection of the signal beam by the meter detection system ensures a  $T_m$  equal to the meter detection efficiency. For the signal transfer,  $T_s$ , there is no longer an optimum feedforward gain point. In the limit of high gain, the signal imposed by the modulator will far exceed the noise of the squeezed beam therefore making  $T_s$  at best equal to  $T_m$ . The value of  $V_{s|m}$  is restricted, as before, by the amount of squeezing on the meter beam. The performance of the system at high gain and  $\varepsilon = 0$  is shown by line *s* on figure 4.4. By the QND criteria presented thus far, this system clearly achieves the best QND measurement. In the sense that we completely measure the signal of interest and then recreate it on a separate beam, the  $\varepsilon = 0$  case is analogous to the work of Roch *et al.* [98] and Goobar *et al.* [44] who fully detected the signal beam then used that signal to drive a light emitting diode (LED). The difference between our scheme and the LED work is that the signal output of our system may be coherent with the signal input. This is achieved by generating the squeezed source using an OPA which has been seeded with a portion of the original laser beam. Our scheme also allows QND on the phase or amplitude quadratures whereas the LED experiments were restricted to amplitude.

A final feature of the beamsplitter experiment that deserves a mention is the possible

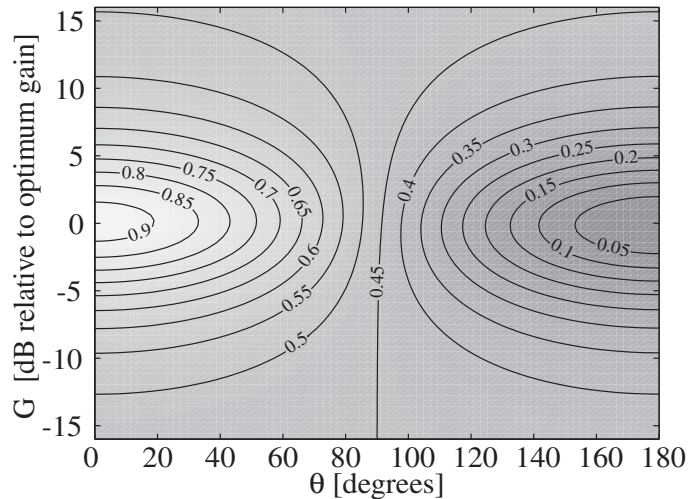


**Figure 4.3:** The effect of feedforward on  $T_s$  as a function of gain magnitude  $G$  and feedforward phase,  $\theta$ , for a non-squeezed vacuum at the beamsplitter. The values of  $T_s$  are shown as contours in intervals of 0.05. The gain has been normalised to the optimum value so that the point  $G = 0\text{dB}$  and  $\theta = 0$  gives the optimum  $T_s$  of 0.925. Parameters used for the plot are  $\varepsilon = 0.5$ ,  $\eta_m = 0.95$ ,  $\eta_s = 0.9$  and  $V_m = 1$ .

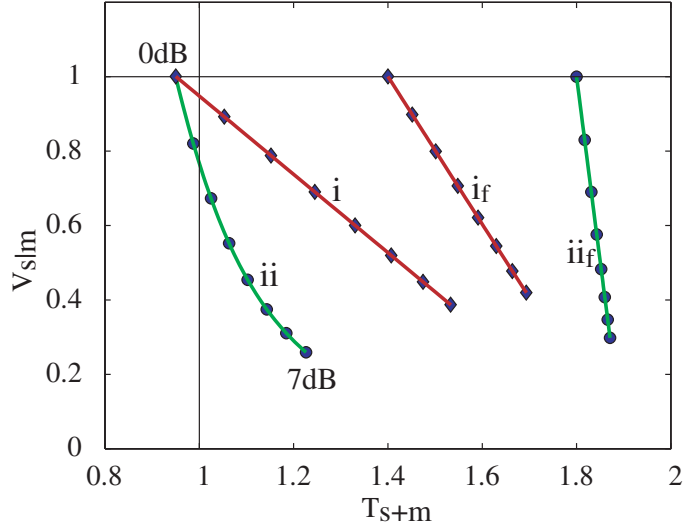


**Figure 4.4:** Beamsplitter QND with varying amounts of meter squeezing. lines  $i$  and  $i_f$  show the results for a 50/50 beamsplitter ( $\varepsilon = 0.5$ ) without and with feedforward respectively. Lines  $ii$  and  $ii_f$  show results for  $\varepsilon = 0.1$  without and with feedforward respectively. Other parameters used are  $\eta_m = \eta_s = 0.95$  with no feedforward. With feedforward we assume  $\eta_s = 0.9$  to account for 5% loss in the modulator.  $G$  is optimised to give maximum  $T_s$ . Line  $s$  shows the special case of  $\varepsilon = 0$ . Here the parameters are the same as the other cases except for  $G$  which is made very large to maximise  $T_s$ , in this case  $G = 100$ .

attenuation of the input beam. Although all the signals have been shown to satisfy the QND criteria, the power of the output beam is reduced by the transmission of the beamsplitter. (This is most apparent in the extreme case of interaction free QND, where there is no beamsplitter at all.) If the optical power is important for some reason, a simple solution is to use a bright squeezed beam. The power in the squeezing may be chosen to exactly cancel out any attenuation due to the beamsplitter. Indeed, if the power in the squeezing were tunable, the system would provide a method of adjusting the output beam intensity to any required level.

### Example 2: the OPA

Feedforward enhancement may also be applied to more complex QND systems. It has been shown by Bruckmeier *et al.* that the interaction of two beams inside an optical parametric amplifier (OPA) can give QND measurements [20]. This experiment was also the first demonstration of QND enhancement via meter squeezing. The amount of squeezing available was 3.4dB below the QNL. The detailed operation of this QND device is not important for the discussion of feedforward, which is a general technique. All we require is the matrix of the system to use in equation 4.13. The calculations of Bruckmeier *et al.* showed the matrix to be

$$\begin{pmatrix} 1-r & -\sqrt{r} & -r^{3/2} \\ \sqrt{r} & -r^2/2 & r \end{pmatrix}, \quad (4.16)$$

where  $r^2$  is equal to the passive loss per round-trip of the OPA, divided by the parametric de-amplification. For the experiment by Bruckmeier this parameter was determined to be  $r^2 = 0.179$ . This system may now be modelled as for the beamsplitter using equations 4.9, 4.12 and 4.14. Figure 4.5 shows the effect of feedforward and meter squeezing on the OPA system. Again we see the effectiveness of feedforward in improving the value of  $T_{s+m}$ .

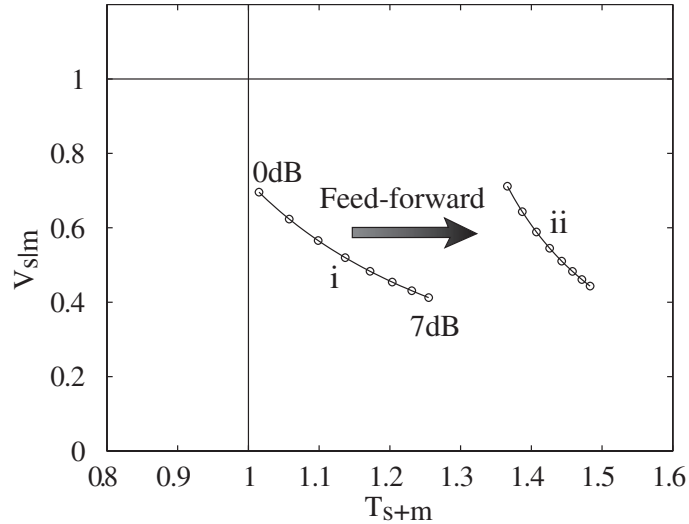


**Figure 4.5:** OPA QND with varying amounts of meter squeezing. With no feedforward (line *i*)  $\eta_m = \eta_s = 0.95$ . With feedforward (line *ii*) we have  $\eta_s = 0.9$  to account for 5% loss in the modulator. The loss parameter,  $r^2$ , is 0.179.  $G$  is optimised to maximise  $T_s$ .

## 4.4 The sensitivity

Despite the credible performance of the feedforward loop as described by the QND parameters, there is a significant objection to the description of the above examples as QND. As described by Lam *et al.* [72], a feedforward loop is a noiseless signal amplifier. Although we have shown that the output of a QND machine with feedforward post-enhancement has all the right signal transfer and correlation characteristics according to the regular QND parameters (as defined in section 4.2), the output of the feedforward loop is actually amplified well above the QNL. It is therefore more robust to loss than the input state. This could be seen as an advantage in systems where optical loss is a problem. However, it is a little imprecise to describe the whole process as QND if the input and output states have different properties with respect to optical attenuation. If the output of the QND machine were required for a quantum noise limited measurement, a robust amplified signal will not do. For this reason another parameter may be appropriate to distinguish the amplified signals from their originals. We therefore define the “sensitivity”,  $S$ , as in [96]

$$S = \frac{V_s^{\text{in}}}{V_s^{\text{out}}}. \quad (4.17)$$

Under this definition, an ideal QND machine has  $S = 1$ , i.e. the signal input variance is at 0dB relative to the size of the signal output variance. A system which requires a quantum

noise limited beam from the output of a QND machine will not function if  $S < 0$ dB. By way of comparison, the sensitivity of the squeezed light beamsplitter with feedforward is  $-11$ dB, assuming a beamsplitter ratio of  $\varepsilon = 0.1$  and  $7$ dB of squeezing, which gave the best QND results in section 4.3.2.

This sensitivity problem is by no means confined to feedforward. Any QND system with noiseless amplification properties is equally prone to poor sensitivity. Levenson *et al.* [77] investigated the use of an OPA as a noiseless amplifier and found that it can satisfy the QND criteria. The authors also suggest that this is not really QND because of the amplification. Their experiment records a  $9$ dB amplification which gives a sensitivity of  $-9$ dB. Similarly, the OPA modelled in section 4.3.2 has a sensitivity of  $-3.7$ dB. Another QND scheme is to fully detect the signal and then re-emit using an LED. The noiseless amplification, and therefore sensitivity, in such experiments is rather extreme. In the work of Roch *et al.* [98] the sensitivity was around  $-20$ dB and Goobar *et al.* [44] recorded  $S = -8$ dB.

The sensitivity may be rectified by using a second stage of post-enhancement. This consists of a bright squeezed beam incident on a second beamsplitter with transmission  $\tau$  as shown in figure 4.6.

The power in the bright beam may be chosen to bring the intensity of the output state back to that of the original. The squeezing of this bright beam pulls the amplified signal back onto the quantum noise-floor without adding any additional noise, i.e. the squeezed light beamsplitter is a noiseless de-amplifier. This extra feature may be incorporated into the linearised description of the system by writing

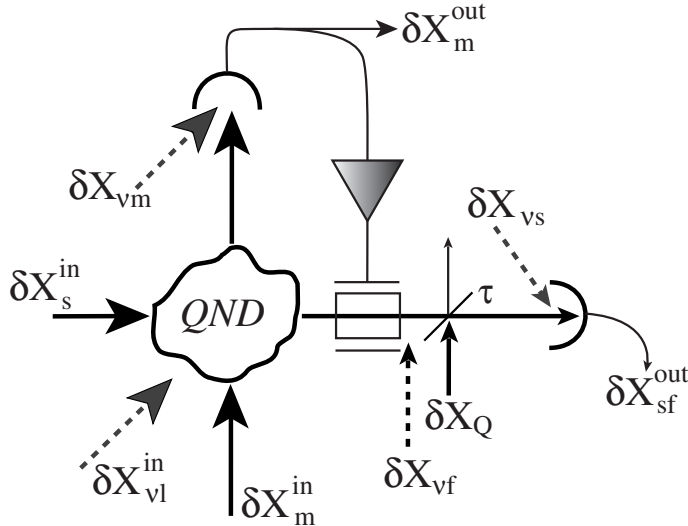


**Figure 4.6:** Scheme for improving the sensitivity of the QND system. A bright squeezed beam with fluctuation operator  $\delta X_Q$  is incident on a beamsplitter with transmission  $\tau$ . Other parameters:  $\delta X_{\nu f}$  is the vacuum noise due to the modulator attenuation,  $\delta X_s^{\text{in}}$  is the signal input,  $\delta X_m^{\text{in}}$  is the meter input,  $\delta X_{\nu l}^{\text{in}}$  is the quantum noise due to internal loss,  $\delta X_{\nu m}$  is the quantum noise due to meter detector efficiency,  $\delta X_{\nu s}$  is the quantum noise due to the signal detector efficiency,  $\delta X_m^{\text{out}}$  and  $\delta X_s^{\text{out}}$  are the meter and signal output photocurrents respectively.

$$\begin{pmatrix} \delta\tilde{X}_{sf}^{\text{out}} \\ \delta\tilde{X}_m^{\text{out}} \end{pmatrix} = \begin{pmatrix} \sqrt{\eta_f\eta_s\tau} & G\sqrt{\eta_f\eta_s\eta_m\tau} \\ 0 & \sqrt{\eta_m} \end{pmatrix} \begin{pmatrix} a & b & c \\ d & e & f \end{pmatrix} \begin{pmatrix} \delta\tilde{X}_s^{\text{in}} \\ \delta\tilde{X}_m^{\text{in}} \\ \delta\tilde{X}_{\nu l} \end{pmatrix} \quad (4.18)$$

$$+ \begin{pmatrix} \sqrt{1-\eta_s} & G\sqrt{\eta_f\eta_s\tau(1-\eta_m)} & \sqrt{\eta_s\tau(1-\eta_f)} & \sqrt{\eta_s(1-\tau)} \\ 0 & \sqrt{1-\eta_m} & 0 & 0 \end{pmatrix} \begin{pmatrix} \delta\tilde{X}_{\nu s} \\ \delta\tilde{X}_{\nu m} \\ \delta\tilde{X}_{\nu f} \\ \delta\tilde{X}_Q \end{pmatrix}.$$

With the inclusion of a squeezed source between the modulator and detector in the signal beam we cannot incorporate the modulator attenuation into the signal detection efficiency, as we did when deriving equation 4.2. Instead we explicitly include the vacuum noise,  $\delta\tilde{X}_{\nu f}$ , due to the non-unity modulator transmission  $\eta_f$ .

The improvement of the sensitivity due to the addition of the bright squeezed source is shown in figure 4.7. The dashed line shows the value of  $S$  for the feedforward system as modelled in section 4.3.2 with 7dB meter squeezing and  $\varepsilon = 0.1$ . The solid line shows the variation of  $S$  as a function of the beamsplitter ratio  $\tau$  with  $V_Q = -7$ dB. At  $\tau = 0.06$  the sensitivity is shown to be brought back to 0dB.

The performance of the sensitivity compensated system may also be investigated in terms of the parameters  $T_{s+m}$  and  $V_{s|m}$ . From equation 4.18 we obtain new equations for  $T_s$  and  $V_{s|m}$ . These are:

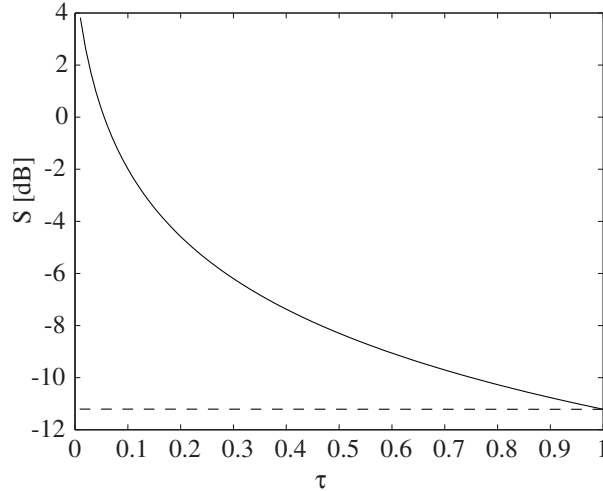


**Figure 4.7:** Repairing the sensitivity using an additional squeezed beam. The dashed line is the sensitivity level of the system analysed in section 4.3.2 with  $\varepsilon = 0.1$ . The solid line includes the addition of a bright squeezed beam, and shows the resulting sensitivity as a function of the beamsplitter ratio  $\tau$ . Other parameters used are  $\eta_m = 0.95$ ,  $\eta_s = 0.95$ ,  $\eta_f = 0.95$ ,  $V_m = -7$ dB and  $V_Q = -7$ dB.  $G$  is optimised to maximise  $T_s$ .

$$T_s = \left\{ \eta_s \eta_f \tau |a + G\sqrt{\eta_m}d|^2 \right\} / \left\{ \eta_s \eta_f \tau \left[ |a + G\sqrt{\eta_m}d|^2 + |b + G\sqrt{\eta_m}e|^2 V_m^{\text{in}} + |c + G\sqrt{\eta_m}f|^2 + |G|^2(1 - \eta_m) \right] - \eta_s \eta_f \tau - \eta_s(1 - \tau)(1 - V_Q) + 1 \right\} \quad (4.19)$$

and

$$V_{s|m} = \frac{\eta_s \eta_f \tau \left[ |a|^2 V_s^{\text{in}} + |b|^2 V_m^{\text{in}} + |c|^2 \right] - \eta_s \eta_f \tau - \eta_s(1 - \tau)(1 - V_Q) + 1}{\eta_m \left[ |d|^2 V_s^{\text{in}} + |e|^2 V_m^{\text{in}} + |f|^2 \right] + 1 - \eta_m} \quad (4.20)$$

Using equations 4.19 and 4.20 we model the effect of sensitivity correction on the beamsplitter QND system with  $\varepsilon = 0.1$ . Line  $i$  of figure 4.8 shows the QND system with feedforward and no sensitivity correction. This is identical to line  $ii_f$  of figure 4.4. As before the circles represent meter squeezing in intervals of 1dB. The performance of the compensated system is shown in two parts. Line  $ii$  shows the performance of the system with no meter squeezing ( $V_m = 0\text{dB}$ ) and varying amounts of bright squeezing  $V_Q$ . The squares are in 1dB steps. The results of line  $ii$  shows that we may make an efficient QND system with  $S = 0\text{dB}$  by using only feedforward and sensitivity post-enhancement. We do not require meter squeezing pre-enhancement to perform QND with a beamsplitter. This system is similar to that described by Ralph [96]. The value of  $\tau$  required to obtain  $S = 0\text{dB}$  varies as a function of  $V_Q$ . With  $V_Q = 0\text{dB}$  in line  $ii$   $\tau$  is close to 0, while at  $V_Q = -7\text{dB}$ ,  $\tau = 0.07$ . The addition of meter squeezing  $V_m$  takes the performance from the end of line  $ii$  along line  $iii$ . As  $V_m$  is increased in line  $iii$ ,  $\tau$  decreases to 0.06. This due to the higher feedforward gain used as the squeezing  $V_m$  is increased.

The sensitivity corrected system is shown to have worse  $T_{s+m}$  characteristics than the uncompensated case. This is due to the small amount of extra noise introduced by  $V_Q$ . The conditional variance, on the other hand, is improved in the compensated system due to the overall reduction in the signal noise level.

For the particular case of the beamsplitter with feedforward, the sensitivity becomes poor due to the gain ( $G$ ) of the feedforward loop. The amount of gain was chosen initially to optimise the signal transfer  $T_s$ . Instead, we may sacrifice some of the signal transfer and choose a gain which gives a sensitivity of 0dB. Doing this for the case of  $\varepsilon = 0.1$  gives the line  $iv$  of figure 4.8. The results of this method are seen to be better than those obtained with the extra squeezed beam. Reducing the feedforward gain is not, however, a general method for sensitivity correction. It is only applicable when the feedforward is the reason for the loss of sensitivity, as is the case for the beamsplitter. If the QND device were an OPA, the signal gain which ruins the sensitivity is present without feedforward amplification. In this case an additional squeezed beam would be required to recover the sensitivity.

The special case of  $\varepsilon = 0$  may also be investigated in terms of the sensitivity. As for  $\varepsilon = 0.1$ , the sensitivity is easily retrieved by reducing the gain. This situation is shown by line  $s$  of figure 4.8. This system is not as effective as the  $\varepsilon = 0.1$  case. The reason is that the transfer of signal onto the signal output beam with  $\varepsilon = 0$  relies solely on the feedforward. With a reduction in gain the signal drops proportionally. In the case of  $\varepsilon = 0.1$  not all the signal travels through the feedforward. Some of the signal still leaks straight through the beamsplitter in to the signal output. Reducing the gain therefore has

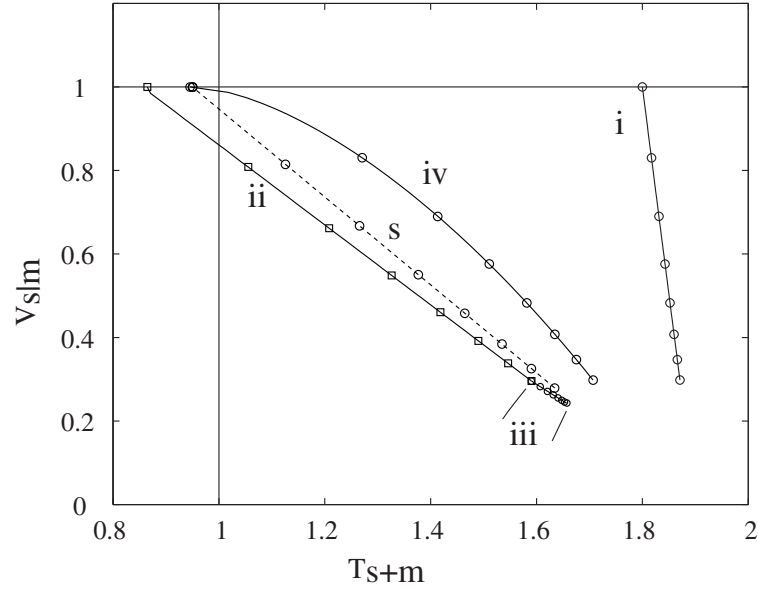


**Figure 4.8:** Comparison of the standard QND parameters, with and without the addition of sensitivity correction, for a  $\varepsilon = 0.1$  beamsplitter QND system. Line *i* is the performance of the system as previously shown in line *ii<sub>f</sub>* of figure 4.4 with no sensitivity correction and  $V_m$  varying from 0 to -7dB. The circles again represent 1dB intervals of  $V_m$ . Line *ii* shows the effect of sensitivity correction with  $V_Q = -7$ dB,  $V_m = 0$ dB and  $\tau$  chosen to give  $S = 0$ dB. The squares are 1dB intervals of  $V_Q$ . Line *iii* shows the effect of turning on the meter squeezing  $V_m$  with  $V_Q$  held constant at -7dB. The circles represent 1dB intervals of  $V_m$ .  $\tau$  is again chosen to give  $S = 0$ dB. For lines *i*, *ii* and *iii*  $G$  is chosen to optimise  $T_s$ . Lines *iv* and *s* show the retrieval of the sensitivity by reducing the gain of the feedforward instead of using an additional bright squeezed source. In both cases the squeezing  $V_m$  is varied from 0 to -7dB. Line *iv* shows the  $\varepsilon = 0.1$  case and line *s* is the special case of  $\varepsilon = 0$ . Other parameters for lines *ii*, *iii*, *iv* and *s* are  $\eta_m = 0.95$ ,  $\eta_s = 0.95$  and  $\eta_f = 0.95$ .

a less drastic effect. We may conclude that the special case of QND with no interaction at the beamsplitter is better if the sensitivity is regarded as unimportant (as shown in figure 4.4). However, with sensitivity correction achieved by altering the gain of the feedforward loop it is better to have some signal passing through the beamsplitter.

## 4.5 Conclusion

We have shown the utility of feedforward as a post-enhancement tool for a general QND scheme. Examples of the beamsplitter and optical parametric amplifier were considered and the potential benefits under realistic experimental conditions were shown to be significant. Feedforward may also be used in conjunction with squeezed meter pre-enhancement to further improve a range of QND devices. The sensitivity of the output state from a feed forward loop was shown to be well below that required for quantum noise limited measurements. This problem may be overcome for any QND system with the use of a bright squeezed light beamsplitter to de-amplify the output state back to its original size.

For the particular case of QND performed with a squeezed vacuum beamsplitter and



feedforward, where the only source of signal amplification is the feedforward, the sensitivity may be more easily corrected by reducing the feedforward gain. We have also examined a limit of the beamsplitter system where the signal and meter input beams do not interact optically. This system is shown to have an advantage over the normal beamsplitter QND arrangement provided the sensitivity is not important.

---

# Suppressing radiation pressure noise with feedback

---

In this chapter a model of electro-optic feedback is developed. The theory shows that feedback can suppress laser intensity noise inside a cavity by a factor of two below the quantum limit. This result is then applied to a thermal noise detection system. The reduced intensity noise leads to suppressed radiation pressure noise, therefore giving improved thermal noise sensitivity. The result proves that the modified noise properties of light inside a feedback loop can be used to reduce quantum measurement noise.

Work in this chapter has been published as “Suppression of classic and quantum radiation pressure noise by electro-optic feedback”, B.C. Buchler, M.B. Gray, D.A. Shaddock, T.C. Ralph, and D. E. McClelland, *Optics Letters*, **24**, 259, (1998).

## 5.1 Introduction

Perhaps the most extreme of all precision measurement devices are about to become operational. These are the interferometric gravitational wave detectors, several of which are nearing completion in the United States (LIGO), Japan (TAMA) and Europe (GEO600 and VIRGO). It is hoped that these giant Michelson interferometers will measure the distortion of space due to passing gravitational waves [102]. The expected deformation of space, over the kilometre length scales on which these detectors are being built, is only  $10^{-18}$ m. To be able to detect such small changes in length has required substantial improvements to a range of technologies. These include high power single mode lasers [36], low loss mirror coatings to cope with the massive amounts of laser power in the interferometer [24] and suspension systems to isolate from seismic noise [10]. The gravitational wave detection effort has also inspired some basic research into the noise sources of interferometers, such as thermal noise. This is the vibration of an object due to its intrinsic thermal energy. Thermal vibration of the mirrors in a gravitational wave detector may hide the gravitational wave signal. Unless the interferometer is cooled, thermal noise is fairly unavoidable. The best way to minimise its effect is to build mirror suspension systems with very high mechanical Q and resonant frequencies outside the detection bandwidth of the interferometer. The thermal noise fluctuations will then be concentrated into a narrow range of frequencies outside the gravitational wave detection bandwidth.

Careful suspension and mirror design will certainly reduce the effect of thermal noise. Models suggest that thermal noise will decrease in power very rapidly away from the mechanical resonance frequencies [102]. However, to be sure of the exact size of ‘off-resonance’ thermal noise, a direct measurement is required. To date, measurements of off-resonance

thermal noise have proved difficult and very few experiments have succeeded [43, 67, 130]. Measuring thermal noise is tough simply because of the very small size of the signal. Experiments must overcome technical noise sources such as seismic noise, acoustic noise and noise of the electronics monitoring the experiment. Assuming that these technical noise sources may be overcome with some careful engineering, the next barrier to broadband thermal noise measurement is the quantum noise of the optical detection system. The quantum noise may be reduced up to a point by increasing the laser power used to probe the experiment. However the power cannot be increased indefinitely. Ultimately, too much light leads to radiation pressure noise. Radiation pressure noise is a consequence of fluctuations in laser power (including the unavoidable quantum fluctuations) exciting mirror motion. Apart from limiting the performance of thermal noise measurement experiments, radiation pressure noise is also expected to be a limiting factor in the next generation of gravitational wave interferometers [50].

The quantum mechanics of radiation pressure noise have been well modelled. It has been shown that appropriate use of squeezing may reduce the effects of radiation pressure noise in the readout of the mirror motion in a cavity [88]. This works by anti-correlating the radiation pressure noise with the phase noise of the laser. The final detection is therefore (in the limit of perfect squeezing) immune to radiation pressure and laser phase noise. This analysis was carried out for a single sided cavity in a Michelson interferometer. Other work in the area of quantum opto-mechanical coupling has concentrated on the regime where the radiation pressure is the dominant source of mirror motion. This has shown:

- The radiation pressure coupling of field fluctuations into mirror motion means that a cavity may behave as a Kerr medium and thereby generate squeezed states [34, 80].
- More generally, a cavity with a movable mirror may be capable of generating a range of non-classical states, including Schrödinger cats [9] and entanglement [42].
- Detecting the motion of the cavity mirror via a Piezo crystal on the mirror [91] or the phase fluctuations of the field reflected from the cavity [57, 65] allows a quantum nondemolition measurement of the fluctuations in the cavity photon number.

The aim of this chapter is to generate a model of the thermal noise measurement experiment being built in our laboratories [48]. Using this model, which includes the quantum noise of the laser beam, we then propose a method that can reduce the amount of radiation pressure noise by a factor of two below the quantum limit of our measurement system, without resorting to the injection of squeezing into the cavity. Our scheme is based on the properties of a laser beam inside a feedback loop. It has been shown by many authors [23, 56, 79, 110, 115, 121, 124] that the noise of a laser inside a feedback loop may be perfectly suppressed. These reduced fluctuations will not, however, couple out into the ‘real world’ unless there is a QND system to measure the in-loop field [23, 120, 121, 124]. It is the QND nature of the coupling between the phase quadrature of the field reflected from a cavity and the radiation pressure noise that allows our system to work.

The layout of the chapter is as follows: in the next section I give an overview of the properties of light inside a feedback loop. In section 5.3 I show how cavity detuning due to thermal and radiation pressure noise may be measured using the light reflected from the input mirror. Section 5.4 combines the feedback theory and the detuning measurement theory to show how feedback suppresses radiation pressure noise. The final two sections, 5.5 and 5.7, model a thermal noise measurement experiment and show the potential increase in detection bandwidth due to the feedback system.

## 5.2 Quantum feedback theory

To begin, the nature of light inside a feedback loop will be explored. A simple optical feedback system is shown in figure 5.1. Here a beamsplitter, of transmissivity  $\varepsilon$ , is used to tap off some light for the out-of-loop field while the transmitted field is detected and the resultant photocurrent used to control the laser intensity via a modulator. The modulator is modelled as adding a fluctuation term,  $-(1/2)\delta X_r^+$ , due to the feedback. We therefore find

$$A_{\text{in},1} = A_0 - \frac{1}{2}\delta X_r^+. \quad (5.1)$$

The scaling of the feedback by  $-1/2$  is arbitrary as the sign and gain of the feedback is ultimately dictated by the electronics in the loop. The reason for the negative sign is to be consistent with standard feedback theory notation [29]. The feedback term is written as a Hermitian quadrature operator because it is derived from a measurement of the amplitude quadrature of the beam at the feedback detector. It also means that the phase quadrature of the beam is unaffected by the modulation, implying ideal amplitude modulation of the input beam. The fluctuations of the amplitude quadrature of  $A_{\text{in},1}$  are then given by

$$\delta X_{\text{in},1}^+ = \delta X_0^+ - \delta X_r^+. \quad (5.2)$$

What remains is to express the feedback in terms of the detected field  $A_{\text{in},2}$ . Referring to equation 2.52 the photocurrent,  $I$ , due to the field  $A_{2,\text{in}}$  is given by

$$I = \eta \bar{A}_{\text{in},2}^2 + \sqrt{\eta} \bar{A}_{\text{in},2} (\sqrt{\eta} \delta X_{\text{in},2}^+ + \sqrt{1-\eta} \delta X_D^+) \quad (5.3)$$

where the vacuum term  $\delta X_D^+$  comes from the photodetector efficiency,  $\eta$ , and  $\bar{A}_{\text{in},2}$  is the classical field amplitude at the detector. The fluctuating part of this current is fed-back to the modulator through some amplification and filtering electronics. These have a time domain response of  $k(t)$  so that the amplitude quadrature fluctuation operator,  $\delta X_r^+$ , may be expressed as the convolution integral of  $k(t)$  with the fluctuating part of the photocurrent over the total detection time  $T$ :

$$\delta X_r^+ = \sqrt{\eta} \bar{A}_{\text{in},2} \int_0^T k(\tau) \left( \sqrt{\eta} \delta X_{\text{in},2}^+(t-\tau) + \sqrt{1-\eta} \delta X_D^+(t-\tau) \right) d\tau. \quad (5.4)$$

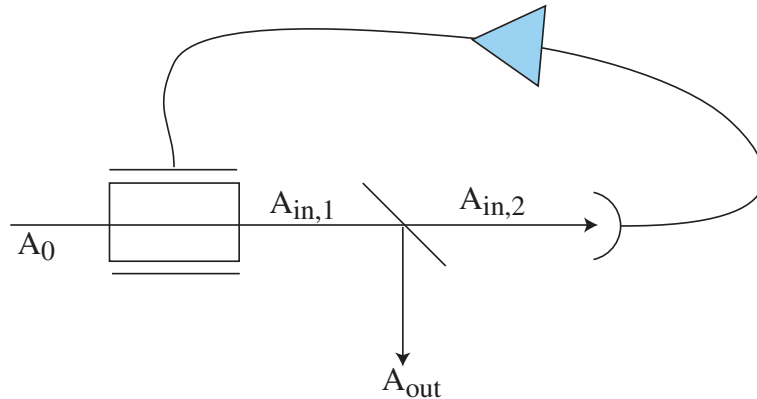


**Figure 5.1:** An electro-optic feedback loop

We also know that the field fluctuations,  $\delta X_{\text{in},2}^+$ , are related to the fluctuations of the field at the modulator output,  $\delta X_{\text{in},1}^+$ , via

$$\delta X_{\text{in},2}^+ = \sqrt{\varepsilon} \delta X_{\text{in},1}^+ - \sqrt{1-\varepsilon} \delta X_{\nu}^+. \quad (5.5)$$

Combining Equations 5.2, 5.4 and 5.5 gives

$$\begin{aligned} \delta X_{\text{in},1}^+ &= \delta X_0^+ \\ &- \sqrt{\eta} \bar{A}_{\text{in},2} \int_0^T k(\tau) \left( \sqrt{\eta} (\sqrt{\varepsilon} \delta X_{\text{in},1}^+(t-\tau) - \sqrt{1-\varepsilon} \delta X_{\nu}^+(t-\tau)) + \sqrt{1-\eta} \delta X_D^+(t-\tau) \right) d\tau. \end{aligned} \quad (5.6)$$

The solution to equation 5.6 lies in the Fourier domain where the convolution integral will become the product of the Fourier transforms of  $k(t)$  and the fluctuation operators. Defining  $\mathcal{F}[k(t)] = K(\omega)$ , where  $K(\omega)$  may be complex (to include the phase response of the feedback) we find:

$$\begin{aligned} \delta \tilde{X}_{\text{in},1}^+ &= \delta \tilde{X}_0^+ - \bar{A}_{\text{in},2} K(\omega) \left( \eta \sqrt{\varepsilon} \delta \tilde{X}_{\text{in},1}^+ - \eta \sqrt{1-\varepsilon} \delta \tilde{X}_{\nu}^+ + \sqrt{\eta(1-\eta)} \delta \tilde{X}_D^+ \right) \\ \Rightarrow \delta \tilde{X}_{\text{in},1}^+ &= \frac{\delta \tilde{X}_0^+ + G(\omega) \left( \sqrt{1-\varepsilon} \delta \tilde{X}_{\nu}^+ - \sqrt{\frac{1-\eta}{\eta}} \delta \tilde{X}_D^+ \right)}{1 + G(\omega) \sqrt{\varepsilon}} \end{aligned} \quad (5.7)$$

$$\text{where } G(\omega) = \eta \bar{A}_{\text{in},2} K(\omega).$$

This equation may be used with the beamsplitter relation at the feedback beamsplitter to find the other amplitude quadratures that matter in this problem, namely  $\delta \tilde{X}_{\text{out}}^+$  and  $\delta \tilde{X}_{\text{in},2}^+$ :

$$\begin{aligned} \delta \tilde{X}_{\text{out}}^+ &= \frac{\sqrt{1-\varepsilon} \delta \tilde{X}_0^+ + (\sqrt{\varepsilon} + G(\omega)) \delta \tilde{X}_{\nu}^+ - G(\omega) \sqrt{\frac{1-\eta}{\eta}} \sqrt{1-\varepsilon} \delta \tilde{X}_D^+}{1 + G(\omega) \sqrt{\varepsilon}} \\ \delta \tilde{X}_{\text{in},2}^+ &= \frac{\sqrt{\varepsilon} \delta \tilde{X}_0^+ - \sqrt{1-\varepsilon} \delta \tilde{X}_{\nu}^+ + G(\omega) \sqrt{\frac{1-\eta}{\eta}} \sqrt{\varepsilon} \delta \tilde{X}_D^+}{1 + G(\omega) \sqrt{\varepsilon}}. \end{aligned} \quad (5.8)$$

Equations 5.7 and 5.8 give the spectra of the in and out-of-loop fields to be

$$\begin{aligned} V_{\text{in},1}^+ &= \frac{V_0^+ + |G(\omega)|^2 \left( 1 - \varepsilon + \frac{1-\eta}{\eta} \right)}{|1 + G(\omega) \sqrt{\varepsilon}|^2} \\ V_{\text{in},2}^+ &= \frac{\varepsilon V_0^+ + 1 - \varepsilon + \frac{\varepsilon(1-\eta)}{\eta} |G(\omega)|^2}{|1 + G(\omega) \sqrt{\varepsilon}|^2} \\ V_{\text{out}}^+ &= \frac{(1-\varepsilon) V_0^+ + |\sqrt{\varepsilon} + G(\omega)|^2 + \frac{(1-\eta)(1-\varepsilon)}{\eta} |G(\omega)|^2}{|1 + G(\omega) \sqrt{\varepsilon}|^2}. \end{aligned} \quad (5.9)$$

In the limit of high-gain ( $G(\omega) \rightarrow \infty$ ), these spectra go to

$$\begin{aligned} \lim_{G(\omega) \rightarrow \infty} V_{\text{in},1}^+ &= \frac{1-\eta\varepsilon}{\eta\varepsilon} \\ \lim_{G(\omega) \rightarrow \infty} V_{\text{in},2}^+ &= \frac{1-\eta}{\eta} \\ \lim_{G(\omega) \rightarrow \infty} V_{\text{out}}^+ &= \frac{1}{\eta\varepsilon}. \end{aligned} \quad (5.10)$$

### 5.2.1 In-loop field properties

The high-gain limits show that the spectrum of the in-loop field  $V_{\text{in},2}^+$  (i.e. that immediately before the detector), may go to 0 in the case of ideal photodetection. The field before the beamsplitter,  $A_{\text{in},1}$ , may also have a spectrum which falls below the QNL provided  $\varepsilon > \frac{1}{2}$ . Yet neither of these are squeezed fields. The feedback does not affect the phase quadrature of the fields in any way, so the noise of the phase quadrature inside the feedback loop may in fact be at the QNL. If the fields were squeezed, the phase quadrature noise would be enlarged, so as to remain consistent with the uncertainty principle. This seems to imply a violation of the uncertainty relation inside the feedback loop. How can this be so?

Extensive theoretical investigations [56, 110] have shown that the field inside a feedback loop is not a free field, and is therefore not required to obey the free-field commutator relations or the uncertainty principle. This may be seen by using equations 5.7 and 5.8. The phase quadratures of the field in the feedback system are given by the normal beamsplitter relations since the feedback is acting only on the amplitude quadrature. Using  $[\delta\tilde{X}^+, \delta\tilde{X}^-] = 2i$  for all the vacuum modes, we find that

$$[\delta\tilde{X}_{\text{in},1}^+, \delta\tilde{X}_{\text{in},1}^-] = \frac{1}{1 + G(\omega)\sqrt{\varepsilon}} [\delta\tilde{X}_0^+, \delta\tilde{X}_0^-] = \frac{2i}{1 + G(\omega)\sqrt{\varepsilon}} \quad (5.11)$$

$$\begin{aligned} [\delta\tilde{X}_{\text{out}}^+, \delta\tilde{X}_{\text{out}}^-] &= \frac{1}{1 + G(\omega)\sqrt{\varepsilon}} \left[ (\sqrt{1 - \varepsilon}\delta\tilde{X}_0^+ + (\sqrt{\varepsilon} + G(\omega))\delta\tilde{X}_\nu^+), (\sqrt{1 - \varepsilon}\delta\tilde{X}_0^- + \sqrt{\varepsilon}\delta\tilde{X}_\nu^-) \right] \\ &= 2i. \end{aligned} \quad (5.12)$$

The Bosonic commutator relation is therefore preserved for the out-of-loop field, but not for the in-loop field.

Inside a feedback loop, correlations exist between electrons in the wire and photons in the beam over a finite frequency interval, which is the bandwidth of the feedback loop. It is the correlations between the electrons and the photons which are measured for the in-loop field, unlike a free field which relies on true two-time correlations between photons in the field for noise suppression.

The in-loop ‘‘squashing’’ [22] of light can be coupled out into the real world via a QND measurement [56, 124, 131]. The most obvious technique is to mix a squeezed state on the feedback beamsplitter. This scheme does not generate any more squeezing than the amount incident on the beamsplitter. The out-of-loop field will, however, be squeezed to a greater degree than is achieved simply mixing a squeezed state with a coherent state on a beamsplitter, indicating the presence of squashing [23].

It has also been shown that the light inside a feedback loop can affect an atom. Illuminating an atom with squashed light causes line narrowing of one quadrature of the atoms fluorescence [122, 123]. Line narrowing was previously thought to be a unique feature of squeezed light. This was the first time that squashed light was shown to be a suitable substitute for real squeezed light.

The idea of a ‘‘squashed’’ quantum state inside a feedback loop has been generalised beyond light to include ‘‘motional squashed states’’ [81]. In this case the vibrational states of an atom are shown to be modified by the action of a feedback loop.

### 5.2.2 Out-of-loop field properties

In the limit of high gain, the noise of the out-of-loop field noise is always bounded above the QNL. For perfect detection, the noise of the out of loop field goes to  $1/\varepsilon$ . A simple explanation of this behaviour can be given in terms of the vacuum noise introduced at the

beamsplitter in the feedback loop. A photon which goes one way through the beamsplitter cannot simultaneously go the other direction through the beamsplitter (The photons on one path are being detected, so this is not a case of Young's double slits). This means that the noise of the beamsplitter introduces anti-correlated quantum noise into the two fields at its output. This is expressed in the model as the vacuum noise being  $+\delta\nu$  in one output of the beamsplitter and  $-\delta\nu$  in the other. The feedback loop therefore does not have complete information about the out-of-loop field, and therefore fails to control it effectively. This is a well known phenomenon [56, 115, 120, 124].

Solid state lasers, such as the Nd:YAG lasers we use in our laboratory, tend to have large amounts of classical intensity noise at low frequencies. One method to control this is to use a high gain feedback loop to suppress the fluctuations [53]. The above theory means that the suppression loop will not push the laser to the QNL. For example, if we detect 10% of the laser light for the feedback, then the output field is suppressed at best to a factor of 10 above the QNL in the high gain limit. Such use of a control loop does not use the full noise suppression abilities of electronic feedback.

Rather than using the feedback gain to suppress the noise, the gain may also be used to increase the noise by reversing the gain (so that  $G < 0$ ). This can only be done for  $-1/\sqrt{\varepsilon} < G$ , otherwise the feedback becomes unstable. In particular, taking equation 5.9 with ideal detection ( $\eta = 1$ ) and gain  $G(\omega) = -\sqrt{\varepsilon}$  gives

$$V_{\text{out}}^+ = \frac{1}{1 - \varepsilon} V_0^+ \quad (5.13)$$

which is an identical result to that found with feedforward amplification (see chapter 3). Feedback may also act as a noiseless amplifier, and like the case of feedforward, the more of the input light is sent to the detector, the higher the signal amplification<sup>1</sup>. This effect has, in fact, been previously noted theoretically [121], and performed experimentally, although not recognised as noiseless amplification [115].

## 5.3 Measurement of cavity detuning

### 5.3.1 Fields exiting the cavity

The effect of thermal noise, and radiation pressure noise, is to excite a vibration in the position of the cavity mirrors, that is we introduce a fluctuating detuning,  $\delta\Delta$ , of the cavity from resonance. Returning to the equation of motion for a cavity (equation 2.89 and diagram 2.8) we find that

$$\dot{a} = -(\kappa + i\delta\Delta)a + \sqrt{2\kappa_{\text{in}}}A_{\text{in}} + \sqrt{2\kappa_l}\delta A_l + \sqrt{2\kappa_{\text{out}}}\delta A_{\text{out}}. \quad (5.14)$$

By substituting  $a = \alpha + \delta a$  we can find an equation for the first order fluctuations of  $a$ :

$$\dot{\delta a} = -\kappa\delta a - i\delta\Delta\alpha + \sqrt{2\kappa_{\text{in}}}\delta A_{\text{in}} + \sqrt{2\kappa_l}\delta A_l + \sqrt{2\kappa_{\text{out}}}\delta A_{\nu}. \quad (5.15)$$

---

<sup>1</sup>The change between  $\varepsilon$  in the case of feedforward and  $1 - \varepsilon$  here, is due to the reflected port being detected in feedforward, and the transmitted port being detected for feedback

Following the method of section 2.7 we find the following field phase and amplitude quadratures for the transmitted, reflected and internal fields:

$$\delta\tilde{X}_a^+ = \frac{\sqrt{2\kappa_{\text{in}}}\delta\tilde{X}_{\text{in}}^+ + \sqrt{2\kappa_{\text{out}}}\delta\tilde{X}_{\nu}^+ + \sqrt{2\kappa_l}\delta\tilde{X}_l^+}{i\omega + \kappa} \quad (5.16)$$

$$\delta\tilde{X}_{\text{trans}}^+ = \frac{2\sqrt{\kappa_{\text{out}}\kappa_{\text{in}}}\delta\tilde{X}_{\text{in}}^+ + (2\kappa_{\text{out}} - \kappa - i\omega)\delta\tilde{X}_{\nu}^+ + 2\sqrt{\kappa_{\text{out}}\kappa_l}\delta\tilde{X}_l^+}{i\omega + \kappa} \quad (5.17)$$

$$\delta\tilde{X}_{\text{ref}}^+ = \frac{(2\kappa_{\text{in}} - \kappa - i\omega)\delta\tilde{X}_{\text{in}}^+ + 2\sqrt{\kappa_{\text{in}}\kappa_{\text{out}}}\delta\tilde{X}_{\nu}^+ + 2\sqrt{\kappa_{\text{in}}\kappa_l}\delta\tilde{X}_l^+}{i\omega + \kappa} \quad (5.18)$$

$$\delta\tilde{X}_a^- = \frac{2\alpha\delta\tilde{\Delta} + \sqrt{2\kappa_{\text{in}}}\delta\tilde{X}_{\text{in}}^- + \sqrt{2\kappa_{\text{out}}}\delta\tilde{X}_{\nu}^- + \sqrt{2\kappa_l}\delta\tilde{X}_l^-}{i\omega + \kappa} \quad (5.19)$$

$$\delta\tilde{X}_{\text{trans}}^- = \frac{2\alpha\sqrt{2\kappa_{\text{out}}}\delta\tilde{\Delta} + 2\sqrt{\kappa_{\text{out}}\kappa_{\text{in}}}\delta\tilde{X}_{\text{in}}^- + (2\kappa_{\text{out}} - \kappa - i\omega)\delta\tilde{X}_{\nu}^- + 2\sqrt{\kappa_{\text{out}}\kappa_l}\delta\tilde{X}_l^-}{i\omega + \kappa} \quad (5.20)$$

$$\delta\tilde{X}_{\text{ref}}^- = \frac{2\alpha\sqrt{2\kappa_{\text{in}}}\delta\tilde{\Delta} + (2\kappa_{\text{in}} - \kappa - i\omega)\delta\tilde{X}_{\text{in}}^- + 2\sqrt{\kappa_{\text{in}}\kappa_{\text{out}}}\delta\tilde{X}_{\nu}^- + 2\sqrt{\kappa_{\text{in}}\kappa_l}\delta\tilde{X}_l^-}{i\omega + \kappa}. \quad (5.21)$$

The most important piece of information in these equations is that the phase quadratures of the reflected and transmitted fields contain information about the detuning of the cavity. In particular, the reflected field phase noise spectrum is given by

$$V_{\text{ref}}^- = 1 + \frac{8\kappa_{\text{in}}\alpha^2 V_{\Delta} + ((2\kappa_{\text{in}} - \kappa)^2 + \omega^2)(V_{\text{in}}^- - 1)}{\omega^2 + \kappa^2}. \quad (5.22)$$

Provided the detuning signal,  $V_{\Delta}$ , is large enough to reach above the quantum noise (which is the origin of the 1 at the front of this expression) a measurement of the reflected field phase quadrature will provide information about the detuning spectrum of the cavity. Equation 5.22 shows that the more power is in the cavity ( $\alpha^2$ ), the better the sensitivity to the fluctuations of the cavity mirror position. For this reason very sensitive thermal noise measurements require high laser powers and high finesse cavities.

### 5.3.2 Cavity configurations

A fundamental challenge of a real thermal noise measurement is eliminating other sources of cavity detuning. Defeating seismic and acoustic noise is particularly difficult as it requires that the experiment be hung from a seismic isolation stack in a vacuum. In our model, seismic and acoustic noise will not be considered. Only sources of detuning inherent to the optical measurement system will be included, namely laser noise and radiation pressure noise.

To simplify the discussion of these noise sources a little, it is safe to assume that the bandwidth of the detuning signal will be well within the cavity linewidth. In other words, we may make the approximation  $\omega \ll \kappa$ . Using this as the starting point, different cavity configurations may now be investigated to see how the sensitivity to thermal noise is affected.

If the cavity is impedance matched then  $2\kappa_{\text{in}} - \kappa = 0$ . Using this (and the earlier assumption that  $\omega \ll \kappa$ ) in equation 5.22 shows that the impedance matched cavity will have low sensitivity to classical laser phase noise ( $V_{\text{in}}^- - 1$ ). Another advantage of impedance matching is that the power reflected from the cavity will be low. Given that the information required from the reflected beam is written on the phase quadrature, a measurement of the detuning will require some form of phase quadrature detection, such as a homodyning. Homodyne detection requires a local oscillator that is much more intense



than the signal beam, so low cavity reflectivity is an advantage.

Impedance matching, however, is not all good news for detuning measurements since it does not provide the best possible signal-to-noise in the reflected beam. Assuming that the laser phase noise may be forced to the QNL (so that  $V_{\text{in}}^- - 1 = 0$ ), equation 5.22 shows that, for a given optical power ( $\alpha^2$ ), the way to maximise the detuning signal is to make  $\kappa = \kappa_{\text{in}}$ . This corresponds to the case of a single ended, fully reflective cavity. Apart from the increased sensitivity to laser phase noise, the disadvantage of using a reflective cavity is the amount of reflected power. To achieve maximum sensitivity, all the reflected power must be detected. This could be of the order of a Watt of optical power. If homodyne detection is used to observe the phase quadrature, the measurement scenario becomes quite impractical given that the local oscillator beam of the homodyne system should be an order of magnitude more powerful than the signal beam.

An alternative to homodyne detection for phase quadrature measurement is the use of the cavity locking signal. (This method is considered in detail in section 5.5.) Outside the bandwidth of the feedback servo, the locking signal will be a representation of the relative fluctuations between the laser and cavity frequencies, and therefore a measurement of the cavity detuning. Using the locking signal to measure the detuning avoids the need for a powerful local oscillator beam. However in the case of a single ended cavity, the power reflected may still be substantial. The derivation of section 5.5 will show that having large optical power incident on the detector adds extra noise to the detuning detection. Furthermore, there will be technical difficulties associated with building a high frequency detector that can also handle high incident power. As the locking signal is typically at some number of Megahertz, this would be a requirement of the locking detector used to measure the motion of a reflective cavity. Therefore, even when using the locking signal instead of homodyne detection, reflective cavities present experimental difficulties.

Instead of using the reflected field from the cavity, one may look at the transmitted field. The phase quadrature of the transmitted field is given by:

$$V_{\text{trans}}^- = 1 + \frac{8\kappa_{\text{out}}\alpha^2 V_{\Delta} + 4\kappa_{\text{out}}\kappa_{\text{in}}(V_{\text{in}}^- - 1)}{\omega^2 + \kappa^2} \quad (5.23)$$

which, like the reflected field, has some dependence on the detuning signal. On the whole, the transmitted field does not perform well. If the cavity is impedance matched, then the transmitted field will be of very high power, so a homodyne measurement is again difficult due to the power requirements. If the cavity is very reflective (such that  $\kappa_{\text{out}} \ll \kappa_{\text{in}}$ ) then the output coupling of the signal will be small. If the cavity is reflective with  $\kappa_{\text{out}} \gg \kappa_{\text{in}}$ , then the coupling of the signal to the output is good, but the input coupling of the laser is poor so the power build up in the cavity will be diminished. In general, therefore, a measurement of cavity detuning is best done using the reflected field.

The bottom line is that a single ended cavity with measurement of the reflected phase information gives the best result in theory. However, the practical difficulties in detecting very large amounts of power (in the case of homodyne detection), or moderately large amounts of power with large bandwidth (in the case of the locking signal), are quite severe. From the standpoint of somebody actually attempting the experiment, measurement of the field reflected from an impedance matched cavity has some significant practical advantages.

### 5.3.3 Power scaling of the detuning signals

A full description of the thermal and radiation pressure noise will be given in section 5.6. For the moment we will simply split the detuning into contributions from thermal and radiation pressure noise and extract the precise dependence of the different signals on the cavity photon number. The fluctuations in the position of the mirror  $\delta\tilde{x}(\omega)$  are given by

$$\delta\tilde{x}(\omega) = \left( \delta\tilde{F}_R(\omega) + \delta\tilde{F}_T(\omega) \right) \chi(\omega), \quad (5.24)$$

where  $\chi(\omega)$  is the mechanical susceptibility of the cavity mirror and its suspension system,  $\delta\tilde{F}_R$  is the fluctuation of force on the mirror due to radiation pressure and  $\delta\tilde{F}_T$  is the force due to thermal noise. This may be converted into an angular-frequency detuning via:

$$\delta\tilde{\Delta} = \frac{-2\pi c}{\lambda L} \delta\tilde{x} \quad (5.25)$$

where  $L$  is the cavity round-trip length and  $\lambda$  is the wavelength of the laser. The force due to photons bouncing off the mirror will be equal to the number of photons bouncing off the mirror per second multiplied by the change in the momentum per photon, i.e.

$$\tilde{F}_R = \frac{2h}{\lambda\tau} \tilde{a}^\dagger \tilde{a} \quad (5.26)$$

where  $\tau = L/c$  is the cavity round-trip time. The fluctuations in this force are therefore given by

$$\delta\tilde{F}_R(\omega) = \frac{2hc}{\lambda L} \alpha \delta\tilde{X}_a^+(\omega). \quad (5.27)$$

Using equations 5.24, 5.25 and 5.27 we can now write

$$V_\Delta = \left( \alpha^2 V_R + V_T \right) \quad (5.28)$$

where the radiation pressure noise spectrum is given by

$$V_R(\omega) = \left( \frac{2\pi c}{\lambda L} \right)^2 \left( \frac{2hc}{L\lambda} \right)^2 |\chi(\omega)|^2 V_a^+ \quad (5.29)$$

and the thermal noise spectrum is

$$V_T(\omega) = \left( \frac{2\pi c}{\lambda L} \right)^2 \langle |\delta\tilde{F}_T(\omega)|^2 \rangle |\chi(\omega)|^2. \quad (5.30)$$

The correct dependence of the radiation pressure noise on the cavity photon number is therefore found to be:

$$V_{\text{ref}}^- = 1 + \frac{2\kappa_{\text{in}}\alpha^2(\alpha^2 V_R(\omega) + V_T(\omega)) + ((2\kappa_{\text{in}} - \kappa)^2 + \omega^2)(V_{A_{\text{in}}}^- - 1)}{\omega^2 + \kappa^2}. \quad (5.31)$$

From this equation it is clear that the radiation pressure noise scales differently to the thermal noise with respect to the number of photons in the cavity. This is not surprising, with no photons there can be no radiation pressure noise even though there is still thermal noise. The significance of this scaling is that is that turning up the laser power and cavity finesse indefinitely will always lead to domination of radiation pressure noise over thermal noise. On the other hand, if the laser power is too small, the detuning signal in the phase

quadrature spectrum will be swamped by the quantum noise. The conclusion is that there is an optimum laser power for thermal noise detection.

## 5.4 Including feedback in the measurement model

Even the best high power lasers, such as the Nd:YAG lasers used in our laboratory [68], typically have large amounts of intensity noise at low frequencies [54]. Excess classical intensity noise will give rise to increased radiation pressure noise, which will reduce the sensitivity of a thermal noise measurement. Some sort of laser intensity stabilisation will therefore be required in a thermal noise measurement system.

Typically when attempting to eliminate intensity noise, one might put a feedback loop on the laser output [53], with the out-of-loop field being sent to the experiment. As described in section 5.2.2, this scheme will not suppress the noise of the laser to the QNL. The alternative proposed here is to put the experiment *inside* the feedback loop as shown in figure 5.2. The thermal noise experiment may now sense the squashed light inside the feedback loop. If this is the case, radiation pressure noise will be reduced well below the level achievable with external feedback. This feedback configuration is only possible when using an impedance matched cavity. A reflective cavity would have no significant amount of transmitted power, therefore making the feedback ineffective. With the feedback around the cavity, large amounts of light will be incident on the feedback detector. However, the detection bandwidth need only coincide with the thermal noise measurement bandwidth, which might be a few kilohertz. This is not as difficult as building a high power, high bandwidth detector, as would be required for the locking of a single ended cavity.

A model will now be developed to verify the effects of squashing on radiation pressure noise.

To begin, consider the situation shown in figure 5.2. This diagram shows a ring cavity, however the theory applies equally to ring and linear cavities. The notation of the fields has been kept consistent with the figure 5.1, so that the input field to the experiment is now labelled  $A_0$ . The input to the cavity is now  $A_{in,1}$ , while the output of the cavity is

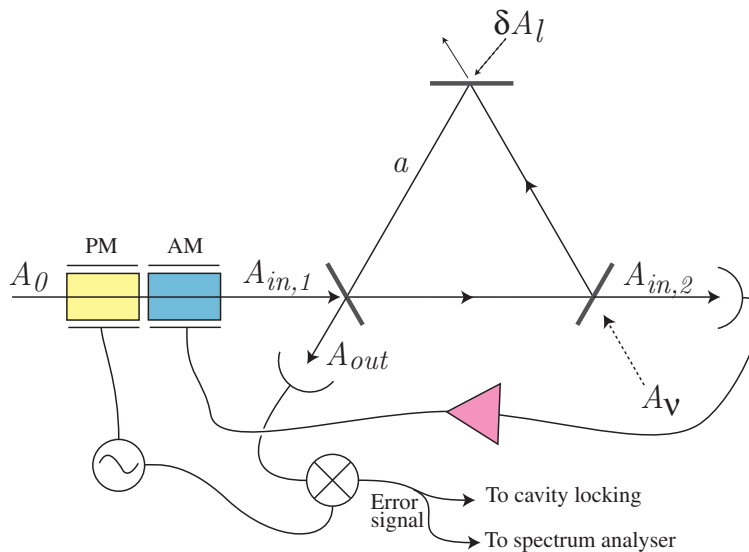


**Figure 5.2:** Feedback acting on the field inside a cavity. PM=phase modulator, AM= amplitude modulator

$A_{in,2}$ . (In the previous discussion of cavities in section 5.3, the input field to the cavity was  $A_{in}$  and the output was  $A_{out}$ .)

The transmitted field of the cavity is fed-back to the input field of the laser via an amplitude modulator. Also shown is the phase modulation and detection required for cavity locking. The feedback equations of section 5.2 must be modified to include the dynamics of the cavity. We start by using  $\delta X_{in,2}^+ = \sqrt{2\kappa_{out}}\delta X_a^+ - \delta X_\nu^+$  (equation 2.92) to rewrite equation 5.4 as

$$\delta X_r^+ = \sqrt{\eta}\bar{A}_{in,2} \int_0^T k(t) \left( \sqrt{\eta}(\sqrt{2\kappa_{out}}\delta X_a^+(t-\tau) - \delta X_\nu(t-\tau)) + \sqrt{1-\eta}\delta X_D^+(t-\tau) \right) dt \quad (5.32)$$

which Fourier transforms to

$$\delta \tilde{X}_r^+ = \sqrt{\eta}\sqrt{2\kappa_{out}}\alpha K(\omega) \left( \sqrt{\eta}(\sqrt{2\kappa_{out}}\delta \tilde{X}_a^+ - \delta \tilde{X}_\nu) + \sqrt{1-\eta}\delta \tilde{X}_D^+(t) \right) \quad (5.33)$$

with the substitution  $\bar{A}_{in,2} = \sqrt{2\kappa_{out}}\alpha$ . Using the Fourier transform of 5.2, together with equations 5.16, and 5.33 we may find the frequency domain fluctuations of the quadrature  $\delta \tilde{X}_a^+$  under the influence of feedback:

$$\begin{aligned} \delta \tilde{X}_a^+ &= \left[ \sqrt{2\kappa_{in}}H(\omega)\delta \tilde{X}_0^+ + \sqrt{2\kappa_l}H(\omega)\delta \tilde{X}_l^+ \right. \\ &\quad + \left( \sqrt{2\kappa_{out}} + \sqrt{2\kappa_{in}}G(\omega) \right) H(\omega)\delta \tilde{X}_\nu^+ \\ &\quad \left. + \sqrt{2\kappa_{in}}\sqrt{\frac{1-\eta}{\eta}}H(\omega)G(\omega)\delta \tilde{X}_D^+ \right] \left/ \left[ 1 + 2\sqrt{\kappa_{in}\kappa_{out}}G(\omega)H(\omega) \right] \right. \quad (5.34) \end{aligned}$$

where,

$$G(\omega) = \sqrt{2\kappa_{out}}, \alpha\eta K(\omega) \quad \text{and} \quad H(\omega) = \frac{1}{i\omega + \kappa}. \quad (5.35)$$

Comparing this result to standard results from control theory [29] we find that this system is unconditionally stable provided that  $G(\omega)$  is real and positive. In this derivation we have ignored the effect of time delays which can also compromise the stability of a feedback system. Time delays are not really an issue in this system as the important feedback frequencies are likely to be low ( $<10\text{kHz}$ ) compared to the very quick electronics ( $<1\mu\text{s}$ ) of the feedback loop. Evaluating the variance of the intra-cavity amplitude quadrature we find

$$V_a^+ = \frac{2\kappa_{in}|H(\omega)|^2V_0^+ + 2\kappa_l|H(\omega)|^2 + |\sqrt{2\kappa_{out}} + \sqrt{2\kappa_{in}}G(\omega)H(\omega)|^2 + 2\kappa_{in}\frac{1-\eta}{\eta}|H(\omega)G(\omega)|^2}{|1 + 2\sqrt{\kappa_{in}\kappa_{out}}G(\omega)H(\omega)|^2}. \quad (5.36)$$

When the gain is turned off, so that  $G(\omega) = 0$ , the cavity photon number fluctuations without feedback are found to be

$$V_a^+ = \frac{2\kappa_{in}V_0^+ + 2\kappa_l + 2\kappa_{out}}{\omega^2 + \kappa^2}. \quad (5.37)$$

The result with no feedback (equation 5.37) agrees with the spectrum that may be found directly from equation 5.16. The first thing to note about the spectrum of the cavity photon number without feedback is that it is very different to that expected for a free field. In particular as  $\omega$  becomes large, the spectrum goes to zero whereas (in the absence of squeezing) a free field is limited above one (i.e. the QNL) at all frequencies. This property

of the in-cavity field is a feature of the frequency domain operators. The usual Bosonic commutation relation (and uncertainty relation) is maintained only when integrating the frequency domain commutator of the intra-cavity field over all frequency modes of the cavity. An extensive discussion of this property, and the proof of the time domain commutator and uncertainty principle for fields inside a cavity, may be found in [56]. For our purposes, the QNL inside the cavity may be defined by assuming an ideal, quantum noise limited laser input to the cavity, i.e.  $V_0^+ = V_0^- = 1$ .

#### 5.4.1 Feedback reduces photon number noise in a cavity

The effect of feedback on the intra-cavity photon number noise will now be calculated. Typically, the resonant frequencies of the mirror system may be of the order of 1 to 100Hz, whereas the cavity linewidth will be no less than 100kHz. It is therefore reasonable to assume that the detuning frequencies of interest are all well inside the cavity linewidth, so that  $\omega \ll \kappa$ . This means that  $H(\omega) \rightarrow 1/\kappa$ . In the limit of high gain (Large positive  $G(\omega)$ ), the intra-cavity photon number noise given by equation 5.36 goes to

$$\lim_{G(\omega) \rightarrow \infty} V_a^+ = \frac{1}{2\eta\kappa_{\text{out}}}. \quad (5.38)$$

To find where this noise lies relative to the QNL, it may be compared to the performance of a cavity with no feedback and an ideal laser. Using  $V_0^+ = 1$  in equation 5.37 gives the QNL inside the cavity to be

$$V_a^+|_{\text{QNL}} = \frac{2}{\kappa}. \quad (5.39)$$

Dividing the noise with feedback (equation 5.38) by the quantum noise (equation 5.39) gives the normalised noise of the cavity photon number to be:

$$V_a^+|_{\text{norm}} = \frac{\kappa}{4\eta\kappa_{\text{out}}}. \quad (5.40)$$

In the case of a loss-free impedance matched cavity ( $\kappa = 2\kappa_{\text{out}}$ ) and ideal photodetection ( $\eta = 1$ ), the photon number noise of the intra-cavity field is a factor of two below the standard quantum limit. This is the desired result: the photon number fluctuations inside the cavity are indeed squashed by the feedback loop. The reduction in the photon number fluctuations mean that the radiation pressure noise is also suppressed by a factor of two below that expected for an ideal, coherent laser input (via equation 5.29).

A more general picture of the effect of feedback on the photon number fluctuations is shown in figure 5.3. This shows a plot of equation 5.40 as a function of the feedback detector efficiency,  $\eta$ , and the impedance matching of the vacuum  $\delta A_\nu$ . The impedance matching is expressed as  $(\kappa_{\text{in}} + \kappa_l)/\kappa_{\text{out}}$ , so that ‘1’ implies perfect impedance matching. The noise contours are in ‘dB’ compared to the quantum noise. The case of a factor of two reduction in photon number fluctuations with an impedance matched cavity is therefore seen at the point  $((\kappa_{\text{in}} + \kappa_l)/\kappa_{\text{out}} = 1, \eta = 1)$ . This figure shows that the performance of intensity noise suppression improves as the rear mirror becomes more transparent ( $\kappa_{\text{out}}$  becomes larger). This is intuitively correct: as the rear mirror disappears, the cavity mode is more similar to the field incident at the feedback detector, so the noise suppression inside the cavity is improved. Although a stronger reduction in the amount of radiation pressure noise would be achieved by using feedback with a less reflective rear mirror, it is not the optimum experimental configuration. As discussed in section 5.3.2, the disadvantage of

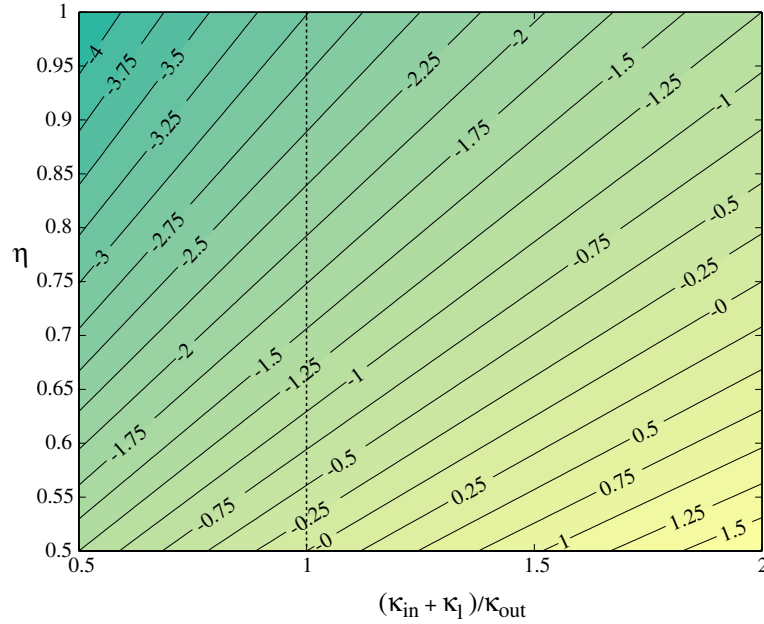


**Figure 5.3:** Contours of -in-cavity intensity noise as a function of  $\eta$  and impedance matching of the vacuum entering the back of the cavity,  $(\kappa_{\text{in}} + \kappa_l)/\kappa_{\text{out}}$ . The noise contours are in dB compared to the QNL inside the cavity.

having a less reflective rear mirror is that the input laser power is poorly coupled into the cavity and the detuning signal is not as strongly recorded on the reflected field. The optimal experimental configuration will be determined in the next section.

#### 5.4.2 What limits does this system beat?

A reduction in the amount of radiation pressure noise due to feedback will be apparent in the reflected phase noise spectrum given by equation 5.31. This means that the squashed in-loop noise has been coupled into an out-of-loop measurement. How is this possible given the nature of the in-loop fields described earlier? It turns out that this system relies on the QND-type coupling of the intra-cavity photon number to the phase quadrature of the reflected field. This coupling was suggested by Jacobs to be a possible method of making a QND measurement of the cavity photon number [65]. To make such a QND measurement would require radiation pressure noise to be the dominant source of cavity detuning. This might be achieved by using very light-weight mirrors and vast amounts of laser power in a high finesse cavity. The reflected phase noise spectrum will then be a faithful reproduction of the intra-cavity photon number fluctuations. In our case, the goal is to eliminate the effect of the radiation pressure noise, rather than use it to make a measurement. It is nevertheless the QND behaviour of the measurement made using the reflected phase quadrature that allows the squashing to benefit the thermal noise measurement scheme.

The radiation pressure noise has apparently been suppressed below the quantum limit. Does this mean that we have can make a better-than-the-quantum-limit measurement of the thermal noise without the use of squeezing? To check this we assume that the laser has quantum limited phase noise,  $V_{\text{in}}^- = 1$ , that we are looking at radiation pressure noise well within the cavity linewidth ( $\omega \ll \kappa$ ) and that the cavity is lossless ( $\kappa_l = 0$ ). We will

also ignore the difficulty of measuring the reflected phase noise spectrum, and assume that we can use a homodyne system to recover maximal phase information. In this case our thermal noise measurement (equation 5.31) becomes

$$V_{\text{ref}}^- = 1 + \frac{2\kappa_{\text{in}}\alpha^2}{\kappa^2}[\alpha^2 V_R + V_T]. \quad (5.41)$$

The effect of squashed intensity noise may be included by modifying the size of the radiation pressure noise contribution,  $V_R$ . If we allow perfect photodetection ( $\eta = 1$ ) then  $V_a^+$  drops by the factor  $\kappa/(4\kappa_{\text{out}})$ , so that we may substitute  $V_R$  with  $V_R\kappa/(4\kappa_{\text{out}})$  to give a thermal noise measurement with feedback of:

$$V_{\text{ref}}^- = 1 + \frac{2\kappa_{\text{in}}\alpha^2}{\kappa^2} \left[ \frac{\kappa}{4\kappa_{\text{out}}} \alpha^2 V_R + V_T \right]. \quad (5.42)$$

Comparing equations 5.41 and 5.42 shows that the amount of radiation pressure noise has been scaled by  $\kappa/(4\kappa_{\text{out}})$ . Now by taking equation 5.41 and making the substitutions:

$$\begin{aligned} \alpha^2 &\rightarrow \left( \frac{\kappa}{4\kappa_{\text{out}}} \right) \alpha^2 \\ \frac{\kappa_{\text{in}}}{\kappa^2} &\rightarrow \left( \frac{4\kappa_{\text{out}}}{\kappa} \right) \frac{\kappa_{\text{in}}}{\kappa^2}, \end{aligned} \quad (5.43)$$

we obtain equation 5.42. In other words, with a different choice of cavity mirrors and input power, a cavity without feedback may achieve the same sensitivity to thermal noise as a cavity with feedback. The feedback can break the quantum limit for a particular configuration, but the same result can be obtained with a different cavity and laser power without feedback assuming, of course, that the laser is at the QNL for both phase and amplitude noise. For example, the performance of a lossless impedance matched cavity ( $\kappa_{\text{in}} = \kappa_{\text{out}} = \kappa/2$ ) with feedback is replicated in a different cavity system by making  $\alpha^2$  a factor of two smaller and  $\kappa_{\text{in}}/\kappa^2$  a factor of two larger. The configuration that satisfies these conditions is a single ended cavity of the same linewidth as the impedance matched cavity and half the intra-cavity power. An ideal impedance matched cavity with feedback therefore provides identical performance to a fully reflective cavity with an ideal laser input, which as discussed in section 5.3.2, gives the theoretical best performance for detuning measurement. The impedance matched cavity is, however, easier to use in a real experiment as the reflected power is much lower.

The use of feedback breaks the quantum measurement limit for an impedance matched cavity, however this is not enough to make it the best possible detuning measurement technique. The work by Pace *et al.* [88] shows that the quantum limit to detuning measurements made with a single ended cavity may be broken by the use of squeezed light. The squeezing is injected into the single ended cavity with a quadrature angle chosen to give cancellation between the radiation pressure noise and the laser phase noise. The feedback system modelled here does not enter this measurement regime. The best possible performance of a feedback loop placed around an impedance matched cavity corresponds to a single ended cavity probed with an ideal coherent state.

To make use of squeezing in a single ended cavity one would need to use homodyne detection, not just locking signal detection, to measure the reflected phase quadrature. The reason is that the noise-floor of the locking signal includes a term that is proportional to the amount of reflected power. (This will be proved in section 5.5.) If one were to use

the locking signal to measure detuning, any advantage due to the squeezing would be more than cancelled out by the extra noise in the locking signal due to the large amounts of reflected power. As stated previously, large amounts of power are difficult to homodyne, so the single ended cavity with squeezing would be a difficult experiment.

### Summary

The results of this section may be summarised as follows: a fully reflective cavity is (in theory) best because all of the detuning signal is forced to leave via a single output coupler, therefore giving the best signal-to-noise. An impedance-matched cavity has two output couplers. This causes half the detuning signal to be lost.

By placing feedback around an impedance matched cavity it is possible to reduce the radiation pressure noise by a factor of two. The reduction in radiation pressure noise gives the impedance matched cavity the same sensitivity to thermal noise as a fully reflective cavity, with the practical advantages of an impedance matched system. These advantages are: 1) low power reflected field which makes phase measurement easier and; 2) A single ended cavity would require external feedback. This cannot push the laser noise down to the QNL. An impedance matched cavity inside a feedback loop has no such problem.

Finally, although the feedback system does break the quantum measurement limit for an impedance matched cavity, one can still do better by using squeezed light in a single ended cavity, provided homodyne detection is possible.

## 5.5 Detuning measurement via the cavity locking signal

We will now turn to a consideration of the measurement of the phase quadrature of the reflected field using the cavity locking signal. Experimentally this may be done in two ways. One is to use a high bandwidth frequency locking loop, so that the signal being used to control the cavity measures the forces acting on the mirrors. Although the motion of the mirrors is eliminated by the feedback, the signal still measures the thermal noise acting on the cavity. The second method is to use have a very narrow frequency locking bandwidth, so that the error signal above the locking bandwidth is a measurement of the actual mirror motion due to the thermal and radiation pressure noise. The theoretical model which follows does not distinguish between these two possibilities.

The derivation given here is similar to that of Jacobs *et al.* [64]. We start by writing the field before the phase modulator as

$$A = \bar{A} + \frac{1}{2}(\delta x^+ + i\delta x^-) + \delta A_q, \quad (5.44)$$

where  $\bar{A}$  is the classical field amplitude, and  $\frac{1}{2}(\delta x^+ + i\delta x^-)$  represents the classical noise of the laser. The spectrum of this noise is typically confined to a narrow frequency band around the laser carrier frequency.  $\delta A$  is the broadband quantum noise of the laser, which spans all frequencies. Assuming small phase modulation, so that higher order Bessel functions may be omitted, we find the phase modulated field to be

$$A_{\text{in}} = [\bar{A}_{\text{in}} + \frac{1}{2}(\delta x^+ + i\delta x^-)](1 + i2\epsilon \cos \gamma t) + \delta A_q, \quad (5.45)$$

where  $\gamma$  is the modulation frequency and  $\epsilon$  is the modulation depth. It is this field which is incident on the resonant cavity. The reflected field may be calculated by using the input-



output relations of equation 2.92 (namely  $A_{\text{ref}} = \sqrt{2\kappa_{\text{in}}}a - A_{\text{in}}$ ). The reflected cavity field is found to be

$$A_{\text{ref}} = \sqrt{2\kappa_{\text{in}}}(\alpha + \delta a) - [\bar{A}_{\text{in}} + \frac{1}{2}(\delta x^+ + i\delta x^-)][1 + i2\epsilon \cos \gamma t] - \delta A_q, \quad (5.46)$$

where  $a$  has been replaced by  $\alpha + \delta a$ . The photocurrent  $I$  generated in a detector of efficiency  $\eta$  may be derived as in equation 2.52 so that:

$$\begin{aligned} I = & \eta |\sqrt{2\kappa_{\text{in}}}\alpha - \bar{A}_{\text{in}} - i2\epsilon \cos \gamma t|^2 \\ & + \sqrt{\eta} [\sqrt{2\kappa_{\text{in}}}\alpha - \bar{A}_{\text{in}}] [\sqrt{2\kappa_{\text{in}}}\delta X_a^+ - \delta X_q^+ - \delta x^+] \\ & + 2i\epsilon \bar{A}_{\text{in}} \sqrt{\eta} \cos \gamma t \left[ \frac{\alpha}{\bar{A}_{\text{in}}} \sqrt{2\kappa_{\text{in}}}\delta x^- + (\delta X_q^- - \sqrt{2\kappa_{\text{in}}}\delta X_a^-) \right] + 4\bar{A}_{\text{in}}\epsilon^2 \cos^2 \gamma t \delta x^+ \\ & + \sqrt{1 - \eta} ([\sqrt{2\kappa_{\text{in}}}\alpha - \bar{A}_{\text{in}}] \delta X_D^+ + 2\epsilon \bar{A}_{\text{in}} \cos \gamma t \delta X_D^-). \end{aligned} \quad (5.47)$$

The first line of this equation is the DC current of the detector, and of no interest. The next 3 lines are the noise terms that contain the information we require. We may use the following substitutions to simplify equation 5.47:  $\bar{A}_{\text{ref}} = \sqrt{2\kappa_{\text{in}}}\alpha - \bar{A}_{\text{in}}$  is the classical amplitude of the reflected field,  $\delta X_{\text{ref}}^+ = \sqrt{2\kappa_{\text{in}}}\delta X_a^+ - \delta X_q^+ - \delta x^+$  is the amplitude quadrature fluctuation of the reflected field and  $\bar{A}_{\text{in}}\delta S = \frac{\alpha}{\bar{A}_{\text{in}}}\sqrt{2\kappa_{\text{in}}}\delta x^- + (\delta X_q^- - \sqrt{2\kappa_{\text{in}}}\delta X_a^-)$  is the part of the signal we wish to extract. The time dependant parts of equation 5.47 are therefore given by:

$$\begin{aligned} \delta I = & \sqrt{\eta} \bar{A}_{\text{ref}} \delta X_{\text{ref}}^+ \\ & + 2\epsilon \sqrt{\eta} \bar{A}_{\text{in}} \cos \gamma t \delta S + 4\bar{A}_{\text{in}}\epsilon^2 \cos^2 \gamma t \delta x^+ \\ & + \sqrt{1 - \eta} (\bar{A}_{\text{ref}} \delta X_D^+ + 2\epsilon \bar{A}_{\text{in}} \cos \gamma t \delta X_D^-). \end{aligned} \quad (5.48)$$

The next step in the derivation is to ‘mix down’ at the modulation frequency, so that the signal we are looking for appears as a fluctuation about 0Hz rather than a fluctuation about the modulation frequency. We do this by multiplying the last equation by  $\cos \gamma t$  to give:

$$\begin{aligned} \delta I_M = & \cos \gamma t \sqrt{\eta} \bar{A}_{\text{ref}} \delta X_{\text{ref}}^+ \\ & + 2\epsilon \sqrt{\eta} \bar{A}_{\text{in}} \cos^2 \gamma t \delta S + 4\bar{A}_{\text{in}}\epsilon^2 \cos^3 \gamma t \delta x^+ \\ & + \cos \gamma t \sqrt{1 - \eta} (\bar{A}_{\text{ref}} \delta X_D^+ + 2\epsilon \bar{A}_{\text{in}} \cos \gamma t \delta X_D^-), \end{aligned} \quad (5.49)$$

Expanding the cosine terms, we find:

$$\begin{aligned} \delta I_M = & \cos \gamma t \sqrt{\eta} \bar{A}_{\text{ref}} \delta X_{\text{ref}}^+ \\ & + \epsilon \sqrt{\eta} \bar{A}_{\text{in}} (1 + \cos 2\gamma t) \delta S + \bar{A}_{\text{in}}\epsilon^2 (3 \cos \gamma t + \cos 3\gamma t) \delta x^+ \\ & + \sqrt{1 - \eta} (\bar{A}_{\text{ref}} \cos \gamma t \delta X_D^+ + \epsilon \bar{A}_{\text{in}} (1 + \cos 2\gamma t) \delta X_D^-). \end{aligned} \quad (5.50)$$

Now taking the Fourier transform gives:

$$\begin{aligned} \delta \tilde{I}_M = & \sqrt{\eta} \bar{A}_{\text{ref}} \left[ \frac{1}{2} \delta \tilde{X}_{\text{ref}}^+(\omega + \gamma) + \frac{1}{2} \delta \tilde{X}_{\text{ref}}^+(\omega - \gamma) \right] \\ & + \epsilon \sqrt{\eta} \bar{A}_{\text{in}} \left[ \delta \tilde{S}(\omega) + \frac{1}{2} \delta \tilde{S}(\omega + 2\gamma) + \frac{1}{2} \delta \tilde{S}(\omega - 2\gamma) \right] \\ & + \bar{A}_{\text{in}}\epsilon^2 \left[ \frac{3}{2} \delta \tilde{x}^+(\omega + \gamma) + \frac{3}{2} \delta \tilde{x}^+(\omega - \gamma) + \frac{1}{2} \delta \tilde{x}^+(\omega + 3\gamma) + \frac{1}{2} \delta \tilde{x}^+(\omega - 3\gamma) \right] \end{aligned}$$

$$\begin{aligned}
& +\sqrt{1-\eta}[\bar{A}_{\text{ref}}(\frac{1}{2}\delta\tilde{X}_D^+(\omega+\gamma)+\frac{1}{2}+\delta\tilde{X}_D^+(\omega-\gamma))] \\
& +\sqrt{1-\eta}[\epsilon\bar{A}_{\text{in}}(\delta\tilde{X}_D^-(\omega)+\frac{1}{2}\delta\tilde{X}_D^-(\omega+2\gamma)+\frac{1}{2}\delta\tilde{X}_D^-(\omega-2\gamma))]. \tag{5.51}
\end{aligned}$$

Evaluating the spectral variance as  $\langle |\delta\tilde{I}_M|^2 \rangle$  we obtain:

$$V_{I_M} = \frac{1}{2}\bar{A}_{\text{ref}}^2 + \epsilon^2\bar{A}_{\text{in}}^2\eta[V_S(\omega) + \frac{1}{2}] + \frac{3}{2}(1-\eta)\epsilon^2\bar{A}_{\text{in}}^2. \tag{5.52}$$

where  $V_S$  is the spectrum of  $\delta\tilde{S}$ . To get this final equation, we have assumed that the modulation frequency,  $\gamma$ , is larger than than the maximum extent of the classical laser noise. This means that classical noise terms ( $\delta\tilde{x}^+$ ,  $\delta\tilde{x}^-$ ) at multiples of the modulation frequency evaluate to a variance of zero, while the terms that depend on the quantum noise ( $\delta\tilde{S}$ ,  $\delta\tilde{X}_{\text{ref}}^+$ , and  $\delta\tilde{X}_D^+$ ) give variance of 1 at these high frequencies. All that remains now is to evaluate the variance  $V_S$ . Firstly, the fluctuations ( $\delta\tilde{S}$ ) are given by

$$\begin{aligned}
\delta\tilde{S}(\omega) &= \frac{\alpha}{A_{\text{in}}}\sqrt{2\kappa_{\text{in}}}\delta\tilde{x}^- + (\delta\tilde{X}_q^- - \sqrt{2\kappa_{\text{in}}}\delta\tilde{X}_a^-) \\
&= \left(\frac{2\kappa_{\text{in}}}{\kappa}\delta\tilde{x}^- + \delta\tilde{X}_q^-\right) \\
&\quad - \frac{\sqrt{2\kappa_{\text{in}}}\alpha 2\delta\tilde{\Delta} + \sqrt{2\kappa_{\text{in}}}(\delta\tilde{X}_q^- + \delta\tilde{x}^-) + \sqrt{2\kappa_{\text{out}}}\delta\tilde{X}_\nu^- + \sqrt{2\kappa_l}\delta\tilde{X}_l^-}{i\omega + \kappa} \\
&= \frac{2\kappa_{\text{in}}i\omega\delta\tilde{x}^-}{\kappa(i\omega + \kappa)} \\
&\quad + \frac{\sqrt{2\kappa_{\text{in}}}\alpha 2\delta\tilde{\Delta} + (2\kappa_{\text{in}} - \kappa - i\omega)\delta\tilde{X}_q^- + 2\sqrt{\kappa_{\text{in}}\kappa_{\text{out}}}\delta\tilde{X}_\nu^- + 2\sqrt{\kappa_{\text{in}}\kappa_l}\delta\tilde{X}_l^-}{i\omega + \kappa}. \tag{5.53}
\end{aligned}$$

The variance then becomes

$$V_s = \frac{4\kappa_{\text{in}}^2\omega^2V_{cl}^-}{\kappa^2(\omega^2 + \kappa^2)} + \left(1 + \frac{8\kappa_{\text{in}}\alpha^2(\alpha^2V_R + V_T)}{\omega^2 + \kappa^2}\right), \tag{5.54}$$

where  $V_{cl}^-$  is the classical phase noise spectrum,  $\langle |\tilde{x}^-|^2 \rangle$ . Now, finally, the spectrum of the error signal may be written as:

$$V_{I_M} = \frac{1}{2}\bar{A}_{\text{ref}}^2 + \epsilon^2\bar{A}_{\text{in}}^2 \left( \eta \frac{4\kappa_{\text{in}}^2\omega^2V_{cl}^-}{\kappa^2(\omega^2 + \kappa^2)} + \eta \frac{8\kappa_{\text{in}}\alpha^2(\alpha^2V_R + V_T)}{\omega^2 + \kappa^2} + \frac{3}{2} \right). \tag{5.55}$$

The size of the thermal noise detuning ( $V_T$ ) appears in this expression. By comparing the size of the thermal noise signal to the other terms in this equation, the sensitivity of the locking signal to thermal noise may be calculated.

We can compare the locking signal sensitivity to that of homodyne detection with a coherent local oscillator, as derived in section 2.5.3. Using the reflected phase quadrature spectrum (equation 5.31) we find:

$$V_{\text{Hom}} = \eta\bar{A}_{LO}^2 \left( 1 + \eta \frac{2\kappa_{\text{in}}\alpha^2(\alpha^2V_R(\omega) + V_T(\omega)) + ((2\kappa_{\text{in}} - \kappa)^2 + \omega^2)(V_{cl}^-)}{\omega^2 + \kappa^2} \right), \tag{5.56}$$

where  $A_{LO}$  is the amplitude of the local oscillator and we have replaced  $V_{A_{\text{in}}}^- - 1$  with  $V_{cl}^-$ . The effect of the classical laser noise is seen to be different in the cases of homodyne

and modulation detection. With the locking signal, classical phase noise is not likely to be a problem because the thermal noise frequency is of the order of 10Hz compared to the cavity linewidth of about 1MHz. This means that  $\omega \ll \kappa$ , so that the classical phase noise term in equation 5.55 will be negligible. With the homodyne detection, on the other hand, classical phase noise only behaves this way for an impedance matched cavity.

A second difference between homodyne and locking signal detection is the quantum noise limit of the two systems. For an impedance matched cavity, the well loved ‘1’ of the quantum noise appears as usual in the homodyne detection system, compared to the ‘3/2’ for the locking signal. The origin of this difference is the quantum noise at twice the modulation frequency. This noise beats with the modulation sidebands at the modulation frequency and therefore appears in the DC output of the mixer. This is an experimentally observed effect known as “non-stationary shot noise” [83, 87]. Modulation-demodulation schemes more sophisticated than simple sine wave modulation may be used to overcome non-stationary shot noise [49, 83].

A third difference between locking detection and homodyne detection is the  $1/2 \bar{A}_{\text{ref}}$  term that appears in the locking signal. This only matters when the system is not impedance matched, so that  $\bar{A}_{\text{ref}}$  is non-zero. The origin of this term is the quantum noise of the reflected carrier field. It is this term which makes locking signal detection of cavity detuning a poor choice for reflective cavities.

## 5.6 Thermal noise spectra

It will be assumed that the cavity system is at room temperature. This means the thermal fluctuations of the mirror will be much greater than the quantum uncertainty in the mirror position, so that the mirror motion may be treated classically.

A suspended mirror in a cavity may be approximated as a pendulum. The calculation of the thermal noise spectrum of a pendulum may be attacked by considering an equation of motion that is a generalisation of Hook’s law [102]:

$$m\ddot{x} = -k(1 + i\phi)x + F(t) \quad (5.57)$$

where  $\phi$  is the loss angle of the system,  $x$  is the position of the pendulum,  $k$  is the spring constant,  $m$  is the mass and  $F(t)$  is the driving force of the pendulum. In general,  $\phi$  may be a function of time. For the case of a pendulum damped by internal friction, the loss angle is approximately constant [102]. This is the expected situation for the pendula we are considering, where the external damping (such as the viscous forces of the air) has been eliminated by placing the system in a vacuum. The Fourier transform of this equation gives

$$x(\omega) = \chi(\omega)\tilde{F}(\omega). \quad (5.58)$$

The mechanical susceptibility,  $\chi(\omega)$ , is given by

$$\chi(\omega) = \frac{1}{m(\omega_0^2 - \omega^2 - i\omega_0^2\phi)} \quad (5.59)$$

where  $\omega_0 = \sqrt{k/m}$  is the resonant frequency. This response is identical to the case of a viscously damped harmonic oscillator when  $\phi = \omega/(\omega_0 Q)$  [90] where  $Q$  is the quality factor of the pendulum. In our case we have a constant  $\phi$  so we may identify  $\phi = 1/Q$ .

This gives

$$\chi(\omega) = \frac{1}{m(\omega_0^2 - \omega^2 - i\omega_0^2/Q)}. \quad (5.60)$$

Next we consider the form of the thermal noise force of equation 5.24. Fluctuation-dissipation theorem [76] gives the spectrum of the driving force to be [43, 90]:

$$\langle |\delta\tilde{F}_T(\omega)|^2 \rangle = \frac{-4k_B T}{\omega} \Im \left( \frac{1}{\chi(\omega)} \right). \quad (5.61)$$

The spectrum of the detuning due to thermal noise is therefore given by

$$\begin{aligned} V_T(\omega) &= \left( \frac{2\pi c}{\lambda L} \right)^2 \langle |\delta\tilde{F}_T(\omega)|^2 \rangle |\chi(\omega)|^2 \\ &= \left( \frac{2\pi c}{\lambda L} \right)^2 \frac{4k_B T}{\omega} \frac{\omega_0^2}{Q} \frac{1}{m((\omega_0^2 - \omega^2)^2 + \omega_0^4/Q^4)}. \end{aligned} \quad (5.62)$$

The equation of the radiation pressure noise detuning spectrum comes from equation 5.29 to give:

$$\begin{aligned} V_R &= \left( \frac{2\pi c}{\lambda L} \right)^2 \left( \frac{2hc}{L\lambda} \right)^2 |\chi(\omega)|^2 V_a^+ \\ &= \left( \frac{2\pi c}{\lambda L} \right)^2 \left( \frac{2hc}{L\lambda} \right)^2 \frac{1}{m^2((\omega_0^2 - \omega^2)^2 + \omega_0^4/Q^4)} V_a^+. \end{aligned} \quad (5.63)$$

As noted by Saulson [102], there is a vital difference between the radiation pressure (equation 5.63) and thermal noise (equation 5.62) power spectra. At frequencies above the mechanical resonance,  $\omega_0$ , the thermal noise declines as  $\omega^{-5}$  whereas radiation pressure noise is proportional to  $\omega^{-4}$ . This means that the radiation pressure noise will be a more important effect as the frequency of interest becomes much larger than  $\omega_0$ .

To convert the locking signal spectrum to an expression for the cavity mirror motion, we look to equations 5.28 and 5.55. The factors that relate the displacement noise,  $\langle |\delta\tilde{x}|^2 \rangle$ , to the detuning locking signal,  $V_{I_M}$ , may then be extracted. The variance of the displacement can then be written as:

$$\langle |\delta\tilde{x}|^2 \rangle = \left( \frac{\lambda L}{2\pi c} \right)^2 \frac{\omega^2 + \kappa^2}{8\kappa_{\text{in}}\alpha^2\eta\epsilon^2\bar{A}_{\text{in}}^2} V_{I_M}. \quad (5.64)$$

Equation 5.55 can then be substituted into this expression to give the displacement noise  $\sigma_x$ :

$$\begin{aligned} \sigma_x &= \sqrt{\langle |\delta x|^2 \rangle} = \\ &= \frac{\lambda L}{2\pi c} \sqrt{\frac{2\kappa_{\text{in}}}{\kappa^2} \bar{A}_{\text{in}}^2 V_R + V_T + \frac{1}{\bar{A}_{\text{in}}^2} \left[ \left( 1 - \frac{\kappa}{2\kappa_{\text{in}}} \right) \frac{\omega^2 + \kappa^2}{4\epsilon^2\eta} + \frac{\omega^2 V_{cl}^-}{4} + \frac{3}{2} \frac{\kappa^2(\omega^2 + \kappa^2)}{16\kappa_{\text{in}}^2\eta} \right]} \end{aligned} \quad (5.65)$$

where the cavity field amplitude,  $\alpha$ , has been expressed in terms of the laser input amplitude  $\bar{A}_{\text{in}}$  (via  $\alpha = \bar{A}_{\text{in}}\sqrt{2\kappa_{\text{in}}/\kappa}$ ). The first two terms of equation 5.65 contain the signal due to actual displacement of the mirror due to thermal ( $V_T$ ) and radiation pressure ( $V_R$ ) noise. The remainder of the expression contains the noise terms due to classical laser phase noise and quantum noise sources which give apparent mirror displacement.

## 5.7 Thermal noise detection models

With inclusion of the mechanical response of the mirror pendulum in the thermal noise model, we may now plot the expected result of a thermal noise measurement using equation 5.65. We take the following parameters:

- Pendulum mechanical properties:  $m = 0.1\text{kg}$ ,  $Q = 10,000$ ,  $\omega_0 = 1\text{Hz}$  and temperature is 300K.
- Optical cavity properties: Cavity length = 1cm. Input mirror transmissivity  $t_{\text{in}} = 0.015\%$ , which gives  $\kappa_{\text{in}} = 2.25 \times 10^6 \text{s}^{-1}$ . Internal loss  $10^{-3} \%$  per round-trip, so that  $\kappa_l = 75,000 \text{s}^{-1}$ . For impedance matching we therefore require  $\kappa_{\text{out}} = 2.175 \times 10^6$ , so that  $t_{\text{out}} = 0.0145\%$ . Cavity finesse is therefore  $\mathcal{F} = 10500$ .
- Laser properties: wavelength  $\lambda = 1.064 \times 10^{-6}\text{m}$ , phase noise is at the quantum limit so that  $Vcl^- = 0$ , locking detection efficiency and feedback detection efficiency are ideal so that  $\eta = 1$ . Unless otherwise stated, the intensity noise is controlled via the feedback loop, so that the radiation pressure noise with these parameters is reduced by a factor of 2 below the QNL. The modulation sidebands contain 1% of the laser power, so that  $\epsilon^2 = 0.01$ .

We start by investigating the effect of laser power on thermal noise detection bandwidth. The laser power appears in the equations for the noise spectra through  $\bar{A}_{\text{in}}^2$ , which is the average number of photons incident on the cavity per second. The laser power is therefore given by

$$\text{Power} = \frac{hc}{\lambda} \bar{A}_{\text{in}}^2. \quad (5.66)$$

Using this relation, an impedance matched cavity with squashing feedback may be examined. Figure 5.4 shows two extremes of laser power. Trace (i) is the thermal noise, while all other traces show the noise sources that compete with thermal noise. For 10mW

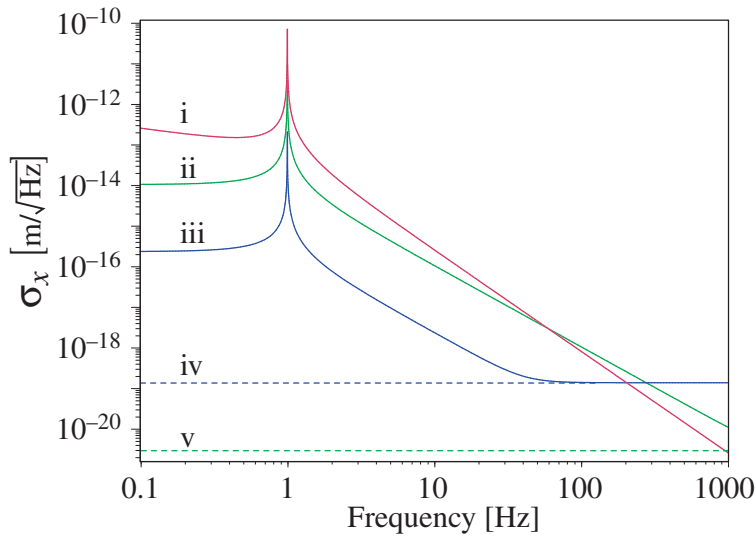


**Figure 5.4:** The thermal noise signal compared to other noise sources. i): Thermal noise; ii) Sum of radiation pressure and quantum noise with 20W input power; iii) Sum of radiation pressure and quantum noise with 10mW input power; iv) Quantum noise-floor with 10mW input power; v) Quantum noise-floor with 20W input power.

of laser power, the thermal noise (trace i) is easily detected over the radiation pressure noise (trace iii), but sinks into the quantum noise-floor (trace iv) at 200Hz. For high laser powers, the quantum noise-floor drops, but the radiation pressure noise becomes a problem. With 20W of laser power, the thermal noise (i) crosses the radiation pressure noise (ii) at 60Hz.

From figure 5.4, it is evident that the best laser power will be a compromise between avoiding radiation pressure noise and lowering quantum noise. We may find this optimum power by plotting the frequency at which the total noise-floor noise becomes equal to the thermal noise, as a function of the laser input power. That is, we solve

$$V_T - \left\{ \frac{2\kappa_{\text{in}}}{\kappa^2} \bar{A}_{\text{in}}^2 V_R + \frac{1}{A_{\text{in}}^2} \left[ \left( 1 - \frac{\kappa}{2\kappa_{\text{in}}} \right) \frac{\omega^2 + \kappa^2}{4\epsilon^2\eta} + \frac{\omega^2 V_{cl}^-}{4} + \frac{3\kappa^2(\omega^2 + \kappa^2)}{2 \cdot 16\kappa_{\text{in}}^2\eta} \right] \right\} = 0 \quad (5.67)$$

for  $\omega$  as a function of the input power  $A_{\text{in}}^2$ . The values of the frequency found in this solution correspond to the point at which the thermal noise may be detected with a signal-to-noise ratio of one. This will be referred to as the thermal noise detection bandwidth. Solutions to equation 5.67 are shown for a variety of thermal noise detection systems in figure 5.5. For each measurement configuration, the optimum laser power is the one that maximises the thermal noise detection bandwidth. These maxima are indicated by the lines shown on this plot. The best performance is achieved by the configuration of trace (i): an impedance matched cavity with squashed intensity noise. The maximum thermal noise detection bandwidth is 465Hz with 1.2W of laser input power. The other cases (traces ii to iv) all have inferior performance to the squashed system at every laser power. These traces correspond to other possible experimental configurations that will be considered in the following section. However one may already conclude that, no matter what laser power one has, an impedance matched cavity with squashing is always the best choice.

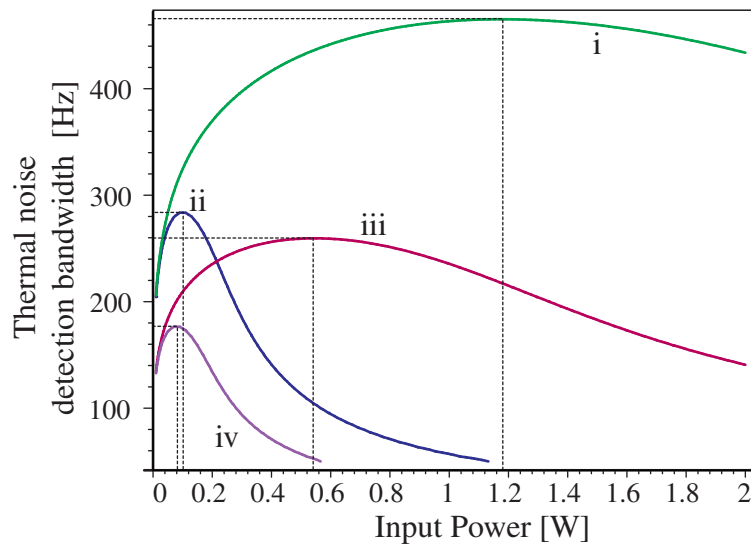


**Figure 5.5:** Finding the optimum input power to maximise the thermal noise detection bandwidth. i) Impedance matched cavity with squashing; ii) Impedance matching with laser 10 times above QNL; iii) Single ended cavity with laser at QNL; iv) Single ended cavity with laser 10 times above QNL

### 5.7.1 Impedance matched cavities with and without squashing.

The performance of the squashing setup may be compared to an impedance matched cavity with external feedback. We assume that 10% of the light is used to feedback to the laser, so that at best the laser intensity noise is 10dB above the QNL. In this case the best results are achieved by turning down the laser power to compensate for the increase in laser noise, as shown by figure 5.5 line (ii). The thermal noise detection bandwidth is reduced by 40% to 282Hz with a laser input power of 100mW. The noise spectra for this setup are shown in figure 5.6. The minimum measurable thermal noise displacement with squashing is  $5.0 \times 10^{-19} \text{m}/\sqrt{\text{Hz}}$  compared to  $9.3 \times 10^{-19} \text{m}/\sqrt{\text{Hz}}$  with external feedback.

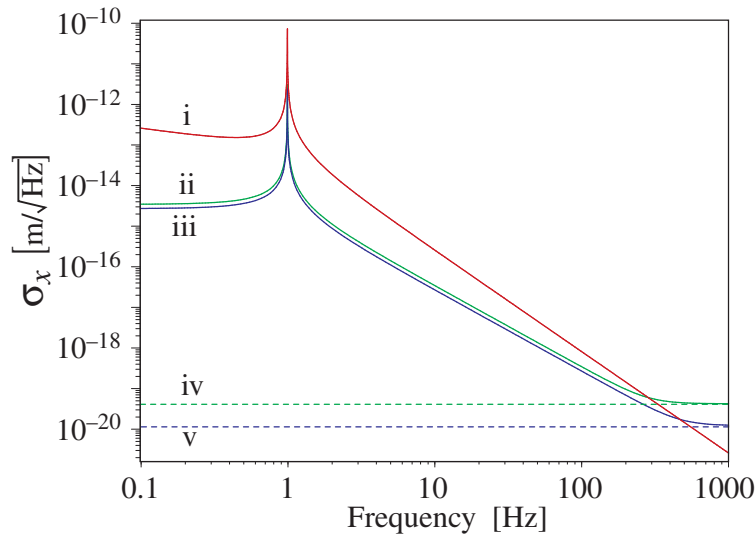


**Figure 5.6:** Detection of radiation pressure noise with optimised power. i) Thermal noise; ii) All other noise sources with 100mW of input power and input intensity noise 10 times the QNL. iii) All other noise sources with 1.2W of input power and intensity noise feedback; iv) Quantum noise-floor with 100mW of input power v) Quantum noise-floor 1.2W of input power

### 5.7.2 Reflective single ended cavities

The squashing/feedback system may also be compared to that of a single ended cavity, which as argued earlier, may achieve the same sensitivity to thermal noise. The equality in performance is, however, only achieved if the phase signal of the reflected field from the cavity is monitored using ideal homodyne detection and the laser used in the reflective cavity has phase and intensity noise at the QNL.

If the cavity motion is measured using the locking signal we have the situation shown in figure 5.7. The single ended cavity gives a maximum detection bandwidth of 260Hz with a laser input power of 0.54W, as determined from trace (iii) of figure 5.5. The minimum measurable thermal noise displacement in this configuration is  $1.3 \times 10^{-18} \text{m}/\sqrt{\text{Hz}}$ . The reduced detection performance of the single ended cavity is due to the large amount of reflected power that is incident on the locking detector. This was shown in section 5.5 to be a source of additional detection noise. In this model it is also assumed that the laser intensity noise is at the QNL. This is somewhat unrealistic because a single ended cavity configuration would use external laser intensity feedback which, as shown in section 5.2.2, cannot suppress the intensity noise to the QNL.

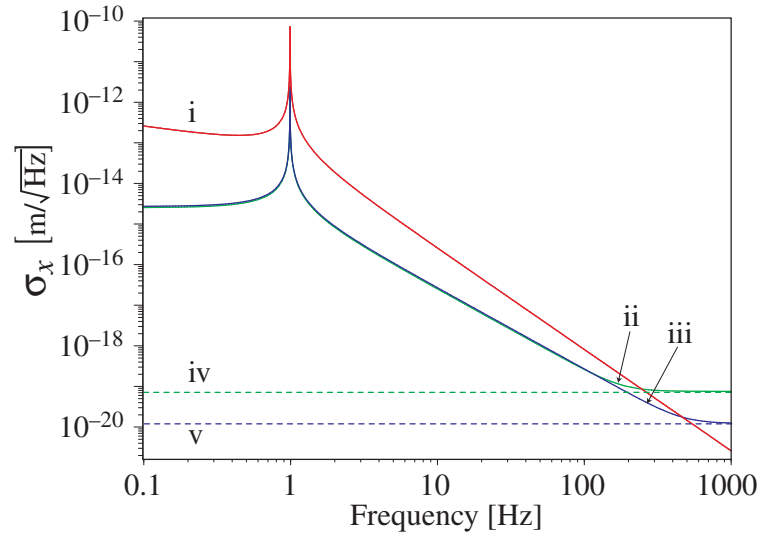


**Figure 5.7:** Thermal noise detection with feedback and an impedance matched cavity compared to a fully reflective cavity. The parameters for the reflective cavity which vary from the impedance matched case are  $\kappa_{\text{in}} = \kappa = 4.5 \times 10^6$  and laser input power = 0.54W. Traces are: i) thermal noise; ii) Sum of other noise sources for reflective cavity; iii) Sum of other noise sources for impedance matched cavity with feedback; iv) Quantum noise-floor for the reflective cavity; v) Quantum noise-floor for impedance matched cavity with feedback.

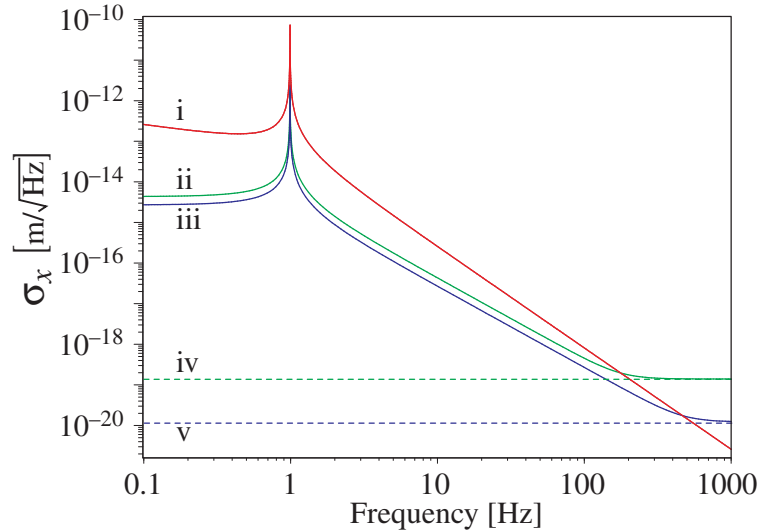


**Figure 5.8:** Thermal noise detection with feedback on an impedance matched cavity compared to a fully reflective cavity. The parameters for the reflective cavity which vary from the impedance matched case are  $\kappa_{\text{in}} = \kappa = 4.5 \times 10^6$ , laser intensity noise is 10 times the QNL and laser input power = 80mW. Traces are: i) thermal noise; ii) Sum of other noise sources for reflective cavity ; iii) Sum of other noise sources for impedance matched cavity with feedback; iv) Quantum noise-floor for reflective cavity; v) Quantum noise-floor for impedance matched cavity with feedback.



A more realistic reflective cavity situation is shown in figure 5.8. Here we assume that the input laser has intensity noise 10 times the QNL. The laser power must be reduced to 80mW to obtain the maximum possible bandwidth of 176Hz, as found from trace (iv) of figure 5.5. The minimum measurable thermal noise displacement is now  $9.0 \times 10^{-18} \text{m}/\sqrt{\text{Hz}}$

The results for all the different cavity configurations are summarised in table 5.1.

Configuration	Thermal noise detection bandwidth (Hz)	Thermal noise sensitivity ( $\text{m}/\sqrt{\text{Hz}}$ )	Required laser power (mW)
Impedance matched cavity, squashing feedback	465	$5.0 \times 10^{-19}$	1200
Impedance matched cavity, 10% external feedback	282	$9.3 \times 10^{-19}$	100
Single ended cavity, QNL laser	260	$1.3 \times 10^{-18}$	540
Single ended cavity, 10% external feedback	176	$9.0 \times 10^{-18}$	80

**Table 5.1:** Summary of thermal noise detection models.

## 5.8 Conclusions

This work has shown that placing a feedback loop around a thermal noise measurement experiment has the potential to reduce the radiation pressure noise to a level much lower than would be possible with an external feedback loop. In the case of an ideal impedance matched cavity as the thermal noise source, the squashing system may provide a level of radiation pressure noise that is a factor of two below the radiation pressure noise due to an ideal quantum noise limited laser. This proves that the squashed light inside a feedback loop can reduce quantum measurement noise.

Theoretically, the best signal-to-noise for thermal noise detection is achieved in a single ended cavity, rather than an impedance matched cavity. The single ended cavity is, however, a very difficult system to manage experimentally due to the large amounts of reflected power. The net effect of squashing is to convert an impedance matched cavity into a system that has the signal-to-noise of a single ended cavity, without the large amounts of reflected power.

Detailed modelling of a thermal noise measurement made using the cavity locking signal shows that the best thermal noise detection bandwidth is always achieved by using an impedance matched cavity with squashing.

---

# Second harmonic generation

---

The tilt-locking method presented in the introductory theory chapter is a modulation free technique. This is an advantage in optical harmonic generation where modulation sidebands may take part in the nonlinear process, therefore leading to a noisy harmonic spectrum. In this chapter, tilt-locking is applied to a second harmonic generation cavity to produce a modulation free second harmonic wave. The second harmonic generator is required as the pump source for the optical parametric amplifier discussed in chapter 7. The chapter begins with a general discussion of three-wave mixing and optimisation of second harmonic generation systems.

This work has been published as “Modulation-free control of a continuous-wave second-harmonic generator”, D.A. Shaddock, B.C. Buchler, W.P. Bowen, M.B. Gray and P.K. Lam, *J. Opt. A* **2**, 400 (2000).

## 6.1 Introduction

Optical second harmonic generation (SHG) was first achieved by Franken *et al.* in 1961 [35]. They used a quartz crystal pumped by a pulse from a ruby laser at 694nm. The conversion efficiency achieved was approximately  $2 \times 10^{-6}$  %, resulting in an output pulse of  $6 \times 10^{-8}$  J. Since this time, SHG has become an important and far more efficient process. Many high power commercial lasers with emission in the visible regime are in fact solid state infra-red lasers which have been frequency doubled (for example the 10W “Verdi” manufactured by Coherent). Conversion efficiencies of continuous wave (cw) systems are now as high as 89% [105]. The 532nm radiation generated by frequency doubled Nd:YAG lasers is also used as a frequency standard when locked to an iodine transition [33, 60].

In our laboratory, frequency doubled Nd:YAG radiation is used as the pump source for the optical parametric amplifier of chapter 7. We therefore have an interest in building stable, high efficiency cw SHG systems. In the following section, the basic requirements of a second harmonic generator are outlined. This is followed by a detailed theory of cavity second harmonic generation in section 6.3 and a discussion of locking techniques in section 6.4. The remainder of the chapter presents results from our experiment that compared the performance of modulation locking and tilt-locking.

## 6.2 Requirements of a frequency doubler

### 6.2.1 Nonlinear susceptibility

Second harmonic generation is the conversion of energy at frequency  $\Omega$  to the new frequency  $2\Omega$  (see figure 6.1). SHG is typically done inside a crystalline material. An obvious

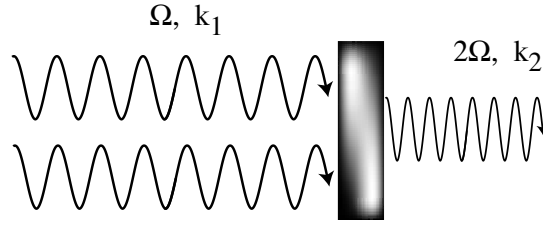


**Figure 6.1:** Frequency doubling.

question is: what qualities are required in a crystal to enable efficient second harmonic generation? The electric polarisation  $\mathcal{P}$  of a crystal describes the response of the outer valence electrons in the lattice to an electric driving force,  $E$ , via the equation [101]

$$\mathcal{P} = \epsilon_0(\chi^{(1)}E + \chi^{(2)}E^2 + \chi^{(3)}E^3 \dots). \quad (6.1)$$

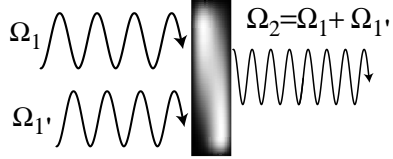
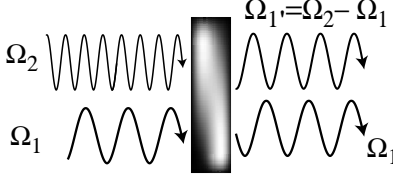
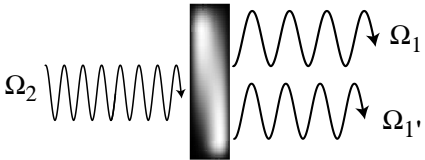
The  $\chi$  terms describe the strength with which the crystal material responds to the different exponential powers of the optical driving field. The first term,  $\chi^{(1)}$ , is related to the refractive index by  $n = \sqrt{1 + \chi^{(1)}}$ , so that for a typical material  $\chi^{(1)} \sim 1$ . The terms  $\chi^{(n)}$ , where  $n > 1$ , are the  $n^{\text{th}}$  order nonlinear susceptibilities. A material with strong second order susceptibility has  $\chi^{(2)} \sim 10^{-10} - 10^{-13} \text{mV}^{-1}$ . Reasonable third order susceptibilities are around  $10^{-18} - 10^{-23} \text{m}^2 \text{V}^{-2}$ . Second harmonic generation relies on the  $\chi^{(2)}$  of the material. To see why this is, consider the case of a crystal driven by an electric field  $\cos \Omega t$ . The second order susceptibility will give rise to a polarisation term proportional to  $\cos^2 \Omega t$  which oscillates at a frequency  $2\Omega$ . The component of the electron motion in the  $2\Omega$  mode will therefore give rise to a propagating electric field with frequency  $2\Omega$ . The small size of  $\chi^{(2)}$  means that for a substantial nonlinear effect, the size of the input electric field must be very large to induce a significant proportion of the polarisation vector, and hence optical output, in the  $2\Omega$  mode.

Over the years, people have used a variety of methods to concentrate optical power in SHG materials. Pulsed laser systems, where the peak power in the laser pulses give very intense fields, yield conversion efficiencies of up to 65% [74]. When a cw second harmonic field is required, it is possible to get some amount of conversion by strong focussing of the light into the crystal. However, if high efficiency cw SHG is required, then intra-cavity SHG is the best choice. This may be done internally, where the nonlinear crystal is included inside the laser cavity, or externally, where a pump laser is mode-matched and locked to a cavity containing a nonlinear crystal. External cavity SHG has been demonstrated with efficiencies up to 89% [105]. Our SHG is required as the pump source for an optical parametric amplifier (see chapter 7). The design of the OPA means we need about 300mW of cw light at 532nm. As a resource, we have a cw 700mW laser at 1064nm laser. External cavity SHG is therefore the only system which meets our power requirements, given the laser we have available.

### 6.2.2 Phase matching

Having a strong second order susceptibility and high laser intensity is not enough to ensure efficient SHG. Another requirement is conservation of photon momentum through the conversion process [11]. In non-linear optics, momentum conservation is often referred to as phase matching, for reasons that will become apparent shortly.

In general, SHG is a special case of three-wave mixing. Three-wave mixing describes a wide range of processes, all governed by the same fundamental equations. The different categories of three-wave mixing are shown in figure 6.2. The only process, other than SHG, investigated in this thesis is degenerate optical parametric amplification (DOPA), in chapter 7.

- Sum frequency generation: combination of 2 low energy photons ( $\Omega_1, \Omega_{1'}$ ) into a single high energy photon ( $\Omega_2 = \Omega_1 + \Omega_{1'}$ ). When  $\Omega_1 = \Omega_{1'}$ , this is SHG. 
- Optical parametric amplifier: A low energy photon ( $\Omega_1$ ) and a high energy photon ( $\Omega_2$ ) give the difference energy  $\Omega_{1'} = \Omega_2 - \Omega_1$ . An additional photon is also generated at  $\Omega_1$ . The case of  $\Omega_1 = \Omega_{1'}$  is the degenerate OPA (DOPA). 
- Optical parametric oscillation (OPO): A single high energy photon ( $\Omega_2$ ) converting to two lower frequency photons ( $\Omega_1 + \Omega_{1'} = \Omega_2$ ). The case of  $\Omega_1 = \Omega_{1'}$  is the degenerate OPO (DOPO). 

**Figure 6.2:** Three-wave mixing processes.

Every field of frequency  $\Omega_j$  in figure 6.2 will have a corresponding wave vector  $\mathbf{k}_j$ . In all cases, momentum conservation requires

$$\mathbf{k}_2 = \mathbf{k}_1 + \mathbf{k}_{1'}. \quad (6.2)$$

For SHG and DOPA,  $\mathbf{k}_{1'} = \mathbf{k}_1$ , as the low frequency fields are degenerate. Rewriting the  $\mathbf{k}_j$  vectors in terms of the refractive indices,  $n_j$ , of the interaction region, taking the degenerate case of SHG, and assuming that the modes of the field propagate colinearly, we find that momentum conservation places constraints on the refractive index of the optical material for the fundamental and second harmonic frequencies:

$$\frac{n_2 \Omega_2}{c} = 2 \frac{n_1 \Omega_1}{c}. \quad (6.3)$$

For SHG and DOPA,  $\Omega_2 = 2\Omega_1$ , which means

$$n_2 = n_1. \quad (6.4)$$

The result simply implies that the fundamental and second harmonic modes must propagate at the same speed through the crystal. This is the origin of the term ‘phase matching’. If the waves get out of step in the crystal, then the conversion process is no longer effective. SHG can still occur when this condition is not perfectly satisfied, but only at the expense of efficiency and beam quality. The phase mismatch,  $\Delta k$ , is used to quantify the degree of mismatch in a nonlinear system, and is given by

$$\Delta k = k_2 - 2k_1. \quad (6.5)$$

Phase matching can be achieved in various ways depending on the crystal type. In the absence of an electronic resonance in the nonlinear crystal (which may lead to anomalous dispersion), normal dispersion means that the refractive index of the material will simply increase with increasing frequency. For a single polarisation, the refractive index condition (equation 6.4) will not be achievable. This problem can often be overcome by using the birefringence of nonlinear media. If the second harmonic is aligned with the fast axis of the crystal and the fundamental is aligned with the slow axis, it may be possible for the birefringence to cancel with the dispersion. This is known as ‘type I’ phase matching. Unless you are extremely lucky, the phase matching will not automatically be satisfied by choosing the correct polarisations of the optical waves. The crystal still needs to be tuned to obtain exact phase matching. In our experiments, we use magnesium oxide doped lithium niobate (MgO:LiNbO<sub>3</sub>). The refractive index of this crystal is strongly dependant on the temperature, so that controlling the temperature of the crystal is an excellent method for achieving type I phase matching. The temperature and wavelength dependence of the phase matching condition for MgO:LiNbO<sub>3</sub> is described by the Selmeier equation [32]

$$\Delta k = -8666\left(1 - \frac{\lambda_0}{\lambda}\right) + 7.49(T - T_0) \quad (6.6)$$

where  $\lambda$  is the pump wavelength,  $T$  is the crystal temperature in °C,  $\lambda_0 = 1064\text{nm}$  and  $T_0 = 107.05^\circ\text{C}$ . To know exactly what effect the phase mismatch has on the efficiency of second harmonic generation, we note that the power of the second harmonic output beam,  $P_{2\Omega}$  (for a single pass through the crystal), is given by [11]

$$P_{2\Omega} = P_{2\Omega}^{\max} \times \text{sinc}^2(\Delta k z / 2) \quad (6.7)$$

where  $z$  is the length of the interaction and  $P_{2\Omega}^{\max}$  is the maximum second harmonic power, which depends on experimental details such as crystal quality, pump power and beam focussing. Using the previous 2 equations we may plot a graph of conversion efficiency as a function of the phase matching (figure 6.3). This shows the efficiency of the degenerate process to be greatest at  $107.05^\circ\text{C}$ . As the temperature increases beyond this point, the phase matching of the crystal favours a non-degenerate interaction, as indicated by the double humped structure.

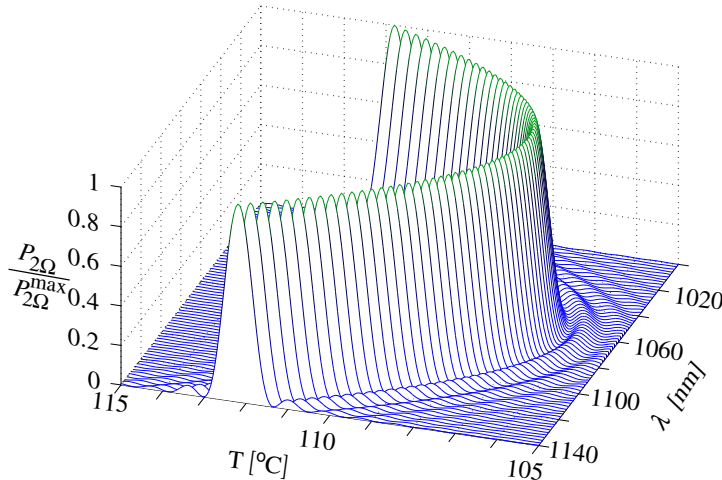


**Figure 6.3:** Harmonic conversion efficiency as a function of temperature and wavelength

### 6.3 Equations of cavity SHG

The equations of SHG and DOPA inside an optical cavity will now be developed. In this chapter,  $\chi^{(2)}$  interactions are only considered in the classical regime. However the parametric amplification process used to generate squeezing in chapter 7 requires a quantum treatment. Since the two processes are governed by identical equations, the quantum model will be developed here so that it may be used again later. The classical equations may be found quite easily from the quantum model.

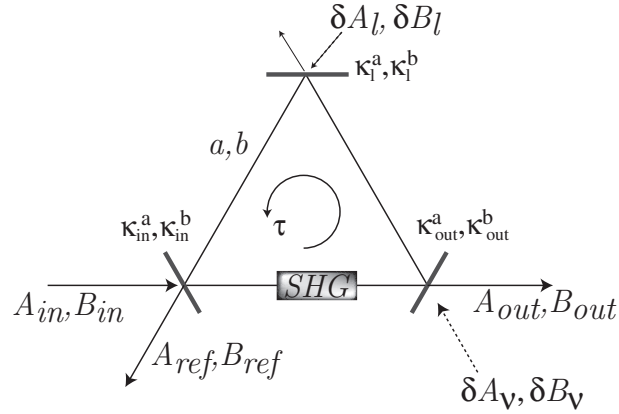


**Figure 6.4:** The inputs and outputs of a quantum model for SHG and parametric amplification

We will again use the quantum Langevin treatment to model the system (see section 2.6). The reversible Hamiltonian has a term  $\hbar\Omega_1 a^\dagger a$  for the fundamental mode, a term  $\hbar\Omega_2 b^\dagger b$  for the harmonic mode, and terms to describe the swapping of photons between these modes, so that  $H_{rev}$  is given by [117]

$$H_{rev} = \hbar\Omega_1 a^\dagger a + \hbar\Omega_2 b^\dagger b + \frac{i\hbar\epsilon}{2}(a^{\dagger 2} b - a^2 b^\dagger). \quad (6.8)$$

The coefficient  $\epsilon$  is the coupling strength between the fundamental and harmonic modes. This depends on the second order susceptibility  $\chi^{(2)}$ , as well as all the experimental realities such as beam focussing, crystal imperfections and phase matching.

The interaction of the cavity with the rest of the universe is dictated by the fluctuation ( $\delta$ ) input terms shown in figure 6.4<sup>1</sup>. These terms are just those we had in the cavity derivation of section 2.7, except that the terms are duplicated to account for the fundamental and harmonic modes of the cavity. The equations of motion for the cavity modes may then be obtained through the quantum Langevin equation as:

$$\begin{aligned} \dot{a} &= -\kappa_a a + \epsilon a^\dagger b + \sqrt{2\kappa_{in}^a} A_{in} + \sqrt{2\kappa_{out}^a} \delta A_\nu + \sqrt{2\kappa_l^a} \delta A_l \quad \text{and} \\ \dot{b} &= -\kappa_b b - \frac{\epsilon}{2} a^2 + \sqrt{2\kappa_{in}^b} B_{in} + \sqrt{2\kappa_{out}^b} \delta B_\nu + \sqrt{2\kappa_l^b} \delta B_l. \end{aligned} \quad (6.9)$$

At this stage, input power to the cavity has been assumed at both the fundamental mode ( $A_{in}$ ) and the harmonic mode ( $B_{in}$ ). For the case of an SHG, we will have no power in the mode  $B_{in}$  so this will reduce to the vacuum term  $\delta B_{in}$ .

Considering for the moment just the classical dynamics of these equations, we can

<sup>1</sup>This figure shows a ring cavity, however the equations derived here are equally valid for a linear cavity.

ignore all the fluctuation operators. The remaining operators are replaced with their expectation values, so that  $b \rightarrow \beta$  and  $a \rightarrow \alpha$ . We also assume that the value of  $\alpha$  is real. The classical equations for SHG are therefore given by

$$\begin{aligned}\dot{\alpha} &= -\kappa_a \alpha + \epsilon \alpha \beta + \sqrt{2\kappa_{\text{in}}^a} A_{\text{in}} \\ \dot{\beta} &= -\kappa_b \beta - \frac{\epsilon}{2} \alpha^2.\end{aligned}\quad (6.10)$$

The output coupling,  $\kappa_{\text{out}}^b$ , is generally chosen to be very large to ensure that the harmonic light escapes efficiently from the cavity. This situation, where the pump is in a strong cavity and the harmonic wave is in a weak cavity, is commonly described as ‘singly resonant SHG’. The alternative is ‘doubly resonant SHG’, where the harmonic light is also contained in a strong cavity.

Strong harmonic wave output coupling means that the total harmonic cavity loss rate,  $\kappa_b$ , will be dominated totally by the output mirror, so that  $\kappa_b \approx \kappa_{\text{out}}^b$ . The pump cavity will be quite strong, as required for good concentration of the pump power in the crystal, therefore implying the condition  $\kappa_b \gg \kappa_a$ . This disparity between the two cavity decay rates means that the evolution of the harmonic mode will be rapid compared to the evolution of the pump mode. The pump mode is therefore insensitive to the rapid motion of the harmonic mode. This allows the adiabatic elimination of  $\beta$  [86, 125]. In other words, on the time-scales relevant to  $\alpha$ , it is possible to assume  $\dot{\beta} \approx 0$ . When used in equations 6.10, this gives

$$\dot{\alpha} = -\left(\kappa_a + \frac{\epsilon^2 \alpha^2}{2\kappa_b}\right) \alpha + \sqrt{2\kappa_{\text{in}}^a} A_{\text{in}}. \quad (6.11)$$

The decay rate of the cavity has been increased compared to the case of the empty cavity by the new term  $\epsilon^2 \alpha^2 / (2\kappa_b)$ . This is the nonlinear loss of the fundamental mode due to the coupling of energy into the harmonic mode.

To find the steady state output of the SHG system, we set  $\dot{\alpha}$  to zero. Using the cavity boundary conditions (equation 2.92) we obtain

$$\frac{\epsilon^2 \alpha^3}{2\kappa_b} + \kappa_a \alpha - \sqrt{2\kappa_{\text{in}}^a} A_{\text{in}} = 0 \quad (6.12)$$

$$\beta = -\frac{\epsilon \alpha^2}{2\kappa_b} \quad (6.13)$$

$$B_{\text{out}} = \sqrt{2\kappa_{\text{out}}^b} \beta \quad (6.14)$$

which may be solved for the harmonic output amplitude,  $B_{\text{out}}$ , as a function of the input fundamental amplitude  $A_{\text{in}}$ . Assuming that  $\kappa_b^{\text{out}} = \kappa_b$ , a condition which is satisfied by the weak harmonic cavity, we find

$$B_{\text{out}} = \frac{\epsilon \alpha^2}{\sqrt{2\kappa_b}}, \quad (6.15)$$

where  $\alpha$  is found as a function of the input amplitude,  $A_{\text{in}}$ , from the solution to the cubic equation 6.12. The conversion efficiency of the cavity is the power of the harmonic output divided by the power of the fundamental input:

$$\text{Efficiency} = \frac{(\hbar\Omega_2) B_{\text{out}}^2}{(\hbar\Omega_1) A_{\text{in}}^2} = \frac{2B_{\text{out}}^2}{A_{\text{in}}^2} \quad (\text{Using } \Omega_2 = 2\Omega_1) \quad (6.16)$$

Experiments with MgO:LiNbO<sub>3</sub> have shown that the value of  $\epsilon$  may be  $\sim 6000$  [119]. This figure may be used in the above equations to find the cavity mirrors that optimise second harmonic generation efficiency. For the OPA system of chapter 7, we have 700mW of ‘red’ light at 1064nm, about 650mW of which can be spared to pump the SHG cavity. The output of the system is some amount of ‘green’ harmonic light at 532nm. The SHG cavity is designed to be ‘single ended’. In other words, the values of  $\kappa_{out}^a$  and  $\kappa_{out}^b$  are made as small as possible by using a high reflectivity coating. The parameter to be varied is the reflectivity of the input coupler which determines  $\kappa_{out}^a$ . A plot of the efficiency of the SHG for different input mirrors is shown in figure 6.5. This suggests that a 94% reflective input coupler is the right choice for our SHG system.

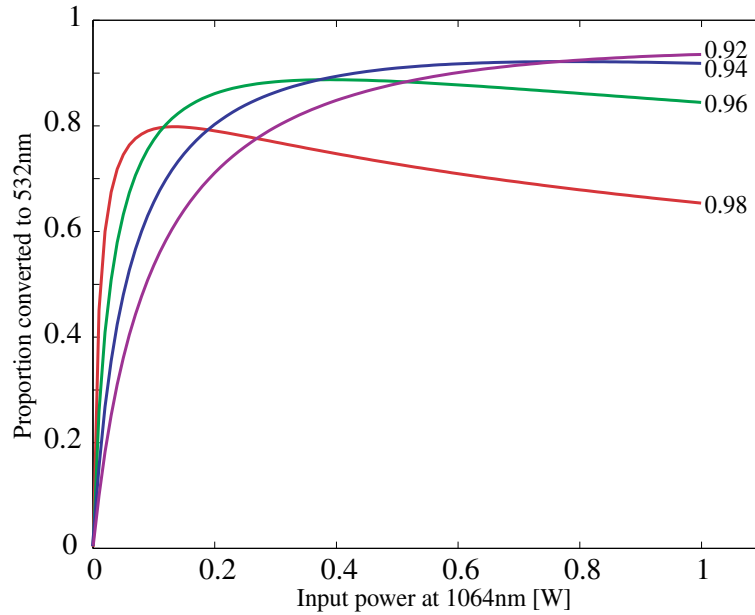


**Figure 6.5:** Plot of conversion efficiency for different input/output couplers, labelled by the reflectivity. The value of  $\kappa_{in}^a$  is calculated using equation 2.90. Other parameters are input mirror harmonic reflectivity of 10% and internal red loss of 0.1% per centimetre. This gives:  $\kappa_b = 2.6 \times 10^9$ , and  $\kappa_a = \kappa_{in}^a + 9.4 \times 10^6$ . Also assumed is  $\epsilon = 6000$ .

## 6.4 Locking cavity SHG

### Modulation locking

Successful intra-cavity SHG requires the cavity to be locked on resonance with the pump laser. Methods for locking were introduced in section 2.8. Typically SHG cavities have been locked via a modulation technique [3, 66, 71, 105]. This may be done using external modulation, by phase modulating the pump beam, or internal modulation, where the electro-optic effect of the SHG crystal is used to generate a cavity length modulation. In the case of intra-cavity modulation, the modulation frequency must be within the cavity linewidth, otherwise the modulation will be lost inside the cavity. The modulation applied to the cavity will be subject to the  $\chi^{(2)}$  interaction, just like the carrier frequency, so the second harmonic output will also be modulated.

To avoid modulation of the second harmonic, external modulation may be an answer. However SHG cavities tend to be short and of low finesse ( $F \sim 100$ ) so that the linewidths



are typically quite broad ( $\sim 100\text{MHz}$ ). High frequency external modulation is therefore necessary to prevent the modulation sidebands from entering the cavity. A major factor in favour of intra-cavity modulation is the cost saving achieved by eliminating a high speed external modulator.

A closer examination of intra-cavity modulation shows that the nonlinearity of the system will lead to a veritable forest of sidebands about the second harmonic carrier. Only the first order interactions (Those which involve a carrier either at the fundamental or the second harmonic) are shown in figure 6.6, for a modulation frequency of  $\gamma$ . Definitions of the acronyms in this figure may be found in figure 6.2.

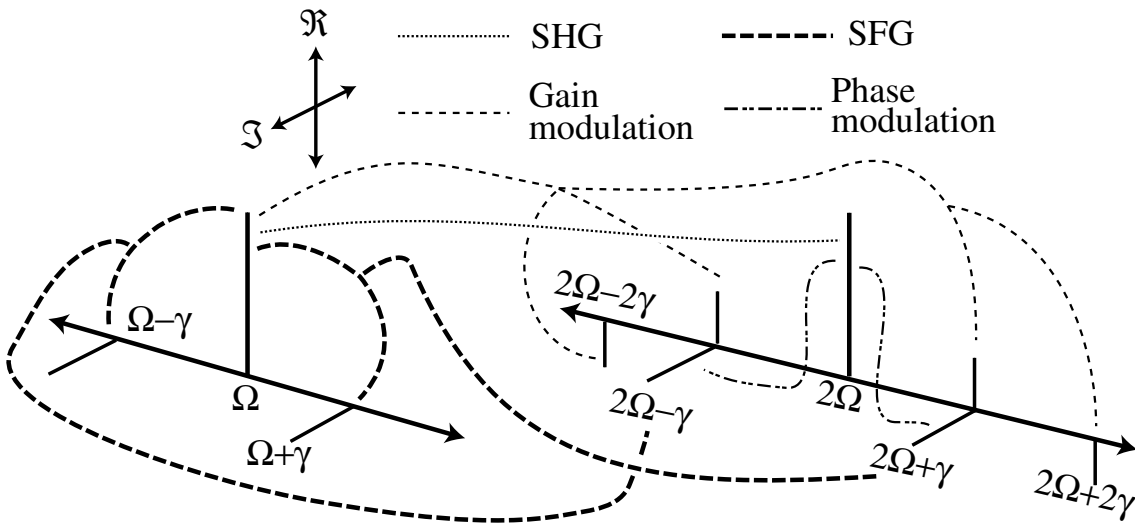


**Figure 6.6:** Sidebands generated in the second harmonic by cavity modulation at frequency  $\gamma$ .

The possible interactions in the cavity are:

- The electric field across the cavity will give direct phase modulation of the harmonic wave, giving phase sidebands at  $2\Omega \pm \gamma$ .
- The phase sidebands on the fundamental mode,  $A_s e^{i(\Omega \pm \gamma)t + i\pi/2}$ , will interact with the carrier,  $A_c e^{i\Omega t}$ , via sum frequency generation (SFG) to give phase sidebands ( $\propto A_s A_c e^{i(2\Omega \pm \gamma)t + i\pi/2}$ ) at frequencies  $2\Omega \pm \gamma$  on the second harmonic wave .
- Modulation of the electric field across the crystal modulates both the resonance condition of the cavity and the phase matching condition, since the electric field does not act symmetrically on the fundamental and harmonic modes, which are orthogonally polarised. If the phase matching and resonance conditions are at a maximum, then this modulation couples into amplitude sidebands at  $2\Omega \pm 2\gamma$ . If the conditions are not at a maximum, then there will be amplitude modulation at  $2\Omega \pm \gamma$ . These processes are grouped together as ‘gain modulation’ in figure 6.6.
- Rotation and differential attenuation of whatever phase sidebands turn up on the second harmonic is possible because the weak cavity in which the harmonic is generated is not guaranteed to be resonant. The mirrors on the crystal have their own dispersion which is different to that of the bulk crystal. The phase of the pump and harmonic fields is therefore not guaranteed to be preserved on reflection. This gives the weak harmonic cavity a different apparent length to the pump cavity, so that

the harmonic cavity is not optimally resonant. This effect also has implications for the optimisation of the phase matching [119]. It means that the dependence of the phase matching is different to the  $\text{sinc}^2$  single pass behaviour. The optimum phase matching will be a compromise between the reflection phase of the pump and harmonic beams and the phase matching in the crystal. (This process is not represented in figure 6.6.)

It is this final effect which is likely to be the greatest in terms of generating amplitude modulation of the harmonic beam at  $\pm\gamma$ , since some care is generally taken to ensure that the resonance and phase matching conditions are at a local maximum. A measurement of the intensity noise of our second harmonic wave at 532nm is shown in figure 6.7. (The details of this SHG system will be described in section 6.5.) This measurement was made by shining the output of the SHG onto a single photodetector and measuring the photocurrent on a spectrum analyser. The cavity was locked using intra-cavity modulation at 30MHz. Intensity noise is clearly visible at 30, 60 and 90MHz.

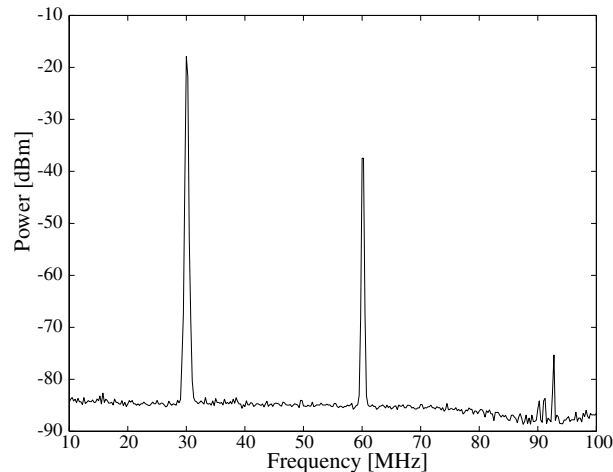


**Figure 6.7:** The spectrum of our SHG locked using cavity modulation at 30MHz. RBW=100kHz, VBW=30kHz.

In summary, it is reasonable to assert that internal modulation of the SHG cavity, while cheaper than high frequency external modulation, has drawbacks if spectral purity is an important factor.

### Alternatives to modulation locking

There are cost effective alternatives to internal modulation when spectral purity is required. One such alternative is Hänsch-Couillaud locking [52]. This method of locking is analogous to tilt-locking, except that rather than a  $\text{TEM}_{01}$  mode being non-resonant and acting as a local oscillator for the error signal detection, an orthogonal non-resonant polarisation mode is used. The light reflected from the cavity is passed through a quarter waveplate and then a polarising beamsplitter. The power at the output ports of the beamsplitter may be balanced by appropriate orientation of the quarter waveplate. As the resonant polarisation mode drifts away from perfect resonance, the phase rotation relative to the non-resonant mode changes the splitting ratio at the polarising beamsplitter. Subtracting the photocurrents measured at the two outputs of the beamsplitter gives the cavity locking signal. This system has been used for SHG [8].

The tilt-locking technique is also an alternative. Prior to this work, tilt-locking had never been used to lock a cavity SHG system. As discussed in section 2.8.2, tilt-locking is modulation free and cheap. Our SHG system may be locked via internal modulation, so a logical experiment was to add a tilt-locking system and compare the performance of the two methods.

## 6.5 Experimental comparison of tilt and modulation locking

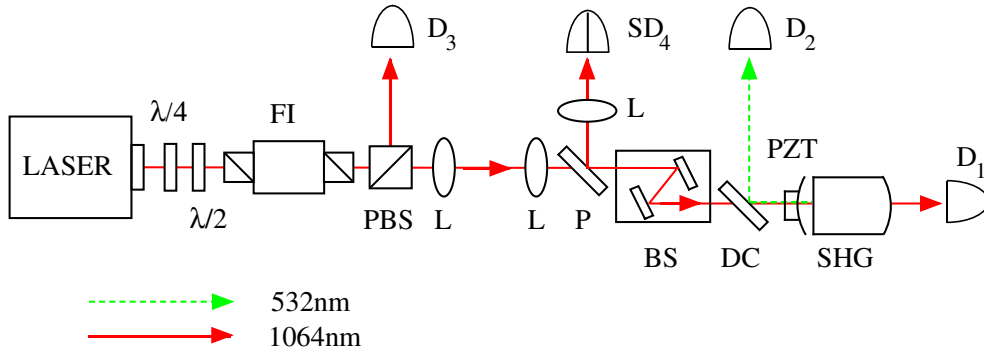


**Figure 6.8:** Schematic of the second harmonic generation experiment. F.I.=Faraday isolator; L=lens;  $\lambda/2, \lambda/4$ =half and quarter wave plates; PBS=polarising beamsplitter; SHG=MgO:LiNbO<sub>3</sub> crystal; DC=dichroic beamsplitter; BS=beam steerer; P=4% reflective pellicle; D=photodetector; SD=split photodetector; PZT=piezo-electric actuator. D<sub>1</sub> is used for modulation locking of the SHG. D<sub>2</sub> is for monitoring the second harmonic output power. D<sub>3</sub> is used for monitoring the input pump power. This beam can also be directed to a reference cavity for the frequency locking of the pump laser.

Our experimental setup is shown in Figure 6.8. The second harmonic generator was a hemilithic cavity consisting of a  $5 \times 7.5 \times 2.5$ mm MgO:LiNbO<sub>3</sub> nonlinear crystal and an output coupler with 94%/4% reflectivity at 1064/532nm. The back surface of the crystal had a 10mm radius of curvature and was harmonically coated for high reflectance ( $R > 99.96\%$ ) for both wavelengths and the front crystal surface was polished flat and anti-reflection coated at both wavelengths ( $R < 0.1\%$ ). The output coupler had a radius of curvature of 25mm. It was placed 23.1mm from the front surface of the crystal, forming a  $27\mu\text{m}$  waist for the 1064nm light within the crystal. This nonlinear crystal was pumped with a nonplanar ring diode-pumped cw Nd:YAG laser with a maximum output power of 700mW at 1064nm. The combination of a half and a quarter waveplate controlled the polarisation of the fundamental beam and a Faraday isolator prevented retro-reflection to the laser. The fundamental power was monitored using photodetector D<sub>3</sub>. The remaining fundamental beam was mode-matched into the SHG cavity.

The crystal was heated using resistors in the crystal housing. The power to the resistors was delivered by a temperature controller (see appendix B) which monitored the crystal housing temperature with a negative temperature coefficient thermistor. The temperature of the crystal was approximately 107°C. We infer a control precision of  $\pm 2\text{mK}$  from the readout of the voltage across the thermistor.

For tilt-locking a small amount of tilt was introduced to the pump beam using the beam steerer located just before the SHG cavity. Note that this does not affect the mode

of the SHG output, as this is determined solely by resonant fundamental mode in the SHG cavity. For the purpose of modulation locking, we made use of the electro-optic properties of the MgO:LiNbO<sub>3</sub> crystal. A 7dBm, 30MHz electric field was applied across the SHG crystal to produce phase modulation sidebands on the fundamental beam. The transmitted fundamental beam was detected by D<sub>1</sub> and demodulated to produce the necessary error signal. In order to obtain an error signal for tilt-locking, a pellicle was used to remove a small amount of the reflected fundamental radiation which was detected and analysed by the split detector SD<sub>4</sub>. The second harmonic light was extracted from the reflected beam by a dichroic mirror with high reflection at 532nm placed immediately in front of the nonlinear crystal and detected by D<sub>2</sub>.

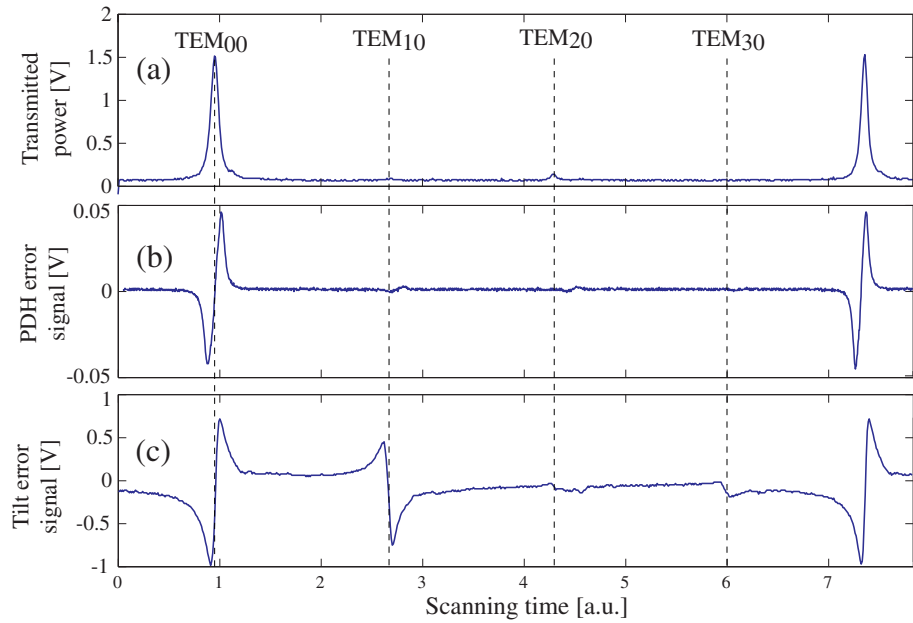


**Figure 6.9:** (a) Transmitted power of the fundamental beam. The various misalignment and mismatch modes are indicated by dotted lines. (b) Error signals generated via modulation locking technique and, (c) via tilt-locking technique.

### 6.5.1 Results

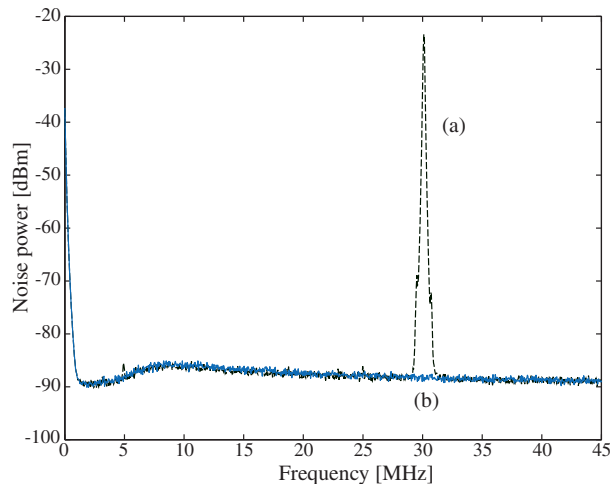
#### Error signals

Figure 6.9 (a) shows the transmitted intensity of the fundamental beam, (b) the modulation error signal and (c) the tilt-locking error signal as the SHG cavity was scanned using the input coupler PZT. Note that the error signals were not recorded simultaneously; there was no modulation during the tilt-locking measurement and no deliberate tilt during the modulation measurement. We note that an extremely small amount (just visible in Figure 6.9) of the TEM<sub>10</sub> mode is sufficient to generate a large error signal and to facilitate tilt-locking. The TEM<sub>20</sub> mode however, is present only due to the imperfect mode-matching of our frequency doubler. Whilst in modulation locking a useful error signal is only produced for the TEM<sub>00</sub> mode, tilt-locking generates large error signals for

both the  $\text{TEM}_{00}$  and  $\text{TEM}_{10}$  modes as well as a smaller error signal for  $\text{TEM}_{30}$  mode<sup>2</sup>. We observe that the error signal for tilt-locking is much broader than that for modulation locking. This increases the capture range of the locking system. Furthermore, the tilt-locking error signal is well over an order of magnitude larger than that obtained using modulation locking. This can be an advantage if electronic noise in the servo systems is significant.

### Second harmonic output spectra

Figure 6.10 shows the second harmonic amplitude spectra obtained from modulation and tilt-locking. The low frequency features are due to the roll off of the photodetector electronics and the low frequency noise of the pump laser. The  $>60\text{dB}$  spike at  $30\text{MHz}$  observable in the modulation locking spectrum is a direct result of the modulation of the crystal required to obtain an error signal. The tilt-locking spectrum, on the other hand, exhibits no such noise spike. Aside from the noise features associated with this locking modulation the two spectra are indistinguishable. Thus tilt-locking is preferable for applications that rely on high spectral purity such as spectroscopy [2, 33, 82, 134].



**Figure 6.10:** Second harmonic amplitude spectra from (a) modulation and (b) tilt locking.

### System stability

We use several measures to quantify the stability of the modulation and tilt locking techniques in our system. Table 6.1 gives a comparison of some modulation and tilt-locking parameters for a measurement period of 100 minutes.

The average second harmonic power,  $\bar{P}_G$ , and standard deviation,  $\sigma_{P_G}$ , are often the most critical parameters in many applications. In our setup, we obtained identical average second harmonic output power for the two techniques, with  $420\text{mW}$  produced from  $650\text{mW}$  of IR. The conversion efficiency is therefore  $65\%$ , which is some way below the  $90\%$  predicted by figure 6.5. Possible reasons for this include the imperfect mode-matching,

<sup>2</sup>Because of the large error signals produced by these modes, tilt-locking can be readily achieved for cavity modes other than the  $\text{TEM}_{00}$ .

Parameters	Modulation-locked	Tilt-locked
$P_{\text{IR}}$ (mW)	$650 \pm 5$	$650 \pm 5$
$\sigma_{P_{\text{IR}}}$ (%)	$1.05 \pm 0.05$	$1.10 \pm 0.05$
$P_{\text{G}}$ (mW)	$420 \pm 5$	$420 \pm 5$
$\sigma_{P_{\text{G}}}$ (%)	$1.05 \pm 0.05$	$1.06 \pm 0.05$
$\sigma_{P_{\text{G}'}}$ (%)	$0.65 \pm 0.05$	$0.70 \pm 0.05$
$\bar{\varepsilon}$ (%)	$0.21 \pm 0.02$	$0.25 \pm 0.02$
$\sigma_{\varepsilon}$ (%)	$0.74 \pm 0.05$	$0.80 \pm 0.05$
Locking stability (mrad)	$0.61 \pm 0.05$	$0.67 \pm 0.05$
$C(P_{\text{G}} : \varepsilon^2)$	$-0.06 \pm 0.03$	$-0.15 \pm 0.03$

**Table 6.1:** Stability parameters of the second harmonic generator locked using both modulation and Tilt techniques.

which reduced the amount of power coupled into the cavity and the cavity design, which includes intra-cavity surfaces that can be contaminated with dust, thereby increasing the loss.

The standard deviation of the power for the two locking methods is very similar at 1.05% and 1.06% for modulation and tilt-locking, respectively. The majority of the fluctuations can be directly attributed to the long term fluctuations in the IR pump power ( $\sigma_{P_{\text{IR}}} = 1.05\%$  and  $1.10\%$  for modulation and tilt-locking runs respectively), most probably due to a 12 minute cycle of the laboratory air conditioning. After normalising to the long term drift of the pump power, the standard deviations of the green power,  $\sigma_{P_{\text{G}'}}$ , produced using modulation and tilt-locking were inferred to be 0.65% and 0.7%, respectively. Another significant factor contributing to this fluctuation was the temperature stability of the nonlinear crystal. In our experiment, the crystal oven was controlled to within  $\pm 0.002^\circ\text{C}$ . However, this does not guarantee a similar temperature stability at the crystal core, which will also be affected by the laser power in the cavity. Crystal core temperature fluctuations alter the phase matching conditions and this results in corresponding fluctuations in second harmonic power.

A more direct measure of locking stability can be obtained from the analyses of the error signals of the two techniques. The error signal used to lock the system is suppressed by the (large) gain of the servo, thus it cannot readily be used to evaluate its own locking performance. However, if we observe the error signal not in use (obtained simultaneously using the alternative technique), we can determine the difference between the two techniques and also check for any correlations with the second harmonic power. For the remaining results in table 6.1 measurements are presented for one technique whilst locking with the other.

The mean of the unused error signal,  $\bar{\varepsilon}$ , gives an indication of the relative long term performance of the two techniques. A value of 100% represents a whole peak-to-peak error (see Figure 6.9) corresponding to the cavity full width half maximum (FWHM). The average error signal is found to be +0.21% and +0.25% of the FWHM for modulation and tilt locking respectively. This suggests that both techniques agree quite well as to the position of the cavity resonance. Ideally, we would expect the mean of the modulation error signal to be the negative of the mean of the tilt-locking error signal. This can be understood by imagining that the tilt locking signal locks the cavity with some offset  $s$

relative to the modulation technique. If the system is tilt-locked, and the modulation error signal is observed, then the frequency offset sensed by the modulation error signal will be  $+s$ . Conversely, if the system is modulation locked and the tilt signal is observed, the frequency offset seen by the tilt signal will be  $-s$ . The fact that the two error signals are the same sign and approximately the same size suggests that the non-zero mean arises not from the error signal generation but from an offset in the frequency locking servo.

The standard deviation of the two error signals was found to be 0.74% and 0.80% of the peak to peak error signal value for modulation and tilt-locking, respectively. As the peak values of the error signal occur at the cavity linewidth, multiplying by the hot cavity linewidth ( $\sim 100\text{MHz}$ ) converts this to an absolute locking stability of 740kHz for modulation and 800kHz for tilt-locking. These may appear large, however they are a consequence of the relatively low finesse ( $\sim 37$ ) and large free spectral range (3.80GHz) of the SHG cavity. The locking stability in terms of round trip cavity phase is 0.61mrad and 0.67mrad, for modulation and tilt-locking respectively.

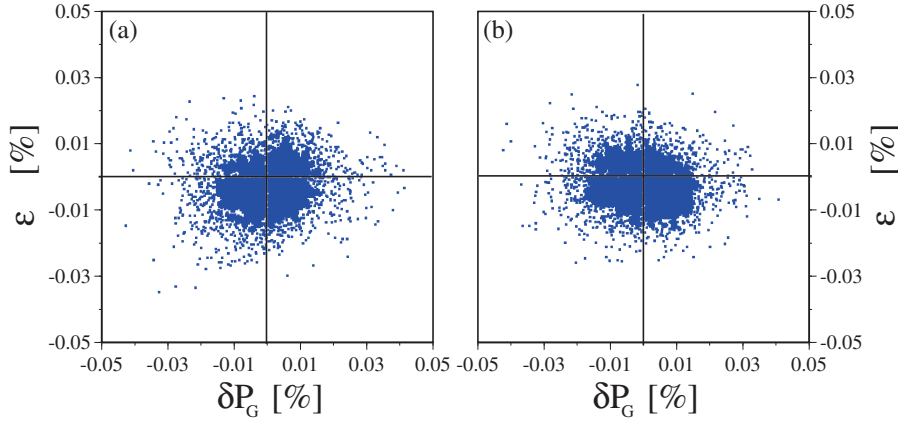


**Figure 6.11:** Plots of green output power fluctuations versus error signals (a) Tilt-locked modulation signal and (b) modulation-locked Tilt signal.

The last parameter investigated is the correlation coefficients between the error signals and the second harmonic output power. Correlation existing between these quantities would indicate poor locking quality of the scheme under interrogation. For example, if the system is tilt-locked and the modulation error signal shows strong correlations with the second harmonic output power, then it could be concluded that the modulation error signal represents a better error measure for the output power fluctuations.

The cavity transmission peak of the second harmonic output is a Lorentzian which can be approximated by a quadratic function near resonance. The error signals, however, are linear near resonance as shown in figure 6.9. Thus, we compare the transmitted second harmonic power,  $P_G$ , with the square of the unused error signal,  $\epsilon^2$ . This results in a linear correlation between the two quantities, where a small correlation coefficient implies good locking performance.

The correlation coefficients of the output green power with the square of the error signal are -0.06 and -0.15, respectively for modulation and tilt locked runs. As expected, the correlations are negative as the error signals are minimised when the green power is at a maximum. Although the modulation system shows a slightly smaller correlation than the tilt locking system, we believe that for most practical applications the difference is

negligible.

If the cavity were locked substantially away from resonance there would be a linear correlation between the error signal,  $\varepsilon$ , and the second harmonic power fluctuations,  $\delta P_G$ . Figure 6.11 shows scatter diagrams for fluctuating green power and error signals. Neither locking scheme exhibits any measurable correlation between the investigative error signal and the second harmonic output power.

In summary, tilt-locking was shown to provide performance comparable to that of modulation locking. The major advantage of the tilt-locking technique is the absence of the modulation peak in the RF spectrum.

### 6.5.2 Mechanical stability and optimisation

Our setup for tilt-locking can be improved to minimise noise in the locking due to mechanical vibrations. The spatial manner in which a tilt-locking error signal is generated makes it very sensitive to any mechanical vibrations present in the system. Our experiment was non-ideal in this respect. The primary flaw was the long beam path (450mm) between the second harmonic generator and the split detector. This has the effect of magnifying any beam jitter present on the  $\text{TEM}_{00+10}$  beam. Using the current SHG cavity design, this could be reduced to a distance of less than 50mm, therefore improving the stability. Ideally, the second harmonic generator would be a ring cavity. The tilt error signal could then be extracted directly from the input mirror, therefore eliminating the need for a pellicle to extract the  $\text{TEM}_{00+10}$  and reducing the beam path even further. (This detection scheme is used in the next chapter for a passive ring cavity, see figure 7.3.)

Impedance matching, beam size and  $\text{TEM}_{10}$  power are three optical parameters which strongly influence lock stability for a given mechanical stability of the detection system.

If the SHG cavity is close to impedance matched, very little  $\text{TEM}_{00}$  mode power will be reflected on resonance. Any beam jitter on the input light produces a  $\text{TEM}_{10}$  mode on reflection from the SHG cavity. In the absence of  $\text{TEM}_{00}$  light, the  $\text{TEM}_{10}$  modes' power is equally balanced across the photodiode halves and so does not contribute to the error signal. Similarly, the result of any mechanical motion of the photodetector is also reduced for an impedance matched cavity. As the  $\text{TEM}_{10}$  has negligible power near the centre of the beam, any small motion of the photodetector does not change the amount of power on each half of the photodiode. Thus tilt-locking on an impedance matched cavity is, to first order, insensitive to mechanical vibrations of the photodetector or input beam jitter.

In situations where mechanical vibration is the limiting noise source of the tilt locking system, the accuracy of the error signal can be increased by coupling more power into the  $\text{TEM}_{10}$  mode. By increasing the power of the  $\text{TEM}_{10}$  mode relative to the  $\text{TEM}_{00}$  mode the absolute size of the locking error signal can be increased while the beam jitter and detector motion contributions remains relatively constant. The extra power in the  $\text{TEM}_{10}$  mode degrades the shot noise performance of the system, but as mechanical noise is dominant this is of no consequence. Increasing the  $\text{TEM}_{01}$  power is analogous to increasing the modulation depth in modulation locking to overcome electronic noise.

The lock stability can also be increased by ensuring that the beam diameter is large at the detector surface. For a given phase signal, the beam position will move by some fraction of the beam diameter, so the absolute distance the beam moves is proportional to the beam diameter. Therefore, maximising the beam diameter at the detector surface reduces the phase shift required to overcome any displacement noise. In this experiment, a lens was required to focus the beam onto the quadrant photodiode because of the high



divergence angle of the beam reflected from the SHG cavity. The detector was moved away from the beam waist until the beam filled the entire active area of the photodiode.

In the work of Shaddock *et al.* [108], the detector was situated at the cavity input coupler and at the waist of the beam. In this situation the misalignment required for an efficient error signal is predominantly beam tilt. The situation in this experiment is slightly different as the detector was neither at the cavity input coupler nor at the beam waist. The Guoy phase shift must therefore be considered as the TEM<sub>00</sub> and TEM<sub>10</sub> modes propagate from the cavity to the photodetector. Recall that the Guoy phase shift causes spatial modes to acquire a relative phase shift as they propagate or pass through a lens [111]. The condition for an ideal error signal is that the TEM<sub>10</sub> mode should produce tilt only (that is have a phase of  $\pi/2$  relative to the TEM<sub>00</sub> mode) at the surface of the detector. To achieve this, the misalignment required at the cavity surface will be, in general, some combination of beam tilt and beam offset.

## 6.6 Conclusion

A summary of second harmonic generation and three-wave mixing was given. This theory was used to explain the noise behaviour of a modulation locked second harmonic generation cavity.

A second harmonic generation experiment was then used to test the relative performance of modulation and tilt locking. The average second harmonic power and long-term stability were found to be almost identical. The tilt-locking error signal had a much larger magnitude which has advantages for systems with low fundamental power or high electronic noise. The second harmonic intensity noise spectra were almost identical, apart from a large spike in the spectrum obtained from the modulation locked cavity.

---

# Squeezing from an optical parametric amplifier

---

This chapter presents results from a squeezing experiment based on an optical parametric amplifier (OPA). The experiment shows a maximum of 5.5dB of stable amplitude quadrature squeezing. The stability of the squeezing made it possible to perform a time domain measurement of photocurrent correlations due to the squeezing. This new measurement technique allows the simultaneous determination of the squeezing and conditional variance between the photocurrents. The chapter begins with a historical overview of OPA squeezing and a theoretical model.

## 7.1 Introduction

A comparison of different quadrature squeezing experiments may be found in the paper of Andersen *et al.* [1]. A statistic that may be taken from this paper, and experiments performed since its publication, is that OPAs have consistently generated the best quadrature squeezing results. In fact, since squeezing was first generated by Slusher *et al.* in 1985 [112], the record for the most quadrature squeezing has been broken 5 times. On all but one of those occasions, the experiment was based on an OPA.

Squeezing generated with an OPA was first shown by Wu *et al.* in 1986 [126, 127], just one year after the first generation of a squeezed state by Slusher *et al.* [112]. Wu generated a squeezed vacuum state with noise suppression 63% (4.3dB) below the quantum limit using a MgO:LiNbO<sub>3</sub> crystal pumped by a frequency doubled Nd:YAG laser. This stood as the record until 1991 when a pulsed squeezing experiment using  $\chi^{(3)}$  nonlinearity in an optical fibre showed 68% (5dB) noise suppression [7]. In 1992 an OPA reclaimed the record when Polzik *et al.* [94] used a frequency doubled Ti:Sapphire laser to pump a KNbO<sub>3</sub> crystal resulting in noise suppression 75% (6dB) below the quantum limit at 852nm. All these early OPA experiments suffered from the problem that the squeezing was not stable. The phase of the squeezed quadrature could not be controlled relative to the phase of the coherent field. In 1995, Brietenbach *et al.* [16], also using a Nd:YAG/LiNbO<sub>3</sub> system, locked the phase of the squeezed vacuum, and showed stable suppression of the vacuum noise to 72% (5.5dB) below the QNL. This experiment used the orthogonal polarisation mode to probe the OPA cavity and generate a locking signal for the laser.

Parametric amplifiers can also generate “bright” squeezing. By adding a small seed beam to the OPA, the output will also have some coherent amplitude. This power may be used to generate all the required locking signals. In 1996 Schneider *et al.* [103] achieved this goal and showed stable squeezing of 63% (4.3dB) below the quantum limit. This was

directly detected with 0.15mW of output power. Later work on this experiment showed squeezing of 78% (6.5dB) below the quantum limit [104], after correction for the electronic noise-floor. This experiment broke the 1992 squeezing record of Polzik *et al.*

In 1999, Lam *et al.* [75] observed 80% (7dB) quantum noise suppression from an OPA, also using a Nd:YAG/LiNbO<sub>3</sub> system. This is currently the record for single beam squeezing. The closest alternative technology is pulsed squeezing generated in fibres. Yu *et al.* [135] used a fibre laser with a 1GHz repetition rate to pump an 80 metre fibre Sagnac interferometer with an observed noise suppression of 75% (6dB) below the QNL.

In the following section the quantum theory of an OPA is presented. This is followed, in section 7.3, by a detailed description of our OPA squeezing experiment. The squeezing results are discussed in section 7.4 along with possible limitations to our system. Finally, a new method for looking at squeezing via direct correlation measurements is presented in section 7.5.

## 7.2 OPA theory

To show how a squeezed state may be generated by the OPA process, we may start with the equations of second harmonic generation derived in section 6.3.

$$\begin{aligned}\dot{a} &= -\kappa_a a + \epsilon a^\dagger b + \sqrt{2\kappa_{\text{in}}^a} A_{\text{in}} + \sqrt{2\kappa_{\text{out}}^a} \delta A_\nu + \sqrt{2\kappa_l^a} \delta A_l \\ \dot{b} &= -\kappa_b b - \frac{\epsilon}{2} a^2 + \sqrt{2\kappa_{\text{in}}^b} B_{\text{in}} + \sqrt{2\kappa_{\text{out}}^b} \delta B_\nu + \sqrt{2\kappa_l^b} \delta B_l.\end{aligned}\quad (7.1)$$

In this case we are interested in the behaviour of the mode  $a$ . We can simplify matters a little by treating the pump mode,  $b$ , as a classical field, and combining this with the nonlinearity term,  $\epsilon$ , to create a combined quantity,  $g$ , that describes the total nonlinear gain. By treating the pump classically, we effectively assume that the power of this mode is not depleted by the parametric process [117]. The simplified equations are:

$$\begin{aligned}\dot{a} &= -\kappa_a a + g a^\dagger + \sqrt{2\kappa_{\text{in}}^a} A_{\text{in}} + \sqrt{2\kappa_{\text{out}}^a} \delta A_\nu + \sqrt{2\kappa_l^a} \delta A_l \\ \dot{a}^\dagger &= -\kappa_a a^\dagger + g^* a + \sqrt{2\kappa_{\text{in}}^a} A_{\text{in}}^\dagger + \sqrt{2\kappa_{\text{out}}^a} \delta A_\nu^\dagger + \sqrt{2\kappa_l^a} \delta A_l^\dagger.\end{aligned}\quad (7.2)$$

### 7.2.1 Classical parametric amplification

Before showing how an OPA generates squeezing, the classical behaviour will be explored. The classical intra-cavity photon number in steady state is given by setting  $\dot{a} = 0$  and  $\langle a \rangle = \alpha$ . We may also choose a phase reference, without loss of generality, by assuming that the classical amplitude of the input field,  $\bar{A}_{\text{in}}$ , is real. Provided  $g < \kappa_a$ , we find

$$\alpha = \frac{\sqrt{2\kappa_{\text{in}}^a} (1 + g/\kappa_a)}{\kappa_a (1 - |g|^2/\kappa_a^2)} \bar{A}_{\text{in}}.\quad (7.3)$$

If there is no seed field ( $A_{\text{in}} = 0$ ) we see that this solution gives  $\alpha = 0$ . This is only true when  $g < \kappa_a$ . When  $g = \kappa_a$ , the nonlinear gain becomes equal to the passive cavity loss rate. Consequently, when  $g > \kappa_a$ , the threshold for optical parametric oscillation (OPO) has been surpassed and there is a solution that allows  $\alpha \neq 0$ . We do not reach this point in our experiment, and above threshold behaviour will not be treated here.

The amplitude of the transmitted field  $\bar{A}_{\text{out}}$  is given by  $\alpha\sqrt{2\kappa_{a_{\text{out}}}}$  (see equation 2.92). From equation 7.3, we find therefore find

$$\bar{A}_{\text{out}} = \frac{2\sqrt{\kappa_{a_{\text{out}}}\kappa_{a_{\text{in}}}}(1 + g/\kappa_a)}{\kappa_a(1 - |g|^2/\kappa_a^2)}\bar{A}_{\text{in}}. \quad (7.4)$$

Comparing this to the transmitted amplitude without gain ( $\bar{A}_{\text{out}}|_{g=0}$ ) we obtain

$$\Rightarrow \frac{\bar{A}_{\text{out}}}{\bar{A}_{\text{out}}|_{g=0}} = \frac{(1 + g/\kappa_a)}{1 - |g|^2/\kappa_a^2}. \quad (7.5)$$

Finally, in terms of the optical power transmitted through the cavity,  $P_{\text{out}}$ , we reach

$$\Rightarrow \frac{P_{\text{out}}}{P_{\text{out}}|_{g=0}} = \frac{(1 + g/\kappa_a)^2}{(1 - |g|^2/\kappa_a^2)^2}. \quad (7.6)$$

We may equate the term  $g/\kappa_a$  with the ratio of the pump field amplitude to the threshold pump field amplitude,  $\bar{B}/|\bar{B}_{\text{ths}}|$ . The result is

$$\Rightarrow \frac{P_{\text{out}}}{P_{\text{out}}|_{g=0}} = \frac{(1 + \bar{B}/|\bar{B}_{\text{ths}}|)^2}{(1 - |\bar{B}/\bar{B}_{\text{ths}}|^2)^2}. \quad (7.7)$$

This equation describes the regenerative gain of the parametric process. Provided we are below the OPO threshold, we find that there are distinct cases for amplification and deamplification of the input beam. These are given by considering the phase of the pump  $\bar{B}$  to be real and positive for the case of amplification or real and negative in the case of deamplification. A plot of the regenerative gain of the OPA is shown in figure 7.1

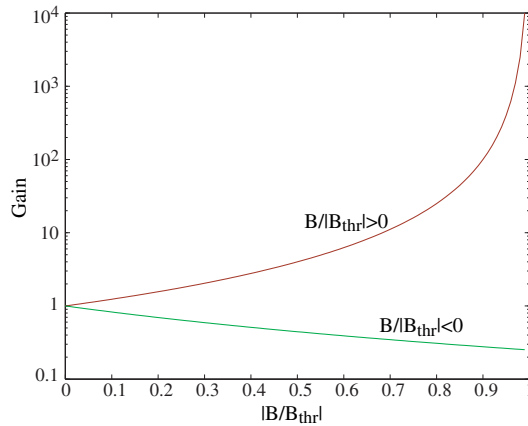


Figure 7.1: Regenerative gain of an optical parametric amplifier.

### 7.2.2 Quantum behaviour of an OPA

The classical properties of the OPA are mimicked in the quantum behaviour. When the OPA is deamplifying, the quantum fluctuations in the amplitude quadrature are also deamplified leading to amplitude squeezing. In the case of amplification, the amplitude quadrature fluctuations are amplified, but the phase quadrature fluctuations become squeezed.

To show this we return to the quantum equations for  $a$  and  $a^\dagger$  to find the amplitude and phase quadrature fluctuations. Assuming that  $g$  is real we find

$$\begin{aligned}\delta\dot{X}_a^+ &= (g - \kappa_a)\delta X_a^+ + \sqrt{2\kappa_{\text{in}}^a}\delta X_{\text{in}}^+ + \sqrt{2\kappa_{\text{out}}^a}\delta X_\nu^+ + \sqrt{2\kappa_l^a}\delta X_l^+ \\ \delta\dot{X}_a^- &= -(g + \kappa_a)\delta X_a^- + \sqrt{2\kappa_{\text{in}}^a}\delta X_{\text{in}}^- + \sqrt{2\kappa_{\text{out}}^a}\delta X_\nu^- + \sqrt{2\kappa_l^a}\delta X_l^-. \end{aligned} \quad (7.8)$$

Using the cavity input/output relations of equation 2.92 and including a loss term,  $\eta$ , with corresponding vacuum  $\delta X_d$  to describe the downstream losses in the detection system we find the frequency domain output field quadrature in the usual way to give

$$\begin{aligned}\tilde{X}_{\text{out}}^+ &= \sqrt{\eta} \frac{(2\kappa_{\text{out}}^a - i\omega - \kappa_a + g)\delta\tilde{X}_\nu^+ + 2\sqrt{\kappa_{\text{out}}^a\kappa_{\text{in}}^a}\delta\tilde{X}_{\text{in}}^+ + 2\sqrt{\kappa_{\text{out}}^a\kappa_l^a}\delta\tilde{X}_l^+}{i\omega + \kappa_a - g} + \sqrt{1 - \eta}\delta\tilde{X}_d^+ \\ \tilde{X}_{\text{out}}^- &= \sqrt{\eta} \frac{(2\kappa_{\text{out}}^a - i\omega - \kappa_a - g)\delta\tilde{X}_\nu^- + 2\sqrt{\kappa_{\text{out}}^a\kappa_{\text{in}}^a}\delta\tilde{X}_{\text{in}}^- + 2\sqrt{\kappa_{\text{out}}^a\kappa_l^a}\delta\tilde{X}_l^-}{i\omega + \kappa_a + g} + \sqrt{1 - \eta}\delta\tilde{X}_d^-. \end{aligned} \quad (7.9)$$

These quadratures lead to the field spectra:

$$\begin{aligned}V_{\text{out}}^+ &= 1 + \eta\eta_{\text{esc}} \frac{4(g/\kappa_a) + 4(\kappa_{\text{in}}^a/\kappa_a)(V_{\text{in}}^+ - 1)}{\omega^2/\kappa_a^2 + (1 - g/\kappa_a)^2} \\ V_{\text{out}}^- &= 1 + \eta\eta_{\text{esc}} \frac{-4(g/\kappa_a) + 4(\kappa_{\text{in}}^a/\kappa_a)(V_{\text{in}}^- - 1)}{\omega^2/\kappa_a^2 + (1 + g/\kappa_a)^2}, \end{aligned} \quad (7.10)$$

where we have defined the escape efficiency  $\eta_{\text{esc}} = \kappa_{\text{out}}^a/\kappa_a$ . This determines the efficiency with which the squeezing may exit the cavity. Better efficiency is achieved by making the output coupling very large, and all other loss terms small, so that  $\eta_{\text{esc}} \approx 1$ . The value of  $\kappa_{\text{out}}^a$  cannot be made arbitrarily large. If the total cavity decay rate,  $\kappa_a$ , is too big, the pump power required to generate the nonlinear gain,  $g$ , becomes excessive.

In the limit that the input field to the OPA is at the QNL ( $V_{\text{in}} = 1$ ), or that the input coupling is very weak ( $\kappa_{\text{in}}^a/\kappa_a \approx 0$ ), we may ignore the second term in the numerator of the above equations. Also,  $g/\kappa_a$  may again be replaced with the ratio of the pump field amplitude to the threshold pump field amplitude,  $\bar{B}/|\bar{B}_{\text{ths}}|$ . This gives

$$\begin{aligned}V_{\text{out}}^+ &= 1 + \eta\eta_{\text{esc}} \frac{4\bar{B}/|\bar{B}_{\text{ths}}|}{\omega^2/\kappa_a^2 + (1 - \bar{B}/|\bar{B}_{\text{ths}}|)^2} \\ V_{\text{out}}^- &= 1 - \eta\eta_{\text{esc}} \frac{4\bar{B}/|\bar{B}_{\text{ths}}|}{\omega^2/\kappa_a^2 + (1 + \bar{B}/|\bar{B}_{\text{ths}}|)^2}. \end{aligned} \quad (7.11)$$

The optimum squeezing is found as  $|\bar{B}/\bar{B}_{\text{ths}}| \rightarrow 1$ . For amplitude squeezing, we require  $\bar{B}/|\bar{B}_{\text{ths}}| \rightarrow -1$  indicating that the pump and seed beams are out of phase with each other, giving deamplification of the classical field amplitude as well as amplitude squeezing. Conversely, phase quadrature squeezing occurs as  $\bar{B}/|\bar{B}_{\text{ths}}| \rightarrow +1$ , along with amplification of the classical amplitude. We also note that equations 7.11 describe a minimum uncertainty state ( $V_{\text{out}}^+ V_{\text{out}}^- = 1$ ) only when  $\eta\eta_{\text{esc}} = 1$ . The amount of loss dictates the degree to which the state deviates from minimum uncertainty.

In the analysis above, the classical and quantum behaviour appears to be quite different. Classically, the best deamplification was found to be 1/4, whereas (in theory at least) the squeezing of the quantum noise is limitless, provided the system is lossless ( $\eta\eta_{\text{esc}} = 1$ ). This difference is not contradictory. In the classical analysis, the factor of 1/4 deamplification is found for a beam injected through the input coupler, with coupling rate  $\kappa_{\text{in}}$ . In

the quantum analysis, noise entering through this mirror is ignored via the assumption  $\kappa_{in} \ll \kappa$ . The squeezing results from the processing of the vacuum entering at the output mirror with coupling rate  $\kappa_{out}$ . A closer look at equations 7.10, shows that any noise entering at input mirror ( $V_{in}^{\pm} - 1$ ) is in fact deamplified by 1/4 as one would expect from the classical result.

## 7.3 Experimental design

A complete layout of the squeezing experiment is shown in figure 7.2. The laser used to drive the squeezing experiment was the same as that used for the second harmonic generation experiment described in chapter 6. It provided 700mW of TEM<sub>00</sub> radiation at 1064nm. The nature of experiments with optical cavities means that there will be times when an unlocked cavity will reflect very large amounts of light back towards the laser. This has the potential to damage the diode lasers that pump the Nd:YAG laser crystal. For this reason the optical isolator placed after the laser was of great importance. Our isolator (Gsänger FR 1060/5) provided 40dB of isolation from reflective elements, meaning that the most power ever likely to be returned to the laser head was 70 $\mu$ W.

The laser was only stable for certain temperatures of the laser crystal, which corresponded to points where the laser mode was near the peak of the laser gain bandwidth. Tuning the crystal temperature was an effective way to tune the laser frequency only until the resonant mode moved too far away from the peak of the gain bandwidth. The laser was then seen to “mode-hop”. Care was taken to operate the laser in a single mode regime. For our laser this meant a crystal temperature of 20.4 to 21°C.

Of the 700mW of laser power, 650mW was used to pump the second harmonic generator (SHG). A detailed account of the setup and locking of the SHG was given in chapter 6. For the squeezing work we used modulation locking to stabilise the SHG cavity. The modulation sidebands on the harmonic wave were found to be a useful source of error signals, as will be described below.

### 7.3.1 The mode cleaner cavity

The laser power not used to pump the SHG was sent to a mode cleaning cavity. The concept behind the mode cleaner was twofold. Firstly, it filtered out laser frequency and intensity noise above the bandwidth of the cavity and secondly, it defined a high quality spatial mode. The output of the mode cleaner was therefore well prepared for use as the OPA seed beam, and as the local oscillator required for the eventual squeezing detection. The three mirrors used for this cavity were coated by Research Electro-Optics, and specified as shown in figure 7.3.

The overall goal was for a finesse of 4000 for the s-polarisation, with transmission of 90%. The advantage of having such a high finesse cavity is the potential to generate squeezing at lower frequencies. Maximum squeezing is predicted by the theory to occur at 0Hz, assuming an ideal laser source. Experimentally, low frequency squeezing is limited by excess laser noise on the seed beam injected into the OPA crystal (see equation 7.10). As demonstrated in section 2.7, the power transmitted through a cavity may be stripped of excess noise above the cavity linewidth. A finesse of 4000 would give a cavity linewidth of about 100kHz, for a round-trip length of 50cm. If the transmitted power of such a cavity were used as the seed beam for the OPA, sub-1MHz squeezing might be a possibility.

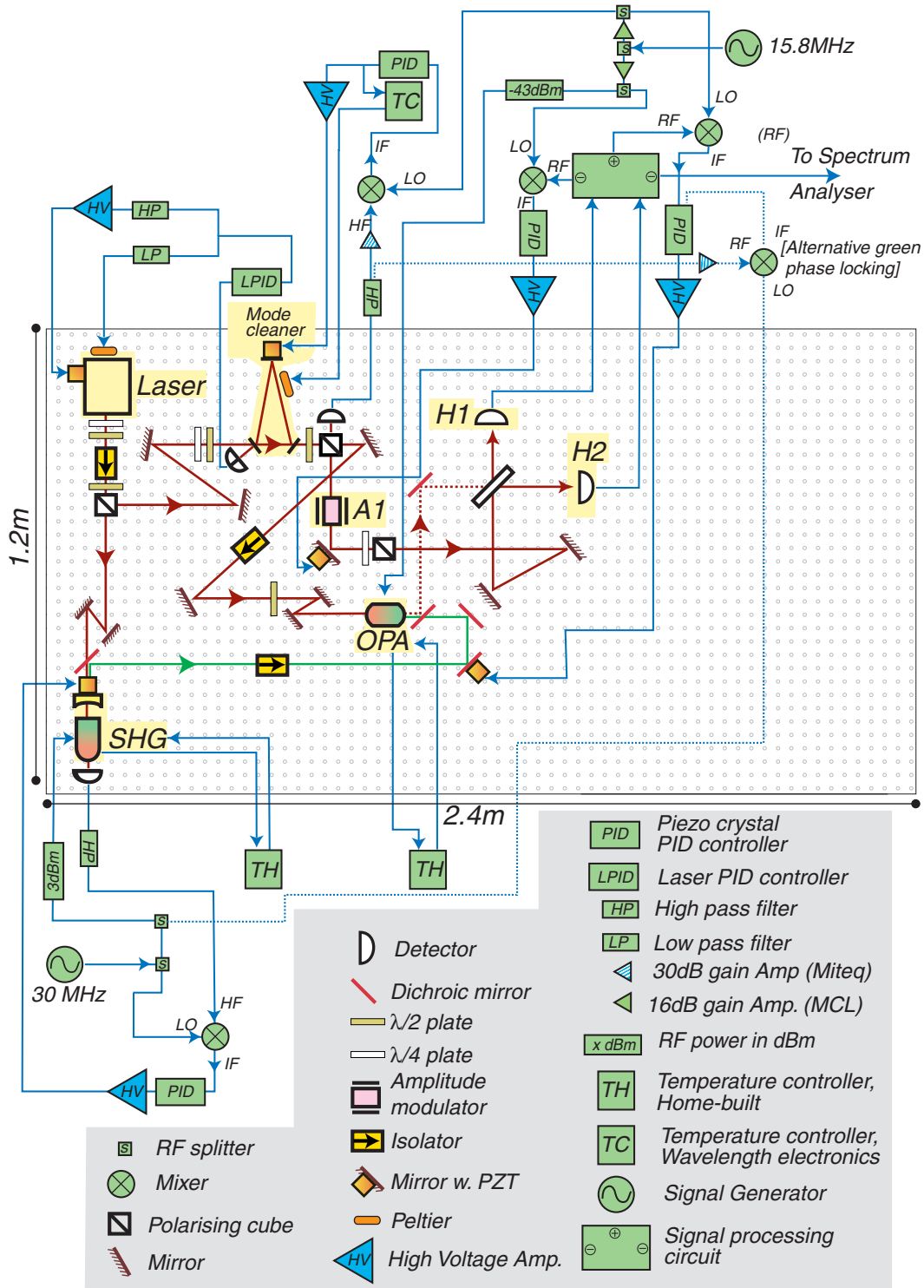
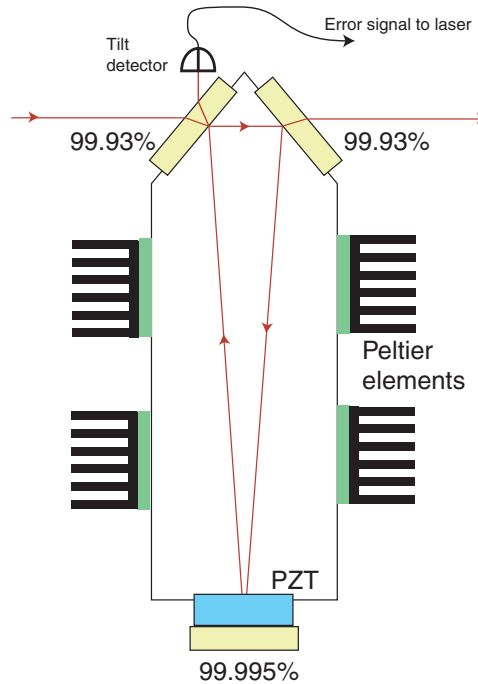


Figure 7.2: Detailed diagram of the OPA squeezing experiment.



**Figure 7.3:** Mode cleaner cavity with Peltier elements for active temperature stabilisation, a piezo-electric actuator (PZT) for active length control and a tilt detector for collecting the error signal that is fed-back to the laser.

Unfortunately, the specifications for the mode cleaner mirrors were not reached. We found transmission of about 50% for the s-polarisation and 80% for the p-polarisation. The p-polarised light had a finesse of 400. Due to the power requirements of the SHG, 50% loss in the mode cleaner could not be tolerated. Instead we turned to the low finesse mode. The frequency filtering was not nearly as good. A finesse of 400 gave a cavity linewidth of approximately 1MHz. However, the spatial mode characteristics were good enough to give a fringe visibility of 98.5% for the interference of the local oscillator and the output beam of the OPA<sup>1</sup>. All our experiments were done using this low finesse cavity mode.

The laser frequency was tilt-locked to the mode cleaner via a split photodetector which monitored the power reflected from the mode cleaner. The tilt-locking error signal was divided into two parts by the laser controller (see circuit diagram in appendix B). Low frequency (<1Hz), high dynamic range ( $\sim 9$ GHz) control of the laser frequency was implemented by feeding back to the laser crystal temperature. Higher frequency (1 to 50kHz), low dynamic range ( $\sim 500$ MHz) control was obtained by feeding back to a Piezo-electric actuator that compressed the laser crystal. The net result was robust and stable laser frequency locking.

The mode cleaner cavity length could be controlled in two ways. One was via a piezo actuator, which provided laser frequency tuning of about 700MHz with a control bandwidth of 0 to 7kHz. The other method was via temperature control of the cavity spacer. Our cavity spacer was made of aluminium, which has a thermal expansion coefficient of  $2.34 \times 10^{-6} K^{-1}$ . For a 50cm round-trip length, this corresponds to 6.6GHz tuning range per degree  $K$  of temperature change. The control bandwidth of the mode cleaner temper-

<sup>1</sup>This compares to 90% without a mode cleaner [73].



ature was low ( $\sim 1\text{Hz}$ ) due to the large heat capacity of the cavity spacer. The temperature control was achieved via four high capacity Peltier heat pumps. These pumps were always fighting against the rather good thermal contact between the optical table and the cavity spacer. Heat that was pumped into, or out-of, the spacer was rapidly conducted into the metallic optical table. For stable temperature control, the spacer was held slightly above room temperature, so that heat was pumped from the air into the aluminium. When the cavity was cooled below room temperature, the heat fins on the Peltier elements became too hot and the temperature control failed. The temperature of the cavity was sensed by a negative temperature coefficient thermistor and controlled by a commercial 40W temperature controller (Wavelength Electronics LFI-3551).

Between the mode cleaner and the OPA, was a Faraday rotator. This, in combination with the polarising beamsplitter at the output of the mode cleaner, allowed the monitoring of the light reflected from the OPA cavity. This light was used to collect a locking signal for the mode cleaner, which was locked to the OPA.

### 7.3.2 The OPA cavity

The OPA crystal was the same as that used for past squeezing experiments in our group [73, 75]. It was made from a single crystal of magnesium oxide doped lithium niobate, cut, polished and coated as shown in figure 7.4. The crystal material had internal loss of

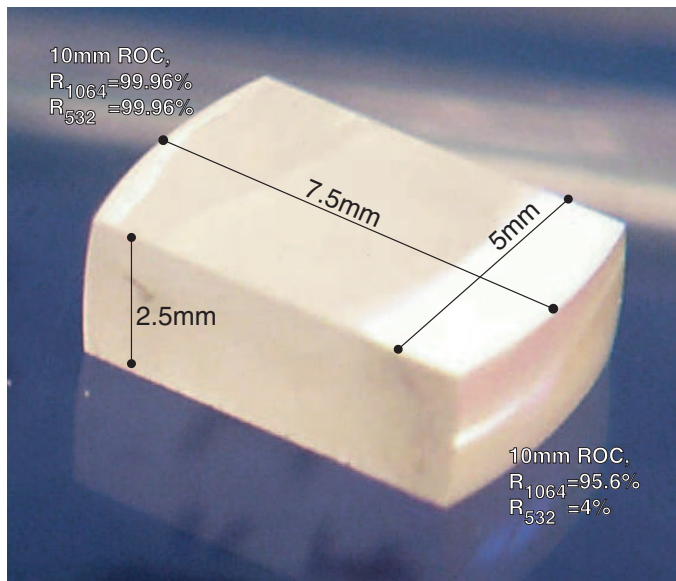


**Figure 7.4:** The OPA crystal. ROC= radius of curvature.

approximately  $0.1\%cm^{-1}$  at  $1064\text{nm}$  and  $4\%cm^{-1}$  at  $532\text{nm}$ . The cavity formed by the two polished surfaces had a finesse of 136, free spectral range of  $9\text{GHz}$  and HWHM linewidth of  $33\text{MHz}$ . The temperature of the OPA was controlled by an identical temperature controller to that used for the SHG (see appendix B). Temperature was sensed by a negative temperature coefficient thermistor embedded in the crystal housing. To reduce the time delay in this feedback loop, and keep the feedback stable, the thermistor was placed very close to the heating resistors. The thermistor did not, therefore, accurately sense the actual crystal temperature. However, the method did ensure stability of the temperature feedback to the oven. Measurements on the stability of the SHG oven (which was identical) indicated that the temperature was stable to  $\pm 2\text{mK}$ .

Because the OPA was monolithic, the length could not be tuned to any great degree<sup>2</sup>. It was therefore natural to use this cavity as the frequency reference for the rest of the experiment. Quite apart from the fact that there was no other choice, locking the experiment to the OPA was a good way to ensure good overall experimental stability. The active temperature control, combined with the monolithic design, gave better frequency stability than any of the other cavities in the experiment.

The locking signal for the OPA cavity was generated by applying a 15.8MHz electric field across the monolith. This, like the modulation locking of the SHG cavity, gave phase modulation sidebands to the reflected and transmitted cavity fields. The reflected light was detected via a polarising beamsplitter between the Faraday rotator (Messeloff) and the mode cleaner output. This signal was then mixed down at 15.8MHz to give the error signal which was fed-back to the mode cleaner cavity. The laser was locked to the mode cleaner, so that indirectly, the laser was also locked to the OPA. The mode cleaner frequency, as described above, could be temperature tuned and piezo-electrically tuned. Both these methods were used to give high speed and high dynamic range feedback.

The power from the SHG cavity was extracted via the dichroic mirror at the front of the SHG and then passed through an optical isolator for 532nm (Gsänger FR 532). Poor isolation of the SHG tended to make the SHG cavity unstable, so good isolation (>30dB) was critical. The green light was passed through three additional dichroic filters to remove residual infra-red light. Finally, the green beam was sent into the OPA cavity.

At this stage, all the equipment required to actually generate squeezing has been described. What remains is the locking of the squeezing quadrature and the homodyne detection.

### 7.3.3 Locking the squeezing quadrature

The quadrature angle of the squeezing (relative to the seed beam) may be chosen by locking the system to either a maximum or minimum of the power output from the OPA cavity. A minimum corresponds to amplitude quadrature squeezing, while a maximum gives phase quadrature squeezing. Typically, we locked to a minimum in the output power to obtain amplitude squeezing. The obvious locking technique was therefore to sum the power detected by the homodyne detectors H1 and H2 and demodulate this sum at 15.8 or 30.0 MHz. At these two frequencies there was relative modulation of the green and red phase and therefore an error signal in the demodulated photocurrent. This method was used for the majority of the work with the squeezer. The sum of the H1 and H2 photocurrents was gathered using the sum output of the signal box (see design in appendix B). The disadvantage of this method was that it relied on the same detectors used to monitor the squeezing. The locking was therefore not independent of the squeezing detection.

A less obvious quadrature locking method is to look at the signal reflected from the OPA. The phase of the green beam controls the regenerative gain of the OPA, and therefore the impedance matching of the cavity. Modulation of the green phase at 30.0MHz therefore causes a modulation in the impedance matching of the OPA cavity. When the green phase does not correspond to a minimum or maximum in the reflected seed beam power, this

---

<sup>2</sup>The only method of ‘length’ tuning was the application of a voltage across the crystal. The linear electro-optic effect leads to shift of optical length and therefore a change in resonant frequency of the cavity. This method was used in the set-up phase of the experiment, while the mode matching of the seed beam into the OPA was being optimised. The dynamic range of this method was low, even with the 700V that was applied.

beam will have a 30.0MHz amplitude modulation. Demodulation of the reflected signal at 30.0MHz will therefore provide an error signal for the phase of the pump and seed beams. This method has the advantage that the phase of the squeezing will be locked without dependence on downstream detection. In either case the error signal was fed, via a high voltage amplifier, to a piezo actuator in the green beam. Both methods provided stable pump beam control.

### 7.3.4 Homodyne detection locking

The squeezed light tended to have only a small coherent amplitude (typically 10 to  $30\mu\text{W}$ ). This amount of power was not large enough to bring the quantum noise-floor above the electronic noise of the detectors. Direct detection was therefore not possible. Instead we used a homodyne detection system. The local oscillator beam was mixed with the squeezed beam on 50/50 beamsplitter and the outputs were detected via the photodetectors H1 and H2.

The final locking stage required to stabilise the squeezer, was to fix the phase of the local oscillator relative to the squeezed beam. Detection of amplitude squeezing required locking the homodyne system to a ‘dark’ fringe. In other words, the power on the homodyne beamsplitters was maximally asymmetric. This required demodulation of the difference between the photocurrents of H1 and H2 at 15.8MHz. A difference signal was provided by the signal box. The homodyne detection error signal was fed, via a high voltage amplifier, to a piezo actuator in the local oscillator beam.

The detectors used for measuring the squeezing were built around ETX500 photodiodes. These were measured to have a quantum efficiency of  $93 \pm 5\%$ . The detector design may be found in appendix B. To optimise the common mode rejection of the signals from these detectors, we used the amplitude modulator A1 in the local oscillator beam. The subtracted output from the signal box was monitored on the spectrum analyser. By changing length of cables between the detectors and the signal box, the amplitude modulation observed on a spectrum analyser was minimised. “Good” common mode rejection was  $>30\text{dB}$  below the modulation observed in the sum of the detector outputs.

## 7.4 Experimental results

### 7.4.1 Regenerative gain

The first stage of the OPA squeezing experiment was the optimisation of the classical parametric gain of the OPA. A plot of observed gain versus pump power is shown in figure 7.5. We see a maximum gain of 75 times and deamplification of 0.3 times. The output power with no pump was  $\sim 0.1\text{mW}$ . The deamplification of 0.3 indicates that the system is close to the OPO threshold, where the deamplification approaches 0.25. When making these measurements it is important to check the temperature of the OPA oven for each new pump power. The crystal temperature is sensed by a negative temperature coefficient thermistor which is housed in the aluminium casing around the crystal. However, the important temperature for phase matching is that sensed by the seed beam as it travels through the crystal. This will depend on the power of the pump beam which, due to the  $4\% \text{cm}^{-1}$  absorption of radiation at 532nm, heats the mode volume inside the crystal. Optimum gain is therefore only obtained by adjusting the temperature controller for each new pump power.

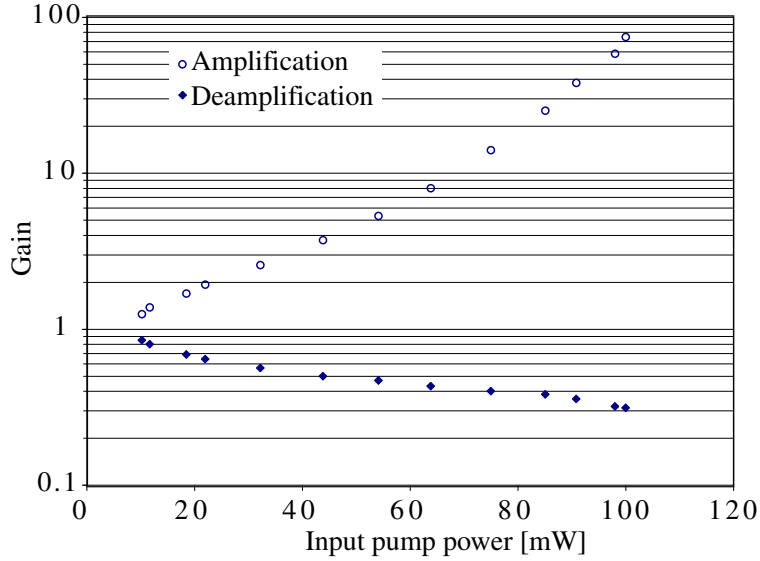


Figure 7.5: Measured regenerative gain of the OPA as a function of pump power.

#### 7.4.2 Vacuum squeezing

The first type of squeezing to be generated with the OPA was vacuum squeezing, where the seed beam was blocked. The output beam will therefore have no coherent amplitude, and we cannot lock either the green phase or the phase of the detection. The phase of the local oscillator was simply scanned and the amount of squeezing measured from the subtraction of the H1 and H2 photocurrents<sup>3</sup>. The electronic noise-floor for these measurements was at -92.0dBm (With RBW=300kHz and VBW=1kHz). This noise power has been subtracted from the quantum noise and the squeezing data (see appendix A). We do not, however, correct for the quantum efficiency of the detectors. Vacuum squeezing of 5dB ( $V=0.31$ ) is shown in figure 7.6.

This plot also illustrates an important point about the operation of our squeezer. The anti-squeezed quadrature shows noise 13dB ( $V=20$ ) above the quantum noise. This is a long way from the minimum uncertainty predicted for a lossless OPA system. (A minimum uncertainty state would have anti-squeezing of only 5dB above the quantum noise.) Even when taking all the known efficiencies into account, this result is in contradiction to the theoretical output of an OPA given by equation 7.11. How much extra loss is required to obtain the results of figure 7.6? We assume that there is a level of underlying squeezing,  $V$ , and anti-squeezing,  $1/V$ , which is detected with total efficiency  $\eta_t$  to give the result of figure 7.6, that shows squeezing of 0.31 and anti-squeezing 20. We therefore have the equations

$$\begin{aligned} (1 - \eta_t) + \eta_t V &= 0.31 \\ (1 - \eta_t) + \frac{\eta_t}{V} &= 20 \end{aligned} \quad (7.12)$$

that may be solved for the total loss and underlying squeezing. Doing this gives  $\eta_t = 0.72$  and  $V = 0.04$ . This suggests that we have 14dB of squeezing with a total detection efficiency of only 72%. Given that  $\eta_t$  should be the product of the escape efficiency (0.96),

<sup>3</sup>Since we do not lock the experiment in this configuration, the signal box was not required so we made use of a passive subtractor (Minicircuits ZFSCJ-2-1) to measure the photocurrent subtraction.

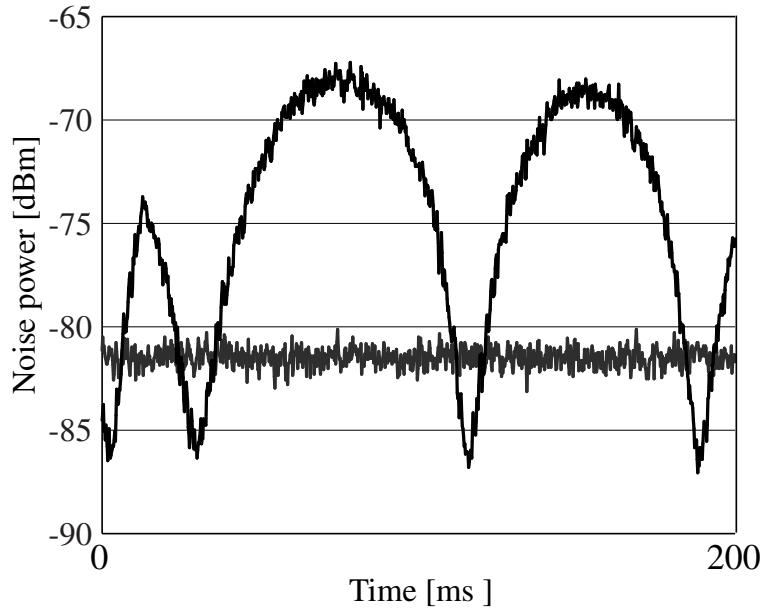


**Figure 7.6:** Scanned squeezed vacuum measurement. The squeezing seen here is 5dB below the quantum noise limit and the beam has no coherent amplitude. RBW=300kHz, VBW=1kHz.

the homodyne efficiency (0.97) and the detection efficiency ( $0.93 \pm 0.05$ ), we expect to find  $\eta_t = 0.88 \pm 0.05$ . This indicates that we require an additional inefficiency of  $\sim 0.81$  somewhere in the system to account for the observed amounts of squeezing and anti-squeezing. This still relies on the assumption that we actually have, somewhere buried under the loss, 14dB of squeezing.

### GRIIRA?

The OPA has been shown previously to be capable of generating minimum uncertainty states [126, 16], however this is certainly not a consistent feature of these systems, as seen in [15, 113]. One possible source of extra loss and noise is green induced infra-red absorption (GRIIRA) [78]. Recent measurements of MgO:LiNbO<sub>3</sub> show that this effect may actually be quite strong. For a green power of 2.5kW/cm<sup>2</sup> Furukawa *et al.* [38] found infra-red loss of 0.6%, which is a factor of six higher than the linear loss of our crystal. If this amount of extra loss were present in our crystal, it would make our escape efficiency 82%, giving a total detection efficiency of 73%. The estimated green power at the waist in our crystal is  $\sim 7$  kW/cm<sup>2</sup>, which is enough to cause significant absorption according to the measurements of Furukawa. In short, GRIIRA is a very good candidate for the cause of the non-minimum uncertainty state we observe.

Other groups have also suggested induced infra-red absorption as a limit to the performance of OPA squeezing. Andersen *et al.* [1] concluded that blue induced infra-red absorption (BLIIRA) was limiting the squeezing available in their waveguide experiments. Sørensen *et al.* [113] also invoked BLIIRA as the limit to their OPA squeezing, which was generated by a Ti:Sapphire laser pumped KNbO<sub>3</sub> crystal.

Induced absorption places restrictions on OPA crystal design. Without GRIIRA we expect that the optimum design is to have the highest possible escape efficiency, which makes the OPO threshold large. This means that more green will be required for the pump in order to approach threshold, where the squeezing is expected to be best. Increased pump

power means more GRIIRA. The implication is that the optimum escape efficiency will be a compromise to between minimising GRIIRA and maximising the escape efficiency.

GRIIRA may also explain the different operating points of our crystal. In the work of Lam *et al.*, 7dB of squeezing was observed, with a near minimum uncertainty state. This was the same crystal, so what has changed? The most likely candidate is the nature of the pump beam, both in power and mode shape. As the power is increased so too does the induced loss, shifting the state away from minimum uncertainty. The effect of mode matching of the pump into the OPA cavity may also be important. Changing the mode matching will change the green power distribution in the cavity and therefore change the amount of GRIIRA. This is particularly hard to quantify since the OPA has no cavity for the green light therefore making it difficult to verify the quality of the green pump mode.

### 7.4.3 Locked squeezing results

Vacuum squeezing suffers from the technical disadvantage that there is no coherent amplitude. When mixed with a local oscillator there is no classical interference and therefore no straightforward method of generating an error signal to lock the homodyne detection phase. There are ways around this, for example, the phase may be locked by using higher order spatial modes [16]. The method used here is to seed the OPA with a dim beam so that the squeezed output has some small coherent amplitude [15, 104]. This, as described in section 7.3, allows locking of the squeezed output. Results for the locked squeezing are shown in figure 7.7. The best squeezing of 5.5dB occurs at 4MHz.

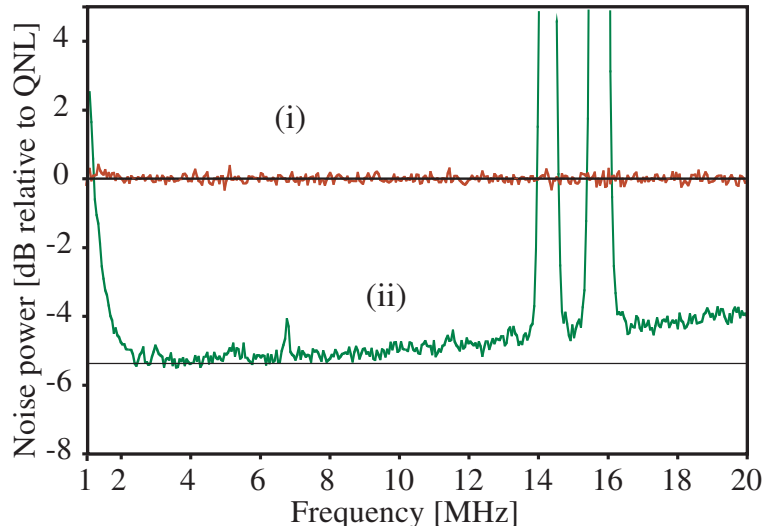


**Figure 7.7:** Frequency spectrum of the squeezed output relative to the quantum noise. RBW=100 kHz, VBW=30 Hz. Optical power in the beam is  $30\mu\text{W}$ .

The advantage of having a locked squeezing system is the ability to make long term measurements, for example, the injection of squeezing into interferometers used for the detection of gravitational waves [26, 117]. The stability of our squeezer is shown in figure 7.8. Our squeezing is shown to be locked and stable for a period in excess of one hour. The two spikes correspond to instances where the experiment was disturbed by the collection of data from the spectrum analyser. In these cases, the locking of the green phase or the homodyne detector was kicked out of range, and settled into the adjacent fringe. The most important limit to system stability is long term drift in the temperature

of the laboratory. The heating of the lab during the day changes the relative path lengths of the beams and therefore the lock point of the various interferometers.

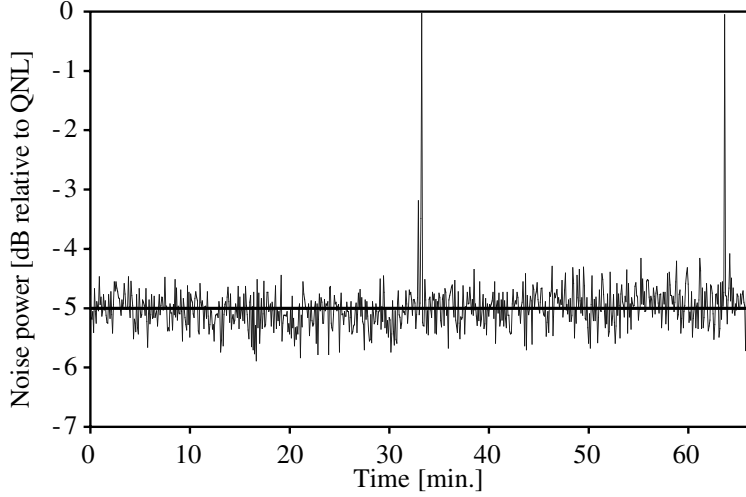


**Figure 7.8:** Time stability of the squeezing. RBW=30 kHz, VBW=30 Hz.

Given that the detector efficiency ( $\eta_d$ ) of 93% and the homodyne fringe visibility of 98.5%, we may infer the amount of squeezing at the output of the OPA to be

$$V_{inf} = \frac{V_{meas} - \eta_d \eta_h + 1}{\eta_d \eta_h} \quad (7.13)$$

where the homodyne efficiency,  $\eta_h$ , is the square of the fringe visibility. The best squeezing of 5.5dB then corresponds to 6.9dB, and the long term measurement of 5dB becomes 6.2dB.

## 7.5 Correlation measurements

Most published squeezing results tend to look something like the ones presented in the previous section: a power spectrum measured with a spectrum analyser. However, there is more to squeezing than noise power. Maximal quantum information about a state may be obtained by measuring the Wigner function via optical homodyne tomography [17]. This is a powerful technique which also requires powerful computing to reconstruct the Wigner function via the inverse Radon transform. The advantage of measuring a Wigner function is the possibility to detect any non-Gaussian behaviour in the light beam, such as a superposition state.

Another way to look at squeezing is to consider it in terms of correlations. Increasingly in quantum information applications, squeezing is the suggested tool for the generation of quantum correlation and entanglement [97]. How may we demonstrate the generation of quantum correlation with a squeezed source? What does it mean to have a quantum correlation?

In general, a quantum correlation between two light beams means that by measuring the signal on one of the beams we may infer, to better than the QNL, the signal on the other beam. That is to say, the conditional variance between the beams is below the QNL. One way to demonstrate the effect of quantum correlation is by doing the experiment shown in figure 7.9. In this setup, the photocurrents from the homodyne detectors were sent through identical mixers (Minicircuits ZAD-8). The mixer local oscillator frequency

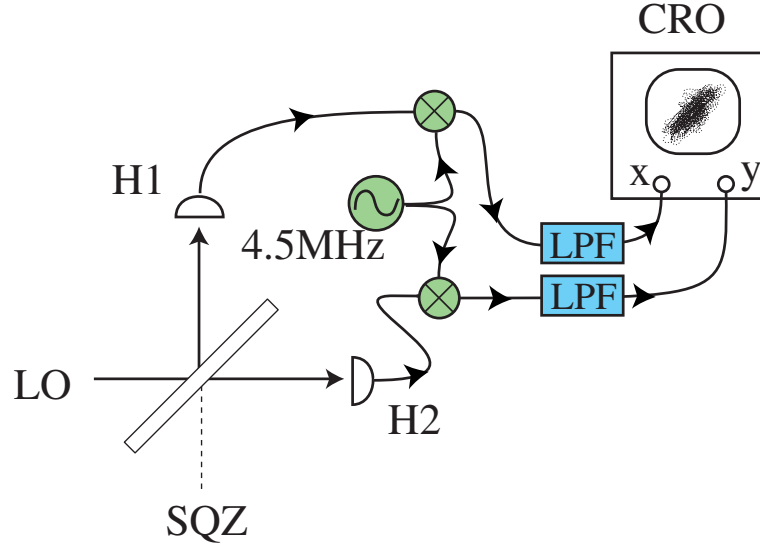


**Figure 7.9:** Setup for measuring quantum correlations

was set at 4.5MHz which corresponds to the regime of optimum squeezing. The output of the mixers was then sent through low pass filters with a corner frequency of 100kHz. This gave an effective measurement bandwidth of 200kHz, i.e.  $4.5 \pm 0.1$ MHz. The result was a real time view of the photocurrents in a 200kHz bandwidth as seen from a reference frame rotating at 4.5MHz. When the squeezing was blocked, and only the local oscillator beam was incident on the beamsplitter, we obtained the data shown in figure 7.10 (a). There is no correlation in this data ( $C^2 = 0.007 \pm 0.01$ ). This indicates that the local oscillator has the same noise statistics as the quantum vacuum incident on the empty beamsplitter port, meaning that the local oscillator beam is at the QNL. If the local oscillator contained a signal above the quantum noise, then a signal would appear on both the photocurrents and we would see a correlation along the line  $H1=H2$ . The variance of the individual photocurrents H1 and H2 is the variance of the data in the H1 and H2 directions respectively.

An amplitude squeezed state was then injected into the beamsplitter in place of the vacuum. The reduced noise of the squeezing created a correlation between the photocurrents ( $C^2 = 0.17 \pm 0.01$ ), as shown in figure 7.10 (b). The amount of squeezing present for these measurements was measured at 3.8dB without correction for the detector dark noise<sup>4</sup>. The variance of the data in the H1 and H2 directions has been reduced, indicating that both photocurrents are squeezed below the quantum noise. The correlated nature of the data suggests that a measurement of the photocurrent H1 will allow prediction of H2 with uncertainty below the QNL.

To make this “handwavy” explanation of correlation more concrete, we may calculate the conditional variance of the experimental data as a function of the data angle. The conditional variance is given by

$$V_{H1|H2} = V_{H2} (1 - C^2) \quad (7.14)$$

<sup>4</sup>Subtracting the dark noise in this case gives 4.5dB of squeezing. The reason for quoting the non-corrected figure is that we cannot subtract the dark noise from the correlation data, so it is the uncorrected number that we require.



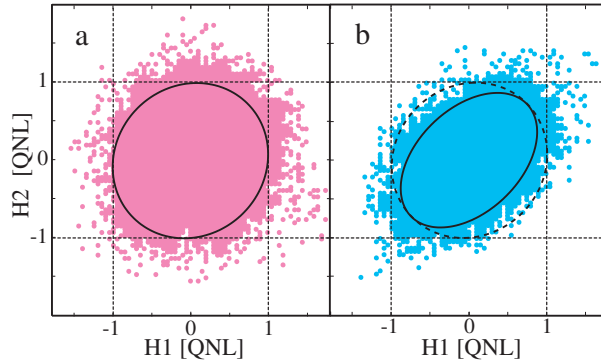


**Figure 7.10:** Correlation between the photocurrents of H1 and H2 at 4.5MHz for (a) vacuum noise and (b) amplitude squeezing incident on the beamsplitter. The quantum noise is shown for reference. The ellipses are the square root of the conditional variance, normalised to the QNL. Data is not to scale with the conditional variance.

To calculate a contour of conditional variance, we evaluate the variance of the data in the H2 direction ( $V_{H2}$ ) and the correlation coefficient between the H1 and H2 directions ( $C^2$ ). The data is then rotated by 1 degree and the variance in the H2 direction is recalculated along with the correlation coefficient. This is repeated until all angles have been spanned.

The lines plotted on figure 7.10 are actually the conditional deviation, which naturally enough, is given by

$$\sigma_{H1|H2} = \sqrt{V_{H2}(1 - C^2)}. \quad (7.15)$$

On figure 7.10 (a), the data yielded a near circle. Ideally this would be exactly circular, however the residual correlation ( $C^2 = 0.007 \pm 0.01$ ) means that this line is slightly elliptical, although this is of no statistical significance. With squeezing, the conditional deviation is found to give the ellipse shown in figure 7.10 (b). The ellipse lies inside the quantum noise circle found from the data of (a).

Using the scale defined by the quantum noise circle, the ellipse of figure 7.10 (b) may be used to find the conditional variance between the photocurrents and thereby verify the existence of quantum correlation. The conditional variance,  $V_{H1|H2}$ , is equal to the square of radius of the ellipse at the point where it crosses the H2 axis. Similarly the conditional variance  $V_{H2|H1}$  is the square of the radius of the ellipse as it crosses the H1 axis. In both cases a conditional variance of  $0.62 \pm 0.03$  is found. This conditional variance may be compared to that predicted for a 50% beamsplitter with 3.8dB of squeezing, as calculated in chapter 4 in the context of QND measurement. From equation 4.12, we expect to find a conditional variance of 0.59, which is good agreement with the correlation measurement.

### 7.5.1 A more detailed theory of correlation measurement

At  $0^\circ$  and  $90^\circ$ , the ellipse of figure 7.10 gives the conditional deviation between the photocurrents. What is the significance of the other angles? We now consider the squeezed quadrature incident on the homodyne beamsplitter to be  $\delta X_a$ , and the vacuum noise to be  $\delta X_b$ . These may be phase or amplitude quadratures so the usual superscripts have been omitted. The quadratures  $\delta X_1$  and  $\delta X_2$  incident on the detectors are therefore given by:

$$\delta X_1 = \frac{1}{\sqrt{2}}(\delta X_b + \delta X_a)$$

$$\delta X_2 = \frac{1}{\sqrt{2}}(\delta X_b - \delta X_a) \quad (7.16)$$

These two quadratures are detected via the photocurrent of the detectors, and we calculate the conditional variance between the two photocurrents. We must now include the anticlockwise-rotation by angle  $\theta$  into the calculation. We do this by writing:

$$\begin{pmatrix} \delta X_{1r} \\ \delta X_{2r} \end{pmatrix} = \begin{pmatrix} \cos \theta & -\sin \theta \\ \sin \theta & \cos \theta \end{pmatrix} \begin{pmatrix} \delta X_1 \\ \delta X_2 \end{pmatrix} \quad (7.17)$$

The conditional variance between the rotated quadratures  $\delta X_{1r}$  and  $\delta X_{2r}$  will then be given by:

$$V_{1r|2r} = \frac{1}{2}(1 - \sin 2\theta)V_b + \frac{1}{2}(1 + \sin 2\theta)V_a - \frac{(V_b - V_a)^2 \cos^2 2\theta}{2(1 + \sin 2\theta)V_b + 2(1 - \sin 2\theta)V_a} \quad (7.18)$$

The conditional deviation, as plotted in figure 7.10, is given by the square root of equation 7.18.

The meaning of our conditional variance at different angles now becomes clear. In particular we note that

$$\text{when } \theta = \pi/4, \quad V_{r1|r2} = V_a \quad (7.19)$$

and

$$\text{when } \theta = -\pi/4, \quad V_{r1|r2} = V_b \quad (7.20)$$

The conditional deviation curve therefore contains a measurement of the noise present in the beams incident on the beamsplitter. Going back to the ellipse in figure 7.10, we see that the conditional deviation at  $\theta = -\pi/4$  is indeed at the QNL, as expected. At  $\theta = \pi/4$  we find a radius of  $0.65 \pm 0.01$ , which when squared gives a variance of  $0.41 \pm 0.02$ , or  $3.7 \pm 0.1$ dB of squeezing, as expected.

### Correlation measurement of an entangled beam

One could imagine that this type of measurement may be useful in the measurement of ‘‘EPR’’ entangled optical beams. A pair of entangled beams may be manufactured by mixing two squeezed sources on a beamsplitter with a  $\pi/2$  phase shift between the squeezed quadratures [97]. In equation 7.16, we assume that the quadrature  $\delta X_b$  contains the excess anti-squeezing noise from one of the squeezed beams, and  $\delta X_a$  contains the squeezed noise of the other beam. The entangled beams are therefore individually noisy, yet the correlation between the two beams is strong. For entanglement we require that the conditional variance of the two photocurrents should be less than one, indicating that the beams are quantum correlated. Using the above model, we expect the outcome of the correlation measurement to look like figure 7.11 for the mixing of two minimum uncertainty, 6dB squeezed beams (6dB squeezing is equal to a variance of 0.25 on a linear scale). The radius  $a=0.5$  is the standard deviation of  $\delta X_a$ ,  $b=2$  is the standard deviation of the anti-squeezing in  $\delta X_b$  and  $c=0.67$  is the conditional deviation between the beams. A positive correlation with conditional variance below the QNL is clearly evident.

So far we have only investigated a single quadrature of the entanglement, and found the two beams to be correlated. Entangled beams are, however, entangled in any orthogonal quadrature basis. To look at the conjugate quadrature, we return to equations 7.16 and

assume that  $\delta X_a$  is anti-squeezed while  $\delta X_b$  is squeezed. This is the reverse of the previous situation and therefore represents the orthogonal quadrature to that shown in figure 7.11. The expected correlation diagram is shown in figure 7.12 where  $a=2$  is the standard deviation of the anti-squeezing  $\delta X_a$ ,  $b=0.5$  is the standard deviation of the squeezing in  $\delta X_b$  and  $c=0.67$  is the conditional deviation between the beams. In this case a conditional variance below the QNL is seen, however the correlation is now negative unlike the case of figure 7.11.

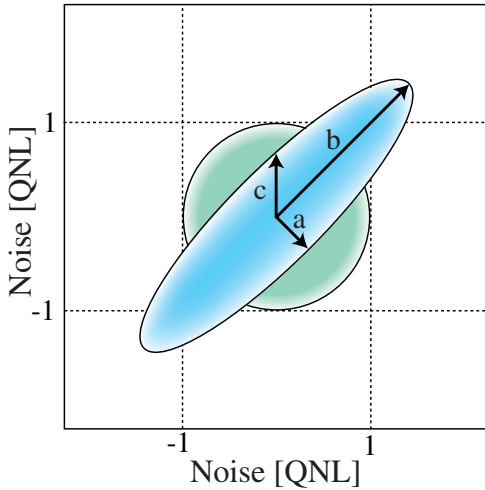


**Figure 7.11:** Expected result of a correlation measurement on one quadrature of an entangled beam. The circle shows the quantum noise, the radius  $a$  is the squeezing of  $\delta X_a$ ,  $b$  is the anti-squeezing of  $\delta X_b$  and  $c$  is the conditional deviation.

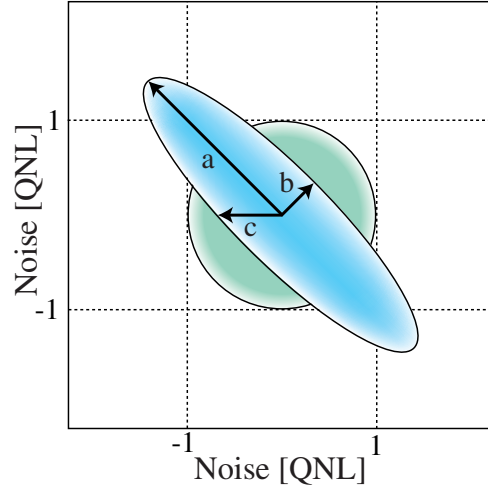


**Figure 7.12:** Expected result of a correlation measurement on one quadrature of an entangled beam. The circle shows the quantum noise, the radius  $a$  is the anti-squeezing  $\delta X_a$ ,  $b$  is the squeezing  $\delta X_b$  and  $c$  is the conditional deviation.

## 7.6 Conclusions

The experiment described in this chapter was shown to be capable of generating 5.5dB of observable amplitude squeezing, with locked quadrature phase. The amount of squeezing may have been limited by ‘green induced infra-red absorption’. Recent characterisation of this effect has shown it to be significant in our crystal material.

The stability of our experiment made possible a time domain measurement of the quantum correlations created by squeezing. Analysis of the results gave the noise of both beams incident on the homodyne beamsplitter and the conditional variance between the homodyne photocurrents. This technique may be a useful method of characterising entangled quantum states.

---

# Quantum nondemolition experiments: realisation of enhancement

---

This chapter contains the results of our QND experiment. In particular, it is shown that a feedforward loop may be used to enhance the quality of the signal output beam by improving the signal-to-noise ratio, as suggested in chapter 4. The end result is a QND system that shows a record signal transfer efficiency while also achieving good conditional variance.

## 8.1 Introduction

In Chapter 4, I discussed the possibility of improving a QND measurement using feedforward. In particular, the enhancement of a QND experiment based on a squeezed light beamsplitter was modelled. In chapter 7, I presented results of a squeezing experiment that showed strong, stable amplitude squeezing. Prior to this, in chapter 3, results of a feedforward experiment clearly demonstrated noiseless amplification using feedforward. All the pieces of the QND enhancement scheme are therefore in place. In this chapter the pieces are put together. The QND device to be enhanced is a squeezed light beamsplitter. The squeezing is in the amplitude quadrature, so amplitude quadrature feedforward is used for the enhancement of the QND measurement.

To evaluate the success of the QND measurements, the two quantities used to quantify QND in chapter 4 will be measured experimentally. These are the total signal transfer coefficient,  $T_{s+m}$ , which is defined in equation 4.6, and the conditional variance, as defined in equation 4.11.

Extensive discussion of the literature and methods relevant to the various components of this experiment may be found in the preceding chapters. The methods and results of the QND experiments will therefore be presented without further introduction.

The chapter is laid out as follows: the next section contains a brief description of the experimental design. Results taken with a 50% beamsplitter are then presented in the section 8.3. The problems associated with signal amplification and attenuation are discussed in section 8.4. In section 8.5 the beamsplitter ratio is changed to 92% and the results improve as suggested by the theoretical modelling in chapter 4. Finally, the results of our experiment are compared to previous QND experiments in section 8.6.

## 8.2 Experimental design

The resource used for the QND system is the squeezing experiment described in detail in the preceding chapter. The only change required for an initial test of the QND system is the use of the amplitude modulator A1 shown in the experimental setup of figure 7.2. A simplified diagram of the essential experimental components is shown in figure 8.1. The

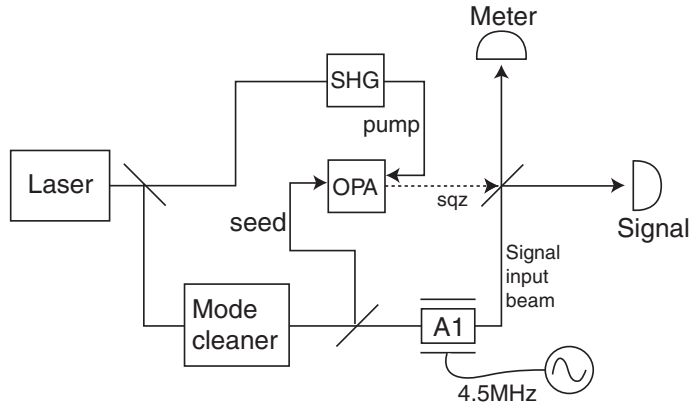


**Figure 8.1:** Simplified diagram of the QND experiment with a beamsplitter. The detectors H1 and H2 of figure 7.2 are now the “signal” and “meter” detectors.

detectors H1 and H2 of figure 7.2 now become the meter and signal detectors for the QND system. The modulator A1 is used to place a test signal on the input to the QND system to allow testing of the meter and signal transfer coefficients using the same methods applied in chapter 3.

## 8.3 QND results with the 50% beamsplitter

As discussed in chapter 4, the performance of the QND system with feedforward is strongly dependant on the beamsplitter ratio. We therefore performed the QND experiment with two different beamsplitter reflectivities, 50% and 92%. The 50% beamsplitter experiment was naturally performed first as the balanced homodyne beamsplitter was already in place. The first step was to measure the transfer coefficients  $T_s$  and  $T_m$ . This is the same measurement as that performed in the phase feedforward work (chapter 3) and the measurement was performed in precisely the same way.

An important issue in the QND experiments that follow is the calibration of measurements to the QNL. For the squeezing experiments of chapter 7, the noise of the squeezing was calibrated using a balanced homodyne detection system. The vacuum input to the homodyne beamsplitter was used as the calibration noise source, as described in section 2.5.3. In the case of the QND experiments, the meter and signal beam measurements are made using single detectors, and some other method of calibrating the signals to the QNL is required.

The calibration method used for the QND work relies on the measured noise statistics of the signal input beam at 4.5MHz. The “signal input beam” in the QND experiments was referred to as the “local oscillator beam” in the context of squeezing measurements. Measurements in the previous chapter showed the signal input beam to be quantum noise limited at 4.5MHz. The best proof of this is the correlation measurement shown in figure 7.10 (a). If the noise on the signal input beam were above the QNL, then this data

would show a positive correlation. As it does not, we may safely calibrate the QNL of our meter and signal detectors at 4.5MHz on the basis of the noise power present on the signal input beam. The laser noise will also lie at the QNL for all frequencies above 4.5MHz due to the filtering effects of the mode cleaner. However, at higher frequencies the squeezing decreases. 4.5MHz is therefore the best operating point.

### 8.3.1 The definition and measurement of the transfer coefficients.

The modulator A1 was used to place a small test signal on the input to the QND system. It is this signal that is used to probe the signal transfer abilities of the QND system. The first step involved in determining signal transfer coefficients was to measure the signal-to-noise ratio at the input to the beamsplitter. This was found by measuring the sum of the meter and signal detector outputs. All of the light incident on the QND system is measured by these detectors. The sum of their photocurrents therefore represents the total signal input to the QND system. A measurement of the sum photocurrent is shown by the curves (a) of figures 8.2 and 8.3. The height of the signal at 4.5MHz is 2.4dB above the quantum noise background, which gives the signal-to-noise ratio to be 0.74 on a linear scale. (Note that a signal which has the same power as the noise-floor yields a signal 3dB above the noise. This is why a signal 2.4dB above the noise has a signal-to-noise ratio of less than 1.) This result may be compared to the data in curves (b) of figures 8.2 and 8.3. This data was taken with no squeezing incident on the beamsplitter, and shows the signal-to-noise ratios for the individual meter and signal detectors. The loss in signal-to-noise ratio compared to the input signal is clearly evident. In both cases the signal-to-noise ratios are found to be 0.37 (again on a linear scale). This gives  $T_s = T_m = 0.50 \pm 0.03$ . This is in agreement with the predictions of a 50/50 beamsplitter with lossless detection. Although our detectors are not really lossless, if we measure the input signal with the same detectors as those used to measure the signal and meter outputs, then the efficiency of detection cancels out of the measurement. The sum of the meter and signal transfer coefficients gives  $T_{s+m} = 1$  as expected .

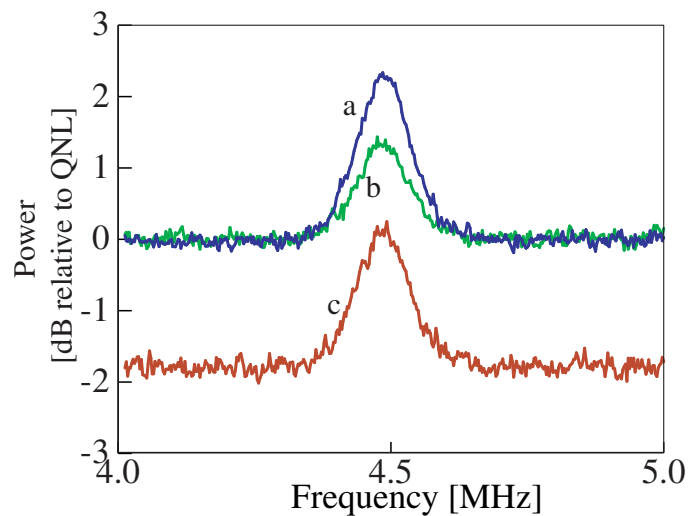


**Figure 8.2:** Data used to calculate  $T_s$  for a 50/50 beamsplitter with no feedforward. **a:** input signal level; **b:** output signal without squeezing; **c:** output signal with squeezing. All results taken with RBW=30 kHz, VBW=30 Hz, over an average of 3 traces.

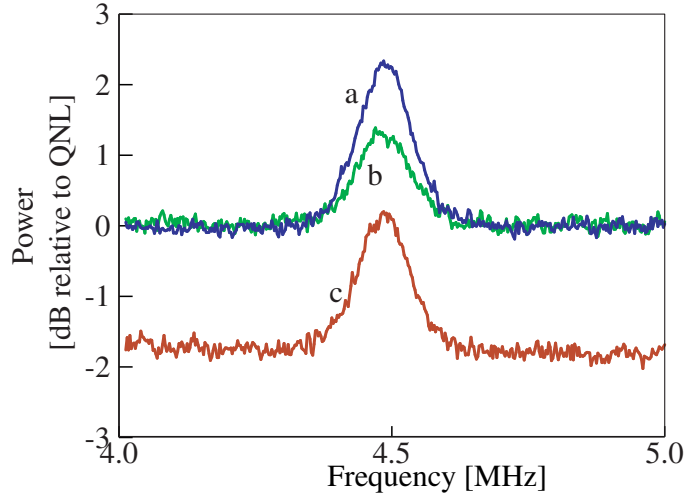


**Figure 8.3:** Data used to calculate  $T_m$  for a 50/50 beamsplitter with no feedforward. **a:** input signal level; **b:** output meter without squeezing; **c:** output meter with squeezing. All results taken with RBW=30 kHz, VBW=30 Hz, over an average of 3 traces.

The theory of chapter 4 calculated the transfer coefficients by comparing the meter and signal photocurrents to the optical signal of the input beam to the QND system. This is fine to do in a theoretical model, however when it comes to interpreting an experiment, things are not quite so easy. The optical signal at the input of the QND system cannot be measured except by using detectors which do not have perfect efficiency. The optical signal-to-noise ratio,  $\text{SNR}_{\text{optical}}$ , on the input beam must therefore be inferred by using the detector efficiency. In our case, with a quantum efficiency of  $\eta_d = 0.93 \pm 0.05$  and a measured input signal-to-noise ratio ( $\text{SNR}_{\text{measured}}$ ) of 0.74, the input optical signal-to-noise ratio is found to be:

$$\text{SNR}_{\text{optical}} = \frac{\text{SNR}_{\text{measured}}}{\eta_d} = \frac{0.74}{0.93} = 0.80. \quad (8.1)$$

Using  $\text{SNR}_{\text{optical}}$  as the input signal-to-noise ratio, the transfer coefficients may be recalculated as  $T_s = T_m = 0.47$  and  $T_s + T_m = 0.93 \pm 0.05$ . Not surprisingly, the total signal transfer is now equal to the efficiency of the detectors, as was the case in the models of chapter 4.

Both these methods of measuring the transfer coefficients are valid. The choice of which to use depends upon what is important to the particular application of the QND device and whether one wishes to describe the whole measurement system, or just the optical part of the QND device. The two types of transfer coefficient will be referred to as the “loss-free” type, in which the detector loss is cancelled, and the “lossy” type, in which the detector efficiency is included. Historically, different experiments have used different definitions. For example, Bruckmeier *et al.* [19] and Bencheikh *et al.* [5] used the lossy definition, while Roch *et al.* [100] and Levenson *et al.* [77] used the loss-free definition. We note that there is no such problem comparing the theory and experiment when it comes to the conditional variance. The theory of chapter 4 calculated the conditional variance on the basis of the photocurrents only, and did not depend on knowing anything about actual optical noise. The measured conditional variance is always “lossy” since the detector efficiency is always included.

Having verified the behaviour of the beamsplitter without squeezing, the next transfer coefficient to measure was that with squeezing incident on the beamsplitter. The signal-to-noise ratios in this case are shown in traces (c) of figures 8.2 and 8.3. These results show an obvious improvement in the signal-to-noise ratio over the results with no squeezing. We find a signal-to-noise ratio of 0.55 for the meter beam and 0.53 for the signal beam. This results in loss-free transfer coefficients of  $T_s = 0.72 \pm 0.02$  and  $T_m = 0.75 \pm 0.02$ , so that  $T_{s+m} = 1.47 \pm 0.03$ .

### 8.3.2 Measurement of the conditional variance

The conditional variance was measured in the previous chapter via the correlation measurement. This method showed a conditional variance of 0.62. However, this technique does not provide a measurement free of the effects of detector electronic noise. Instead we may measure the conditional variance using the spectrum analyser and subtract the dark noise in the usual manner (see appendix A).

The conditional variance may be expressed as:

$$V_{s|m} = V_s(1 - C_{(s,m)}^2) = V_s - \frac{|\langle \delta X_s \delta X_m \rangle|^2}{V_m} \quad (8.2)$$

where  $\delta X_{s(m)}$  are the fluctuations of signal (meter) output quadratures,  $V_{s(m)}$  are their corresponding variances and  $C_{(s,m)}$  is the correlation between the signal and meter output beams. The value of the ‘‘cross’’ term may be found by using

$$2 \langle \delta X_m \delta X_s \rangle = \frac{1}{2} \langle (\delta X_m + \delta X_s)^2 \rangle - \frac{1}{2} \langle (\delta X_m - \delta X_s)^2 \rangle = V_{\text{sum}} - V_{\text{diff}} \quad (8.3)$$

where  $V_{\text{sum(diff)}}$  is the variance of the sum (difference) of the meter and signal photocurrents. The sum and difference can be measured with the same equipment previously used for homodyne detection of squeezing.

A second method to measure conditional variance comes straight from the original definition. The conditional variance says how far below the QNL one may infer the information on signal beam, given the information on the meter beam. Implementing this idea, one may subtract the meter and signal beams with variable gain and measure this noise level relative to the QNL of the signal beam (for a good example of this technique see [18]). Both these methods of measuring  $V_{s|m}$  were used at different stages of the QND experiment.

For the 50% beamsplitter, the conditional variance was determined using relation 8.3. This requires knowledge of the spectra of the signal and meter photocurrents as well as the sum and difference of these photocurrents. The sum photocurrent is just a measurement of the input signal beam, which from the correlation measurements of the previous chapter, is known to be at the QNL at 4.5MHz. The noise of the individual photocurrents may be measured from lines (c) of figures 8.3 and 8.2. Away from the modulation peak at 4.5MHz, these traces show the noise of the signal and meter photocurrents. The difference photocurrent is a measurement of the squeezing incident on the beamsplitter and may be measured as in the previous chapter. A measurement of the subtracted signal is shown in figure 8.4 and it shows 4.5dB of amplitude quadrature squeezing. From all these measurements, and equation 8.3, the conditional variance was found to be  $0.51 \pm 0.04$ .



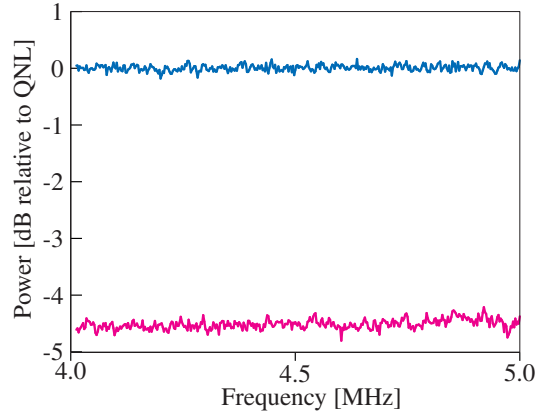


**Figure 8.4:** Squeezing present during the QND experiment as measured by the subtraction of the meter and signal detectors. RBW=30 kHz, VBW=30 Hz, over an average of 3 traces.

### 8.3.3 The addition of feedforward to the 50% beamsplitter

The next step in the experiment was the addition of the feedforward loop, which was predicted in chapter 4 to improve the value of  $T_s$ . The experimental setup is shown in figure 8.5. The high pass filter at 2MHz was required to prevent saturation of the

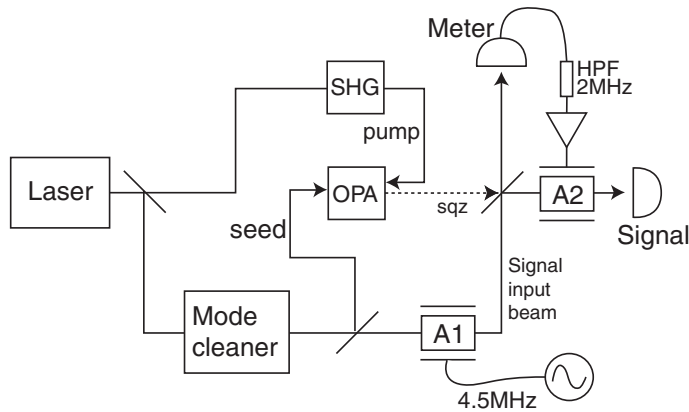


**Figure 8.5:** Simplified diagram of the QND experiment with feedforward.

amplifiers at low frequencies due to the resonant relaxation oscillation of the laser, which lies at 500kHz.

The amplitude modulator, A2, was run in a low loss configuration. An electro-optic amplitude modulator provides the most efficient modulation when the modulator has 50% loss at the output polariser [133]. This amount of loss would spell the death of high performance QND. By adjusting the output polariser, the modulator in our experiment was forced to run at 95% transmission. The disadvantage of this setup is the requirement of higher gain in the feedforward electronics. In our case, we had two amplifiers (Q-BIT QB 538 8745-04 and ANZAC AM 110) which gave a total of 70dB electronic gain. The other factor which is important in feedforward is the phase of the electronic gain, as shown in figure 4.3. In our case, to obtain the correct phase at 4.5MHz, 8 metres of coaxial cable was required as a delay line.

A further complication of the feedforward technique is the behaviour of the modulator. Ideally we want a flat amplitude response over a wide frequency range. In our case the

amplitude modulator (New Focus 4104) had the modulation transfer function shown in figure 8.6. This erratic (but reproducible) transfer function means that the feedforward

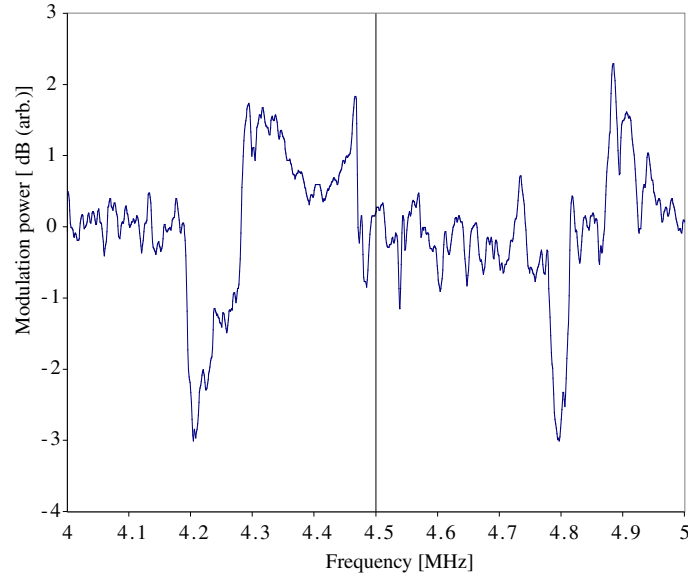


**Figure 8.6:** Response of the New Focus 4104 amplitude modulator measured using the spectrum analyser and tracking generator (0dBm). RBW=100kHz, VBW=300Hz.

gain and phase will be changing rapidly as a function of frequency. This problem may be overcome, in principle at least, through improved modulator design.

In the QND experiment without feedforward, it was possible to compare a signal at 4.5MHz with the noise floor at nearby frequencies to measure the signal transfer coefficients. This will obviously not be possible with feedforward because the noise-floor, even at frequencies close to the signal, will experience different amplification to the signal. Instead, the way to measure the signal transfer is to make separate measurements of the signal and noise floor at 4.5MHz by switching the modulation on and off.

### Transfer coefficient measurement

The point of the feedforward is to improve the value of the signal transfer coefficient  $T_s$ . A measurement of this is shown in figure 8.7. Part (a) shows the input signal-to-noise ratio, and figure (b) shows the output signal-to-noise ratio. Calculation of  $T_s$  from this data give a loss-free  $T_s$  of  $0.90 \pm 0.02$ . The measurement of the meter transfer coefficient is independent of the feedforward and therefore remains unchanged at  $T_m = 0.75 \pm 0.02$  (loss-free). The total loss-free signal transfer is therefore  $T_{s+m} = 1.66 \pm 0.03$ .

### Conditional variance measurement

The conditional variance in this case was measured as before by taking the sum and difference photocurrents. The feedforward means that the sum photocurrent will no longer lie at the QNL. The results are shown in figure 8.8. Using the variance of the individual meter (figure 8.3 c) and signal beams (figure 8.7 b), we find a conditional variance of  $0.55 \pm 0.03$ . The conditional variance in this case has increased due to the loss of the modulator (transmission 95%) and the electronic noise of the meter detector, which is now introduced into the signal beam.

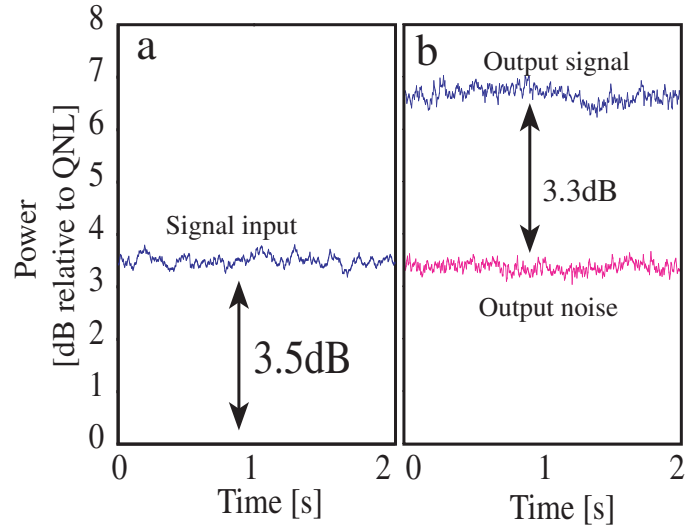


**Figure 8.7:** a) Input signal level, quantum noise is not shown; b) output signal level and output signal noise-floor. All results taken at 4.5 MHz with RBW=30 kHz, VBW=30 Hz.

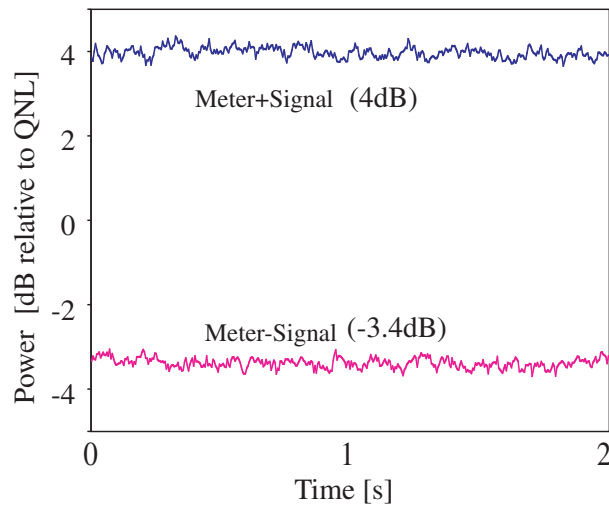


**Figure 8.8:** Noise of the sum and difference photocurrents with feedforward. All results taken at 4.5 MHz with RBW=30 kHz, VBW=30 Hz.

### 8.3.4 Summary of the 50% beamsplitter results

A summary of the QND results is given in table 8.1, along with a comparison to the theoretically predicted values, generated using the equations of chapter 4, assuming 5.2dB of squeezing entering the QND system. The value of 5.2dB is inferred from the squeezing measured in figure 8.4 using the detection efficiency of  $\eta_d = 0.93$ . A graph the lossy experimental values and the theory is shown in figure 8.9. Points (a) and (b) are in good agreement with theoretical predictions. Although the feedforward result, (c), shows improved signal transfer, the increase is smaller than predicted. This may be due to the electronic noise of the detectors which has not been included in the theoretical model.

Conditions	Parameter	Loss-free	Lossy	Theoretical (lossy)
Vacuum Input	$T_s$ ( $\pm 0.02$ )	0.50	0.47	0.47
	$T_m$ ( $\pm 0.02$ )	0.50	0.47	0.47
	$V_{s m}$ ( $\pm 0.03$ )	N/A	1.00	1.00
	$T_{s+m}$ ( $\pm 0.03$ )	1.00	0.93	0.93
Squeezed Input	$T_s$ ( $\pm 0.02$ )	0.72	0.67	0.69
	$T_m$ ( $\pm 0.02$ )	0.75	0.70	0.69
	$V_{s m}$ ( $\pm 0.04$ )	N/A	0.51	0.52
	$T_{s+m}$ ( $\pm 0.03$ )	1.47	1.37	1.38
Squeezed Input with Feedforward	$T_s$ ( $\pm 0.02$ )	0.90	0.84	0.91
	$T_m$ ( $\pm 0.02$ )	0.75	0.70	0.69
	$V_{s m}$ ( $\pm 0.04$ )	N/A	0.55	0.53
	$T_{s+m}$ ( $\pm 0.03$ )	1.66	1.54	1.60

**Table 8.1:** QND results with a 50/50 beamsplitter.

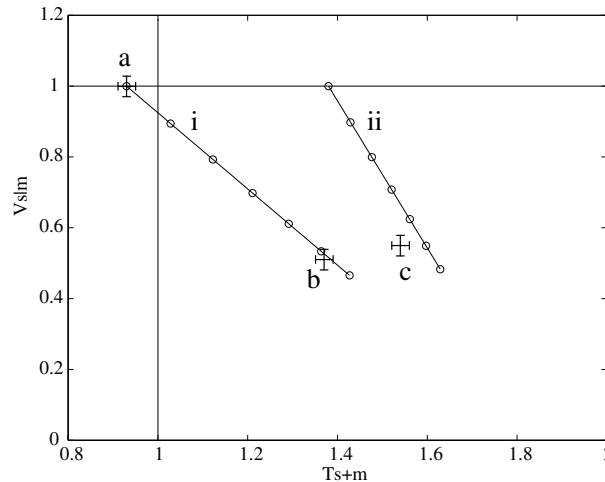


**Figure 8.9:** Comparison of theory to lossy experimental results. a) Normal 50/50 beamsplitter; b) 50/50 beamsplitter with squeezing; c) 50/50 beamsplitter with squeezing and feedforward; i) theory without feedforward; ii) theory with feedforward. Each circle in the theory plots indicates an increase in squeezing of 1dB, starting at 0dB at the top of the lines. The bottom point corresponds to 6dB of squeezing. Parameters used in the model are detection efficiency of 93% and modulator transmission of 95%.

## 8.4 How ND is the QND?

The original idea of QND was to measure a variable without altering it in any way. As outlined in the theoretical discussion of this experiment, there is a problem with a squeezed beamsplitter measurement being called nondemolition when the intensity of the output beam is different to the input, and the signal output is amplified with respect to the QNL.

Both these problems are present in the above measurements. In the case of the beamsplitter with no feedforward, the output beam has half as much power as the input. The noise-floor of the signal output is 1.7dB below the QNL (figure 8.2), whereas the input signal noise-floor was at the QNL. With feedforward, the output intensity is also half the input intensity, and now the noise-floor of the signal output is raised 3.5dB above the QNL. In both cases the output signal will react differently to attenuation compared to the input signal.

As an example, consider the signals shown in figure 8.7. Attenuating the signal shown in part **a** of figure 8.7 by 50% will result in a signal which is 2.1dB above the noise-floor. If we attenuate the output beam shown in part **b** of figure 8.7, then the signal will be 2.5dB above the noise-floor. The output signal with feedforward is therefore less sensitive to loss. In section 4.4 this problem was described theoretically using the sensitivity,  $S$ , and the problem was solved by introducing a bright squeezed beam which deamplified the signal back to the QNL, and corrected for the change in intensity of the output.

We do not have a spare squeezed beam in our experimental setup. Instead, the amplification problem may be overcome by using feedforward in a more considered fashion. In the case of a squeezed light beamsplitter without feedforward, the signal output is de-amplified. The effect of feedforward is to amplify the output signal. There will be a particular feedforward gain that will cancel out the squeezing de-amplification to generate an output signal with the correct noise-floor (as modelled in section 4.4). An experimental demonstration of this technique is presented in section 8.5.

The only other problem is the loss of optical power. In principle, this could be solved if we adjusted our OPA seed beam to high enough power, so that the squeezing was sufficiently bright to add back the power which is lost to the meter detector. Unfortunately this is difficult as the transmission of the OPA cavity is very low (<1%), meaning that the a seed beam of >100mW would be required to provide sufficient power in the squeezed beam. This was not feasible in our experiment due to the amount of laser power required to pump the second harmonic generator.

## 8.5 QND with a 92/8 beamsplitter

By changing the beamsplitter ratio, we may alter the efficiency of the QND machine (see section 4.3.2). A beamsplitter with 8% transmission was chosen. With such an asymmetric power splitting ratio, we are left with the possibility that one detector has about 10 times more incident power than the other detector. This is a problem because the standard detectors need more than 1mW so that the small signals are above the dark noise of the detector, but less than 3mW so that the response of the operational amplifiers is still linear. The meter detector, which will see the most power, was therefore changed to a model with reduced transimpedance gain to ensure linear detector response at high optical powers. The maximum power of the modified detector was 10mW.

### 8.5.1 Measurement of the transfer coefficients.

The meter transfer is now expected to be very high since 92% of the input is sensed by the meter detector, and the vacuum input to the beamsplitter has been plugged by the squeezed source. The measurement of the meter signal transfer with squeezing is shown in figure 8.10 and shows a loss free  $T_m$  of  $0.96 \pm 0.02$ .

As before this transfer coefficient is independent of the feedforward, and therefore constant throughout the experiments. The results for the signal transfer coefficients are summarised in figure 8.11. Subplot (a) shows the input signal level. The output signal with no feedforward, shown in (b), is now very poor because only 8% of the input signal is sent to the signal detector.  $T_s$  was measured as  $0.16 \pm 0.03$ . The noise-floor of the signal, as for the case of the 50/50 beamsplitter, is sub-QNL due to the  $\sim 4.5$ dB of squeezing added at the beamsplitter. The feedforward may now be turned on to maximise the value of  $T_s$  as shown in (c). In this case we find  $T_s = 0.85 \pm 0.02$ . The final result, (d), shows the case of feedforward amplification used to balance the squeezing de-amplification. In this case the noise-floor of the signal output is seen to be at the QNL, just like the signal input. The sensitivity,  $S$ , is therefore 0dB. For this measurement,  $T_s = 0.66 \pm 0.02$ .

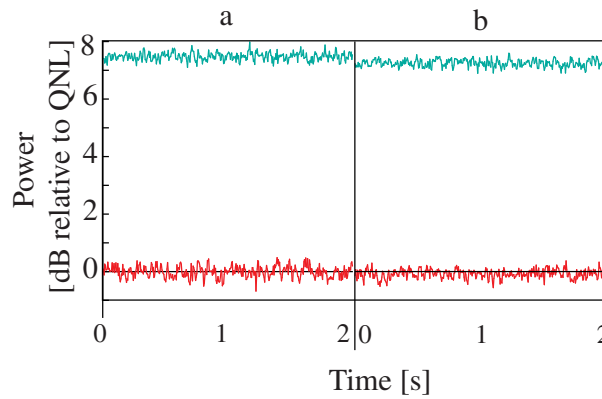


**Figure 8.10:** Meter transfer with a 92% beamsplitter. a) Signal input; b) meter output. All results taken at 4.5 MHz with RBW=30 kHz, VBW=30 Hz.

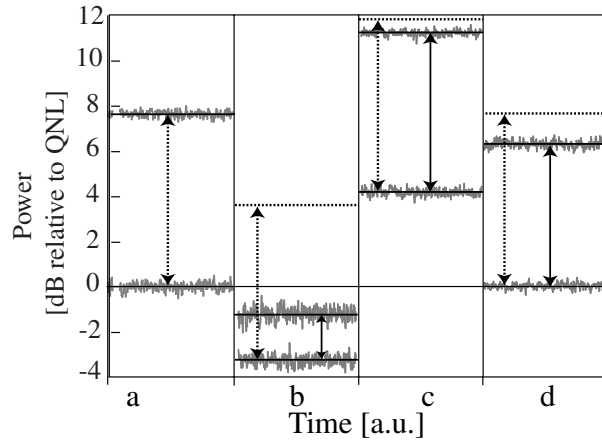


**Figure 8.11:** Data used to calculate the value of  $T_s$  for the 92/8 beamsplitter. **a:** the input signal level, **b:** the output signal with no feedforward, **c:** The output signal with feedforward to maximise  $T_s$  and **d:** the output signal with the gain adjusted to give  $S = 0$ dB. The dashed lines and arrows indicate the input signal level, as measured in **a**. All results taken at 4.5 MHz with RBW=30 kHz, VBW=300 Hz, each trace is averaged 30 times.

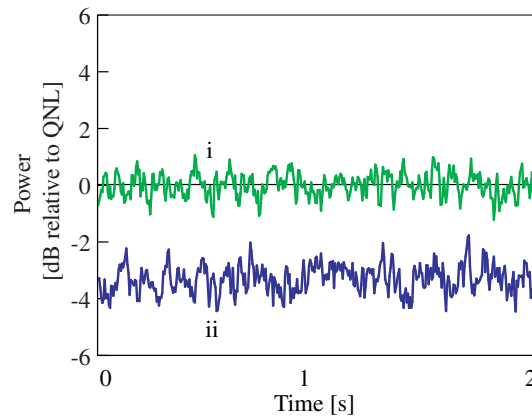


**Figure 8.12:** Conditional variance measurement without feedforward and beamsplitter ratio 92/8. i) Quantum Noise; ii) Conditional variance. All results taken at 4.5 MHz with RBW=30 kHz, VBW=30 Hz.

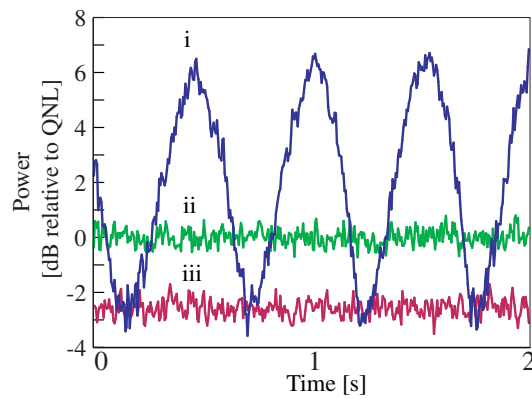


**Figure 8.13:** Conditional variance measurement with feedforward used to maximise  $T_s$  and beamsplitter ratio 92/8. i) Conditional variance as the squeezing phase is scanned, ii) Quantum Noise; iii) Locked conditional variance. All results taken at 4.5 MHz with RBW=30 kHz, VBW=30 Hz.

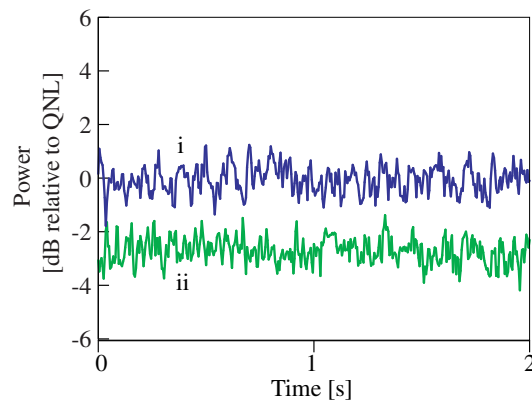


**Figure 8.14:** Conditional variance measurement with feedforward used to correct signal gain and beamsplitter ratio 92/8. i) Quantum Noise; ii) Conditional variance. All results taken at 4.5 MHz with RBW=30kHz, VBW=30Hz.

### 8.5.2 Conditional variance measurements

With the strongly asymmetric power ratio and the non-balanced detectors in the meter and signal, we cannot easily measure the conditional variance by finding the sum and difference of the meter and signal detectors. Instead the conditional variance was measured by minimising the subtraction of the sum and meter photocurrents and comparing this to the signal quantum noise. This gives a noise level to which the signal photocurrent may be suppressed by using the meter photocurrent, as described in the original definition of the conditional variance (section 4.2).

The conditional variance without feedforward is shown in figure 8.12. This is the best conditional variance that we measured with our setup, with a value of  $0.46 \pm 0.03$ . The smaller conditional variance is due to the increased amount of squeezing being directed towards the signal detector, giving lower signal variance.

With the feedforward adjusted to give maximum signal transfer, the conditional variance dropped to  $0.55 \pm 0.03$ , as shown in figure 8.13. This loss is due both to the attenuation of the modulator, which was not present for the previous measurement, and the electronic noise of the meter detector, which is now added to the signal beam.

The final result is that for the conditional variance of the feedforward system with the gain adjusted so that the input and output noise-floors are identical. In this case, the conditional variance is slightly improved since less gain is used in the feedforward loop so less meter detector noise is written onto the signal beam. The conditional variance, as measured from figure 8.14, is  $0.53 \pm 0.03$ .

### 8.5.3 Summary of the 92% beamsplitter results

Results from the asymmetric beamsplitter are summarised in table 8.2, again assuming 5.2dB of squeezing at the OPA output. The theoretically predicted values here do not agree with the measured results as closely as those for the 50/50 beamsplitter. This may be explained by a variety of reasons. The most obvious is that the model is harder to apply. We assumed for these calculations that the amount of squeezing in the beam is 5.2dB, which gives the detected value of 4.5dB as seen in the 50/50 beamsplitter data. However, we cannot actually be sure that this amount of squeezing was present, since the meter and signal detectors no longer constitute a balanced pair of detectors, so the measurement of the squeezing relied on inferring the squeezing from the signal detector which sees 92% of the squeezed beam. This is not as reliable. Another factor is the larger feedforward gain used in these experiments, compared with the symmetric beamsplitter. With increased gain, the amount of electronic noise in the meter detector becomes very important. This noise will be written very strongly onto the signal beam, therefore degrading both  $T_s$  and  $V_{s|m}$ . This is the most likely explanation for the degraded values of  $T_s$  and  $V_{s|m}$  in the presence of feedforward. A graph of the lossy experimental values and the theory is shown in figure 8.15.



Conditions	Parameter	Loss-free	Lossy	Theoretical (lossy)
Squeezed Input	$T_s (\pm 0.02)$	0.16	0.15	0.18
	$T_m (\pm 0.02)$	0.96	0.89	0.90
	$V_{s m} (\pm 0.04)$	N/A	0.46	0.37
	$T_{s+m} (\pm 0.03)$	1.12	1.04	1.09
Squeezed Input with Maximised $T_s$	$T_s (\pm 0.02)$	0.85	0.79	0.91
	$T_m (\pm 0.02)$	0.96	0.89	0.90
	$V_{s m} (\pm 0.04)$	N/A	0.55	0.39
	$T_{s+m} (\pm 0.03)$	1.81	1.68	1.83
Squeezed Input with $S=0\text{dB}$	$T_s (\pm 0.02)$	0.66	0.61	0.70
	$T_m (\pm 0.02)$	0.96	0.89	0.90
	$V_{s m} (\pm 0.04)$	N/A	0.53	0.39
	$T_{s+m} (\pm 0.03)$	1.62	1.51	1.61

**Table 8.2:** QND results with a 92/8 beamsplitter.

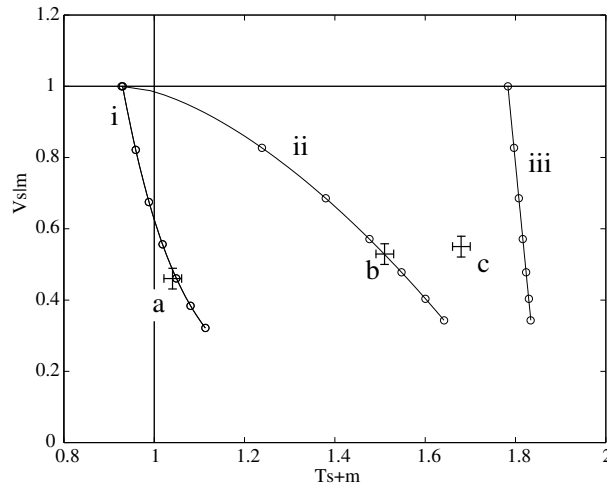


**Figure 8.15:** Comparison of theory to lossy experimental results. a) 92/8 beamsplitter with squeezing; b) 92/8 beamsplitter with squeezing and feedforward used to correct signal amplification; c) 92/8 beamsplitter with feedforward used to maximise  $T_s$ ; i) theory without feedforward; ii) theory with feedforward adjusted to give  $S=0\text{dB}$ ; iii) feedforward used to maximise  $T_s$ . Each circle in the theory plots indicates an increase in squeezing of 1dB, starting at 0dB at the top of the lines. The squeezing at the bottom of the line is 6dB. Parameters used in the model are detection efficiency of 93% and modulator transmission of 95%.

## 8.6 Comparison to other QND experiments

These QND results should be placed in the context of the numerous experiments which have been done over the previous decade. Figure 8.16 shows a plot of our loss-free data with previously published results. We note that our total signal transfer of 1.81 (point E in figure 8.16) is the highest of any of these measurements. The minimum conditional variance that we observed is 0.46 (point A in figure 8.16) compared to 0.45 observed by Roch [100] (point i).

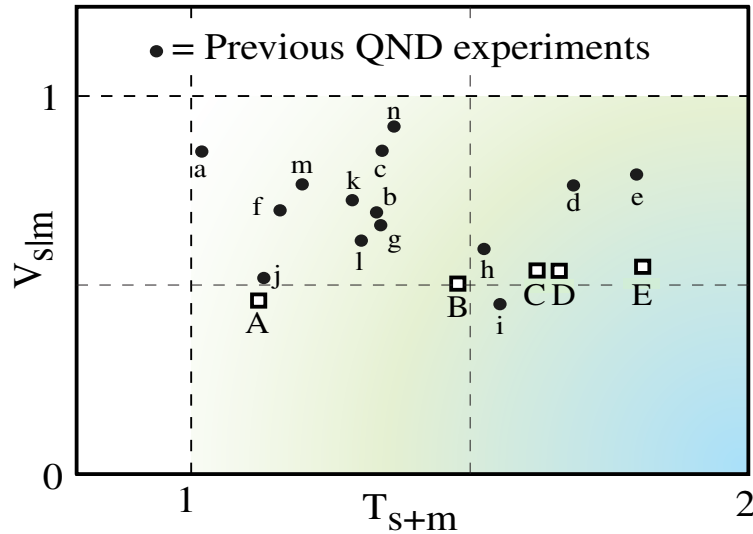


**Figure 8.16:** Summary of QND results compared with other published experiments: a=[99]; b=[77]; c=[92]; d=[44]; e=[98]; f=[89]; g=[4]; h=[5]; i=[100]; j=[20]; k=[19]; l=[118]; m=[37] and n=[70] Our results: A=92% beamsplitter without feedforward; B = 50% beamsplitter without feedforward C = 92% beamsplitter with feedforward tuned to give the output a sensitivity of 0dB; D = 50% beamsplitter with feedforward used to maximise signal transfer and E = 92% beamsplitter with feedforward used to maximise the signal transfer.

## 8.7 Conclusion

The QND results presented in this chapter demonstrate the ability of feedforward to manipulate quantum measurements. The inclusion of feedforward in a QND system also introduces a new level of tunability. The value of the sensitivity and signal transfer may be adjusted by varying the feedforward gain.

The highest total signal transfer measured in our experiment was 1.81, which is a new record. The best conditional variance was measured as 0.46, which is very close to the best previously recorded figure of 0.45. Finally a configuration was demonstrated where the feedforward amplification and squeezing de-amplification could be cancelled out to give a QND result which preserves the sensitivity of the input signal.



---

# Conclusions and future possibilities

---

The major results arising from the work in this thesis were:

- Noiseless amplification of a phase quadrature signal was demonstrated. An electro-optic feedforward loop was used as the amplifying tool. Noiseless amplification had previously been demonstrated only for amplitude quadrature signals.
- The action of electro-optic feedback on the sensitivity of a thermal noise experiment was investigated. Theoretical modelling showed that the suppressed intensity noise inside a feedback loop leads to reduced radiation pressure noise, and therefore improved thermal noise measurement. Feedback was shown to give an impedance matched cavity the same measurement sensitivity as an ideal single ended cavity under less difficult experimental conditions. This model was one of the first to show that the statistics of the squashed light inside a feedback loop can enhance a measurement.
- The tilt-locking method was applied to a second harmonic generation cavity. The stability of this method was shown to be equal to the alternative modulation locking technique. Tilt-locking provided a second harmonic wave that was devoid of modulation and therefore better suited to applications in precision metrology.
- The second harmonic generator was used as the pump source for a squeezing OPA. Our OPA was locked to generate a stable source of amplitude squeezed light. The squeezed beam had a very low intensity of 10 to  $30\mu\text{W}$ . The maximum observed quantum noise reduction was 70% below the standard quantum limit. The high stability of the OPA experiment allowed the use of a new technique that gave a direct visualisation of the quantum correlations due to squeezed light.
- A model of a general QND experiment enhanced by feedforward and meter squeezing was developed. These two techniques were shown to work in parallel to improve overall QND performance. Using the squeezed light source from our OPA, we then implemented this scheme. A squeezed light beamsplitter was shown to have enhanced QND characteristics as a result of the feedforward. The combination of strong squeezing and efficient QND gave our QND experiment record signal transfer efficiency.

Obviously there are exciting new possibilities opened up by the above results which could not be explored in the three years of a doctorate. Below are some suggestions for

future experiments and possible applications of the techniques explored in the course of this thesis.

### **QND measurement of a squashed state**

Having generated a squeezed state and a stable QND system, one obvious direction would be to combine this system with a squashed state generator. Squashed light may only exist inside a feedback loop. The only method by which the effects of the in-loop noise suppression may be felt in the outside world is via a QND measurement of the squashed state. In chapter 5 this QND coupling was the radiation pressure noise. Alternatively, one may measure state squashing via the QND device of chapter 8. Precisely this experiment has been suggested previously [23], but now we have the hardware to actually do it.

In terms of technical details, the most important issue to be addressed before attempting this experiment is the generation of low frequency squeezing. A high gain feedback loop to generate squashed light is likely to work in a stable fashion up to 1MHz. Beyond this frequency, the time delay in the electronics will make the feedback unstable. To make a QND measurement of squashing therefore requires squeezing below 1MHz. We have not verified the low frequency performance of our squeezer, and further effort may be required to generate squeezing at these low frequencies.

### **Use of squashed light in a thermal noise measurement**

Apart from just probing squashed light, the experiment suggested in chapter 5 could actually be implemented. The easiest way to see the benefits of squashing in a thermal noise experiment would be to start with a system that has a very light weight cavity mirror. This increases the effect of radiation pressure noise so that the optimum laser power will be lower. The detection of the light for the intensity feedback will therefore be easier than a full experiment that would require the detection of Watts of optical power.

### **Destructive QND measurement**

As described in chapter 4, the most efficient method for feedforward QND measurement may in fact be to fully detect the input and modulate a squeezed beam to generate the signal output. We were unable to do this primarily due to a lack of laser power. Our squeezing could not be made sufficiently bright. Higher intensity squeezing may be realised by mixing the squeezing on an asymmetric beamsplitter with a bright beam. Modulating the bright beam will allow for efficient modulation of the output signal beam and correct coherent amplitude of the signal output beam.

### **Applications of correlation measurements**

I hope that the correlation measurements of chapter 7 are only the beginning of a new measurement technique. This method has potential as a detection scheme for EPR type entangled sources and other quantum states of light. Our group is currently building an EPR laser source that would be suitable for performing exactly those measurements modelled in chapter 7.

### **Injection of squeezing in to a bench-top gravitational wave detector**

The use of squeezing as a method to improve the performance of a gravitational wave interferometer was suggested many eons ago [26]. Squeezing has been shown to improve the performance of a Mach-Zehnder interferometer [129]. As yet, this idea has yet to be tested in a bench-top gravitational wave interferometer. An obvious step is, therefore, to build a power recycled arm cavity Michelson interferometer and use our stable squeezing to improve the quantum noise performance. This experiment is currently in preparation, and scheduled for completion in late 2001.

### **Investigation of GRIIRA**

Having come to the conclusion that GRIIRA is the reason for restricted squeezing in our OPA, there is a chance that eliminating this effect may lead to a new OPA squeezing frontier. On the basis of the work done by Furukawa *et al.* [38] possible lines of attack include 6% MgO doping instead of 5%, or the new method of crystal growth investigated in this reference. In the absence of GRIIRA, up to 10dB of squeezing should be achievable.

### **Application of feedforward to quantum computing**

All-optical quantum computation has recently been shown as a realistic possibility by Knill *et al.* [69]. The basis of this idea is the ability to control the flow of information in the computer using electro-optic feedforward. The demonstration of feedforward as a tool for enhancing QND indicates that quantum control using feedforward is a reliable technique and could one day form an important part of a quantum computer.



---

# Electronic noise

---

In all of our noise measurements made using the spectrum analyser, the electronic noise, or dark noise, has been eliminated. What does this mean? As an example we show the raw data for a measurement of the squeezed vacuum in figure A.1.

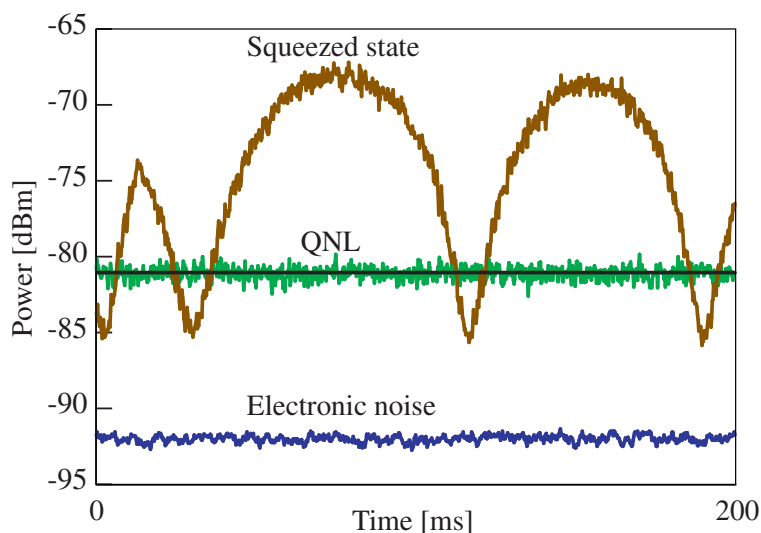


**Figure A.1:** The raw data for the measurement of the squeezing. RBW=300kHz, VBW=1kHz.

The electronic noise is due mostly to the amplifiers in the photodetector circuit. The noise could, in theory, be reduced by cooling the electronics. The problem with electronic noise is that its effect can be quite variable. The amount of noise can change between detectors and the amount of light used in a measurement may vary. The result is that the separation between the electronic noise and the photocurrent noise changes between measurements. Without subtracting electronic noise, it therefore becomes more difficult to compare the results of different measurements.

The clearance between the electronic noise and minimum photocurrent noise shown in this example is typical of our measurements. Obviously the subtraction will become meaningless if the photocurrent noise becomes too close to the electronic noise floor. In the limiting case when the two noise levels coincide, it would be ludicrous to conclude that the photocurrent has no noise at all. In fact, it is simply too small to measure properly. The bottom line is that electronic noise subtraction is useful and valid, but only if the photocurrent noise is obviously much larger than the electronic noise. The minimum clearance for any of the measurements in this thesis is about 5dB.

The effect of electronic noise in this example calculation is to reduce the observed amount of squeezing. By subtracting the electronic noise, the measured squeezing is



increased. To subtract the effect of electronic noise, we make the following definitions:

Measurement data =  $X$  dBm

Electronic noise =  $Y$  dBm,

Measurement data without the electronic noise =  $X'$  dBm;

The corrected values of  $X$  are then given by

$$X' = 10 \log_{10} \left( 10^{X/10} - 10^{Y/10} \right) \quad (\text{A.1})$$

This is repeated for the squeezing data and the quantum noise data. The result is the graph shown in figure A.2, where the electronic noise has been removed and the data is scaled by quantum noise.

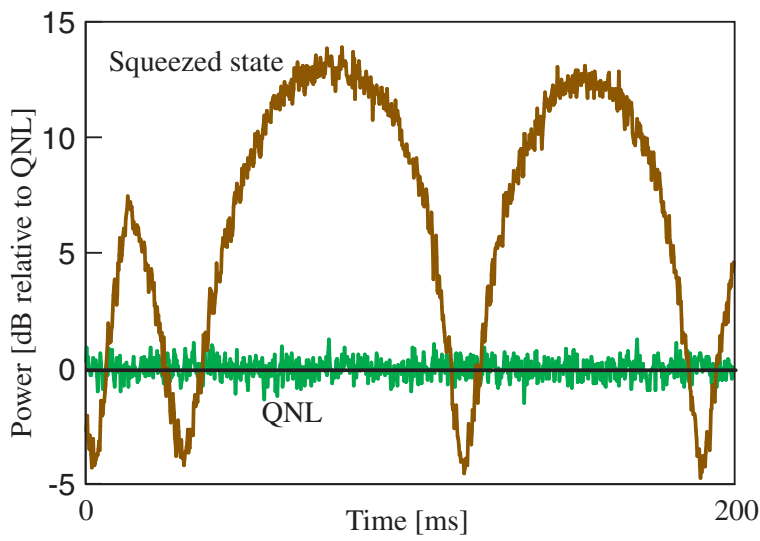


**Figure A.2:** The squeezing data with electronic noise removed and scaled to the quantum noise. RBW=300kHz, VBW=1kHz.

# Circuit designs

## Detectors

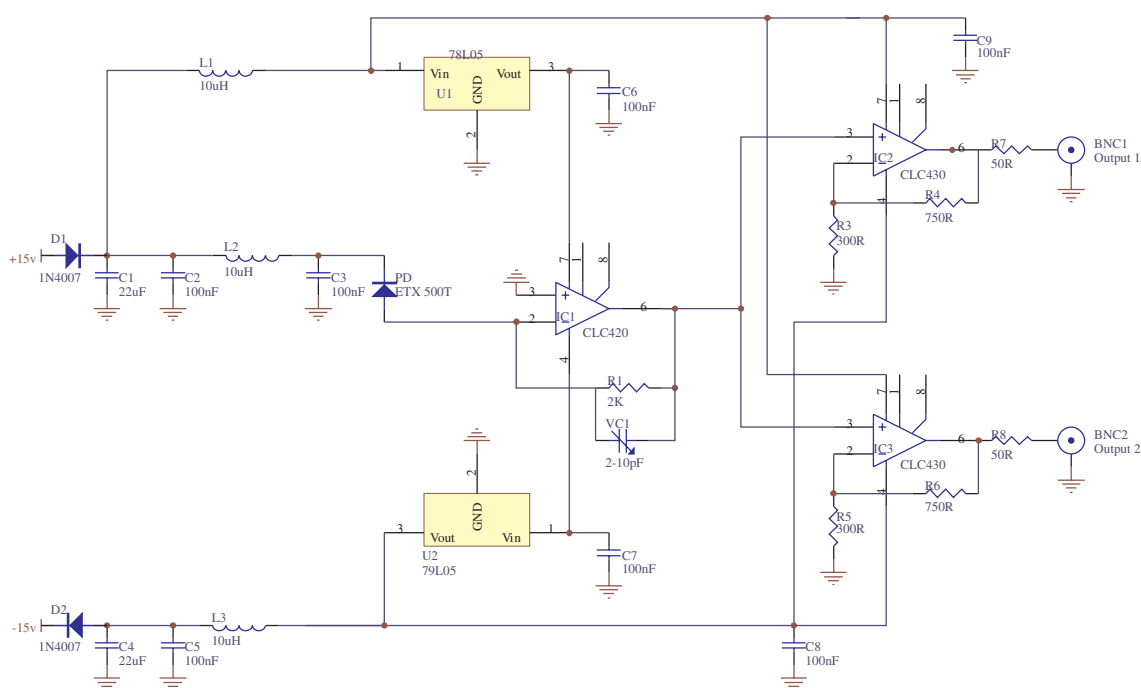


**Figure B.1:** Detectors used for squeezing detection. Original design: Malcolm Gray, Artwork: Russell Koehne

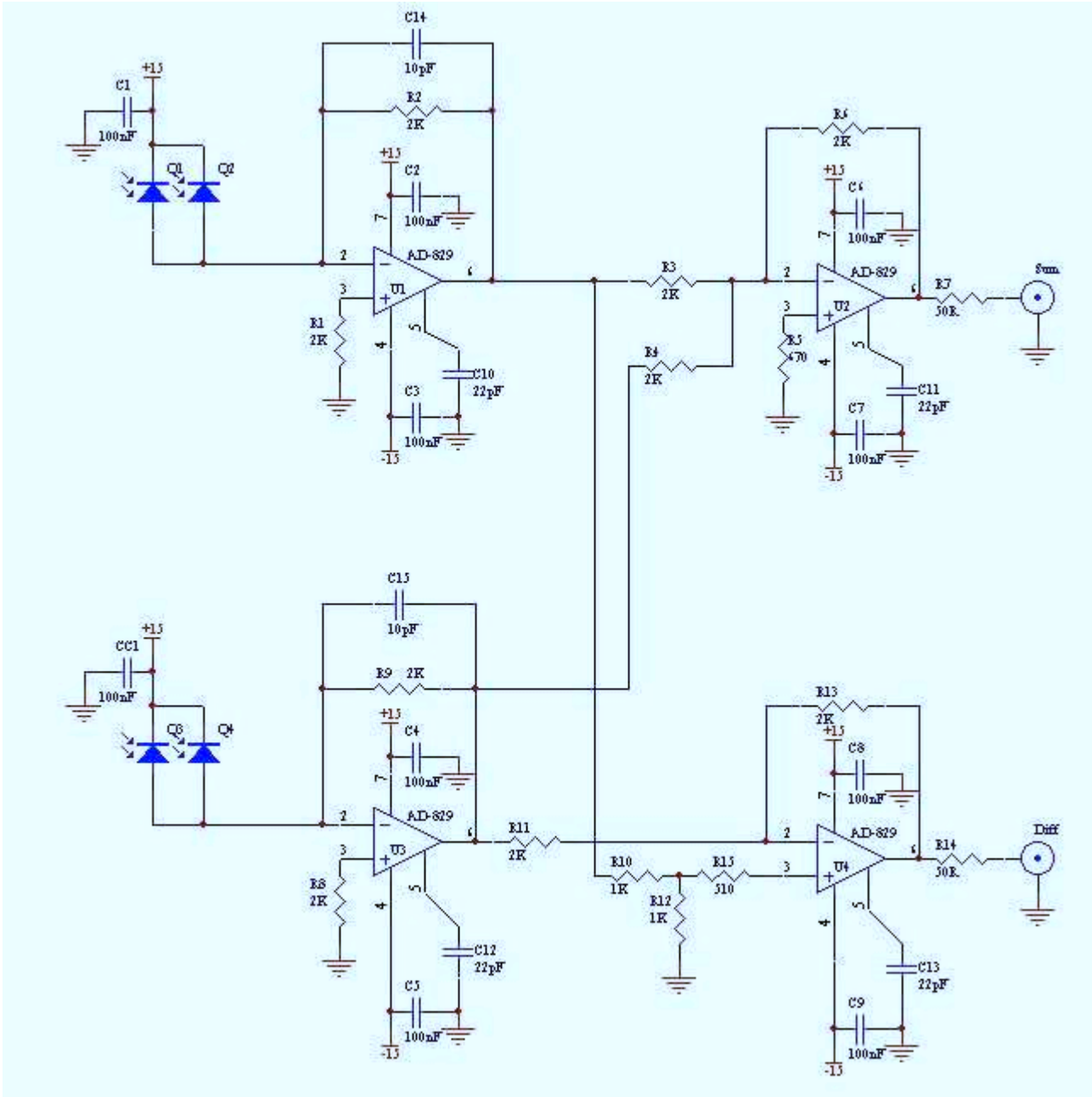


Figure B.2: Tilt detector. Original design: Malcolm Gray, Artwork: Russell Koehne

# Servos

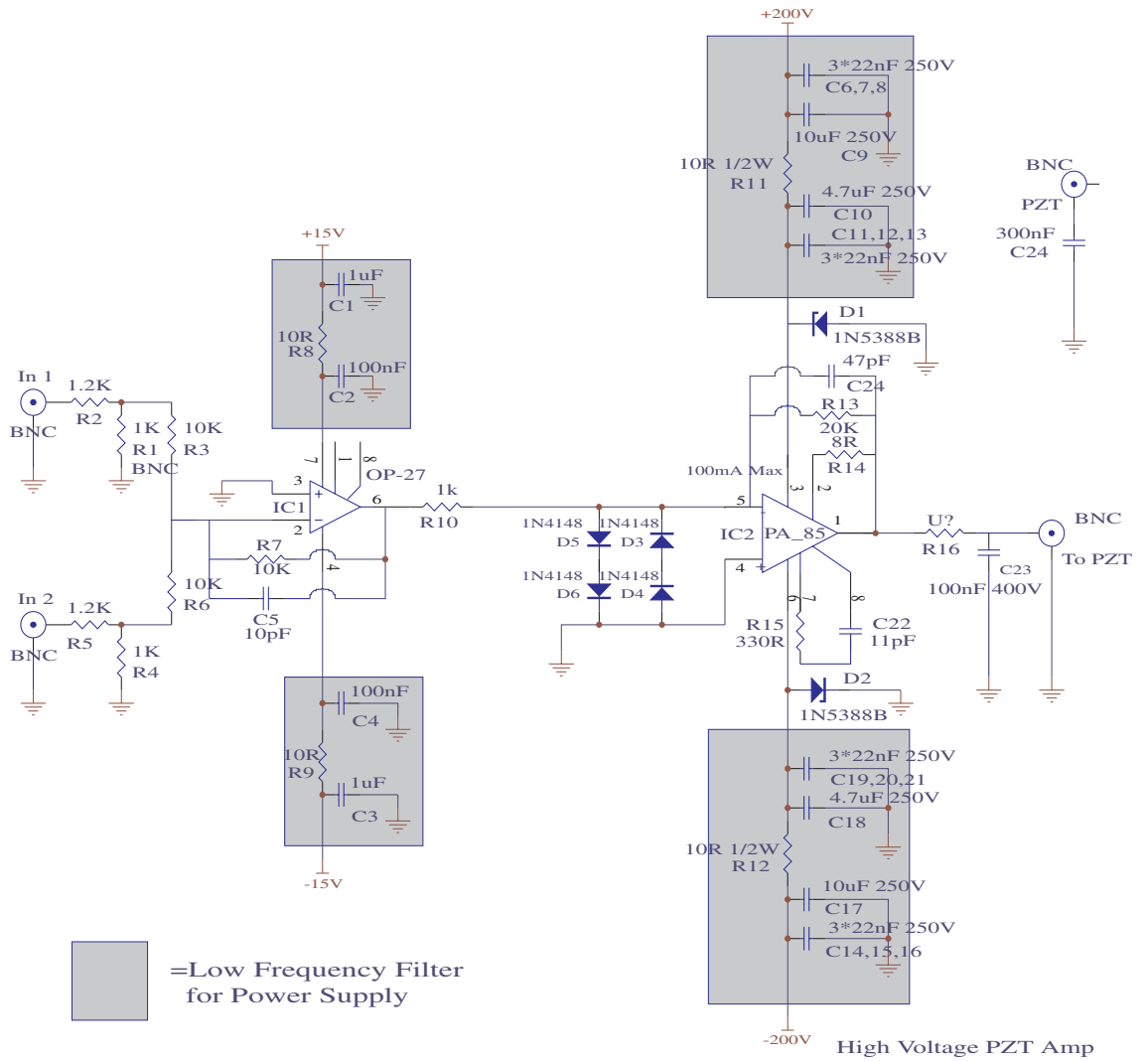


Figure B.3: Piezo servo. Original design: Malcolm Gray, Artwork: Russell Koehne

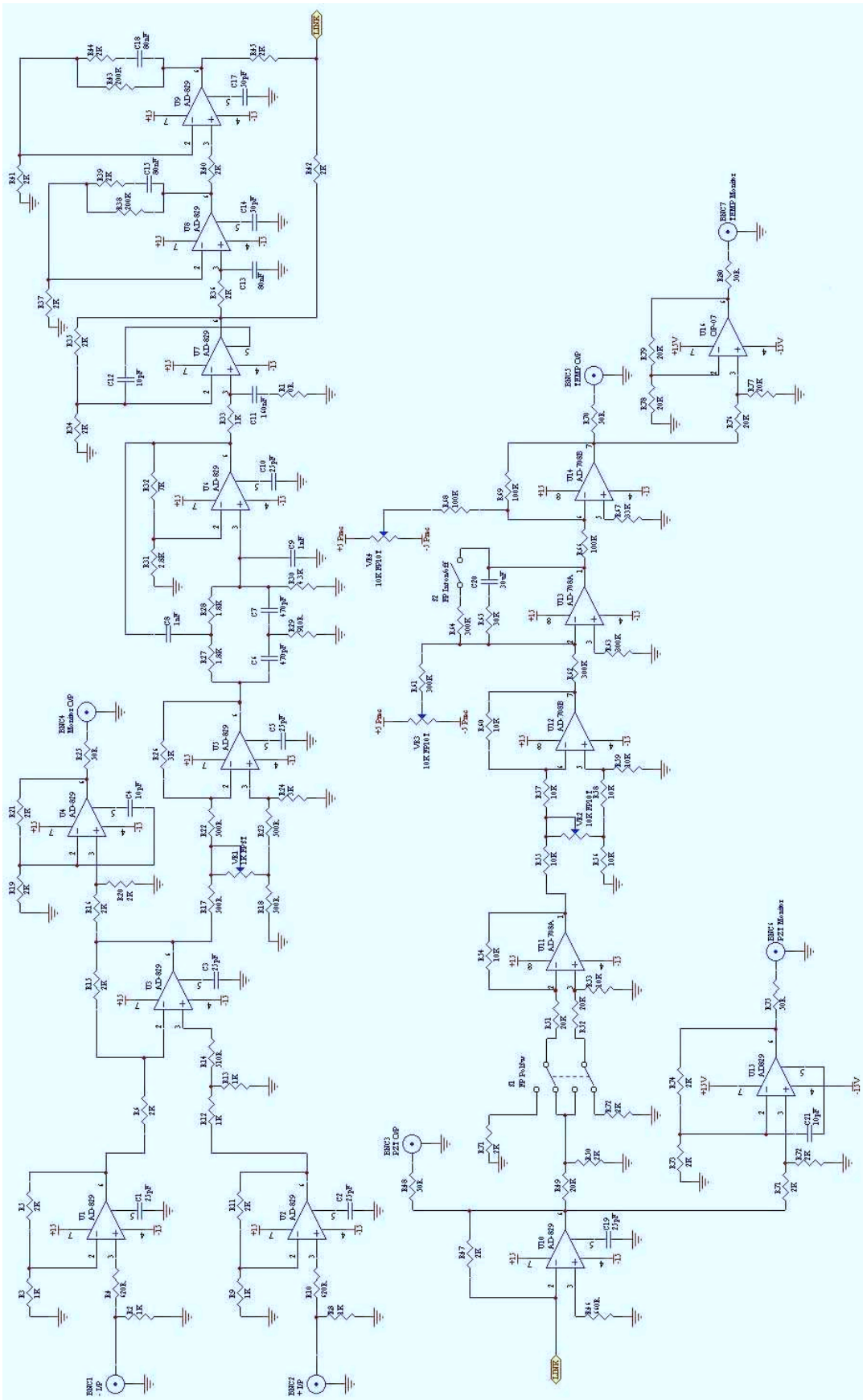
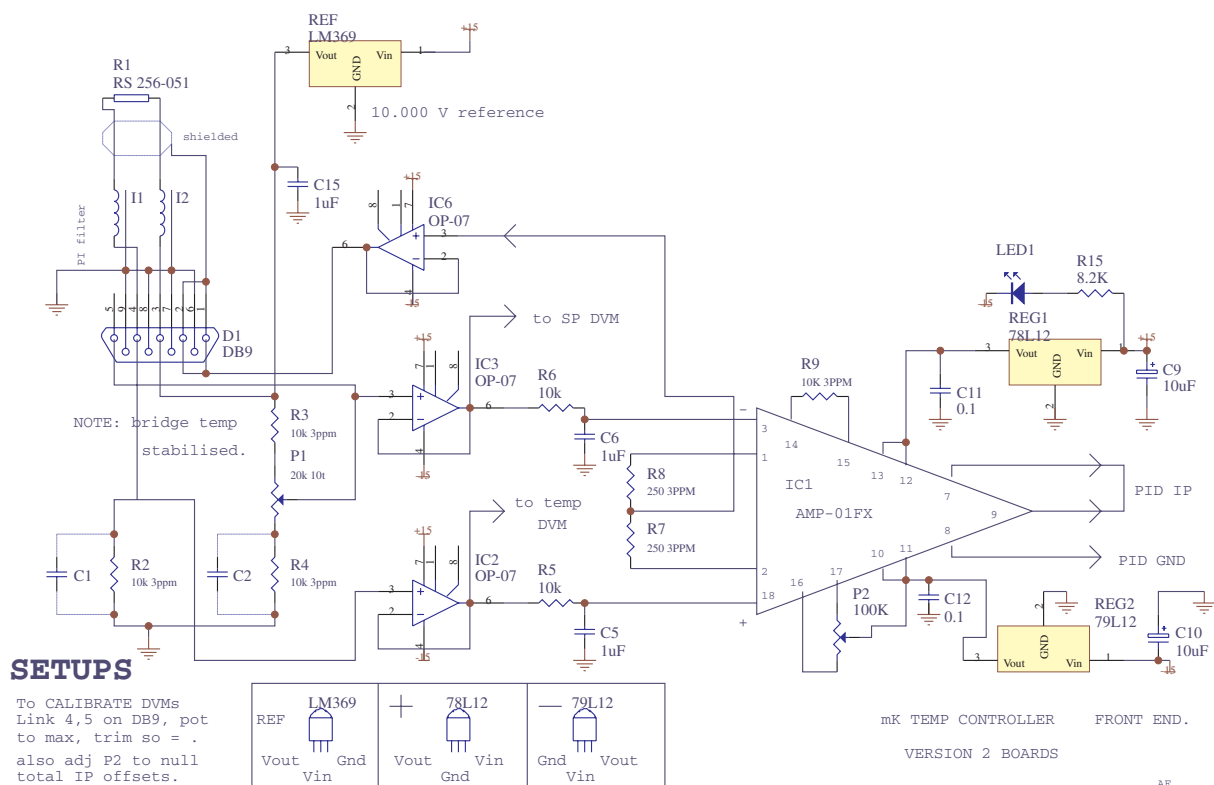
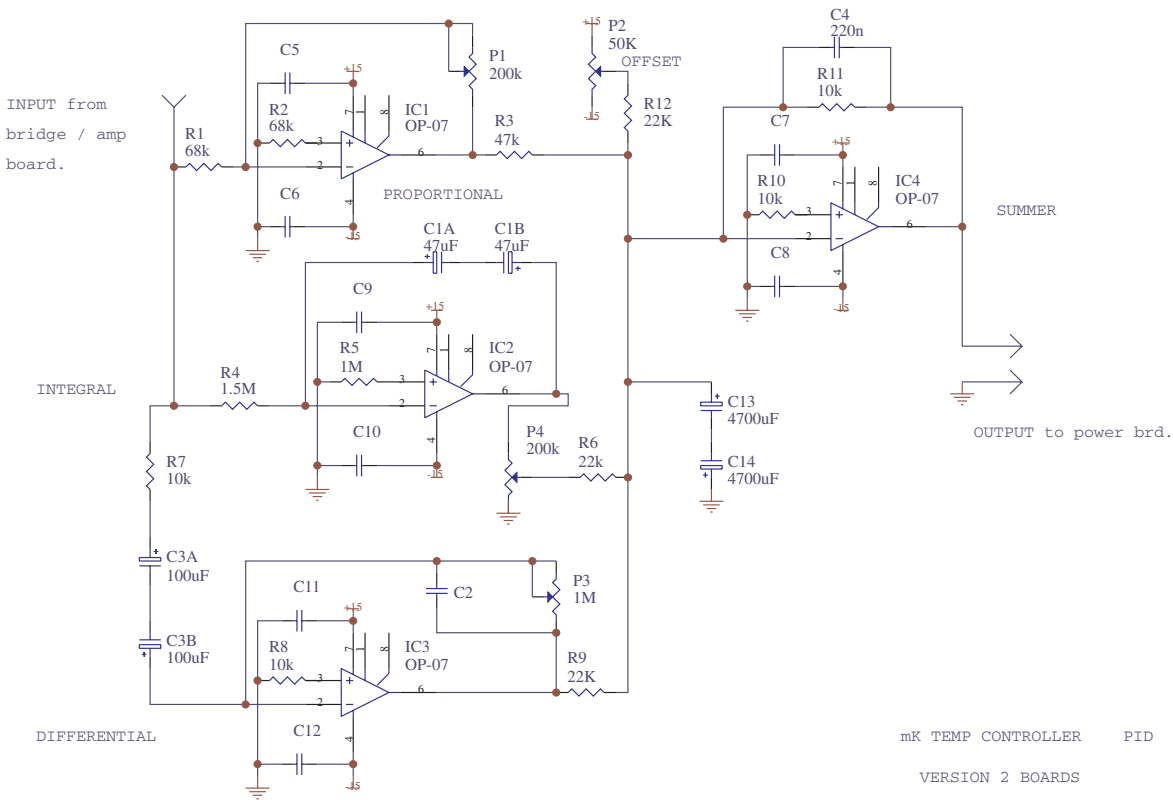


Figure B.4: Laser servo. Original design: Malcolm Gray, Artwork: Russell Koehne

## Millikelvin Temperature controller

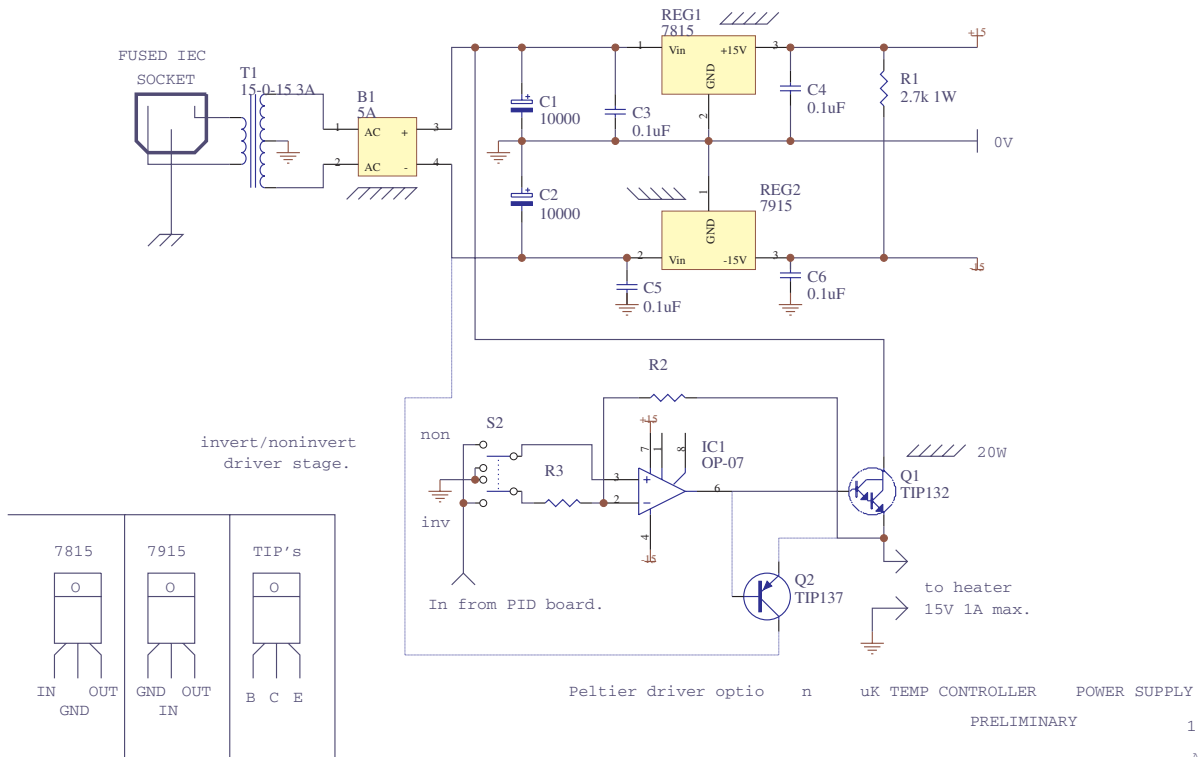


**Figure B.5:** Temperature controller front-end. Original design: Matthew Taubman. Modified :Andrew White and Ping Koy Lam



AE.

**Figure B.6:** Temperature controller PID. Original design: Matthew Taubman. Modified :Andrew White and Ping Koy Lam



1

AE.

**Figure B.7:** Temperature controller power supply. Original design: Matthew Taubman. Modified :Andrew White and Ping Koy Lam

## Signal box

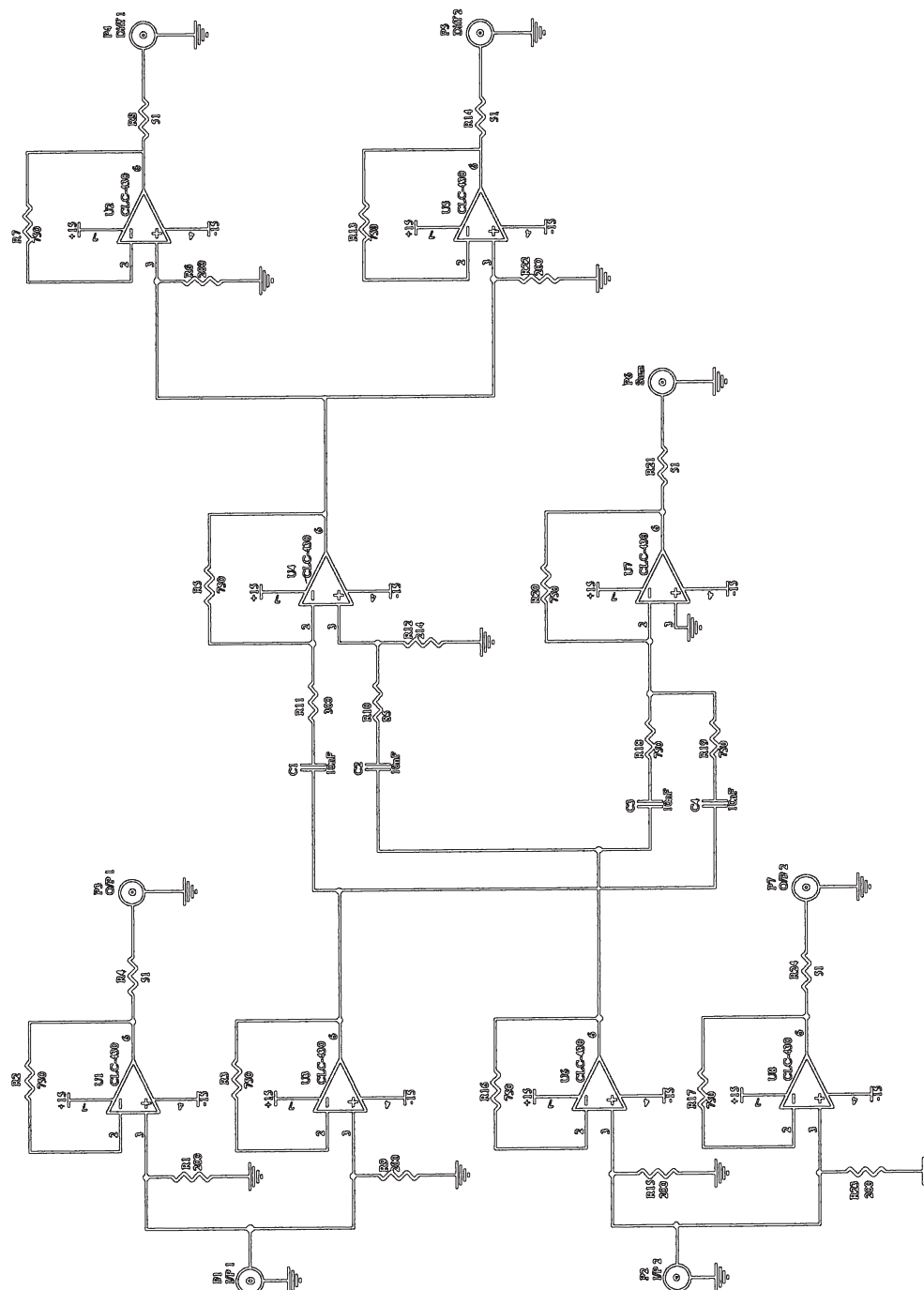


Figure B.8: Signal box. Original design: Malcolm Gray/Ben Buchler, Artwork: Russell Koehne





---

# Bibliography

---

- [1] M.E. Andersen, D.F. McAlister, M.G. Raymer, and M.C. Gupta. Pulsed squeezed-light generation in  $\chi^{(2)}$  nonlinear waveguides. *J. Opt. Am. Soc. B*, 14:3180, 1997.
- [2] A. Arie, S. Schiller, E. K. Gustafson, and R. L. Byer. Absolute frequency stabilization of diode-laser-pumped ndyag lasers to hyperfine transitions in molecular-iodine. *Opt. Lett.*, 17:1204, 1992.
- [3] A. Ashkin, G.D. Boyd, and J.M. Dziedzic. *IEEE J. Quantum Electron.*, QE-2:109, 1966.
- [4] K. Bencheikh, Ph. Grangier J.A. Levenson, and O. Lopez. Quantum nondemolition demonstration via repeated backaction evading measurements. *Phys. Rev. Lett.*, 75:3425, 1995.
- [5] K. Bencheikh, C. Simonneau, and J. A. Levenson. Cascaded quantum optical taps: a robust noiseless optical bus. *Phys. Rev. Lett.*, 78:34, 1997.
- [6] C.H. Bennett and D.P DiVincenzo. Quantum information and computation. *Nature*, 404:247, 2000.
- [7] K. Bergman and H.A. Haus. Squeezing in fibers with optical pulses. *Opt. Lett.*, 16:663, 1991.
- [8] J.D. Bhawalkar, Y. Mao, H. Po, A.K. Goyal, P. Gavrilovic, Y. Conturie, and S. Singh. High-power 390-nm laser source based on efficient frequency doubling of a tapered diode laser in an external resonant cavity. *Opt. Lett.*, 24:823, 1999.
- [9] S. Bose, K. Jacobs, and P.L. Knight. Preparation of nonclassical states in cavities with a moving mirror. *Phys. Rev. A*, 56:4175, 1997.
- [10] A. Bove, L. Di Fiore, E. Calloni, and A. Grado. Optimization of multipendular seismic suspensions for interferometric gravitational-wave detectors. *Euro. Phys. Lett.*, 40:601, 1997. and references herein.
- [11] R.W. Boyd. *Nonlinear Optics*. Academic Press, London, 1992.
- [12] V.B. Braginskii and Yu. I Voronsov. Quantum-mechanical limitations on macroscopic experiments and modern experimental techniques. *Sov. Phys. Usp.*, 17:644, 1975.
- [13] V. B. Braginsky, Yu. I. Vorontsov, and F. Ya. Khalili. *Sov. Phys. JETP*, 46:705, 1977.
- [14] V. B. Braginsky, Yu. I. Vorontsov, and K.S. Thorne. Quantum nondemolition measurements. *Science*, 209:547, 1980.

- 
- [15] G. Breitenbach, F. Illuminati, S. Schiller, and J. Mlynek. Broadband detection of squeezed vacuum: A spectrum of quantum states. *EuroPhys. Lett.*, 44:192, 1998.
- [16] G. Breitenbach, T. Müller, S. F. Pereira and J.-Ph. Poizat, S. Schiller, and J. Mlynek. Squeezed vacuum from a monolithic optical parametric oscillator. *J. Opt. Soc. Am. B*, 12:2304, 1995.
- [17] G. Breitenbach, S. Schiller, and J. Mlynek. Measurement of the quantum states of squeezed light. *Nature*, 387:471, 1997.
- [18] R. Bruckmeier, H. Hansen, and S. Schiller. Repeated quantum nondemolition measurements of continuous optical waves. *Phys. Rev. Lett.*, 79:1463, 1997.
- [19] R. Bruckmeier, H. Hansen, S. Schiller, and J. Mlynek. Realization of a paradigm for quantum measurements: The squeezed light beam splitter. *Phys. Rev. Lett.*, 79:43, 1997.
- [20] R. Bruckmeier, K. Schneider, S. Schiller, and J. Mlynek. Quantum nondemolition measurements improved by a squeezed meter input. *Phys. Rev. Lett.*, 78:1243, 1997.
- [21] B. C. Buchler, P. K. Lam, and T. C. Ralph. Enhancement of quantum nondemolition measurements with an electro-optic feed-forward amplifier. *Phys. Rev. A.*, 60:4943, 1999.
- [22] B.C. Buchler, M.B. Gray, D.A. Shaddock, T.C. Ralph, and D.E. McClelland. Suppression of classic and quantum radiation pressure noise by electro-optic feedback. *Opt. Lett.*, 24:259, 1999.
- [23] B.C. Buchler, E.H. Huntington, C.C. Harb, and T.C. Ralph. Feedback control of laser intensity noise. *Phys. Rev. A*, 57:1286, 1998.
- [24] J. Camp, H. Armandula, S. Bell, G Billingsley, M. Hrynevych, W. Kells, A. Lazarini, D. Li, S. Whitcomb, H. Yamamoto, and R. Weiss. *Requirements and Testing of LIGO Core Optics*. Universal Academy Press, Tokyo, 2000.
- [25] G.L. Cariolaro, P. Franco, M. Midrio, and G.L. Pierobon. Complete statistical characterization of signal and noise in optically amplified fiber channels. *IEEE J. Quantum Electron.*, 31:1114, 1995.
- [26] C. M. Caves. Quantum-mechanical noise in an interferometer. *Phys. Rev. D.*, 23:1693, 1981.
- [27] C. M. Caves. Quantum limits on noise in linear amplifiers. *Phys. Rev. D*, 26:1817, 1982.
- [28] M. Dakna, T. Anhut, T. Opatrný, L. Knöautll, and D.G. Welsch. Generating schrödinger-cat-like states by means of conditional measurements on a beam splitter. *Phys. Rev. A*, 55:3184, 1997.
- [29] R.C. Dorf and R.H. Bishop. *Modern Control Systems*. Prentice Hall, 2000.
- [30] R. W. P. Drever, J. L. Hall, F. W. Kowalski, J. Hough, G. M. Ford, A. J. Munley, and H. Ward. Laser phase and frequency stabilization using an optical resonator. *Appl. Phys. B*, 31:97, 1983.

- 
- [31] Lu-Ming Duan, G. Giedke, J. I. Cirac, and P. Zoller. Entanglement purification of gaussian continuous variable quantum states. *Phys. Rev. Lett.*, 84:4002, 2000.
- [32] R.C. Eckhardt, C.D. Nabors, W.J Kozlovsky, and R.L. Byer. Optical parametric oscillator frequency tuning and control. *J. Opt. Soc. Am. B*, 1991.
- [33] M. L. Eickhoff and J. L. Hall. Optical frequency standard at 532 nm. *IEEE Trans. Instrum. Meas.*, 44:155, 1995.
- [34] C. Fabre, M. Pinard, S. Bourzeix, A. Heidmann, E. Giacobino, and S. Reynaud. Quantum-noise reduction using a cavity with a movable mirror. *Phys. Rev. A*, 49:1337, 1994.
- [35] P.A. Franken, A.E. Hill, C.W. Peters, and G. Weinreich. Generation of optical harmonics. *Phys. Rev. Lett.*, 7:118, 1961.
- [36] I. Freitag, D. Golla, A. Tunnermann, H. Welling, and K. Danzmann. Diode-pumped solid-state lasers as light sources of michelson-type gravitational-wave detectors. *App. Phys. B*, 60:S 255, 1995.
- [37] S.R. Friberg, T. Mukai, and S. Machida. Dual quantum nondemolition measurements via successive soliton collisions. *Phys. Rev. Lett.*, 84:59, 2000.
- [38] Y. Furukawa, K. Kitamura, A. Alexandrovski, R. K. Route, M. M. Fejer, and G. Foulon. Green-induced infrared absorption in mgo doped linbo<sub>3</sub>. *Appl. Phys. Lett.*, 78:1970, 2001.
- [39] A. Furusawa, J. L. Serensen, S. L. Braunstein, C. A. Fuchs, H. J. Kimble, and E. S. Polzik. Unconditional quantum teleportation. *Science*, 282:706, 1998.
- [40] C. W. Gardiner and M. J. Collett. Input and output in damped quantum systems: Quantum stochastic differential equations and the master equation. *Phys. Rev. A*, 31:3761, 1985.
- [41] C.W. Gardiner. *Handbook of Stochastic Methods*. Springer-Verlag, Berlin, 2 edition, 1985.
- [42] V. Giovannetti, S., and P. Tombesi. Radiation pressure induced einstein-podolsky-rosen paradox. *Europhys. Lett.*, 54:559, 2001.
- [43] G.I. González and P.R. Saulson. Brownian motion of a torsion pendulum with internal friction. *Phys. Lett. A*, 201:12, 1995.
- [44] E. Goobar, A. Karlsson, and G. Bjork. Experimental realization of a semiconductor photon number amplifier and a quantum optical tap. *Phys. Rev. Lett.*, 71:2002, 1993.
- [45] P. Grangier, J. A. Levenson, and J.-P Poizat. Quantum non-demolition measurements in optics. *Nature*, 396:537, 1998.
- [46] P. Grangier, J.-Ph Poizat, P. Grelu, F. Castelli, L.A. Lugiato, and A. Sinatra. Back-action-induced squeezed light in a detuned quantum non-demolition scheme. *J. Mod. Opt.*, 41:2241, 1994.

- [47] M.B. Gray, D.A. Shaddock, C.C. Harb, and H.-A. Bachor. Photodetector designs for low-noise, broadband and high power applications. *Rev. Sci. Instr.*, 69:3755, 1998.
- [48] M.B. Gray, B.J.J. Slagmolen, K.G. Baigent, and D.E. McClelland. The anu thermal noise experiment. In *American Institute of Physics Conference Proceedings, no.523*, pp. 439, 2000.
- [49] M.B. Gray, A.J. Stevenson, H.-A. Bachor, and D.E. McClelland. Harmonic demodulation of nonstationary shot noise. *Opt. Lett.*, 64:68, 1993.
- [50] E. Gustafson, D. Shoemaker, K. Strain, and R. Weiss. Lsc white paper on detector research and development: Ligo t990080-00-d. Technical report, LIGO, 1999.
- [51] H. Haken. *Light and Matter I c Band 25, Teil 2 of Handbuch der Physik*. Springer, Berlin, 1970.
- [52] T.W. Hänsch and B. Couillaud. Laser frequency stabilization by polarization spectroscopy of a reflecting reference cavity. *Opt. Commun.*, 35:441, 1980.
- [53] C.C. Harb, M.B. Gray, H.-A. Bachor, R. Schilling, P. Rottengatter, I. Freitag, and H. Welling. Suppression of the intensity noise in a diode-pumped neodymium-yag nonplanar ring laser. *IEEE J. Quantum Electon.*, 30:2907, 1994.
- [54] C.C. Harb, T.C. Ralph, E.H. Huntington, D.E. McClelland, H.-A. Bachor, and I. Freitag. Intensity-noise dependence of nd:yag lasers on their diode-laser pump source. *J. Opt. Am Soc. B*, 14:2936, 1997.
- [55] H.A. Haus and J.A. Mullen. Quantum noise in linear amplifiers. *Phys. Rev.*, 128:2407, 1962.
- [56] H.A. Haus and Y. Yamamoto. Theory of feedback-generated squeezed states. *Phys. Rev. A*, 34:270, 1986.
- [57] A. Heidmann, Y. Hadjar, and M. Pinard. Quantum nondemolition measurement by optomechanical coupling. *Appl. Phys. B*, 64:173, 1997.
- [58] W. Heisenberg. *Z. Phys.*, 43:122, 1927.
- [59] M. J. Holland, M. J. Collett, D. F. Walls, and M. D. Levenson. Nonideal quantum nondemolition measurement. *Phys. Rev. A*, 42:2995, 1990.
- [60] F.L. Hong, J. Ishikawa, J. Yoda, J. Ye, L.S. Ma, and J.L. Hall. Frequency comparison of i-127(2)-stabilized nd : Yag lasers. *IEEE T. Instrum. Meas.*, 48:532, 1999.
- [61] J.C. Howell and J.A. Yeazell. Computation through entangling single photons in multipath interferometers. *Phys. Rev. Lett.*, 85:198, 2000.
- [62] E.H. Huntington, P.K. Lam, T.C. Ralph, D.E. McClelland, and H.-A. Bachor. Noiseless independent signal and power amplification. *Opt. Lett.*, 23:7, 1998.
- [63] N. Imoto and S. Saito. Quantum nondemolition measurement of photon number in a lossy optical kerr medium. *Phys. Rev. A*, 39:675, 1989.

- 
- [64] K. Jacobs, I. Tittoonen, H.M. Wiseman, and S. Schiller. Quantum noise in the position measurement of a cavity mirror undergoing brownian motion. *Phys. Rev. A*, 60:538, 1999.
- [65] K Jaconds, P. Tombesi, M.J. Collett, and D.F. Walls. Qnd measurement of cavity mode with radiation pressure. *Phys. Rev. A*, 49:1961, 1994.
- [66] I. Juwiler, A. Arie, A. Skliar, and G. Rosenman. Efficient quasi-phase-matched frequency doubling with phase compensation by a wedged crystal in a standing-wave external cavity. *Opt. Lett.*, 24:1236, 1999.
- [67] M. Kajima, N. Kusumi, S. Moriwaki, and N. Mio. Wide-band measurement of mechanical thermal noise using a laser interferometer. *Phys. Lett. A*, 264:251, 1999.
- [68] T.J. Kane and R. L. Byer. Monolithic, unidirectional single-mode nd:yag ring laser. *Opt. Lett.*, 10:65, 1985.
- [69] E. Knill, R. Laflamme, and G. Milburn. Efficient linear optics quantum computation. *Nature*, 409:46, 2001.
- [70] F. König, B. Buchler, T. Rechtenwald, A. Sizmann, and G. Leuchs. Qnd detection of the soliton photon number by spectral filtering. In *EQEC, Munich*, 2001.
- [71] W.J. Kozlovsky, C.D. Nabors, and R.L. Byer. Efficient second harmonic generation of a diode-laser-pumped cw nd:yag laser using monolithic mgo:linbo/sub 3/ external resonant cavities. *IEEE J. Quantum Electron.*, 24:913, 1988.
- [72] P. K. Lam, T. C. Ralph, E. H. Huntington, and H.-A. Bachor. Noiseless signal amplification using positive electro-optic feed-forward. *Phys. Rev. Lett.*, 79:1471, 1997.
- [73] P.K. Lam. *Applications of quantum electro-optic control and squeezed light*. PhD thesis, Department of Physics, The Austalian National University, 1999.
- [74] P.K. Lam, I. Freitag, M. Bode, A. Tunnermann, and H. Welling. High average power q-switched second harmonic generation with diode-pumped nd-yag laser. *Electronic Letters*, 34:666, 1998.
- [75] P.K. Lam, Ralph T.C., Buchler B.C., McClelland D.E., Bachor H.-A., and Gao J. Optimization and transfer of vacuum squeezing from an optical parametric oscillator. *J. Opt. B*, 1:469, 1999.
- [76] L. Landau and E. Lifshitz. *Course of Theoretical Physics: Statistical Physics*. Pergamon, New York, 1958.
- [77] J. A. Levenson, I. Abram, T. Rivera, P. Fayolle, J. C. Garreau, and P. Grangier. Quantum optical cloning amplifier. *Phys. Rev. Lett.*, 70:267, 1993.
- [78] H. Mabuchi, E.S. Polzik, and H.J. Kimble. Blue-light-induced infrared absorption in knbo<sub>3</sub>. *J. Opt. Soc. Am. B*, 11:2023, 1994.
- [79] S. Machida and Y. Yamamoto. Observation of sub-poissonian photoelectron statistics in a negative feedback semiconductor laser. *Opt. Comm.*, 57:290, 1986.

- [80] S. Mancini and P. Tombesi. Quantum-noise reduction by radiation pressure. *Phys. Rev. A*, 49:4055, 1994.
- [81] S. Mancini, D. Vitali, and P. Tombesi. Motional squashed states. *J. Opt. B*, 2:190, 2000.
- [82] K. Matsumoto and T. Honda. Modulation-free iodine-stabilized green yag laser with a common-path interferometer. *Opt. Comm.*, 127:283, 1996.
- [83] B.J. Meers and K.A. Strain. Modulation, signal, and quantum noise in interferometers. *Phys. Rev. A*, 44:4693, 1991.
- [84] J. Mertz, A. Heidmann, C. Fabre, E. Giacobino, and S. Reynaud. Observation of high-intensity sub-poissonian light using an optical parametric oscillator. *Phys. Rev. Lett.*, 64:2897, 1990.
- [85] E. Merzbacher. *Quantum Mechanics*. John Wiley and Sons, 2 edition, 1970.
- [86] G.J. Milburn and D.F. Walls. Squeezed states and intensity fluctuations. *Phys. Rev. A*, 27:392, 1983.
- [87] N. Mio and K. Tsubono. Observation of an effect due to nonstationary shot noise. *Phys. Lett. A*, 164:255, 1992.
- [88] A. F. Pace, M. J. Collett, and D. F. Walls. Quantum limits in interferometric detection of gravitational radiation. *Phys. Rev. A*, 47:3173, 1993.
- [89] S. F. Pereira, Z. Y. Ou, and H. J. Kimble. Backaction evading measurements for quantum nondemolition measurements and quantum optical tapping. *Phys. Rev. Lett.*, 72:214, 1994.
- [90] M. Pinard, P. F. Cohadon, T. Briant, and A. Heidmann. Full mechanical characterization of a cold damped mirror. *Phys. Rev. A.*, 63:3808, 2000.
- [91] M. Pinard, C. Fabre, and A. Heidmann. Quantum-nondemolition measurement of light by a piezoelectric crystal. *Phys. Rev. A.*, 51:2443, 1995.
- [92] J. P. Poizat and P. Grangier. Experimental realisation of a quantum tap. *Phys. Rev. Lett.*, 70:271, 1993.
- [93] J.P. Poizat, J.F. Roch, and P. Grangier. Characterization of quantum-nondemolition measurements in optics. *Ann. Phys.-Paris*, 19:265, 1994.
- [94] E.S. Polzik, J. Carri, and H.J. Kimble. Atomic spectroscopy with squeezed light for sensitivity beyond the vacuum-state limit. *Appl. Phys. B*, 55:279, 1992.
- [95] C.A.J. Putman, B.G. De Grooth, N. Van Hulst, and J. Greve. A detailed analysis of the optical beam deflection technique for use in atomic force microscopy. *J. Appl. Phys.*, 72:6, 1992.
- [96] T. C. Ralph. Robust transmission and reconstruction of fragile optical state. *Phys. Rev. A*, 56:4187, 1997.
- [97] T.C. Ralph and P.K. Lam. Teleportation with bright squeezed light. *Phys. Rev. Lett.*, 81:5668, 1998.

- 
- [98] J. F. Roch, J. Ph Poizat, and P. Grangier. Sub-shot-noise manipulation of light using semiconductor emitters and receivers. *Phys. Rev. Lett.*, 71:2006, 1993.
- [99] J. F. Roch, G. Roger, P. Grangier, J. M. Courty, and S. Reynaud. Quantum non-demolition measurements in optics: a review and some recent experimental results. *Applied Phys. B*, 55:291, 1992.
- [100] J. F. Roch, K. Vigneron, A. Sinatra Ph. Grelu, J. Ph. Poizat, and Ph. Grangier. Quantum nondemolition measurements using cold trapped atoms. *Phys. Rev. Lett.*, 78:634, 1997.
- [101] B.E.A. Saleh and T.C. Teich. *Fundamentals of Photonics*. John Wiley & Sons, 1991.
- [102] P.R. Saulson. *Fundamentals of Interferometric Gravitational Wave Detectors*. World Scientific Singapore, 1994.
- [103] K. Schneider, R. Bruckmeier, H. Hansen, S. Schiller, and J. Mlynek. Bright squeezed-light generation by a continuous-wave semimonolithic parametric amplifier. *Opt. Lett.*, 21:1396, 1996.
- [104] K. Schneider, M Lang, J. Mlynek, and S. Schiller. Generation of strongly squeezed continuous-wave light at 1064 nm. *Opt. Ex.*, 2:59, 1997.
- [105] K. Schneider, S. Schiller, J. Mlynek M. Bode, and I. Freitag. 1.1-w single-frequency 532-nm radiation by second-harmonic generation of a miniature nd-yag ring laser. *Opt. Lett.*, 21:1999, 1996.
- [106] M.O. Scully and M.S. Zubairy. *Quantum Optics*. Cambridge University Press, 1997.
- [107] D.A. Shaddock. *Advanced interferometry for gravitational wave detection*. PhD thesis, Department of Physics, The Australian National University, 2000.
- [108] D.A. Shaddock, M. B. Gray, and D. E. McClelland. Frequency locking a laser to an optical cavity by use of spatial mode interference. *Opt. Lett.*, 24:1499, 1999.
- [109] J.H. Shapiro. Optical waveguide tap with infinitesimal insertion loss. *Opt. Lett.*, 5:351, 1980.
- [110] J.H. Shapiro, G Saplakoglu, S.-T Ho, B.E.A. Saleh, and M.C. Teich. Theory of light detection in the presence of feedback. *J. Opt. Soc. Am. B*, 4:1604, 1987.
- [111] A. Siegman. *Lasers*. Univeral science books, 1986.
- [112] R.E. Slusher, L.W. Hollberg, B. Yurke, J.C. Mertz, and J.F. Valley. Observation of squeezed states generated by four-wave mixing in an optical cavity. *Phys. Rev. Lett.*, 55:2409, 1985.
- [113] J.L. Sorensen, J. Hald, N. Jorgensen, J. Erland, and E.S. Polzik. Squeezing with  $\chi^{(2)}$  for atomic physics and spectroscopy. *Quantum Semicl. Opt.*, 9:239, 1997.
- [114] G.E. Stedman. Ring-laser tests of fundamental physics and geophysics. *Rep. Prog. Phys.*, 60:615, 1997.
- [115] M. S. Taubman, H. Wiseman, D. E. McClelland, and H.-A. Bachor. Intensity feedback effects on quantum-limited noise. *J. Opt. Soc. Am. B*, 12:1792, 1995.



- [116] K. S. Thorne, R. W. P. Drever, C. M. Caves, M. Zimmermann, and V. D. Sandberg. Quantum nondemolition measurements of harmonic oscillators. *Phys. Rev. Lett.*, 40:667, 1978.
- [117] D. F. Walls and G. J. Milburn. *Quantum Optics*. Springer-Verlag, Berlin, 1 edition, 1994.
- [118] H. Wang, Y. Zhang, Q. Pan, H. Su, A. Porzio, C. Xie, and Kunchi Peng. Experimental realization of a quantum measurement for intensity difference fluctuation using a beam splitter. *Phys. Rev. Lett.*, 82:1414, 1999.
- [119] A.G. White. *Classical and quantum dynamics of optical frequency conversion*. PhD thesis, Australian National University, 1997.
- [120] H.M. Wiseman. Quantum theory of continuous feedback. *Phys. Rev. A*, 49:2133, 1994.
- [121] H.M. Wiseman. Using feedback to eliminate back-action in quantum measurements. *Phys. Rev. A*, 51:2459, 1995.
- [122] H.M. Wiseman. In-loop squeezing is like real squeezing to an in-loop atom. *Phys. Rev. Lett.*, 81:3840, 1998.
- [123] H.M. Wiseman. Squashed states of light: theory and applications to quantum spectroscopy. *J. Opt. B*, 1:459, 1999.
- [124] H.M. Wiseman and G. J. Milburn. Squeezing via feedback. *Phys. Rev. A*, 49:1350, 1994.
- [125] H.M. Wiseman, M.S. Taubman, and H.-A Bachor. Feedback-enhanced squeezing in second harmonic generation. *Phys. Rev. A*, 51:3227, 1995.
- [126] L.A. Wu, H.J. Kimble, J.L. Hall, and H. Wu. Generation of squeezed states by parametric down conversion. *Phys. Rev. Lett.*, 57:2520, 1986.
- [127] L.A. Wu, M. Xiao, and H.J. Kimble. Squeezed states of light from an optical parametric oscillator. *J. Opt. Soc. Am. B*, 4:1465, 1987.
- [128] C.P. Wyss, D.N. Wright, B.T. King, D.P. Mcleod, S.J. Cooper, and G.E. Stedman. Collision broadening and quantum noise in a very large laser gyroscope. *Opt. Comm.*, 174:181, 2000.
- [129] M. Xiao, L.-A. Wu, and H.J. Kimble. Precision measurement beyond the shot-noise limit. *Phys. Rev. Lett.*, 59:278, 1987.
- [130] K. Yamamoto, S. Otsuka, M. Ando, K. Kawabe, and K. Tsubono. Experimental study of thermal noise caused by an inhomogeneously distributed loss. *Phys. Lett. A*, 280:289, 2001.
- [131] Y. Yamamoto, N. Imoto, and S. Machida. Amplitude squeezing in a semiconductor laser using quantum nondemolition measurement and negative feedback. *Phys. Rev. A*, 33:3243, 1986.
- [132] Y. Yamamoto, S. Machida, and O. Nilsson. Amplitude squeezing in a pump-noise-suppressed laser oscillator. *Phys. Rev. A*, 34:4025, 1986.

- 
- [133] A. Yariv. *Quantum Electronics*. John Wiley & Sons, 3 edition, 1989.
- [134] J. Ye, L. Robertsson, S. Picard, L.-S. Ma, and J. L. Hall. Absolute frequency atlas of molecular i-2 lines at 532 nm. *IEEE Trans. Instrum. Meas.*, 48:544, 1999.
- [135] C. X. Yu, H. A. Haus, and E. P. Ippen. Soliton squeezing at the gigahertz rate in a sagnac loop. *Opt. Lett*, 26:669, 2001.
- [136] H.P. Yuen and J.H. Shapiro. Optical communication with two-photon coherent states. i. quantum-state propagation and quantum-noise reduction. *IEEE Trans. Inf. Theory*, 26:78, 1980.
- [137] B Yurke. Use of cavities in squeezed state generation. *Phys. Rev. A*, 20:408, 1984.